Dissertation
submitted to the
Faculty of Chemistry and Earth Sciences
of the Ruperto-Carola University of Heidelberg
for the degree of
Doctor of Natural Sciences

Put forward by
Master of Natural Science: Xicai Pan
Born in: Yunxian, China

Oral examination: 12 April 2011

Hydraulic and Thermal Dynamics at Various Permafrost Sites on the Qinghai-Tibet Plateau

Referees: Prof. Dr. Kurt Roth

Prof. Dr. Olaf Bubenzer

Abstract

Heat transfer mechanisms governing the permafrost-atmosphere interaction are essential to understand present permafrost degradation. Hydraulic and thermal dynamics of various active layers at four different permafrost sites on the QTP were investigated with various geophysical methods and soil-weather monitoring stations. Complex field data were detected and processed with appropriate methods. The principal physical processes controlling the active-layer thermal regime were characterized with a surface energy balance method at Chumaer, Qumahe and Tianshuihai. As a geophysical tool for characterizing soil properties, multi-channel GPR was further explored. Through Monte Carlo uncertainty analysis and field tests, the accuracy of the multi-channel GPR method and its capability of quantifying field-scale hydraulic properties and processes was validated at a non-permafrost sandy site. Based on precise soil temperature and soil water content data, heat transfer in various active layers were characterized with a transfer function method. Given the characteristics of ground heat transfer at the study sites, an inverse method for seasonal thermal conductivity parameterization was tested. Combining the transfer function method and the multi-channel GPR, a field-scale thermal conductivity parameterization was proposed at the end.

Kurzfassung

Temperaturtransfermechanismen, welche den Austausch von Permafrost und Atmosphäre dominieren, sind von essentieller Bedeutung um den derzeitigen Rückgang des Permafrost zu verstehen. Die hydraulische und thermische Dynamik verschiedener aktiver Schichten an vier verschiedenen Permafrost beobachtungsstellen auf dem QTP wurden mit Hilfe mehrerer geophysikalischer Methoden und Boden-Atmosphäre Beobachtungsstationen untersucht. Komplexe Felddaten wurden ausgewählt und mit passenden Methoden prozessiert. Die grundlegenden physikalischen Prozesse, welche das thermische Regime der aktiven Schicht dominieren, wurden mit der Oberflächenenergiebilanzmethode bei Chumaer, Qumahe und Tianshuihai charakterisiert. Multikanalgeoradar wurde als geophysikalische Methode zur Charakterisierung von Bodeneigenschaften tiefer gehend untersucht. Die Genauigkeit der Multikanalgeoradarmethode und ihre Tauglichkeit zur Quantifizierung hydraulischer Eigenschaften und Prozesse auf der Feldskala wurde mit Hilfe einer Monte-Carlo Analyse zur Fehlerabschätzungs und einem Test auf einem nicht dauerhaft gefrorenen sandigem Feld validiert. Basierend auf präzisen Bodentemperatur- und Bodenwassergehaltsmessungen wurde der Temperaturtransfer in verschiedenen aktiven Schichten mit Hilfe von Transferfunktionen charakterisiert. Eine inverse Methode zur Parametrisierung der saisonalen thermischen Leitfähigkeit wurde mit den gegebenen Charakteristika des Temperaturtransfers im Untergrund an den Testfeldern untersucht. Mit der Kombination der Transferfunktions- und der Multikanalgeoradarmethode wurde eine Parametrisierung der thermischen Leitfähigkeit auf der Feldskala abgeleitet.

Acknowledgments

This research project could not be finished like this without the aid and assistance of many people and institutions. The financial support of the Deutsche Forschungsgemeinschaft (through project RO 1080/10-2) are gratefully acknowledged. The field work was undertaken with Prof. Qihao Yu, Prof. Huijun Jin and other researchers from Cold and Arid Regions Environmental and Engineering Research Institute, Chinese Academy of Science. First and foremost, I would like to sincerely acknowledge Prof. Kurt Roth. Without his support, I can not imagine I can make such progress during the past years. Through various interesting academic trainings, I gained many precious skills throughout my graduate education. I am grateful to his excellent advice and patient guidance throughout the study and valuable insights, as well as suggestions and discussions in this research project.

Dr. Ute Wollschläger is gratefully acknowledged for helping me quickly get into this work. With her generous assistance and advice, I finally found a suitable field site for the GPR experiment. Her friendship and encouragement inspired me during the difficult times throughout my study. With her excellent scholarship and profound expertise in the field of hydro-geophysics and permafrost, she provided insightful ideas, suggestions as well as helps in scientific writing.

I would like to thank Prof. Olaf Bubenzer who agreed to be the second referee for my thesis and provided me some invaluable insights and suggestions in geographical consideration.

Design, setup, and maintenance of the weather stations were taken lots of efforts. All the involved peoples are gratefully appreciated. Assistance of using GPR and and programming for data processing from Dr. Holger Gerhards and Klaus Schneider is greatly appreciated. I would like to thank Partick Klenk and Jens Buchner for their help of suggestions and writing correction for my thesis. Discussions about soil heat transfer and associated mathematic problems with Ulrike Niederle and Gabriele Schenk are gratefully appreciated.

I would like to acknowledge Angelika Gassama, Rebecca Ludwig, Benny Antz for their generous assistance to drive the bus for the field experiments. I also thank help from other colleagues and friends in Heidelberg.

Finally I would like to thank my family. Their encouragement and support accompanied with me during this impressive period.

Contents

List of Figures

List of Tables

Symbols

Lowercase Latin Symbols

a	antenna separation [m]
c_0	free space electromagnetic propagation velocity [m s^{-1}]
c_h	specific heat capacity [$Jkg^{-1}K^{-1}$]
d	reflector depth [m]
$d_{1,2}$	layered reflector depth from surface [m]
f	frequency [Hz]
g	gravity [m s^{-2}]
j_h	sensible heat flux [W m^{-2}]
j_h^s	heat flux for warming ground [W m^{-2}]
j_h^l	heat flux for thawing ground ice [W m^{-2}]
j_g	ground heat flux [W m^{-2}]
j_{h1}^z	ground heat flux estimated with a shallow reference depth z [W m^{-2}]
j_{h2}^z	ground heat flux estimated with a deep reference depth z [W m^{-2}]
j_{nr}	net radiative flux [W m^{-2}]
j_v	vapor flux [mm s^{-1}]
j_v^E	vapor flux estimated from the energy balance model [mm s^{-1}]
j_v^W	vapor flux estimated from the water balance model [mm s^{-1}]
j_{vl}	latent heat flux [W m^{-2}]
l	characteristic length [m]
n_f	freezing n-factor [-]
n_t	thawing n-factor [-]
p	period of CS616 [μ s]
p_a	period of CS616 in air [μ s]
p_w	period of CS616 in water [μ s]
r_t	residual of the projected soil temperature during thawed period [℃]
r_f	residual of the projected soil temperature during frozen period [℃]
t	time [s]
t_a	travel time in air [ns]
t_0	initial time [s]
t_{refl}	measured travel time [ns]
t_{model}	modeled travel time [ns]

t_w	travel time in water [ns]
v	velocity [m s^{-1}]
x_0	central measurement position [m]
x_n	measurement position [m]
z	depth below ground surface [m]
z_p	projected depth below ground surface [m]
z_r	reference depth [m]

Uppercase Latin Symbols

A	amplitude of temperature [℃]
AF	autumn freezing period
A_0	amplitude of ground surface temperature [℃]
C	volumetric heat capacity [J $m^{-3}K^{-1}$]
C_a	heat capacity of air [J $kg^{-1}K^{-1}$]
D	thermal diffusivity of a soil [m^2s^{-1}]
D_h^{app}	apparent thermal diffusivity [m^2s^{-1}]
D_f	apparent thermal diffusivity of frozen soil [m^2s^{-1}]
D_t	apparent thermal diffusivity of thawed soil [m^2s^{-1}]
DDT_s	surface thawing index [℃· day]
DDF_s	surface freezing index [℃· day]
E	areal density of soil heat [MJ m^{-2}]
E_s	areal density of the heat used for warming the soil [MJ m^{-2}]
E_l	areal density of the heat used for thawing ground ice [MJ m^{-2}]
E^g	energy transfered by ground heat flux [J]
E^{nr}	energy transfered by net radiation [J]
E^{vl}	energy transfered by vapor flux [J]
E^h	energy transfered by surface sensible heat flux [J]
G	ground heat flux at ground surface [MJ m^{-2}]
I	freezing or thawing index [℃· day]
I_{fs}	surface freezing index [℃· day]
I_{ts}	surface thawing index [℃· day]
I_{fa}	air freezing index [℃· day]
I_{ta}	air thawing index [℃· day]
K	soil thermal conductivity [W $m^{-1}K^{-1}$]
K_{eff}	effective soil thermal conductivity [W $m^{-1}K^{-1}$]
K_a, K_f, K_t	thermal conductivity of air, frozen soil or thawed soil [W $m^{-1}K^{-1}$]
K_h	heat transfer coefficient of turbulent flow [m^2 s^{-1}]
K_p	coefficient of CS616 [-]
L	volumetric latent heat of soil fusion [J m^{-3}]

L_w	volumetric latent heat of water fusion [J m^{-3}]
L_{sf}	volumetric latent heat of water from solid to fluid [J m^{-3}]
L_{fv}	volumetric latent heat of water from fluid to vapor [J m^{-3}]
$L\downarrow$	incoming longwave radiation [MJ m^{-2}]
$L\uparrow$	outgoing longwave radiation [MJ m^{-2}]
LE	latent heat flux at ground surface [MJ m^{-2}]
MAAT	mean annual air temperature [℃]
MAST	mean annual ground surface temperature [℃]
N_f	freezing N-factor [-]
N_t	thawing N-factor [-]
NR	net radiation [MJ m^{-2}]
Nu	Nusselt number
P	period 365 or 8760 [*day or s*]
Pe	Prandtl number
QTP	Qinghai-Tibet Plateau
Re	Reynolds number
Ra	Rayleigh number
R^E	residual of latent heat flux [MJ $m^{-2}d^{-1}$]
R^W	residual of surface vapor flux [mm d^{-1}]
$S1, 2$	distance between the transmitter and the receiver [m]
SST	spring-summer thawing period
Ste	the Stefan number [-]
T	temperature [℃]
T_0	initial temperature [℃]
T_{proj}	projected temperature [℃]
T_{meas}	measured temperature [℃]
T_{ref}	reference temperature [℃]
T_s	ground surface temperature [℃]
T_a	air temperature [℃]
T_f	fusion temperature [℃]
T_{top}	mean annual temperature at the top of permafrost [℃]
T_{as}	temperature difference between air and ground surface [℃]
WC	winter cooling period
X	the maximum thawing depth [m]

Uppercase Greek Symbols

Θ_d	areal density of soil water content [m^{-1}]

Lowercase Greek Symbols

α	angle of the incline [°]
β	expansion coefficient [K^{-1}]
ν	kinematic viscosity [$m^2 s^{-1}$]
ψ_w	density of potential energy of water [J m^{-3}]
ρ_b	bulk density of porous medium [kg m^{-3}]
ρ_a, ρ_m, ρ_w	mass density of air, solid matrix or water [kg m^{-3}]
$\theta_{1,2}$	volumetric water content from surface to reflector 1 and 2 [-]
$\theta_{int,2}$	volumetric water content of the second layered [-]
θ_w	volumetric water content [-]
θ_w^{CRIM}	volumetric water content estimated with the CRIM model [-]
θ_i	volumetric ice content [-]
ξ	position [m]
τ	time [s]
σ	electrical conductivity [S m^{-1}]
$\sigma_{\varepsilon_r'}$	standard deviation of estimated soil dielectric permittivity [-]
$\sigma_{d'}$	standard deviation of estimated reflector depth [m]
μ	magnetic permeability [H m^{-1}]
μ_r	relative magnetic permeability [-]
ε	dielectric permittivity [F m^{-1}]
ε_0	free space dielectric permittivity [F m^{-1}]
ε_r	relative dielectric permittivity [-]
ε_r^*	complex relative dielectric permittivity [-]
$\varepsilon_r^{'}$	real part of the complex relative dielectric permittivity [-]
$\varepsilon_r^{''}$	imaginary part of the complex relative dielectric permittivity associated with the molecular relaxation [-]
$\varepsilon_a, \varepsilon_i, \varepsilon_s, \varepsilon_w$	relative dielectric permittivity of air, ice, soil matrix or water [-]
ε_c	composite soil dielectric permittivity [-]

Subscript symbols

α	soil component (mineral, ice, water)
N	the maximum number of measurements
K	the maximum number of antenna separation

Mathematical Notation

∂_t	partial derivative with respect to time [s^{-1}]
∂_z	partial derivative with respect to vertical coordinate [s^{-1}]

1
Introduction

Permafrost is usually present if the ground temperature remained below 0℃ for two or more consecutive years [*Hancock and Skinner*, 2000]. Around 24% of the land area in the Northern Hemisphere is occupied by permafrost [*Zhang et al.*, 2008]. As one key component of the terrestrial system, it has significant influence on climate change, ecosystems and hydrologic cycle. The expected thawing of permafrost along with global warming, could result in a changing terrestrial hydrologic cycle and, in turn, in changing ecosystems [*Prowse et al.*, 2006; *White et al.*, 2007]. Besides, the thawing of ice-rich permafrost can destroy the existing landscape and terrestrial system in Arctic region [e.g. *Osterkamp et al.*, 2000; *Jorgenson et al.*, 2001] and on the Qinghai-Tibet Plateau (QTP) [e.g. *Jin et al.*, 2008]. At the same time, green house gases would be released to the atmosphere from the thawing permafrost, and accelerate global warming [*Zimov et al.*, 2006]. In addition, permafrost degradation can harm the engineering constructions in the permafrost regions [e.g. *Esch et al.*, 1990; *Wu*, 2007]. This development is attracting more and more attention from the scientific community and the intergovernmental organizations during the last few decades.

Permafrost degradation is evidently found in most of the permafrost regions on Earth. Temperature boreholes in Siberia show that the temperature at a depth of 10 m increased by about 0.3 to 0.7℃ from the 1960s to 1990s [*Pavlov and Grechishchev*, 1999]. Permafrost change in Alaska has been monitored for a long time. *Osterkamp* [2007] reports a warming of 3 to 4℃ in the Arctic Coastal Plain, 1 to 2℃ for the Brooks Range including its northern and southern foothills, and 0.3 to 1℃ for the region south of the Yukon River from 1977 to 2003. For the mountain permafrost in the Alps, deep borehole measurements show that there is a clear warming trend in permafrost temperatures [*Harris et al.*, 2009]. The measurements of mean annual ground temperature over different periods from 1998 to 2006 on Janssonhaugen, Tarfalaryggen and Juvvasshoe show that the ground temperature has increased by 0.36℃, 0.27℃ and 0.24℃, respectively.

A large area of QTP is underlying by permafrost. Since it is located in the middle latitudes with an average altitude of more than 4000 m, the permafrost is very sensitive to climate change. Observations on the permafrost temperature and climate on the QTP demonstrate that permafrost has experienced significant temperature increase and widespread degradation during the last few decades [e.g. *Cheng and Wu*, 2007; *Wu and Zhang*, 2008]. However, mechanisms of the interaction between permafrost and climate, and the impact of permafrost degradation are still poorly understood [*Wu and Zhang*, 2008; *Yang et al.*, 2004*c*].

A quantitative understanding of the processes underlying the hydraulic and thermal dynamics of permafrost soils is vital for predicting the permafrost change during global warming. Conduction is widely accepted to be the dominant mechanism of heat transfer in soils [*Roth and Boike*, 2001]. Other non-conductive heat transfer mechanisms may also play a significant role at certain conditions [e.g. *Outcalt and Hinkel*, 1989; *Kane et al.*, 2001]. Experimental identification and quantification of heat transfer processes in permafrost soils is still difficult to measure with

current instruments [*Roth and Boike*, 2001]. Permafrost modeling is an effective approach to help us to understand the evolution of permafrost with climate change. There are mainly two types of process-based permafrost models. The first type is the numerical model. It is based on physical processes and solved by numerical methods. There are some studies defining the temporal progression of a ground temperature profile by solving the energy balance equation at the surface and the heat conduction equation in the subsurface [e.g. *Goodrich*, 1982; *Zhang et al.*, 2003*b*; *Marchenko et al.*, 2008]. The second type of permafrost model is the equilibrium model, which defines the existence of permafrost [e.g. *Carlson*, 1952; *Nelson and Outcalt*, 1987], active layer thickness [e.g. *Kudryavtsev et al.*, 1974; *Lunardini*, 1981; *Romanovsky and Osterkamp*, 1997], or permafrost temperature [e.g. *Kudryavtsev et al.*, 1974; *Smith and Riseborough*, 1996], relying on the empirical or statistical relations between the atmosphere and the ground. However, all these models still suffer from an incomplete representation of physical processes and inaccurate parameterizations of material properties [*Roth and Boike*, 2001]. In addition, for spatial permafrost modeling, the spatial and temporal variations of the soil thermal properties in the active layer have significant influences on its accuracy. Therefore, to accurately predict the response of permafrost to climate change, we have to further explore the physical mechanisms controlling the permafrost degradation.

The permafrost distribution on the QTP is characterized by a triple-zonality, which includes the latitude zonality caused by the heat difference between south and north, the zonality of the different drought indexes, and the vertical zonality caused by the variations of heat and moisture with altitude [*Cheng and Francesco*, 1992]. As we know, the reactions of permafrost to climate change are different for various permafrost types and local environmental conditions. Numerous borehole observations of ground temperature on the QTP [*Wu et al.*, 2005] show that the response of permafrost to climate warming is variable in different permafrost regions. However, the mechanisms behind them are still unclear [*Wu and Zhang*, 2008]. Limited by the short period of observations, it is difficult to study the permafrost change and climate change on the QTP. Based on the characteristics of the present permafrost on the QTP, the trend of permafrost degradation could be investigated through studying the permafrost change in space instead of in time.

In our study, four study sites were carefully selected in different permafrost regions. They all have individual characteristics and representativeness. The selection of sites included three steps. Firstly, the areas were primarily chosen according to the permafrost types and nearby borehole measurements. Secondly, ground penetrating radar (GPR) was used to further explore the basic status of the active layers. At last, three different sites (Zuimatan, Qumahe, Chumaer) located in the warm permafrost regions on the northeastern QTP and another one (Tianshuihai) in the cold permafrost region on the western QTP were selected. The detailed measurements support us to take a closer look at the hydraulic and thermal dynamics of various active layers and their governing mechanisms at different permafrost sites.

In this thesis, a further understanding of the physical mechanisms between atmosphere and permafrost governing the responses of permafrost to climate change on the QTP will be provided by characterizing the atmosphere-permafrost interaction, and the hydraulic and thermal dynamics of the active layers at the three sites. In addition, based on the capability of multichannel GPR, and the variability of the thermal conductivity of the active layer, a heuristic field-scale thermal conductivity parameterization with multi-channel GPR for spatial permafrost modeling is proposed and discussed. The sketch of the framework is shown in Figure 1.1. The analyses of permafrost are based on the measured data from the study sites, while the study of applying multichannel GPR was conducted at a non-permafrost site, and it will be transfered to the permafrost study in future.

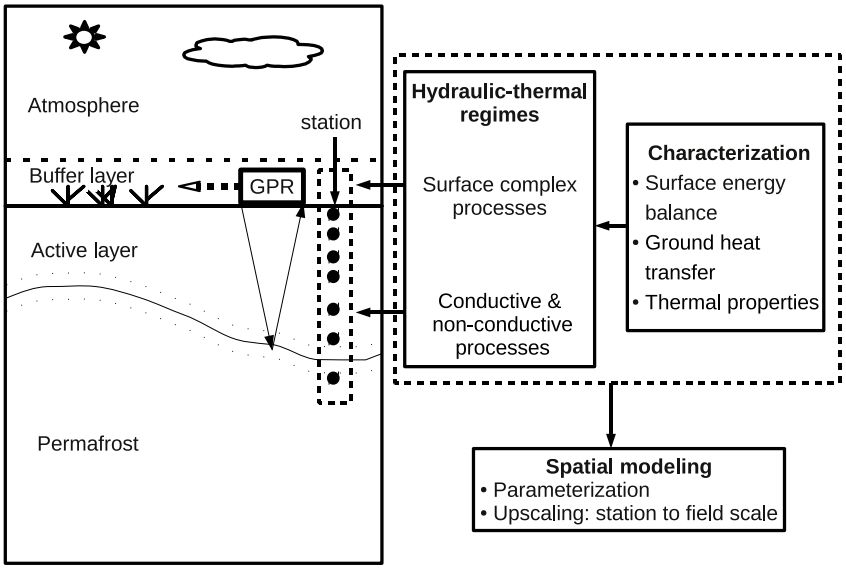

Figure 1.1. Sketch of the framework of this thesis. The left box shows the field GPR exploration and soil-weather measurements in the permafrost area. In the right dashed box, it shows the studies at the point scale from the station. The lower right box explains the attempt of upscaling from the station to the field scale.

The objectives of this thesis are:
(1) to characterize the hydraulic and thermal dynamics of the active layers with records from the soil-weather monitoring stations on the QTP, in order to gain an understanding of the physical mechanisms at the different sites; and
(2) to assess the application of multi-channel GPR to monitor field-scale soil water dynamics and the feasibility of quantifying field-scale thermal conductivity with multi-channel GPR.

The chapters of this thesis may be grouped into three parts. In the first part, chapter 1 and 2 provide relevant background for the permafrost study and the investigations and the evaluation of the measured data at the study sites. The second part includes two chapters. Chapter 3 focuses on interpretation of the interactions between atmosphere and ground surface, and the seasonal thermal patterns in the active layers at the study sites. Chapter 4 characterizes the thermal regimes of the active layers, which include the near surface mechanisms, and ground heat flux within the active layers. In the third part, the capability and applicability of multi-channel GPR for the permafrost studies are discussed. Chapter 5 examines the capability of the multi-channel GPR to monitor field-scale soil water dynamics at a sandy non-permafrost site. Chapter 6 characterizes heat transfer and thermal diffusivity in various active layers, and discuss the applicability of the multi-channel GPR for a field-scale parametrization.

2
Background of the permafrost study

A set of background information for the permafrost study including the evolution of the QTP and the associated permafrost, as well as current climate warming and permafrost degradation is introduced in this chapter. The investigations at the study sites and the basic characteristics of the existing permafrost are presented and discussed. At last, the instrumentation and data evaluation are introduced.

2.1 Evolution of the Qinghai-Tibetan Plateau and permafrost

2.1.1 The uplift of the Qinghai-Tibetan Plateau and associated climate

The QTP is located in the south-west of China. Its boundaries are the deserts of the Tarim and Qaidam Basins in the north, the south and west are surrounded by the Himalayan, Karakorum, and Pamir mountain chains, and its eastern boundaries are the Loess plateau and the Sichuan basin. As a collage of continental fragments, there are four crustal blocks: the Kunlun, Songpan-Ganzi, Qiangtang, and Lhasa terranes, which were added successively to the Eurasian plate during the Paleozoic and Mesozoic eras [*Van der Voo et al.*, 1999]. The development of these terranes initiated at about 70 Ma when the Indian plate and Eurasian plate collided during the Tertiary. The elevation history of the QTP is still a controversy issue so far. This process is generally divided into two stages by the uplifting rate. The first stage is characterized by the subduction of the Tethyan oceanic lithosphere and low altitude. The study of *Li et al.* [1979] shows that there was a tropical or subtropical climate and the average altitude of the QTP was around 1000 m during the Pliocene. From the end of the Pliocene, the uplift rate of the plateau sped up in the second stage. Due to the continuous northward subduction of the Indian plate, the QTP continued uplifting at least 3500 m during the Quaternary [*Wang and French*, 1994]. Particularly, the uplift rate may be more than 10 mm per year during the Late Pleistocene, and the uplift of the Plateau led to the formation of monsoon and loess deposits [*Ma et al.*, 2003]. By the end of the late Pleistocene, the QTP had reached an elevation of more than 4000 m, which formed the basic configuration of the present QTP [*Rowley and Currie*, 2006]. Today the QTP is still uplifting. So far it has been uplifted more than 4 km and the crust under the central part of it has thickened up to 70 km [*Molnar et al.*, 1993; *Yin and Harrison*, 2000].

Along with the uplift of the QTP, there were significant climatic changes during this process. The uplift of the QTP might have changed the atmospheric circulation and strengthened surface weathering. The study of *Raymo and Ruddiman* [1992] shows that a greater chemical weathering rate may have lowered the atmospheric carbon dioxide concentration, it may have caused the global cooling in the Cenozoic, and led to the growth of large continental ice sheets in both hemispheres. When the elevation of the QTP was high enough during the late Pleistocene, the climate changed from a monsoon climate to a continental climate because of the barrier effect of the Himalayas [*Wang and French*, 1994]. Since the barrier of the Himalayas hindered the moist

air from the Indian Ocean to reach the QTP, only scattered mountain glaciers developed on the QTP during the glaciations in the Quaternary [*Shi et al.*, 1990].

2.1.2 Permafrost

Permafrost usually occurs in the region with a yearly continuous negative heat budget at the ground surface, but which can be positive when the permafrost starts degenerating. Permafrost is growing when radiative heat loss from the ground during winter is greater than the supply of heat to the ground surface during the summer. Conversely, it may degenerate when summer heating is greater than winter heat loss. For a long period, the thick permafrost is resulted from an accumulation of the historical heat budget at the ground surface. Global climate change mainly dominates the permafrost evolution. The permafrost history also reflects climate change. During the period of permafrost aggregation, there are many interesting accompanying permafrost or periglacial phenomena such as ground ice, pingo, polygons and stone circles. While during the period of permafrost degradation, relict phenomena usually occur. Those include relict permafrost table, thermokarst lakes, taliks, buried permafrost, permafrost islands, the thickening of the active layers and pingo scars. Sometimes these phenomena can help us to recognize the appearance of permafrost in the field. Besides, they are also important evidences for studying permafrost history.

From studies of permafrost history, we can find that permafrost was dominated by the strong fluctuation of climate. Studies about permafrost history in Russia show that between the culmination of the last interglacial (125,000 years ago) and the last glacial maximum (18,000 years ago) two recognized cold periods of permafrost growth are the period of more than 70,000 years ago and another period from 60,000 to 50,000 years ago [*Hancock and Skinner*, 2000]. During these periods the permafrost was characterized by an extreme low mean annual ground temperature and expanding permafrost in the center of the Russian Plain. However, different from the permafrost history in polar regions, the formation and evolution of permafrost on the QTP were strongly related to the uplifting of the plateau. Along with the rapid uplifting of the QTP during the Quaternary, the extent and altitudinal range of permafrost has changed many times. According to the direct and indirect evidences like the remnants of ancient buried permafrost, thick-layered ground ice, periglacial phenomena and dating of soils, *Jin et al.* [2007] propose the evolution of permafrost on the QTP since the end of the late Pleistocene. They divide this evolutionary history into seven stages: (1) the cold period at the end of the late Pleistocene; (2) the period of significant climatic change during the early Holocene; (3) the Megathermal period in the middle Holocene; (4) the cold period in the late Holocene; (5) the warm period in the later Holocene; (6) the Little Ice Age; and (7) the recent warming period until present. The existing permafrost on the QTP was formed during the last two major glaciations, and strongly shrunk during the warming periods in between [*Zhou*, 1965].

The QTP is underlain by extensive high-altitude permafrost, which covers 70% to 90% of the Plateau [*Cheng and Wu*, 2007]. Since the average altitude is about 4500 m above sea level, most of the areas are depopulated. The studies on permafrost on the QTP are very rare because of unease of access. The main modern studies of permafrost started in 1958, and were done by the Chinese Academy of Sciences. In 1965, the Lanzhou Institute of Glaciology, Geocryology and Desert Research (note: now it is called Cold and Arid Regions Environmental and Engineering Research Institute, Chinese Academy of Science) was established. The first permafrost investigations on the QTP were initiated in the 1960s by the scientists from the Lanzhou Institute. Later due to the construction of the Qinghai-Tibet Highway, comprehensive permafrost investigations were conducted in the areas along the highway in the late 1960s. But

now for the improvement of logistical conditions, the other regions are also becoming accessible and attractive to scientists. Nowadays more and more modern technologies have been used to complete the study on permafrost on the QTP. Particularly with the help of remote sensing, a complete mapping of the permafrost distribution becomes possible. The high-resolution map of permafrost distribution has been created by the Cold and Arid Regions Environmental and Engineering Research Institute [*Li and Cheng*, 1999].

From the GIS-aided map of the permafrost distribution on the QTP [*Li and Cheng*, 1999], the areas of permafrost and seasonally frozen ground are 1,359,209 km^2, and 1,218,898 km^2, respectively. According to the Chinese classification [*Cheng and Wu*, 2007] of permafrost distribution on the present QTP, there is predominantly continuous permafrost (70-90% area underlain by permafrost), predominantly discontinuous permafrost (30-70% area underlain by permafrost) and sporadic island permafrost (less than 30% area underlain by permafrost). The thickness of permafrost on the QTP ranges from a few meters up to 175 m, and the mean annual ground temperature from 0 to -4℃ [*Wang and French*, 1994; *Jin et al.*, 2007]. Due to the sensitivity of permafrost thickness to altitude, it varies differently in the areas of mountainous permafrost and continuous permafrost. The thickness of permafrost increases with a rate of 15 to 20 m per 100 m in altitude [*Zhou and Guo*, 1982]. Another feature of the permafrost distribution on the QTP is the different lower altitudinal limit in the north and south. The observed data along the Qinghai-Tibet Highway in last few decades show that the northern lower limit is at 4150-4250 m and the southern lower limit is at 4450-4560 m [*Jin et al.*, 2007]. In addition, the regional distribution of permafrost and the permafrost thickness are disturbed by site-specific factors such as varying geothermal flux caused by geological structures, surface hydrological conditions, and changing surface cover [*Wang and French*, 1994].

2.2 Current climate warming and permafrost degradation

2.2.1 Climate change

The QTP is situated in the middle-low latitudes and surrounded by mountains with high ridges. These geographical features form a special climate on the QTP. It is characterized as cold and dry climate with low precipitation, and strong solar radiation. A major feature of the atmospheric circulation on the QTP is the weak monsoon effect. The traditional definition of the monsoon is a seasonal reversing wind accompanied by seasonal changes in precipitation [*Ramage*, 1971], but now it is used to describe seasonal changes in the atmospheric circulation and precipitation associated with the asymmetric heating of land and sea [*Trenberth et al.*, 2000]. Monsoons are caused by the seasonal circular difference between land temperature and the nearby ocean's temperature. In summer, the air above the land warms faster and reaches a higher temperature than the air over the ocean, because of the different warming rate of the ocean and the land surface. The rising hot air above the land creates an area of low pressure, which leads to a steady wind flowing from the high pressure areas above the oceans to the land. At the same time, the wind brings the moist near-surface air over the oceans. When the moist ocean air is lifted upwards by mountains, due to the expansion of the moist air in lower pressure areas over the land, the air becomes cooled and produces rainfall. In winter, the cooling of the land is much quicker than that of the ocean. The rising hot air over the ocean creates a low pressure area, and the dry air from the land is blown to the ocean. Although the south Asian monsoon has strong effects on the Indian subcontinent and surrounding regions, little of the summer monsoon rain crosses the Himalayan mountains in front of the QTP. This rain-shadow effect results in the extreme dryness with an annual precipitation of about 20-500 mm [*Jin et al.*, 2007].

Besides the influence of the south Asian monsoon, the climate on the QTP is also influenced by the plateau monsoon and the east Asian monsoon. The height and the complex topography of the QTP have a special influence on the horizontal and vertical circulation patterns [*Ye*, 1981]. *Tang et al.* [1979] proposed the concept of plateau monsoon on the QTP. The plateau monsoon occurs in the middle and higher troposphere. Its intensity strongly relates to the air temperature and precipitation [*Tang*, 1995]. Studies [e.g. *Wu and Qian*, 2003; *Bai et al.*, 2005] on the relation between the plateau monsoon and other Asian monsoons show that their interaction has significant influences on the precipitation on the QTP. As a starter and adjuster of climate change in the northern hemisphere, the QTP even influences the global climate change.

With the global warming, the trend of the mean annual air temperature on the QTP is gradually increasing. At the same time, the regional characteristics of mean annual air temperature change was concerned recently [*Xu et al.*, 2003; *Zhou et al.*, 2005]. As *Zhou et al.* [2005] pointed out, in the last 50 years, the mean annual air temperature was increasing in most study regions, and pronounced warming originated from the winter and spring seasons. Especially at the source areas of the Yangtze and Yellow rivers, *Li et al.* [2006] analyzed the data from 14 weather stations and found that the air temperature were increasing in the last 43 years and the regional variations were different.

Due to the high altitude of the QTP and a special interaction with atmospheric circulation, the surface thermal state embodies a concentrated reflection of thermal dynamic activities driven by climate change like the monsoon on the QTP [*Jiang and Wang*, 2001]. The broad areas of permafrost with freeze-thaw cycle on the QTP play an important role in thermal dynamic activities. Therefore, the study of the difference between ground and air temperature is helpful to understand the responses of permafrost to climate change [*Li et al.*, 2001; *Wu et al.*, 2005]. Through the analysis of the data of ground surface temperature and air temperature during 1960-2000 from 99 weather stations, *Zhang et al.* [2006*a*] point out that the maximum difference between ground temperatures and air temperatures occurred in June and their minimum difference occurred in December; the spatial variations of the differences are related to factors like the geography and permafrost types.

2.2.2 Permafrost degradation and associated environmental challenges

Permafrost is extremely sensitive to climate change at different spatial and temporal scales. The response of permafrost to climate change drew attention over the last few decades [e.g. *Barnett et al.*, 2005; *Anisimov and Reneva*, 2006]. Permafrost degradation may play an important role in the modification of regional climates. But more evidence is still needed to prove that the rapid changes in air temperatures experienced over the past few decades have exerted a profound effect on the state of permafrost and climate over the permafrost areas [*Hancock and Skinner*, 2000]. Permafrost on the QTP is one of the most sensitive regions to climate change [*Liu and Chen*, 2000].

Pronounced changes of permafrost were observed on the QTP, such as increase of ground temperature, thickening of the active layer, and retreat of the lower permafrost limit. Observations evidently show that the permafrost is warming and thawing during the last few decades on the QTP [*Cheng and Wu*, 2007]. Ground temperature measurements at 10 sites on the QTP show that the mean annual permafrost temperature at the depth of 6.0 m has increased by 0.12 to 0.67℃ during the past decade [*Wu and Zhang*, 2008]. Permafrost on the QTP is generally characterized by thick active layers, and thin permafrost. Changes in active layer thickness arising from global warming reflect the negative annual heat balance. The active layer thicknesses monitored from 10 sites along the Qinghai-Tibet Highway show an increase

trend over the period from 1995 to 2007 [*Wu and Zhang*, 2010]. The most evident permafrost degradation can be found in the sporadic permafrost zone on the QTP. It displays as warming ground temperature, thickening of active layers, and disappearing permafrost islands [*Cheng and Wu*, 2007]. Besides, the lower altitudinal limit of permafrost also shows the permafrost degradation on the QTP. Observations show that the lower altitudinal limit of permafrost at Xidatan has risen by 25 m at the northern border of the QTP [*Wang et al.*, 1999], and 50-80 m in the southern lower altitudinal limit of permafrost at Amdo [*Wang*, 1997].

Permafrost degradation is usually related to the hydrologic cycle and ecosystem. Since the dynamics of permafrost is one important factor controlling the active layer thickness and moisture content, it is closely associated with hydrological and thermal processes near the ground surface [*Cheng and Wu*, 2007]. *Cheng and Zhao* [2000] attribute the deteriorating environment like lowering water table, shrinking of grasslands and grazing grasslands to the permafrost degradation. *Yang et al.* [2004*a*] analyzed the reduction of surface runoff in the last 20 years in the source region of the Yellow River and found that it is closely related to permafrost degradation besides the glacier retreat and precipitation change. Evidences show that the freezing and thawing process controls plant growth, soil moisture content according to the study of the Normalized Difference Vegetation Index (NDVI) and ground temperature [*Yang et al.*, 2004*a*]. The warming and drying climate in summer is the major reason for the degradation of the vegetation, desiccation of the high-cold marshland, and the decrease in areas and numbers of lakes and rivers in the middle and northern source regions of the Yangtze and Yellow Rivers [*Yang et al.*, 2007; *Wang et al.*, 2009*b*].

Another consequence of the permafrost degradation may be the desertification on the QTP. Some studies analyzed the relationship between permafrost degradation and desertification [e.g. *Wang et al.*, 2002; *Yang et al.*, 2004*c*]. The results show that the desertification is related to several factors including climate, permafrost, land surface and human activities, and the permafrost degradation would speed up the desertification on the QTP. *Cheng and Wu* [2007] pointed out that the drying ground surface by permafrost degradation and land desertification might be an important environmental issue on the QTP.

2.3 Investigations at the study sites

To further understand the responses of permafrost to climate change at different conditions, four study sites were selected to take a closer look at the existing permafrost state in different regions on the QTP. Based on the strategy of investigating the permafrost degradation in space instead of in time, the study sites represent one seriously degrading permafrost region (Zuimatan), one warm permafrost region with two different environmental elements (Qumahe and Chumaer) and one cold permafrost region (Tianshuihai). They are located in the continuous permafrost region around 35°N latitude on the QTP. In these regions, a variety of field investigations have been conducted such as field expedition, drilling and some geophysical investigations. From the related literature and field investigations, the permafrost states at different sites are presented in the following.

2.3.1 Chumaer and Qumahe

Regional environmental conditions The Chumaer site (35°11´N, 93°57´E) and the Qumahe site (34°54´N, 94°47´E) are both located in the source region of the Yangtze river according to the classification by *Ding et al.* [2003]. As shown in Figure 2.1, the valley up the convergent site of

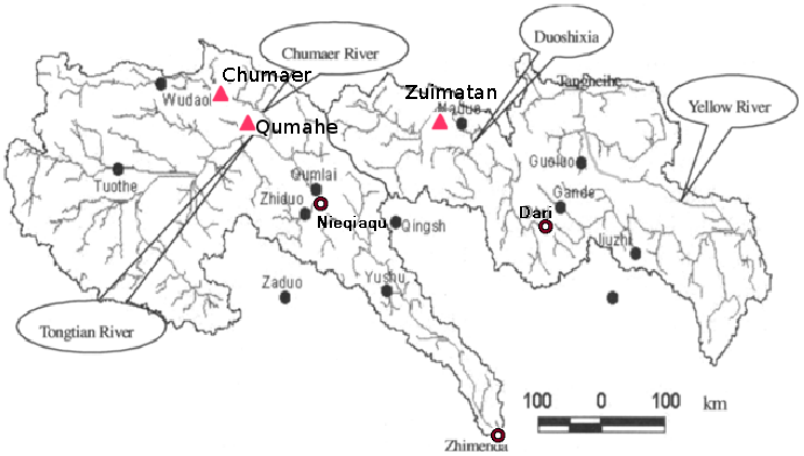

Figure 2.1. Geographical and hydrological ranges of the source regions of the Yangtze and Yellow rivers [*Ding et al.*, 2003] and the study sites of Chumaer, Qumahe and Zuimatan.

Nieqiaqu and Tongtianhe rivers is defined as the source area of the Yangtze river approximately between 32°30´-35°44´N and 90°30´-96°00´E, which covers 10.24×10^4 km^2 [*Ding et al.*, 2003]. The basic geomorphological units in this region are plateau basin and valley. They are made up by the northern boundary of the Kunlun Mountains, the southern boundary of the Tanggula Mountains, the eastern boundary of the Bayankala Mountains, and Wudaoliang Mountains in the middle. The topography of the watershed up the convergent site of Chumaer and Tongtianhe rivers is characterized by an alpine plain and hills [*Wang and Chen*, 1998]. The topography down the convergent site of Nieqia and Tongtianhe river are high mountains and canyons. The terrain between these two convergent sites is the transitional belt of the above mentioned two types of topography. As shown in the appendix (Figure B.1), the Chumaer site is located at the side of the gentle terrain of the Chumaer river up the convergent site of Chumaer and Tongtianhe rivers, and the Qumahe site is also in this region but very close the convergent site. Therefore, its terrain features are similar to the transitional belt.

Due to the high altitude glaciers and permafrost are widely distributed in the source region of the Yangtze river. The study of *Yang and Woo* [1990] show that the area covered by glaciers up the Zhimenda station in this region is about 1192 km^2, which is about 0.87% of the source region (above the Zhimenda site), and the drainage of the glacial melting is about 9.2% of the total runoff at the Zhimenda station. Most of the rivers in this region like Tuotuohe, Dangqu and Gaerqu originate from the glaciers covering the Tanggula mountains, but the Chumaer and Beiluhe rivers are mainly recharged by precipitation. The vast area in the west of the Tuotuohe is characterized as low precipitation (220-300 mm/a), while the downstream area of Tongtianhe river is rich in precipitation (around 480 mm/a at the Yushu station) [*Xie et al.*, 2003]. The Chumaer and Qumahe sites are in between these two typical areas.

In the source region, one of the main resources for runoff of the Yangtze river is precipitation which mainly concentrates in summer [*Jin et al.*, 2005]. Besides, most of the glaciers in this region are retreating because of the global warming, which increases the supplement of the runoff [*Wu and Yu*, 2002]. Observations from the last 40 years show that the runoff of the Tuotuo river, which is one branch of Tongtian river, increased from the middle of the 1980s to the late 1990s, but the runoff of Tongtian river decreased [*Jin et al.*, 2005]. *Jin et al.* [2005] conclude that the influence of precipitation is larger than the glacial in this region. The discharges from rivers in

this permafrost region have varied significantly in last few decades [*Xie et al.*, 2003]. Permafrost degradation may exert some impacts on the hydrologic cycle in this region.

According to the characteristics of the natural zonation and the climatic regionalization on the QTP, the source region of the Yangtze river is classified into two subtypes as the Naqu-Guoluo semi-humid region and the Qiangtang cold alpine semi-arid region [*Ding et al.*, 2003]. The climate at Chumaer and Qumahe is the typical alpine semi-arid climate. The main vegetation types are cold alpine steppe in this region. Vast permafrost distributes in the source region of the Yangtze river. The mean annual air temperature is -5.5 to 4℃ here.

According to the classification of the permafrost distribution in China [*Zhou et al.*, 2000], there is predominantly continuous permafrost in the area around Chumaer. Observations [*Wu and Zhang*, 2008] at two sites CM1 and CM2 in this region shown that the mean annual air temperature was -5.0 to -5.5℃, and the mean annual precipitation was 230 to 250 mm; the active layer thickness was 2.5 to 4.0 m, and permafrost thickness was 10-30 m. The measured ground temperatures at CM1 and CM2 (recording from 1995 to 2001 and from 1995 to 2006, respectively) demonstrate that there were significant changes in soil temperatures in the active layer and underlying permafrost, and the increase of soil temperature at depth 6.0 m were 0.17℃/10a, and 0.26℃/10a, respectively.

In the area around Qumahe site, the permafrost mainly lies on the high mountains, which belong to the discontinuous permafrost [*Zhou et al.*, 2000]. From the investigation of drilling along the Qingshuihe-Budongquan highway in 2006 (participated in Professor Yu Sheng's project), we found that the permafrost only exists on high mountains, which is called permafrost island. The permafrost limit is around 4200 m here. Below this altitude, they are seasonally frozen areas. The measured meteorological data in Qumalai demonstrated a similar climate warming trend as in the Chumaer region [*Zhou et al.*, 2005]. In this area, the permafrost thickness varies largely with different local factors.

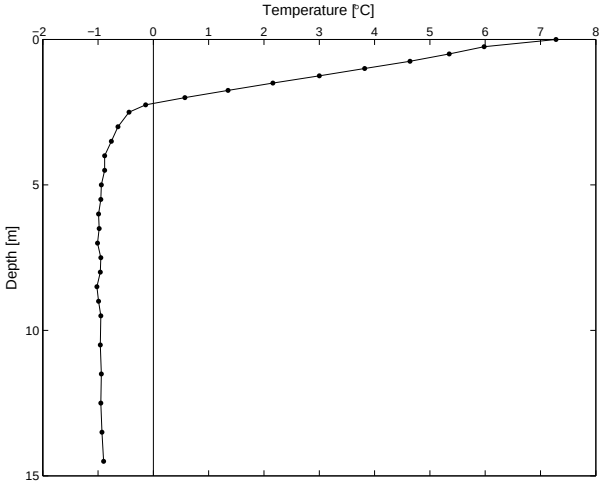

Figure 2.2. Borehole temperature measured on August 30, 2006 at Chumaer.

Field explorations The Chumaer site is located on the Chumaer high plain, about 3 kilometers away from the Chumaer river, and its altitude is 4443 m. The average coverage of vegetation is less than 30% of the ground surface. The Qumahe site is located in a valley with an altitude 4447 m here. Because of the runoff of the melt water, a small seasonal stream lies in the valley bottom, and its lower part is covered with dense vegetation. The point exploration by drilling was conducted in May 2005 by the project of permafrost exploration for the Qumahe-Budongquan

highway (Professor Yu Sheng's project, the author participated). A 15 m deep borehole was drilled about 150 m away from the Chumaer station. The core records are as follows: 0 to 3.5 m, sandy sediments, and groundwater was found around 1.5 m; below 3.5 m, a gray-colored thick layer of severely-weathered mudstone, with several layers of pure ground-ice embedded, having a thickness from a few centimeters to tens of centimeters. It is consistent with the geological study [*Zhang*, 1996] that this region is one part of the Triassic sedimentary basin with marine facies. At Qumahe, a 12 m deep borehole was drilled about 200 m away from the station. The records show that debris ranges from the surface to about 2 m, and below is the bedrock of gray mudstone. Due to the dramatic change of materials from the borehole to the station, completely different permafrost features were found at the climate station.

The measurements in the borehole were made by a string of thermistors with an increment of 0.25 m above the depth of 3 m and an increment of 0.5 m below the depth of 3 m. These thermistors were calibrated in the State Key Laboratory of Frozen Soil Engineering (SKLFSE), and their precision is 0.05℃. The measured ground temperatures on August 30, 2006 at Chumaer site are shown in Figure 2.2. It shows that the gradient of soil temperature below the depth of 6 m is very small, which indicates that this borehole is located in the degrading permafrost according to the classification by *Jin et al.* [2006]. Unfortunately, the borehole measurements at Qumahe site are not available so far.

The second type of field exploration in this region was conducted by Professor Kurt Roth with GPR in 2006. Because of the great advantage of quickly exploring the permafrost with GPR without disturbing the soils, the local permafrost features can be identified effectively. With the GPR explorations, we can quickly capture the permafrost information such as permafrost existence, active layer spatial distribution and rough thawing depth. These are important basis for the site selection.

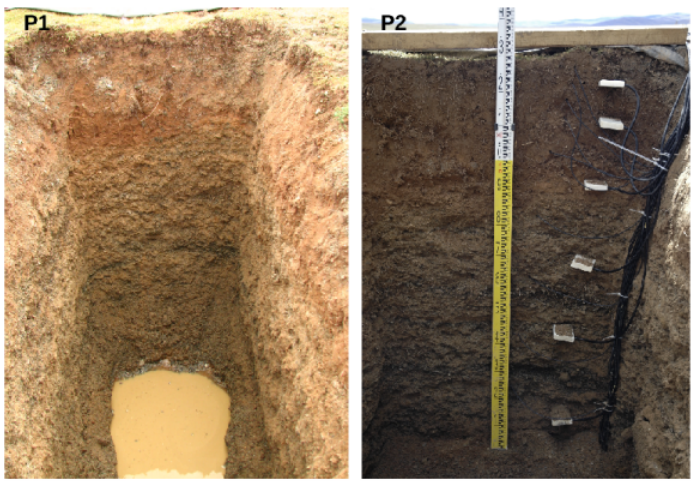

Figure 2.3. Photos of the two profiles (P1 and P2) at Chumaer (photo by Philip Schiwek).

After site selection, excavation and sampling were conducted in the profiles. Two profiles with different surface characteristics were chosen at Chumaer. One is covered with dense vegetation (P1), and the other one exhibits a nearly bare surface (P2). They are several meters away, and the surface of P1 is about 20 cm higher than that of P2. The soil structures are shown in Figure 2.3. The texture analyses of the two profiles are given by *König* [2008]. According to the classification of soil texture by the German DIN 4022, the soil texture is classified by the

percentages of total sand, silt and clay measured by pipette and sieve analysis, and the weight percentages of the grain sizes greater than 2 mm [*Smith et al.*, 1999]. In profile 1, there are three layers: 0-0.23 m, 0.23-0.5 m, and 0.5-2.09 m. They are classified as sandy clay (Ts4), loamy sand (Sl3), sand (S), respectively. In the profile 2, there are also three layers from 0-0.15 m, 0.15-0.35 m, and 0.35-2.28 m, which are classified as loamy sand (Sl3), clayey sand (St3), and sand (S), respectively. Generally, the soil texture of P2 is similar to profile 1, but the porosity distribution is different from profile 1. This may be caused by the sampling from the nonuniform soils. The silt and clay content in the upper layer covered with dense vegetation (P2) is higher than that in the upper layer with bare surface (P1). The high clay content in the uppermost layer indicates the latest deposits by freeze-thaw erosion and eolian erosion. Below the upper layer the main fractions are sand and gravel. The only slightly rounded gravels indicate they have not been transported over a long distance. They might be deposited by the alluvial sedimentation.

One profile was evacuated to 1.57 m at Qumahe site. The soil texture is given by *König* [2008]. From top to bottom the texture of the profile is classified as silt with loam and sand (Uls: 0-0.44 m), sand with loam and silt (Slu 0.44-0.6 m), sand with little loam (Sl3: 0.6-0.85 m), loamy sand (Ls3: 0.85-1.0 m), sand with little loam (Sl3: 1.0-1.21 m), sand with little silt (Su3: 1.21-1.6 m). In general, the grain size increases gradually from top to bottom. In the upper layer, the sandy loamy silt contains a high amount of clay and silt but a low amount of coarse materials. Besides, the soil contains black organic material at the upper layer. It indicates the strong influences of the freezing and thawing processes in the wet soil. Below this layer the coarse fragments increase with depth. The layer structure indicates the major effect of alluvial sedimentation.

Figure 2.4. A photo of the profile at Qumahe (photo by Philip Schiwek).

2.3.2 Zuimatan

Regional environmental conditions The Zuimatan site (35°22´N, 99°08´E) is located in the source region of the Yellow river according to the classification by *Ding et al.* [2003]. As shown

in Figure 2.1, the area up the Dari hydrological station is the source area of the Yellow river approximately between 33°00´-35°35´N and 96°00´-99°40´E, which covers 4.49×10^4 km^2 [*Ding et al.*, 2003]. The topography of the source region of the Yellow river is characterized by an alpine plain with low maintains, wide valleys and marshland. The topographical features up Duoshixia are characterized by plateau lakes and marshland. The topography down Dari is characterized by high mountains and canyons. Glaciers concentrate in Animaqing mountains, while the area covered by glaciers is only 131.44 km^2 in the source region of the Yellow river [*Yang and Woo*, 1990]. It is about 0.11% of the source region, and the drainage of glacial melt water is about 0.63% of the total runoff at the Tangnaihe station [*Yang and Woo*, 1990].

Besides the main river, the Yellow River, its major branches are Kariqu, Duoqu and Lainaqu in this region. There are many lakes such as Xingsuhai, Zhaling Lake, Eling Lake, and Longrecuo. Most of the branch rivers in this region are recharged by local precipitation, the Qiemuqu and Qushian rivers originating from the glaciers in Animaqing mountains are mainly recharged by the glacial melting. Precipitation in this region is larger than that in the source region of the Yangtze river. The measured mean annual precipitation at Maduo station is 300 mm, and it reaches 760 mm at Jiuzhi station in the southeast [*Xie et al.*, 2003].

Two significant types of climate in the source region of the Yellow river exist in the semi-humid region where the precipitation is 500-800 mm/a and the cold alpine semi-arid region where the precipitation is 250-500 mm/a [*Ding et al.*, 2003]. Due to the changes of water and heat in space, the vegetation transforms from shrubs and alpine meadow into steppe in this region [*Ding et al.*, 2003]. The permafrost in this area belongs to the discontinuous permafrost [*Zhou et al.*, 2000]. The boreholes in the permafrost regions show that most of the permafrost tables are very deep in this area and the permafrost thickness is less than 50 m [*Zhang et al.*, 2004]. The altitudinal permafrost limit is around 4200 m. Below this limit, there are seasonally frozen areas and sparse permafrost islands. There are many permafrost-like geomorphological phenomena in the seasonally frozen area, such as pingo, thick vegetation, solifluction and frost heaving, which are typified in permafrost region [*Zhu et al.*, 1996]. From the borehole verifications [*Zhang et al.*, 2004], there is no permafrost or just deep buried permafrost in some places. From the study of the climate in last 43 years [*Li et al.*, 2006], the warming trend in the Yellow River source region is very significant. For instance, the climate tendency rate was up to 0.42℃/10a in the Zeku region. The weather station in the seasonally frozen area in Maduo demonstrated that from the 1980s the maximum seasonal freezing thickness changed from 3.2 m to 2.8 m, and the frozen period was shortening. All these evidences show that permafrost degradation caused by climate change is significant in this region.

Climate change and permafrost degradation in this region would generate a series of irreversible environmental problems [*Zhang et al.*, 2004; *Cheng and Wu*, 2007]. Besides the above mentioned direct observations of permafrost degradation, other indirect phenomena are also obvious. With the deepening of the active layer, the ground water table decreases, and the lakes and rivers may start to recharge the ground water. Ground water observation in wells demonstrated that in last 20 years, the water table decreased by 2-3 m [*Peng et al.*, 2003]. Vegetation is also deteriorating in this region. Black patches, which is one kind of phenomena of vegetation degradation, enlarge in the vegetated area [*Zhang et al.*, 2004]. Besides, along with the degradation of vegetation and permafrost, the threat of desertification is more and more serious [*Huang et al.*, 1993; *Wang et al.*, 2002]. Because of the strong wind and dry climate, permafrost degradation can further strengthen the desertification on the QTP.

Field explorations This study site is located on a plain surrounded by hills, and is about 1.0 kilometer away from the Xining-Yushu Highway as shown in the appendix (Figure B.2). The elevation is 4187 m. The ground surface is covered by sparse grass. We have done similar

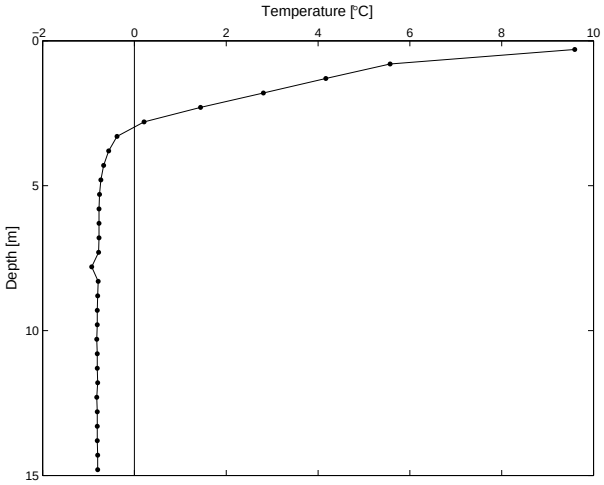

Figure 2.5. Borehole temperature measured on August 26, 2007 at Zuimatan.

explorations in this area as at Chumaer including drilling, GPR explorations and excavation. However, due to the high salt concentration of the ground, GPR does not work well. Therefore, only borehole measurements and profile sampling are presented in the following.

A 15-m deep borehole was drilled by Professor Yu Sheng's project. It is about 5 meters away from the foot of the highway embankment. The ground temperatures measured on August 26, 2007 are shown in Figure 2.5 (data from Professor Yu Sheng). The soil temperature at depth of 10 m was about -0.81℃, which is 0.14℃ higher than that at Chumaer. The gradient of the soil temperature below the depth of 6 m indicates that the permafrost is deteriorating and its thickness should be smaller than that at Chumaer site.

Figure 2.6. The photo of the profile at Zuimatan (photo by Philip Schiwek).

The profile was excavated down to 2.62 m at Zuimatan. The soil structure is shown in Figure 2.6. The texture analysis is given by *König* [2008]. There are several interbedded layers in the profile. From the top to the bottom they are classified as silt with loam and sand (Uls: 0-0.1 m), sand with loam and silt (Lsu: 0.1-0.4 m), sand (S: 0.4-0.6 m), sand with silt (Su2: 0.6-0.97 m), sand (S: 0.97-1.2 m), sand with a large amount of loam (Sl3: 1.7-1.8 m), sand with a medium amount of loam (Sl2: 1.8-2.05 m), loam with a large amount of sand (Ls4: 2.05-2.25 m), and below 2.25 m it is unknown due to sampling artifacts. In upper two layers, the soil contains high clay and silt contents but a low amount of coarse materials. It might be attributed to the sedimentation by the strong wind and surface water transport. This site is located in a low land. During the spring investigation in 2006, the ground surface was always water ponding in the field, and TDR measurements in summer demonstrated a high salt concentration of the surface water. Besides, in the nearby seasonal freezing region, desertification demonstrates that the strong wind in this region may be an important transport tool. Below the upper part, there are interbedded layers, which indicate the repeat sedimentations during the different periods.

2.3.3 Tianshuihai

Regional environmental conditions The Tianshuihai site is located in the western QTP. The topography in this region is mainly made up of three parallel mountain ranges. From north to south they are the Kunlun range, the Kala Kunlun range and the Himalaya range. The major topographical feature is the high elevation difference between mountains and valleys. The study area lies in between the Kunlun range and the Kala Kunlun range as shown in the appendix (Figure B.3). Above 4000-5000 m, the terrain is mountainous cold desertscape, and glaciers and permafrost can be found there. Below 3500 m, the terrain is desertscape with very sparse vegetation.

In this region, the warm and wet air flow from the Atlantic ocean is already very weak, and the southwest monsoon is blocked by the Himalayas. Therefore, this region is one of the driest and coldest mountains in Asia [*Su et al.*, 1998]. The air temperature is mainly controlled by the altitude. The permafrost in this region belongs to the low latitude mountainous permafrost. The altitude is the major controlling factor to the permafrost distribution. In the Tianshuihai basin, the altitude is 4840-4900 m, the active layer thickness is 1.0-1.5 m, and permafrost thickness is larger than 60 m [*Su et al.*, 1998]. The mean annual ground temperature was -3.2℃, and the yearly change of the ground temperature occurs down to a depth of 13-15 m. As a typical permafrost-rich area, in the western Kunlun mountainous region, various periglacial phenomena such as frozen pingos, thick ground ice, stone polygon, frost lifting can be found [*Su et al.*, 1998].

Permafrost investigations and studies on the QTP have largely concentrated on the east and south because of the good accessibility, particularly on the Qinghai-Tibet Highway. *Zhao et al.* [2010] summarized the thermal state of permafrost on the QTP and found that most of the ground temperature measurements in the boreholes along Qinghai-Tibet Highway increased during the period of records. The active layer thickness at 10 sites along the Qinghai-Tibet Highway showed an increase over the period of from 1995 to 2007 [*Wu and Zhang*, 2010]. While on the western QTP, there are only a few studies about permafrost investigation along Xiangjiang-Xizang Highway [*He*, 1991; *Su et al.*, 1998]. So far, there were almost no new progresses of permafrost research in this region. Therefore, it is very significant to do further studies on permafrost, especially about the responses of permafrost to current climate change.

The study site is located in the area of the ancient Tianshuihai lake as shown in Figure B.3. Currently the Tianshuihai lake extends by about 25 kilometers in east-west direction and about

80 kilometers in south-north direction. It is recharged by several springs at the foot of the mountains situated in the southwest [*Su et al.*, 1998]. *Li et al.* [2008] propose that the old lake may cover with the salty lake in the Xiaoerke valley and Aksaichin lake according to the outcrop of lacustrine strata. It had already existed at the beginning of the Quaternary, and started separating from the late Pleistocene [*Li et al.*, 2008]. The evolution of the Tianshuihai lake and the permafrost there were mainly controlled by global climate fluctuations and altitude in different geologic periods. The study of *Li* [1991] shows that the evolution of the lakes in the western Kunlun mountain system had undergone three stages. The lake first appeared in 4,6000 years ago at the first stage. During a second stage, the lake fluctuated strongly with climate change. Due to the continuous uplift of the QTP with a dry climate, the lake shrunk during the third stage. According to observations (35°16´N, 79°33´E, 4840 m) from 1965-1970 in the Tianshuihai region, the mean annual air temperature was -6.3℃, and the mean annual precipitation was 20.6 mm [*Su et al.*, 1998].

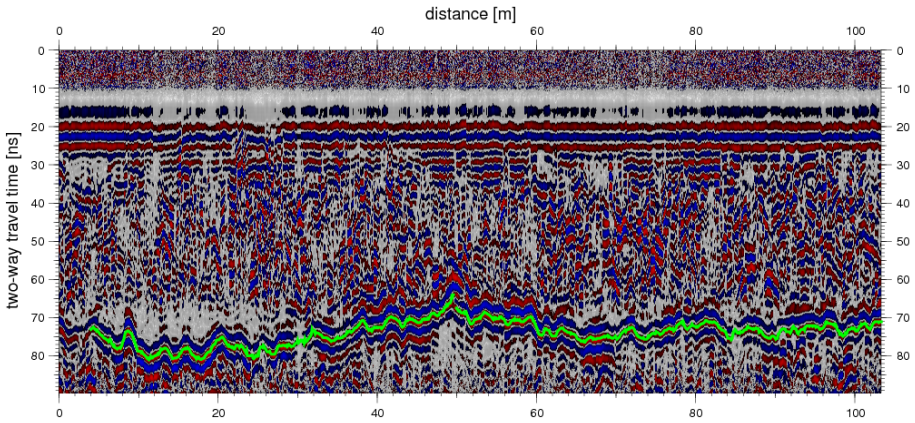

Figure 2.7. The permafrost table (green picks) shown in the GPR radargram at Tianshuihai.

Field explorations Due to the difficulty of logistic supply, only a few expeditions have been conducted in recent years. For our study, the field exploration was conducted in 2006. Along the Xinjiang-Xizang Highway, several permafrost areas were explored with GPR. The permafrost table can be clearly seen in the radargram as shown in Figure 2.7. After the preliminary exploration, the site (35°24´N, 79°33´E, 4739 m) was chosen by a detailed GPR exploration in 2007.

Two profiles were excavated on a flat area between two streams in the ancient lake. They are just a few meters away from each other. The sediments on the surface are fluvial gravels and sands, as well as lacustrine sediments such as clay and loam. As mentioned before, due to the shrinking of Tianshuihai lake, the coarse sediments were transported on top of the lacustrine sediments. The soil structures of two profiles (left: p1, right: p2) are shown in Figure 2.8. Since no samples for soil texture analysis were analyzed, the soil textures were classified from field excavations. In the profile 1, the layers are classified as gravel and fine sand (0-0.2 m), dipping layer of loamy sand and sandy gravel (0.2-1.0 m), loam with a small patches of gravel (1.0-1.46 m), and the underlying frozen ground. In profile 2, from the surface to 0.3 m, fine sand and gravel include a clear sand wedge. Between 0.3 m and 0.86 m, there is a gradual transition from gravel to loam. From 0.86 m to 1.44 m, uniform loam was found. Frozen ground occurs below 1.44 m. The soil structures in two profiles demonstrate that the permafrost has undergone several strong fluctuations of the freeze-thaw cycles and formed groundice when the

soil was wet. The fluvial sediments should be deposited later. On the surface, the fine material should be formed by aeolian erosion and deposition.

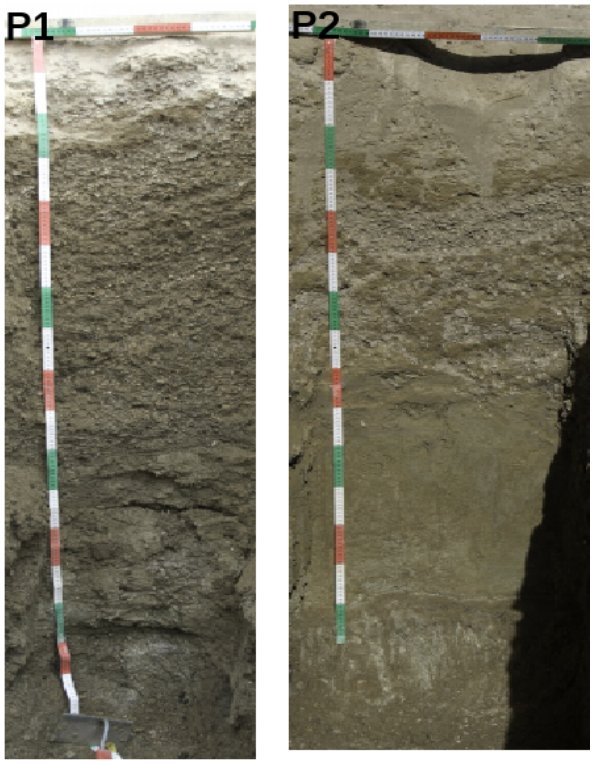

Figure 2.8. Photos of the profiles (P1 and P2) at Tianshuihai (photo by Dr. Ute Wollschläger).

2.4 Instrumentation and data evaluation

To monitor the hydraulic and thermal dynamics of active layers, a variety of methods and techniques have been developed in field studies on permafrost. As presented in the handbook on recommended methods to measure periglacial processes, it includes a variety of topics on geographical, geophysical, geochemical, geomorphological, and geoengineering methods [*Matsuoka and Humlum*, 2003]. Due to the limited of logistical support in the northern and southern polar areas and high altitude regions, methods based on manual measurements can not meet practical requirements. The interval of the observations such as ground temperature and soil water content has been improved from a few months or years to continuous measurements with the help of the newly developed data loggers since the 1990s. Combined with a comprehensive meteorological observatory, soil temperature and soil water content, the hydraulic and thermal dynamics in the active layer can be continuously and concurrently monitored with data loggers in the field for a long time [*Hoelzle et al.*, 1999; *Brown et al.*, 2000]. For large scale permafrost investigations, geophysical methods and remote sensing are useful tools to study various conditions. *Kneisel et al.* [2008] reviewed the recent advances in geophysical methods for permafrost investigations, and analyzed the applicability and reliability of different geophysical techniques for permafrost studies. Our objective is to investigate the physical processes in different active layers in the field and to test the applicability of multi-channel GPR for an upscaling soil thermal

conductivity parameterization. In this section, we mainly introduce the technique of the soil-weather monitoring stations used at the study sites, and discuss the potential problems of this technique. The geophysical technique of multi-channel GPR will be introduced in chapter 5.

2.4.1 Measurements at the soil-weather monitoring stations

The whole monitoring system includes two parts, one is above the ground surface, the other one is under the ground surface. The first part measures the meteorological items including air temperature, relative humidity, net radiation, wind speed and direction, precipitation, snow thickness and atmospheric pressure. The second part measures the soil temperature and soil water content in the ground. These probes are controlled by a datalogger (CR1000, Campbell Scientific Ltd., Logan) and its electric power is supplied by a battery charged by a solar panel. The specifications for probes and additional information are shown in Table 2.1.

The field work on the northeastern QTP was carried out by the German partners Kurt Roth, Philip Schiwek, and Chinese parters of Zhixue Ma, Jichun Wu, Zhi Wei, assistant workers and Xicai Pan at the beginning of September in 2006. At Chumaer, all meteorological items listed in Table 2.1 were installed here. Two soil profiles were excavated until frozen ground was encountered. Soil temperature and soil water content probes (CS616) were horizontally installed in the profiles at depths as shown in appendix A (Table A.1). At Qumahe, one soil profile was excavated down to 50 cm below the permafrost table. Soil temperature and soil water content probes (TDR and CS616) were horizontally installed in the profile at depths as shown in Table A. At Zuimatan, one soil profile was excavated until frozen ground was encountered. Soil temperature and soil water content probes (TDR and CS616) were horizontally installed in the profile at depths as shown in appendix A (Table A.2). All the measurements were measured every 60 minutes.

The field work on the western QTP was carried out by German parters of Kurt Roth, Ute Wollschläger, Tobios Pfaff and Chinese parters Qihao Yu, Huijun Jin, some students and assistant workers and Xicai Pan at the beginning of September 2007. The meteorological items are similar to those at Zuimatan except the snow thickness measurements. Two soil profiles were excavated down to frozen ground. Soil temperature and soil water content probes (TDR) were horizontally installed in the profile at depths as shown in Table A. The measuring interval of meteorological items and soil temperature is 30 minutes and 3 hours for soil water content measurements.

2.4.2 Data evaluation

All the data were processed with the code of the weather station database (version 7). The processing the meteorological data follows the manuals of each sensor. But for soil temperature and soil water content measurements, evaluations are introduced and discussed in the following.

Soil temperature evaluation The soil temperatures in the profile are measured with probes which are composed by an accurate resistance thermistor element and the integrated circuit. The soil temperature is calculated from the resistivity of the temperature probes with specific calibration values for each sensor. It was calculated with the following calibrating formula

$$\begin{cases} T = -\dfrac{a}{2b} - \sqrt{(\dfrac{a}{2b})^2 - \dfrac{r_0 - r_t}{r_0 \cdot b}}, (T \geq 0) \\ r_0 c T^4 + 100 c T^3 + b T^2 + a T + 1 - r_t / r_0 = 0, (T < 0) \end{cases} \tag{2.1}$$

Table 2.1. Measurements of the soil-weather monitoring station and the probe specifications.

probes	measurements	unit	resolution	accuracy	range	sources
MP100A	air temperature	℃	-	±0.5	-40∼60	①
	rel. humidity	%	-	±2	0∼100	
NR-LITE	net radiation	W m^{-2}	-	-	±2000	①
WindSonic	wind speed	m s^{-1}	0.01	±2% of reading	0∼60	②
	wind direction	°	1	±3	0∼360	①
RM Young 52202	rainfall	mm	0.1 mm/tip	2%	-	③
SR50	snow thickness	m	0.1 mm	±1cm	-	①
thermistor	soil temperature	℃	0.015	±0.02°	-	①
CS616	water content	%	-	-	-	①
TDR		%	-	-	-	④

① http://www.campbellsci.com; ② http://www.gill.co.uk; ③ http://www.youngusa.com; ④ http://www.setra.com; ④ Institut für Umweltphysik, Heidelberg.

where, $a = 3.90802 \times 10^{-3}; b = -5.802 \times 10^{-7}; c = -4.27350 \times 10^{-12}$; r_0 is the resistivity of the sensor at 0℃, and r_t is the resistivity that is measured. The soil temperature sensors were calibrated at 0℃ with a precision around 0.015℃ and an absolute error less than ±0.02℃.

Temperature interpolation is required in the data analysis, because sometimes the soil water content sensors and soil temperature sensors are not installed at the same depth, or data gaps occur. Linear interpolation works well, when the main heat transfer process is conduction or convection. However, during phase change occurring in the active layer, linear interpolation can lead serious deviations around the interface between the frozen soil and the thawed soil. As shown in Figure 2.9, the temperatures at the middle position T_m are interpolated from measured values T_u, T_l at the upper position and the lower position with two different approaches. The dashed cyan line is calculated by linear interpolation, which always makes the end time of phase change of the interpolated position close to the upper sensor and the temperature larger than the real value. The reason is the large difference in temperature gradients at the two sides. At the thawed side, the temperature gradient is usually much larger than that at the phase change side because of different heat fluxes above and below interface. These errors can seriously impact on the soil water content evaluation.

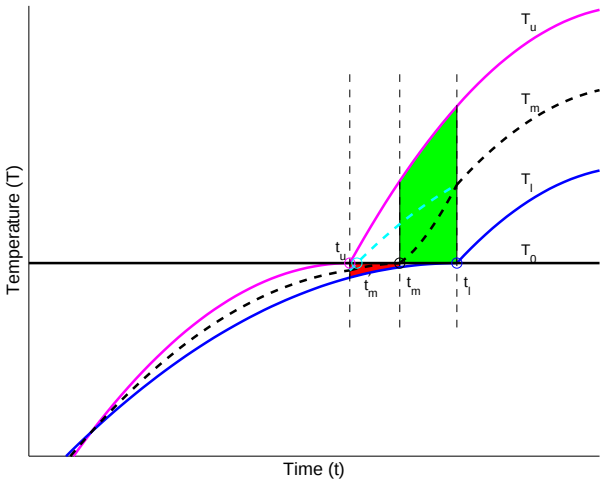

Figure 2.9. The schematic of temperature interpolation between the frozen soil and the thawed soil. T_u, T_l are the measured temperatures (magenta curve, black curve) at the upper and lower positions, respectively, and T_m are are the interpolated temperatures with two different approaches (dashed cyan curve: the linear interpolation, dashed black curve: semi-linear interpolation). t_u, t_l are the time of the critical points of the phase transition (T_0) at the upper and lower positions. t'_m, t_m are interpolated critical points of phase change time.

In the data evaluation, the time is divided into different periods and different temperature interpolation approaches are applied during the periods. The linear interpolation approach is used when the upper and lower sensors are both in frozen or thawed soil, which means heat conduction or convection mainly dominates the heat transfer during this period. While around the interface one sensor is in the frozen soil, the other one is in the thawed soil, a new approach is used. At this situation, the time of the critical points of the phase transition at the interpolated position are required, the temperatures are interpolated with two different temperature gradients. During periods from t_u to t_m, the temperature gradient decreases to zero with time; while from t_m to t_l, it increases with time from zero. The semi-linear interpolation is summarized as following

$$T_m(t) = \begin{cases} (T_0 - T_l)\cdot \dfrac{d_m - d_l}{d_u - d_l}\cdot \dfrac{t - t_m}{t_l - t_m} + T_0, & (t_u < t < t_m) \\ (T_u - T_0)\cdot \dfrac{d_m - d_l}{d_u - d_l}\cdot \dfrac{t_m - t}{t_m - t_u} + T_0, & (t_m < t < t_l) \\ (T_u - T_l)\cdot \dfrac{d_m - d_l}{d_u - d_l} + T_l, & (t_u \geq t, \quad t \leq t_l) \end{cases} \tag{2.2}$$

where, d_u, d_m, d_l are the depths of the upper, middle and lower sensors, and t is the measurement time.

This approach is verified with measured data at Chumaer. Here we use measured data from two sensors to interpolate the temperature of the position between these two sensors and compare them with the real measured data at this position. It shows that the semi-linear interpolation is much better than the linear interpolation in Figure 2.10. Near the end of the phase change, the error from the linear interpolation is significant, while that from the semi-linear interpolation is much better. Here we should note that the time of the critical point of the phase transition is vital to evaluate the soil water content from the TDR or CS616, because it is related to the estimation of ice content.

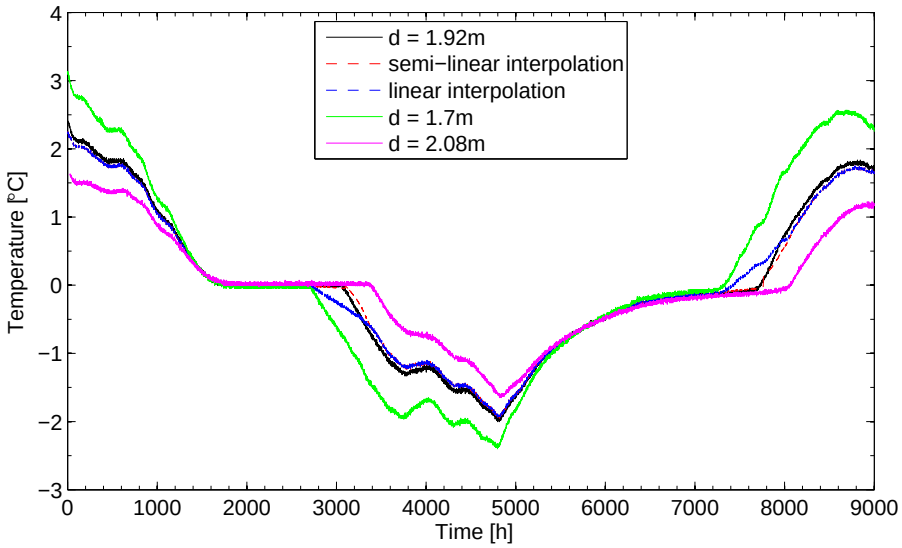

Figure 2.10. The validation of the semi-linear interpolation with real data (the second profile in Chumaer). The green, black and magenta curves are the measured temperatures at depth 1.7 m, 1.92 m and 2.08 m, respectively. The dashed blue and red curves are the interpolated temperatures with the linear interpolation and the semi-linear interpolation.

In the semi-linear interpolation approach, we assume a linear moving front with time within two nearby depths during thawing and freezing. During periods of seasonal phase change, non-conductive heat transfer plays an important role. For instance, phase change occurs in autumn when the active layer is freezing. The release of latent heat in the active layer retards the freezing front advancing from the surface downward and from the bottom upward [*Outcalt et al.*, 1990; *Kane et al.*, 2001]. In the active layer, the moving of the thawing front is usually slower than the freezing fronts, because cooling from the surface and the bottom occur at the same time during freezing in permafrost soils. During thawing, the moving front slows down from the surface to the bottom, which depends on the upper input heat flux and soil properties. For a smooth change of heat flux in a homogeneous soil profile, the thawing front can be approximated to move

uniformly within two nearby depths. On the QTP, without strong change of weather conditions and thick snow cover, the seasonal fluctuation of surface temperature can be approximated as a sinusoidal function. Therefore, the time of the critical point of the phase transition can be linearly interpolated from the time of nearby depths during the thawing period. During the freezing period, it is usually characterized as "zero curtain ". The moving of the freezing front is much faster than the thawing front. Therefore, the influence of weather fluctuations is much weaker. The time of the critical point of the phase transition can be linearly interpolated from the time of nearby depths. However, this approximation may fail when there is a drastic change in water content, for instance at a layer interface or water table, because heat diffusivity is strongly related to soil water (ice) content.

Soil water content evaluation Two kinds of probes were used to measure volumetric water content at the weather stations. They are Time-Domain-Reflectometry (TDR) and Water Content Reflectometry (CS616). The TDR probe works as a wave guide extension on the end of a coaxial cable. A very short fast rise time electro-magnetic pulse is sent into the TDR probe, reflections of the signal along the waveguide will occur when there are impedance changes. The travel time of the reflection is dependent on the velocity of the signal and the length of the waveguide. The velocity of the signal mainly depends on the dielectric number of the surrounding material. The dielectric number of water is much higher than that of other soil constituents. At the weather stations, TDR probes with three metal rods with a length of 20 cm, and a TDR100 (Campbell Scientific, Inc.) were used. The TDR100 generates pulses and samples and digitizes the reflections over a specified length of the transmission line. Through the analysis of the waveform, soil water content can be estimated by corresponding calibration equations described by *Topp et al.* [1980] and *Roth et al.* [1990].

In our data sets, all the soil water contents measured with TDR were calculated as follows. The dielectric permittivity of bulk water ε_w is dependent on frequency and temperature. As *Robinson et al.* [2005] point out for most of TDR measurements the effective frequencies are expected in a range of 0.7-1 GHz, and it should be below 0.6 GHz for measurements in dispersive media. From laboratory experiments, *Kaatze* [1989] suggest an empirical formula for the low-frequency permittivity to estimate soil water permittivity at different temperatures, which can be calculated as

$$\varepsilon_w(\nu = 0, T) = 10^{(1.94404 - 1.991 \times 10^{-3} T)}. \tag{2.3}$$

where, $\nu = 0$ represents the relative permittivity evaluated for a frequency of zero, and T is temperature in units of℃. Because the effective length of TDR rods is determined as a function of the real permittivity. The dielectric permittivity of soil is estimated by the linear interpolation of the calibrations in air and water. With the two calibration measurements in air (t_a, ε_a) and pure water (t_w, ε_w) at the calibration temperature, respectively, we obtain the dielectric permittivity for another measurement with

$$\sqrt{\varepsilon_c} = \frac{(\sqrt{\varepsilon_w} - \sqrt{\varepsilon_a})(t - t_a)}{t_w - t_a} + \sqrt{\varepsilon_a}. \tag{2.4}$$

ε_c is the composite dielectric number of the medium around the TDR probe. t is the measured travel time.

The volumetric liquid water content of a soil can be derived with a mixing model from relative permittivities of main volumetric components such as the soil matrix, air and water. The quantitative relationship between the dielectric permittivity ε_c and the volumetric water content

θ is given as the complex refractive index model (CRIM). When the soil temperature is equal or above the phase change temperature T_0 of the soil, it is calculated by

$$\theta_w^{CRIM} = \frac{\sqrt{\varepsilon_c} - \sqrt{\varepsilon_\mathrm{s}} - \phi\,(\sqrt{\varepsilon_\mathrm{a}} - \sqrt{\varepsilon_\mathrm{s}})}{\sqrt{\varepsilon_\mathrm{w}(T)} - \sqrt{\varepsilon_\mathrm{a}}} \quad . \tag{2.5}$$

When the soil temperature is below the phase change temperature T_0, it is calculated by

$$\begin{aligned} \theta_w &= \frac{\sqrt{\varepsilon_c} - (1-\phi)\sqrt{\varepsilon_\mathrm{s}} - \phi\sqrt{\varepsilon_\mathrm{a}} - \theta_i(\sqrt{\varepsilon_\mathrm{i}} - \sqrt{\varepsilon_\mathrm{a}})}{\sqrt{\varepsilon_\mathrm{w}(T)} - \sqrt{\varepsilon_\mathrm{a}}} \\ &= \theta_w^{CRIM} - \frac{\sqrt{\varepsilon_\mathrm{i}} - \sqrt{\varepsilon_\mathrm{a}}}{\sqrt{\varepsilon_\mathrm{w}(T)} - \sqrt{\varepsilon_\mathrm{a}}} \cdot \theta_i \quad , \end{aligned} \tag{2.6}$$

where, θ_i is the ice content, which is estimated as the difference between soil water content just before freezing at the end of summer and present measured unfrozen water content. Here we assume that the amount of total water content including solid water and fluid water keeps constant in the frozen soil, and it is equal to the total liquid water just before freezing at the end of summer. Notice that the volumetric ice content here is not a real value but just an equivalent water volume. Therefore there is no volumetric expansion.

On account of a non-constant phase change temperature for different soils and the mismatch of the time of the critical points of the phase transition of the temperature sensor and TDR sensor, the phase change temperature and time of each sensor had to be picked by hand. Due to the large differences of the time of the critical point of the phase transition at some weather stations such as Chumaer and Qumahe, the time of the critical point of the phase transition chosen from the temperature sensors are used for temperature interpolation. The time of the critical point of the phase transition chosen from the TDR sensors are used for identifying if the soil is frozen or unfrozen, and then relevant soil water content models were selected.

The CS616 probe works similarly to the TDR probe but it just has two parallel metal rods (30 cm long). It outputs a square wave with amplitude ± 0.7 volts and a frequency that is dependent on the dielectric number of the material surrounding the probe rods. The frequency of pulsing of the CS616 in free air is about 70 MHz. It is scaled down in the Water Content Reflectometry circuit output stages to a frequency easily measured by a datalogger. The CS616 reflectometer measures the number of reflections per second. The output from a datalogger is a period. The probe output period ranges from about 14 microseconds with rods in air to about 42 microseconds with the rods completely immersed in typical tap water. The accuracy of CS616 is $\pm 2.5\%$ using standard calibration with bulk electrical conductivity $\leqslant 0.5$ S m^{-1} and bulk density $\leqslant 1.55$ g cm^{-3} in measurement range 0% to 50% (http://www.campbellsci.com).

In the manual from Campbell Scientific, Inc., some empirical calibration equations to convert the period to volumetric water content are provided. There are several limits for these empirical equations. The most applicable one (method 1) for the study sites is

$$\theta_w = -0.0663 - 0.0063 \times t + 0.0007 \times t^2. \tag{2.7}$$

This equation is valid for mineral soils with bulk electrical conductivity of less than 0.5 dS m^{-1}, bulk density less than 1.55 g cm^{-3} and clay content less than 30%. However, the correction for temperature dependence is only performed over the temperature range from 10℃ to 40℃ for the probe output period. Due to the larger dynamic range of soil temperatures in permafrost, its influence on volumetric water content can not be ignored. Besides, the empirical equation can not consider the influence of ice in winter.

Concerning the above drawbacks of the method 1, we propose a new method (method 2) for the CS616 evaluation. It is similar to TDR evaluation, and assume that the period is proportional to the travel time of reflection in the rods. Although there are some differences of the measuring principles between TDR and CS616, here we assume there is a approximate linear relationship between period (p) and travel time: $t = K_p \times p$, K_p is a coefficient,

$$\begin{aligned}\sqrt{\varepsilon_c} &= \frac{(\sqrt{\varepsilon_w} - \sqrt{\varepsilon_a})(K_p \times p - K_p \times p_a)}{K_p \times p_w - K_p \times p_a} + \sqrt{\varepsilon_a} \\ &= \frac{(\sqrt{\varepsilon_w} - \sqrt{\varepsilon_a})(p - p_a)}{p_w - p_a} + \sqrt{\varepsilon_a} \quad ,\end{aligned} \tag{2.8}$$

The left steps in the procedure of CS616 evaluation are the same as in the TDR evaluation.

2.4.3 Data quality discussion

Drift of temperature sensor Some thermistors drifted with unexplained excursions at Chumaer, Qumahe and Zuimatan sites. There are two kinds of drift in the measurements. One is drift in time, the other one is drift as a whole. For the first kind of drift, sensors are dropped in the analysis, because the phase equilibrium temperature was not stable around 0℃. For instance at Chumaer site, sensors at depth 0.3 m, 0.7 m and 1.7 m in profile 1, and 2.28 m in profile 2 were dropped. For the second kind of drift, the thermistor measurements were corrected with a phase equilibrium temperature in the field. When the temperature drifted as a whole with the calibration value in the laboratory, the measurements during the period of phase change were used to replace calibration values from the laboratory. For instance at Chumaer site, the sensors at depth 1.1 m, 1.9 m, 2.0 m in profile 1, and 1.5 m, 1.92 m, 2.08 m in profile 2 were corrected with this approach.

Accuracy of CS616 The TDR100 produces a series of fast precisely-timed electrical pulses, and digitizes return voltages at intervals down to around 100 picoseconds. The complete reflectance trace is built up over 250 pulses. Therefore, the disadvantage of TDR is the expense of the equipment and the numerical challenges of properly analyzing each trace. The advantage is that measurements are relatively insensitive to salinity and temperature, as long as the salinity does not completely attenuate the reflected signal. Water content measurements of TDR in non-dispersive soils will be expected to lie in the effective frequency range of 0.7-1.0 GHz [*Robinson et al.*, 2005]. While the working frequency of CS616 is much lower than TDR, it has more problems than TDR due to dependence of the output signal on electric conductivity. In the following, we compare the soil water content derived from TDR and CS616 measured in two parallel profiles at Qumahe, and validate the new method for the CS616 evaluation.

At Qumahe, TDR sensors and CS616 sensors were both installed in the profile. The soil profile mainly contains loamy silt and loamy sand. There are three pairs of TDR sensors and CS616 sensors measuring at the same depth. The measured data derived from TDR and CS616 with different evaluations introduced before are shown in Figure 2.11. The estimated soil water content at the depth of 0.1 m is even higher than the measured porosity. Apparently, the method 1 for CS616 evaluation is invalid in the thawed soil at this site. As mentioned before, this empirical method is only valid at defined conditions. Although the clay content [*König*, 2008] is less than 30%, this large estimated soil water content at thawed condition may be caused by the high content of silt and organic materials besides the temperature influence. With the method 2, the values are comparable with those derived from TDR measurements. These values from CS616 are significantly higher than those from TDR measurements at thawed

condition and slightly lower at frozen condition. During the time of the critical point of the phase transition, there are large differences, this is probably because of the different measuring positions. Therefore, the conversion of CS616 evaluation here is considered to be more trustable that the empirical calibration in the manual from Campbell Scientific, Inc.

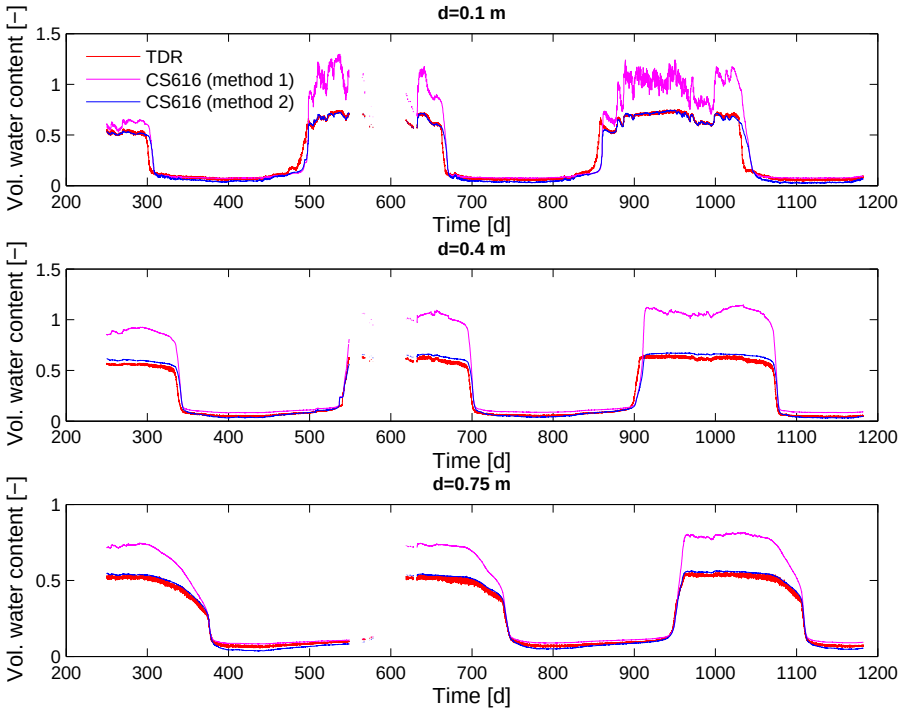

Figure 2.11. Comparison of the soil water contents measured with TDR and CS616 evaluated with different methods at Qumahe.

Because TDR is not available at Chumaer and Zuimatan sites for comparison, We only evaluated the CS616 data with method 1 and 2. At Chumaer, soil water contents measured at three different depths 0.14, 0.33, and 0.9 m are shown in Figure 2.12. The results are better than at the other sites as expected, because the soil conditions nearly meet the requirements of method 1. At Zuimatan, the results (not shown here) from method 1 are even worse than these at Chumaer because of the soil materials with high salt concentration. On account of the better results from method 2 than the method 1, we presume this method is valid. In later analyses, all the data from CS616 measurements were evaluated with the method 2.

In general, the TDR sensor is presumed to be more trustable than the CS616. The accuracy of the measurement of volumetric water content by TDR is estimated to be between 0.02 and 0.05, while the accuracy of the measured volumetric water content by CS616 is estimated to be around 0.05 at Chumaer and 0.02 to 0.1 at Qumahe, and much worse at Zuimatan because of the high salt concentration.

Mismatch of temperature in soil water content evaluation The measurements of soil temperature and soil water content at the same position or depth (homogeneous soils), the freezing and thawing characteristics are usually like in Figure 2.13a. However, sometimes they are often not measured at the same position like our measurements. This can cause some problems. One situation is from the experimental design when the two sensors are not measuring at the same depth, so that the interpolation of soil temperature is needed. However, this interpolation can be

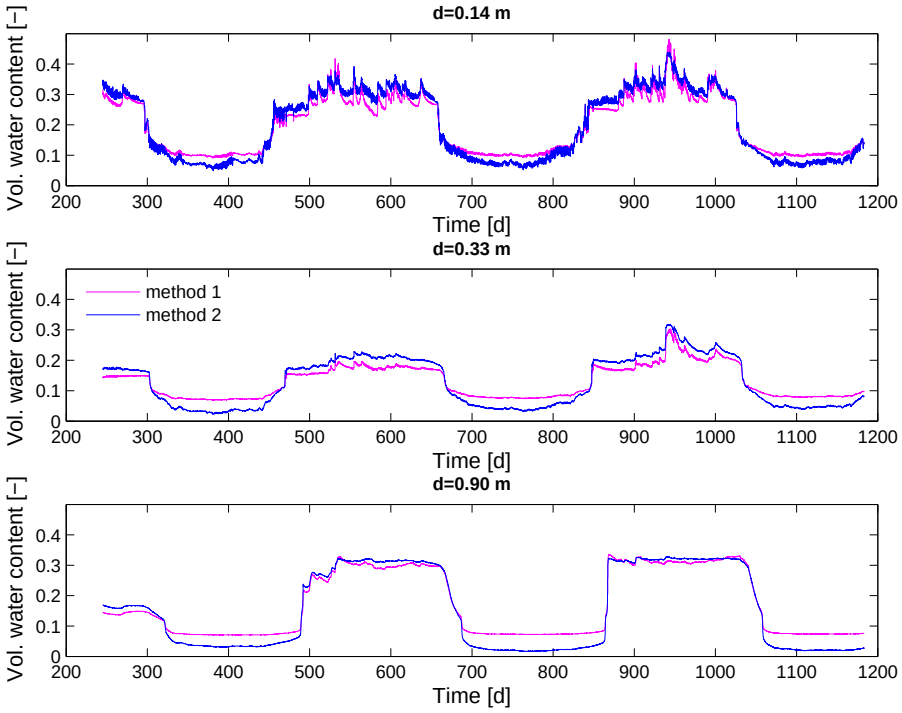

Figure 2.12. Comparison of the soil water contents measured with CS616 evaluated with method 1 and 2 at Chumaer.

not accurate during the phase change which will be discussed later. In one case, the interpolated soil temperature may represent the wrong position which is higher than the sensor for measuring soil water content, then the freezing and thawing characteristics could be as shown in Figure 2.13b. In another case, the interpolated soil temperature may represent a lower position than the sensor of measuring soil water content. Then the freezing and thawing characteristics could be as shown in Figure 2.13c. The second situation is the thawing and freezing cycle could not always be in one dimension. Then the temperature can not represent the true soil temperature at the position of sensor measuring soil water content, although these two sensors were inserted at the same depth. It also can cause two different freezing and thawing characteristics.

Using the CRIM model including ice content to calculate soil water content, the mismatch of soil temperature and soil water content can cause some unreasonable results. When the soil at the position of the soil temperature sensor freezes or thaws earlier or later than the soil at the position of TDR or CS616, it will cause water content jumps. The reason for this phenomenon is from a wrong ice content calculation in Equation 2.6. For the first case, during thawing the ice content is ignored (still frozen) due to the positive temperature which causes a positive jump ($\Delta\theta \approx 0.094 \cdot \theta_i$, ice content is true); during freezing the ice content is overestimated (no ice exists), which causes a negative jump ($\Delta\theta \approx 0.094 \cdot \theta_i$, ice content is artificial but very small, when the total water content is small). These jumps can be seen in the second plot in Figure 2.13b. For the second case, during thawing the ice content is underestimated (already thawing), which causes a positive jump ($\Delta\theta \approx 0.094 \cdot \theta_i$, ice content is near zero); during freezing the ice content is underestimated (wrong ice content calculation, negative value), which causes a negative jump ($\Delta\theta \approx 0.094 \cdot \theta_i$, ice content is artificial but very small, when the total water content is small). These jumps can be seen in the second plot of Figure 2.13c.

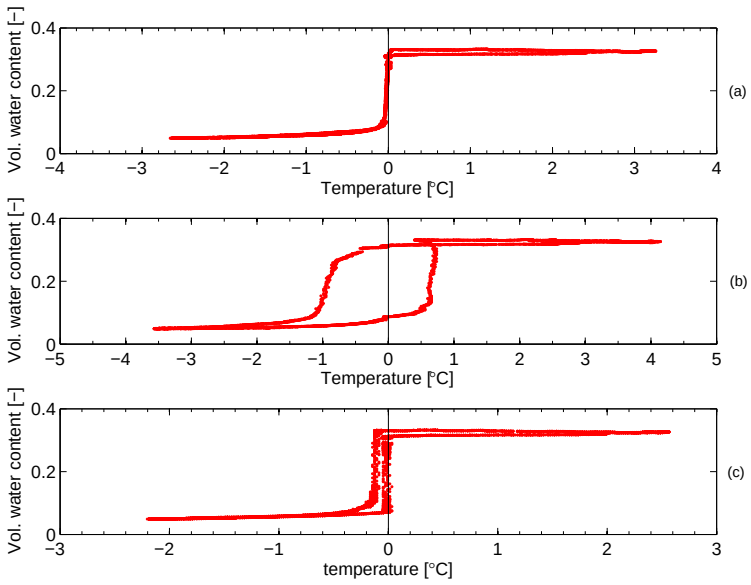

Figure 2.13. The freezing and thawing characteristics using the temperature at different positions. (a) soil temperature and soil water content measured at the same depth, (b) the temperature measured at a higher depth than that of the soil water content, (c) the temperature measured at a lower depth than that of the soil water content.

From the above explanation, we can easily identify these phenomena from freezing characteristics at the four weather stations. For example in the second profile at Chumaer, there is a slight mismatch at depth 1.92 m shown in Figure 2.14. Therefore, the freezing characteristic is an important index to check the data quality for soil water content evaluation.

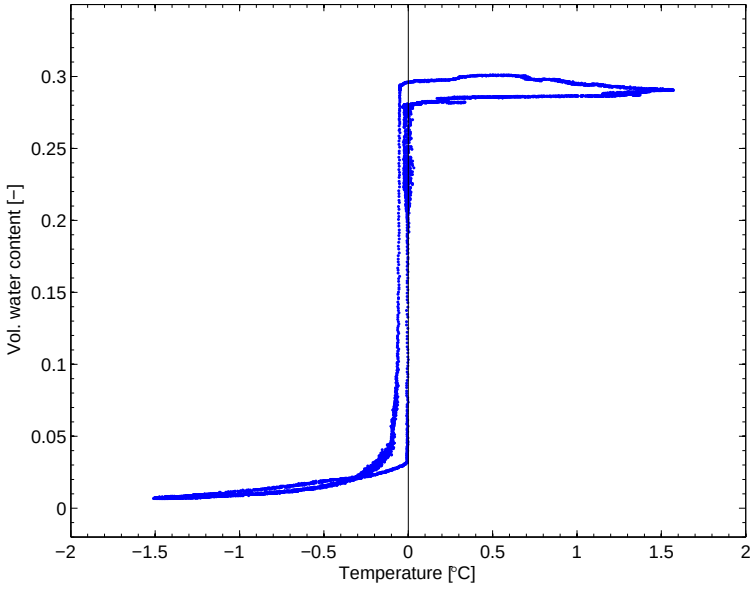

Figure 2.14. The freezing and thawing characteristics at depth 1.92 m at Chumaer station.

In the data evaluation, we found unexpected soil freezing characteristics at some depths. They may be caused by the following situations. The uneven thawing front may occur when there are different surface characteristics or a drastic change of soil or water content between two sensors.

However, the distance between the two sensors is about 10 cm. These kinds of influences should be very small. The error can also come from the improper temperature interpolation. For a semi-linear assumption, it only fits for the pure heat conduction without a drastic change in thermal diffusivity. However, the thermal diffusivity is quite different between the two sides of the water table.

2.5 Summary

In this chapter, a general overview of the permafrost on the QTP and the study sites is given. It includes the evolution of the QTP and the associated climate and permafrost, and current environmental conditions in the study regions. In addition, investigations including the review of the topographical, hydrological and climatological conditions in the study areas, and the field explorations are presented at the study sites. From the investigations, we can conclude that the selected sites can represent different permafrost states for the study of permafrost degradation on the QTP.

Two points were proposed to improve the data evaluation. Based on the characteristics of the heat transfer around the phase change front, a semi-interpolation was proposed to calculate the soil temperature for the soil water content evaluation. It is much better than the linear interpolation. Due to the limitations of CS616 sensors and their working conditions, a new method for evaluating the soil water content was proposed. The results were much better than the empirical formula supplied by Campbell Scientific, Inc. The comparison of TDR and CS616 at Qumahe demonstrated that this method can effectively extend the application of CS616 to our measure conditions.

3
Characteristics of the weather-permafrost interaction at the study sites

3.1 Introduction

In this chapter, the observations at four soil-weather monitoring sites (Chumaer, Qumahe, Zuimatan and Tianshuihai) are examined in detail. The main contents include observations of the soil-atmosphere interaction and the hydraulic and thermal dynamics in the active layers. The objectives of this chapter are: (1) to introduce the materials about the instrumentation and measured data at each site for later further analyses, (2) to confirm the permafrost state and associated factors, (3) to compare the differences of observations at the four study sites.

3.2 Chumaer

As a typical permafrost site, the Chumaer site was selected in this region. The notable features of the permafrost are the thick active layer with a large amount of groundwater, and significantly warming permafrost. Along with climate warming, the permafrost degradation may influence the hydrologic cycle in this region. Through analyzing the data from the soil-weather monitoring station, the characteristics of the permafrost and associated factors are presented in the following sections.

The data used here were recorded from August, 2006 to March, 2009, and the station is still running so far. During the period of past measurements, the air temperature sensor went wrong in 2007 from April 4 to April 11 and from April 18 to August 11, then it was replaced with a new sensor. Measurements of net radiation were disturbed by bird drops. There were three periods (November 17, 2006 - April 11, 2007; October 16, 2007 - January 26, 2008; March 11, 2008 - May 7, 2008), in which the net radiation is obviously abnormal. We found bird drops covered on the surface of net radiation sensor during retrievals, it worked as usual after cleaning. On May 7, 2008, the weak bird proof was replaced with a stronger one, and after that it worked well. There are four failed soil temperature sensors in profile 1. The sensor at depth 0.10 m failed from September 5, 2008, and the sensor at depth 0.20 m failed from July 5, 2007. In profile 2, the sensor at depth 0.05 m provided non-reliable results sometimes and failed from July 19, 2008.

3.2.1 Interaction between atmosphere and ground surface

Meteorological conditions Due to the high-altitude and low-latitude of the QTP, the current climate on the QTP is characterized as arid and cold [*Zhou et al.*, 2000]. The characteristics of the measured air temperatures at this site are shown in Figure 3.1. We can find large differences in air temperatures during day and night, which is one typical characteristic of the climate on the QTP. From day number 246 to 1182, the minimum and maximum values of daily mean air temperature were -25.5℃ and 10.1℃, respectively; the minimum and maximum measured

temporal values were -36.5℃ and 21.4℃, respectively. Besides, the diurnal range of the air temperature shows a seasonal fluctuation, and the diurnal range of air temperature in winter is larger than that in summer. In 2008, the mean annual air temperature was -4.9℃, and the mean diurnal range of air temperature was 14.0℃.

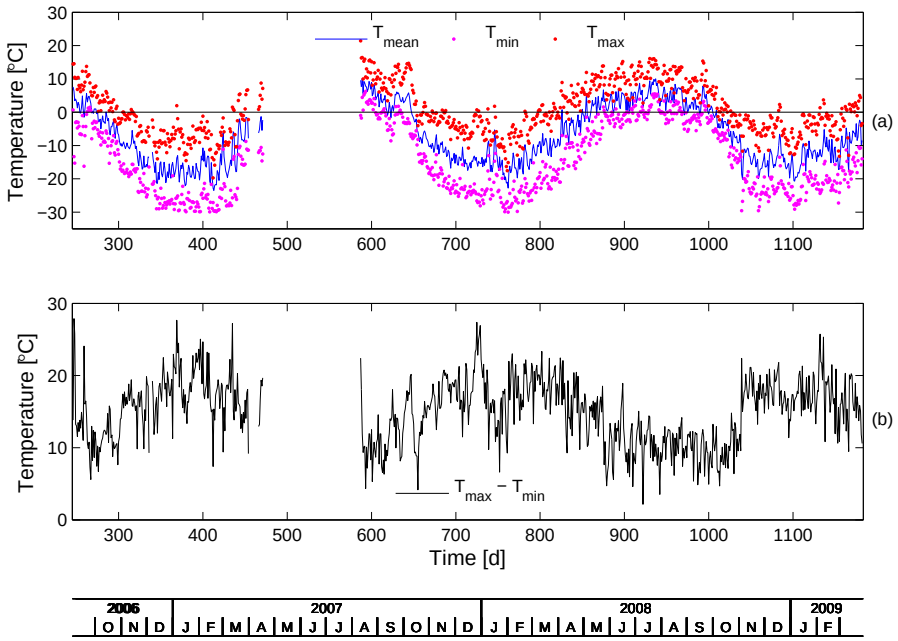

Figure 3.1. Air temperature at Chumaer from day number 246 to 1182. (a) daily mean, maximum and minimum air temperature ($T_{mean}, T_{min}, T_{max}$). The blanks correspond to missing data. (b) diurnal range of air temperature

The net radiation is the difference between the radiant energy absorbed and the radiant energy emitted at the ground surface, which depends on the fluxes of short-wave radiation and terrestrial long-wave radiation. The net radiation balance for the Earth's surface is defined as sum of solar radiation absorbed, terrestrial radiation absorbed and terrestrial radiation emitted [*Pidwirny*, 2006]. Figure 3.2 shows the temporal development of the net radiation. The maximum net radiation was 919 W m^{-2} and the maximum daily mean net radiation was 188 W m^{-2}. Due to the disturbed data, it is not possible to calculate the mean annual net radiation at this site.

As a plateau continental climate, the precipitation is mainly controlled by the summer monsoon at Chumaer. According to the analysis of data from the weather stations in this region from 1962 to 2004 [*Li et al.*, 2006], the proportions of seasonal precipitation were 16.1% (spring), 59.5% (summer), 22.2% (autumn), 2.3% (winter). Besides, they found that there was an increasing trend in precipitation during the study period, and the major increases of precipitation were during spring and winter.

At Chumaer, rainfall and snow thickness were measured. After correction with temperature, the measured snow thickness is not equal zero most of the time. This may be caused by the soil settlement after the setup of the tower. Its average dynamic range is around 3 cm when there is no snow cover. This may be caused by the shaking of the tower caused by the strong wind. Besides, the random large values may also caused by the disturbance of moving objects like people under the sensor. Due to the strong noise, it is difficult to clearly identify the snowfall acts from the measured data. From Figure 3.3a, we can find that the snowfall was small and

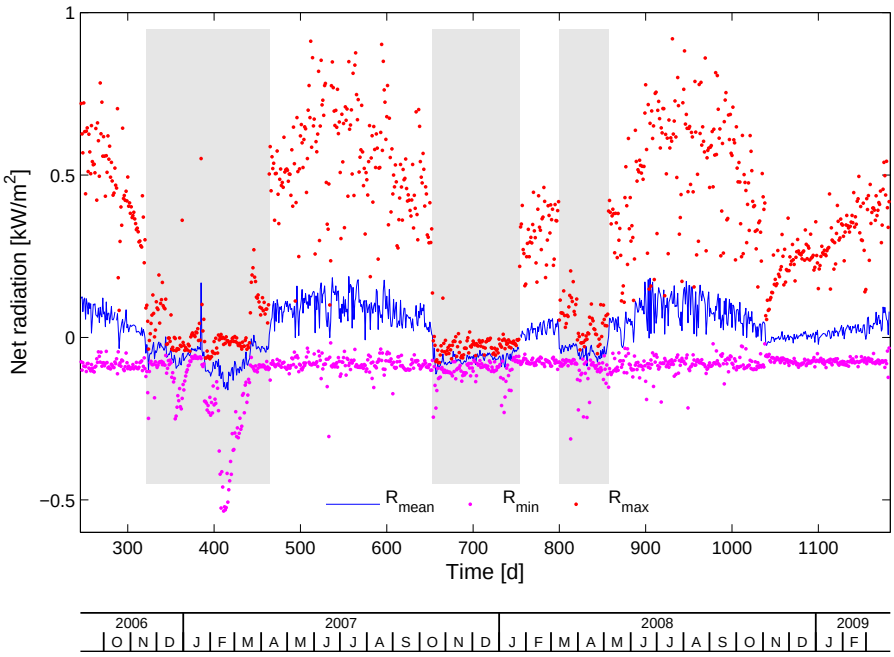

Figure 3.2. Characteristics of net radiation at Chumaer from day number 246 to 1182. $R_{mean}, R_{min}, R_{max}$: daily mean, minimum and maximum net radiation, respectively. The gray bars correspond to disturbances by bird drops

occurred just occasionally. In the spring of 2007, there was a large snowfall. Its maximum thickness reached about 13 cm, and maintained for about 36 days. In the winter of 2008, there was a clear snowfall (day number 1038), snow cover only maintained about 18 days and the maximum thickness was only about 10 cm. Apparently, the characteristics of the snowfall at this site is typical on the QTP, which is characterized for thin snow cover and short duration. In Figure 3.3b, it shows that the rainfalls mainly concentrated in summer. The measured total rainfalls in 2007 and 2008 were 266 mm and 317 mm, respectively.

The wind characteristics at this site are presented in Figure 3.4. The mean wind speed was 3.6 m s^{-1}, and the maximum wind speed reached 24.4 m s^{-1}. Usually the strongest wind occurred in spring from the middle of January to end of February. The daily fluctuation of wind speed in Figure 3.4b shows that the daily strong wind occurred from middle night to the morning in coordinated universal time (UTC) time (8 hours lag behind the local Beijing time). This might be caused by the local topography. The Kunlun mountains lie along west-east direction in this region, and most of the mountains are over 5000 m covered with glaciers. Since the heating and cooling rates of the glacial surface and normal ground surface are different during day and night, it might strengthen the local atmospheric circulation. From the statistics of wind direction in Figure 3.4c we can find that the main wind directions are Northwest and South-Southeast. Generally, the prevailing winds in the middle latitudes between 35 and 65 degrees latitude blow from the west to the east. In the Northern hemisphere the winds are predominantly from the southwest [*Grotzinger et al.*, 2007]. Therefore, the wind should be mainly influenced by local factors at this site.

Characteristics of the interaction between ground surface and atmosphere The interaction between ground surface and atmosphere is mainly through heat and mass exchange. In permafrost region, the primary factors influencing this interaction are weather, vegetation, snow cover, and surface hydrologic regime during the thawing season [*Romanovsky and Osterkamp*,

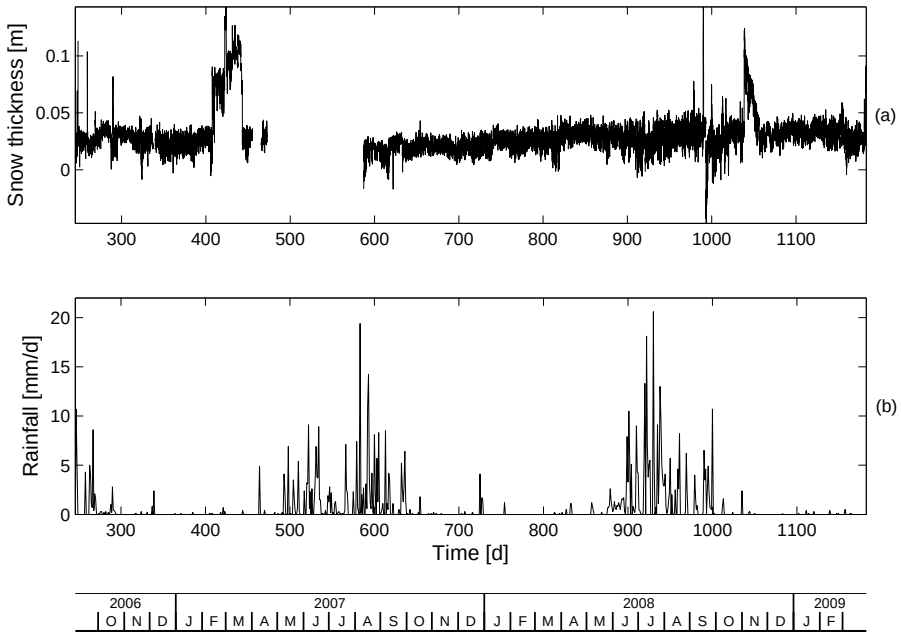

Figure 3.3. Measured precipitation at Chumaer from day number 246 to 1182. (a) snow thickness, blanks correspond to no available air temperature for the sensor correction; (b) rainfall.

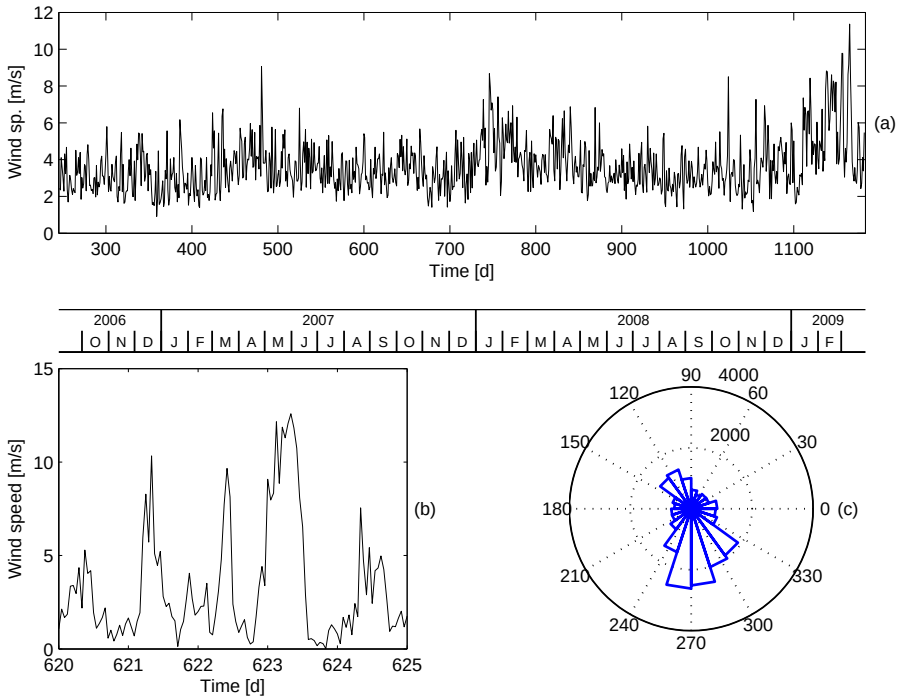

Figure 3.4. Wind characteristics at Chumaer. (a) daily mean wind speed from day number 246 to 1182; (b) daily wind speed from day number 620 to 630; (c) statistics of wind direction.

1995; *Zhang et al.*, 1996; *Wang et al.*, 2009a]. Due to the difficulty of measuring the ground surface temperature, the soil temperature at a depth of 5 cm below the ground surface was used to study the relationship between air and ground surface temperatures (T_a, T_s). Note that all the ground surface temperatures mean the measured soil temperatures near the surface.

The characteristics of the interaction between the ground surface and the atmosphere at Chumaer are presented in Figure 3.5. Blanks are caused by the failure of the sensor. Besides, the soil temperature sensor at a depth of 5 cm in profile 2 failed sometimes. Therefore, the deviated data from day number 313 to 631 were dropped. This sensor stopped working from day number 931. In Figure 3.5b, it shows that the temperature differences between the air and the ground surface ($\Delta T_{as} = T_a - T_s$) are generally larger in winter than in summer. The significant drops in winter were caused by snowfalls (February in 2007 and November in 2008). However, positive values (maximum 2.7℃) occurred occasionally, namely air was warmer than the near surface soil, for instance, in January 2008. The climatic factors should be responsible for these transient effects. For instance, the strong wind in January 2008 might indicate the drastic change of the weather, which can disturb the normal relationship between the air temperature and the ground surface temperature in a short time.

In Figure 3.5c, it shows the seasonal variations of the diurnal ranges of the ground surface temperature (profile 1) and the air temperature. During summer, they were close each other. While the diurnal range of the ground surface temperature was much larger than that of the air temperature during winter. This may be mainly caused by the frequent precipitations, then the water evaporation at the surface makes the soil-atmosphere interaction closer. In addition, the diurnal range of the ground surface temperature was significantly reduced when the snow cover occurred. As shown in Figure 3.5c, the snow cover appearance could be identified from the variations of the diurnal range of the ground surface temperature during the periods such as day number 345-385, 405-441 and 1038-1067.

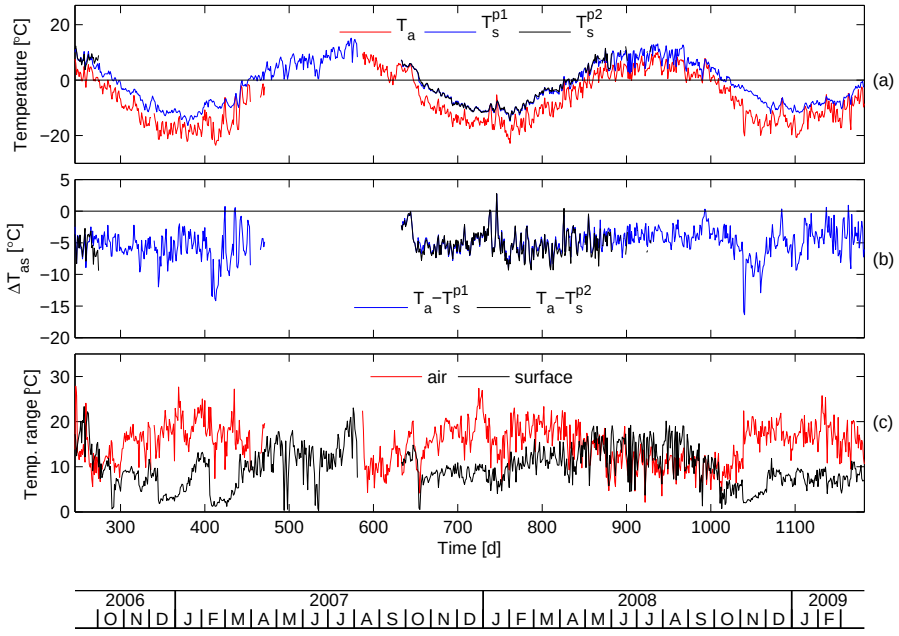

Figure 3.5. Characteristics of the air temperature T_a (2.0 m above the ground surface) and the ground surface temperature T_s (0.05 m below the surface) at Chumaer. (a) the measured air temperature and the ground surface temperature; (b) the differences between air temperature and ground surface temperature; (c) the diurnal range of air temperature and ground surface temperature.

In general, ΔT_{as} and the diurnal range differences between the air temperature and the ground surface temperature both demonstrate that the coupling of surface and atmosphere in summer was stronger than in winter. To explain these differences it is necessary to examine the factors

which influence the heat exchange between ground surface and atmosphere. Most of these factors mainly take effects in summer, for instance, the hydrologic processes of the surface. Besides, the vegetation provides excellent heat insulation, which reduces both the upward heat flux during frozen period and the downward heat flux during the thawing period [*Wang et al.*, 2009*a*]. From April to September in 2008, ΔT_{as} decreased slightly, which may result from the increase of relative humidity, because of the summer monsoon. While in winter, particularly in November 2008, there was a significant increase of ΔT_{as}, which acted as an insulator during snow cover appearance [*Zhang et al.*, 1996]. It made the near surface soil temperature at 5 cm in November 4.4℃ and 4.2℃ warmer than that in October and December, respectively.

The process of evapotranspiration is one of the main consumers of solar energy at the Earth's surface. Weather parameters and surface characteristics are major factors affecting evaporation and transpiration. The principal weather parameters affecting evapotranspiration are solar radiation, air temperature, humidity and wind speed. Due to the dry and cold weather at Chumaer, as well as sparse vegetation on the ground surface, the evaporation was not strong. As roughly estimated by *König* [2008], the evapotranspiration was 82.7 mm in October 2006. Due to small water availability of the frozen surface in winter, evapotranspiration should be even smaller.

3.2.2 Seasonal hydraulic and thermal dynamics of the active layer

In active layers, the freeze-thaw cycle couples the hydraulic and thermal dynamics. The hydraulic and thermal regime is dominated by the soil water content and thermal properties of the soils [*Hinkel et al.*, 2001]. The characteristics of various active layers have been investigated in detail in numerous studies [*Kane et al.*, 1991; *Boike et al.*, 1998; *Roth and Boike*, 2001; *Hinkel et al.*, 2001; *Ishikawa et al.*, 2006]. On the QTP, the thermal regime of the active layer has been explored in several studies [*Zhou et al.*, 2000; *Zhao et al.*, 2000]. According to the characteristics of the hydraulic and thermal regime, it is divided into three periods as spring and summer thawing (SST), autumn freezing (AF) and winter cooling (WC) in this study. The major characteristics of the hydraulic and thermal regime in each period is summarized in the following.

The spring-summer thawing regime starts from the start of the thawing front in spring at the surface until the beginning of the freezing front in late summer or autumn at the surface. During this period, the soil temperature gradient increases quickly in the first stage, then in the second stage it decreases slowly until the thawing front reaches the maximum thickness of the active layer. Particularly in the second stage, the thermal regime is typified by a large daily dynamic range of soil temperatures and rapid response to the weather fluctuations. In the active layer, it includes thawed soil, thawing front and frozen soil above the permafrost table during this period. The major processes in the active layer include heat conduction, heat convection caused by infiltration, and phase change at the thawing front.

The autumn freezing regime starts from the start of the freezing at the surface until the disappearance of the freezing front at the bottom. At the beginning of this period, the surface soil temperature undergoes a daily freeze-thaw cycle, which maintains the soil temperatures near 0℃ for a certain time. During this period, the active layer is refreezing from the top down and from the bottom up, which is normally defined as zero-curtain. Then the freezing front moves quickly downward, and compresses the zero-curtain layer.

The winter cooling regime starts from the disappearance of the zero-curtain until the start of thawing at the surface. During this period, the phase change is usually negligible in the active layer, and the heat conduction is the main heat transfer mechanism.

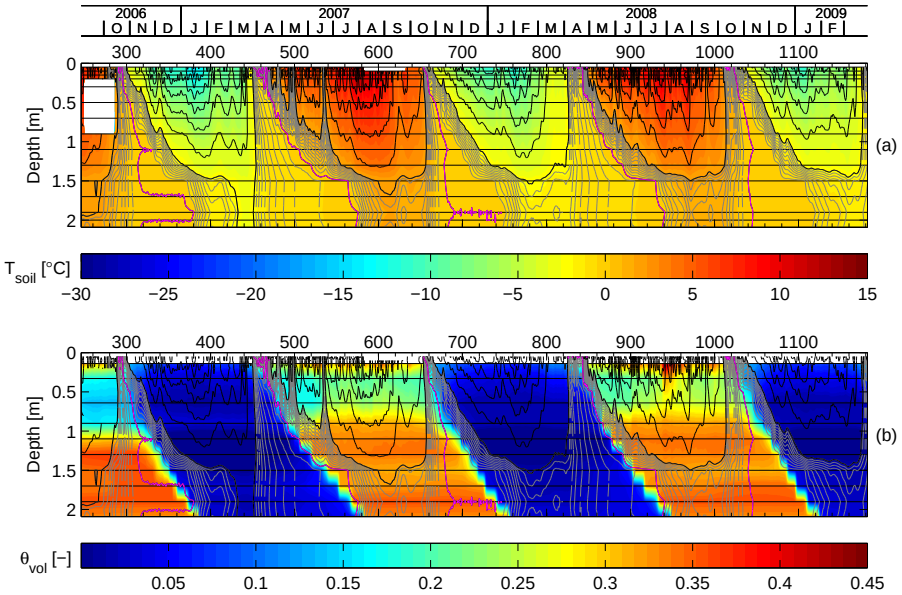

Figure 3.6. Temporal evolution of soil temperature and volumetric soil water content in profile 1 at Chumaer. (a) contour lines of soil temperature are drawn with increments of 2℃ (solid line) and 0.2℃ (dashed line), respectively, 0℃ magenta lines) and around 0℃ (gray lines). (b) all contour lines repeated from (a) to facilitate cross-referencing. Blank areas indicate missing data, and horizontal black lines indicate the positions of the probes.

At Chumaer, due to the strong influence of groundwater, the active layer has two contrasting layers with different water contents. The hydraulic and thermal dynamics in profile 1 and profile 2 are presented in Figure 3.6 and 3.7, respectively. Due to the similar characteristics of both profiles, profile 1 was chosen to analyze the characteristics of the hydraulic and thermal pattern in the following.

`(1) Spring-summer thawing regime (SST)`

As shown in Figures 3.6 and 3.7, there were two periods of SST (SST1: day number 475-660, SST2: day number 850-1020). Apparently, the duration of SST1 was longer for about 15 days than SST2. This was because of the colder winter before SST1. In Figure 3.6 and 3.7, there was a key point in both profiles, where the thawing speed was slowing down. They were around 1.1 m and 1.3 m in profile 1 and profile 2, respectively. This was consistent with the water table in each profile. The evident slowing thawing front is attributed to the larger soil water content below the water table than the upper part.

During summer thawing period in both profiles, weather conditions had a significant influence on the thermal regime. For example, as shown in Figure 3.3b, during SST1 there were two rain events at day numbers 498 and 532, which affected the thermal regime of the active layer in profile 1 clearly. Although there was no available air temperature data in Figure 3.2, we still can find that the net radiation decreased during these rain events. To lower and homogenize the soil temperature in such a short time, there must be strong processes which can take away the heat quickly. During the rainfalls, the cold rain water infiltration can lower the soil water temperature quickly. However, from the observation of soil water content, we can find that these small rain events did not change the soil water content too much in the active layer. Therefore, reduced solar radiation and evaporation may be the major reasons for the drastic cooling active layer. Because the strong wind and high water content at the surface are in favor of evaporation, which can take much larger amount of heat energy than the cold rain water infiltration.

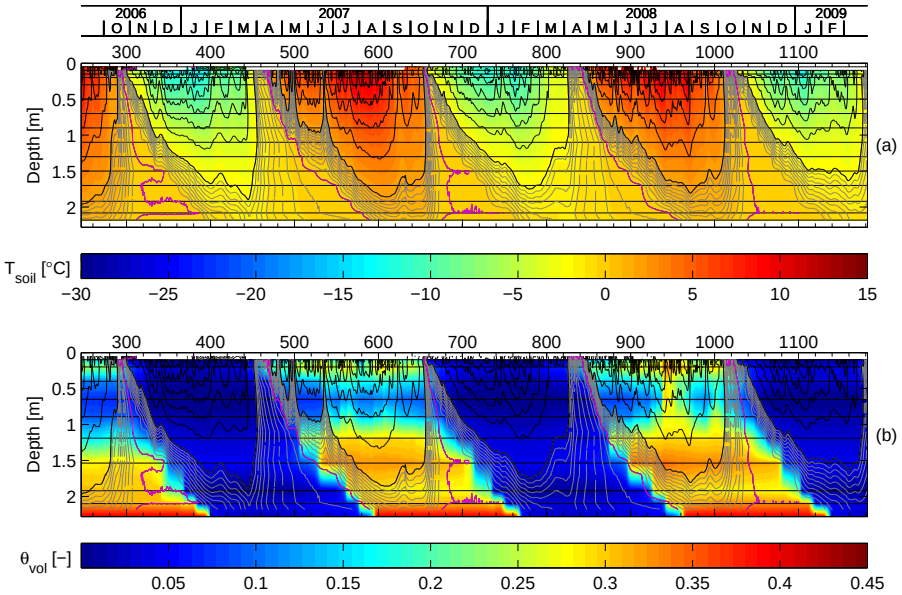

Figure 3.7. Temporal evolution of soil temperature and volumetric soil water content in profile 2 at Chumaer. (a) contour lines of soil temperature are drawn with increments of 2℃ (solid line) and 0.2℃ (dashed line), respectively, 0℃ magenta lines) and around 0℃ (gray lines). (b) all contour lines repeated from (a) to facilitate cross-referencing. Blank areas indicate missing data, and horizontal black lines indicate the positions of the probes.

As shown in Figure 3.6 during SST2, the most clear interruption of strong precipitation to the thermal regime was from day number 930 to 960. The soil temperature fell down and lasted for about 30 days. As shown in Figure 3.3b and Figure 3.2, the amount of rainfall was much larger in July (912-943) than in August, and the net radiation increased in August. Besides, air temperature dropped down from July to August. However, the soil kept warming in July but dropped down in August. This might be caused by stronger evaporation in August.

From the above analysis, it shows that the weather in summer can quickly and strongly disturb the thermal regime at Chumaer. Due to the dry soil at the upper part of the active layer, there is no clear soil water content increase with the downward thawing front. But down to the original groundwater table in late summer, it works as a water pool above the permafrost.

`(2) Autumn freezing regime (AF)`

As shown in Figures 3.6 and 3.7, the durations of AF were around 120 days. For instance, in profile 1 there were three AF periods such as AF1 (day number: 290-400), AF2 (day number: 650-770), AF3 (day number: 1020-1140). The AF duration mainly depends on the soil water condition in the active layer. The higher the water content, the longer the zero-curtain duration. During these periods, the main disturbances were snowfalls. Normally the major snowfall occurred in spring, and the snowfall in winter was occasional on the QTP [*Zhou et al.*, 2000]. Only one significant snowfall occurred during AF3. Its thickness was about 10 cm and lasted for about 20 days. Due to the low air temperature during this period in Figure 3.1a, the snow may sublimate directly, which further cools the surface soil. Therefore, there was no obvious insulating effects of the snow cover.

Non-conductive processes played an important role in the isothermal region during AF. Due to the osmotic potential variations induced by the freeze-thaw cycle at the ground surface, vapor transport and internal distillation mechanisms produce and maintain the zero-curtain for the wet active layer [*Outcalt et al.*, 1990]. However, the zero curtain effect occurred very late in

autumn and appeared around the groundwater table at this site. The dry soil in the upper part was frozen easily and quickly. After quick freezing it kept frozen at the surface during this period. The evapotranspiration was weakened due to little unfrozen water at the surface. When the freezing front met the groundwater table, the speed of downward moving front slowed down by the zero-curtain.

(3) Winter cooling regime (WC)

In Figure 3.6, there were three periods of WC (WC1: day number 390-450, WC2: day number 760-820, WC3: day number 1140- –). There were no large differences in the duration of each period. During WC1, the snow cover existed from day number 405 to 440 (Figure 3.3a), which obviously disturbed the ground thermal regime. However, the fluctuation of the thermal regime of the active layer was consistent with the air temperature change. The air temperatures underwent quickly two times of warming and cooling during this period. It demonstrated that the insulating effect of the snow cover was not so strong that the variation of air could still influence the thermal regime of the active layer. The heat energy below the snow cover might be taken away by sublimation, because the low humidity and strong wind could facilitate the sublimation during this period.

During WC2, the soil temperature underwent a smooth warming but the persistence of the soil temperature from isoline -4℃ to -2℃ took much longer than WC1 and WC2. During WC3, it started warming about 35 days earlier than WC1 and WC2. But from day number 1137, the air temperatures went down until day number 1155, then went up and fell sharply down to -17.9℃ on day number 1166 in Figure 3.1a. Correspondingly, the soil temperature fluctuated with the air temperature variations.

3.3 Qumahe

At Qumahe, the data were recorded from September, 2006 to March, 2009. Due to fail of multiplexer during the period from 01:00:00 July 21 to 18:00:00 September 12, 2007, there were several missing data. Some thermistors drifted with unexplained excursions in the field. There are two kinds of drift. One kind of sensors at depths 0.2 m, 0.4 m, 0.9 m, 1.1 m, 1.25 m and 1.3 m were dropped because of non-constant drift. The other kind of sensors at depths 0.55 m, 0.7 m, 1.2 m, 1.45 m and 1.57 m were given a constant offset according to the phase equilibrium temperature of 0℃ in these measurements. Besides, one TDR sensor at depth 1.2 m failed occasionally and it was dropped in the calculations.

3.3.1 Interaction between atmosphere and ground surface

Meteorological conditions At Qumahe, the temporal development of the daily mean, minimum and maximum values of air temperature are shown in Figure 3.8a, which are similar to Chumaer site. From day number 250 to 1181, the minimum and maximum values of daily mean air temperature are -24.8℃ and 10.0℃, respectively; the minimum and maximum measured temporal values are -35.6℃ and 17.2℃, respectively. Due to several missing data, this statistics can just give a reference. Besides, as shown in Figure 3.8b the seasonal variations in the diurnal range of air temperature are also similar to Chumaer. It is larger in winter than in summer. Using the complete year round data of 2008, the mean annual air temperature is -4.8℃.

Having no disturbances like at Chumaer, the net radiation measurements are completely shown in Figure 3.9. The maximum net radiation was 902 W m^{-2} and the maximum daily mean net radiation was 215 W m^{-2}. The mean annual net radiation was 71 W m^{-2} in 2008.

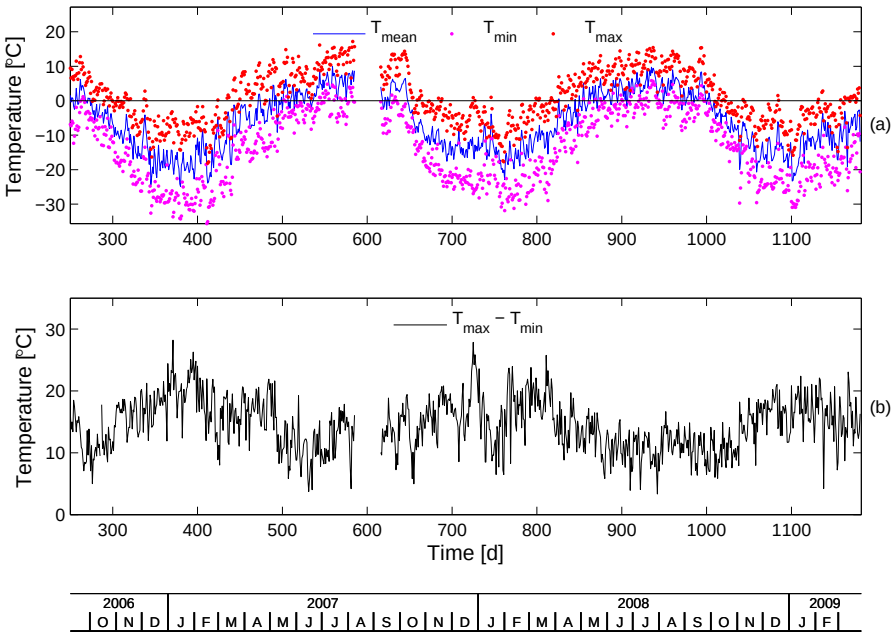

Figure 3.8. Air temperature at Qumahe from day number 250 to 1181. (a) daily mean, maximum and minimum air temperature ($T_{mean}, T_{min}, T_{max}$). (b) diurnal range of air temperature

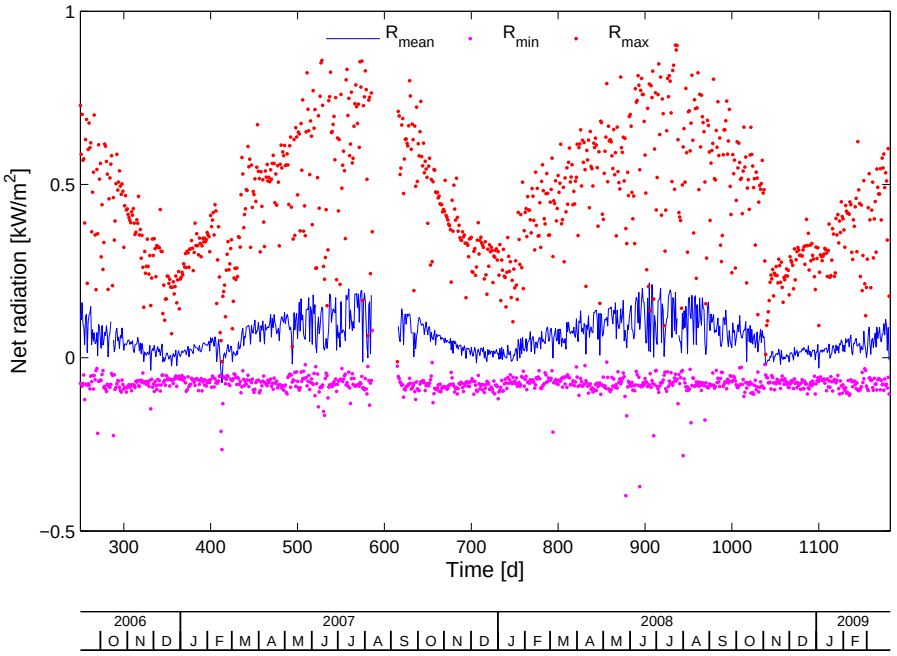

Figure 3.9. Characteristics of net radiation at Qumahe from day number 250 to 1181. $R_{mean}, R_{min}, R_{max}$: daily mean, minimum and maximum net radiation, respectively.

Rainfall and snow height were both measured at this site. The abnormal heavy rainfalls during winter seasons are doubtful. From the observations of precipitation in last 43 years in the rivers source regions, the mean precipitation in winter was less than 20 mm [*Li et al.*, 2006]. Since strong wind occurred during winter, it would fake the rainfall measurements. As shown

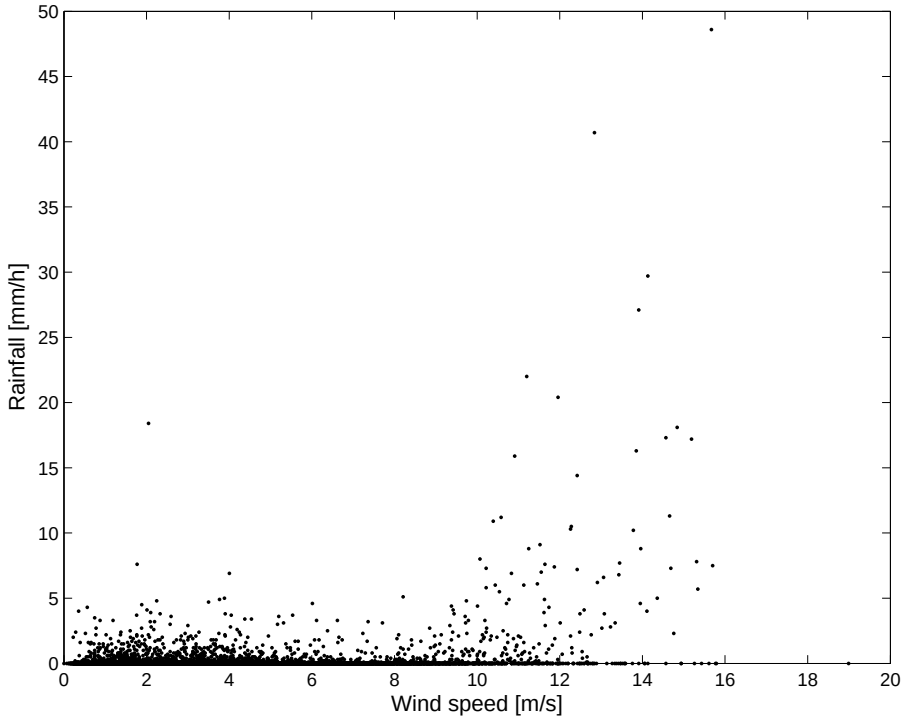

Figure 3.10. The relation between measured rainfall and wind speed at Qumahe. Here the used data of rainfall are hourly measurements measured at the same time with wind speed measurements.

in Figure 3.10, the abnormal rainfall always occurred when the wind speed was over 11 m s^{-1}. Therefore, these high measurements should be caused by the shaking of the tower. For the above reasons the measurements over 11 m s^{-1} and during day numbers 700-800 and 1060-1170 will be replaced with zero in later calculations. Although it would miss the small precipitation, the total amount should be very small in winter. Except the snow, the amount of rainfalls were about 260 and 410 mm in 2007 and 2008, respectively. After temperature correction, the measured snow cover thickness was about 5 cm most of the time. This should be a systematic measure error caused by loosened soil at the beginning. Besides, seasonal fluctuation of the systematic error might be caused by freezing ground formation or vegetation. As discussed for Chumaer, the little snowfall was difficult to be identified from the measured data here. In Figure 3.11a, notable snowfalls can be found in the winter of 2006 and the spring of 2008 and 2009. During these periods, snowfall also occurred at Chumaer, but the snow cover was thicker at Qumahe. Particularly, the snow thickness reached about 17 cm and the snow cover lasted for 45 days. In Figure 3.11b, it shows that the rainfall was also controlled by the monsoon. The abnormal rainfall measured from January to March should be caused by the artifacts of wind. In the calculation, these values were removed.

The characteristics of the wind are shown in Figure 3.12. The mean wind speed was 3.1 m s^{-1}, and the maximum wind speed reached 19.0 m s^{-1}. The strongest wind occurred in spring from the middle of January to the end of February. Figure 3.12b shows the daily fluctuation of wind speed. The wind direction in Figure 3.12c shows that the main wind directions are southeast. It is different from the prevailing winds in the middle latitudes of northern hemisphere. The wind direction is consistent with the valley orientation. All the above characteristics indicate the wind is mainly controlled by local factors.

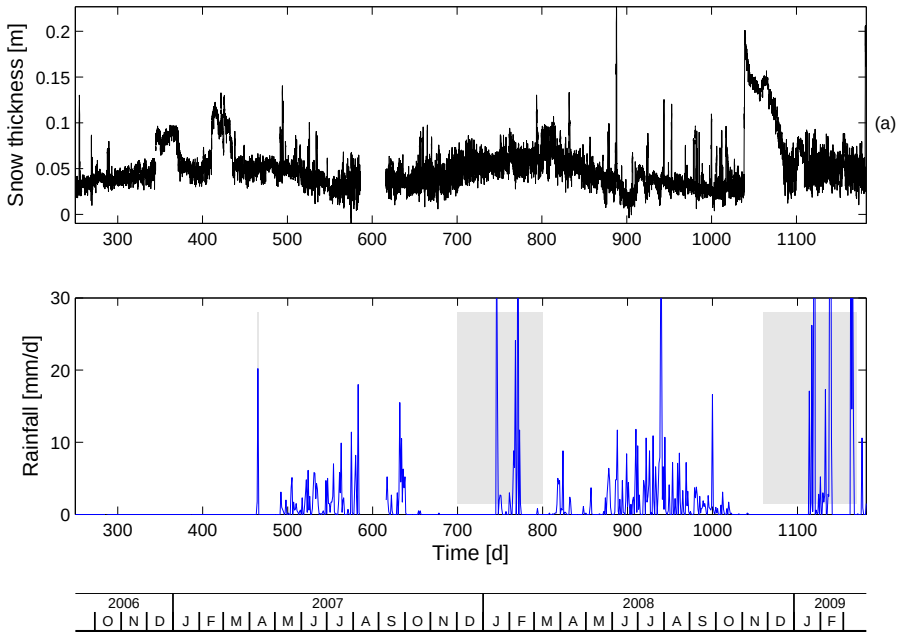

Figure 3.11. Measured precipitation at Qumahe from day number 250 to 1181. (a) snow thickness; (b) rainfall. The gray bars indicate unreasonable measurements of rainfall, and the large values are cut off.

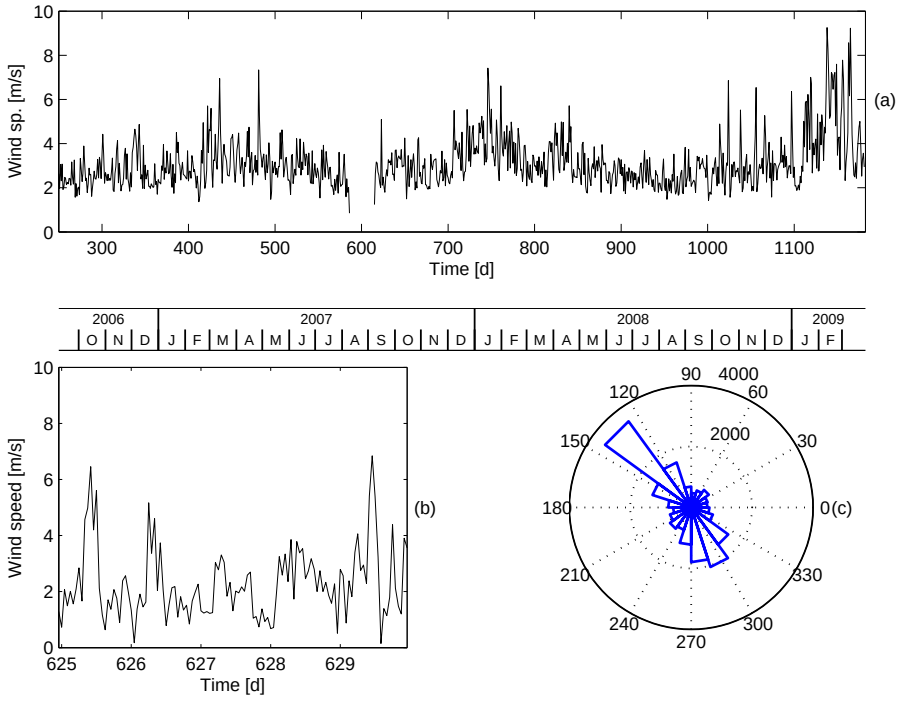

Figure 3.12. Wind characteristics at Qumahe. (a) daily mean wind speed from day number 250 to 1181; (b) daily wind speed from day number 625 to 630; (c) statistics of wind direction.

Characteristics of the interaction between ground surface and atmosphere The characteristics of the interaction between ground surface and atmosphere are presented in Figure 3.13. The seasonal fluctuation of the differences between air temperature and near surface temperature is

much stronger than that at Chumaer. In Figure 3.13b, the maximum value of the temperature differences reached about 15℃ during the winter period, while during the summer period it was about 3℃. It indicates the strong change of the interaction between ground surface and atmosphere from summer to winter. As shown in Figure 3.13c, the diurnal range of the ground surface temperature and the air temperature also shows the similar seasonal characteristic as shown in Figure 3.5c. But they were almost equal each other during summer at this site.

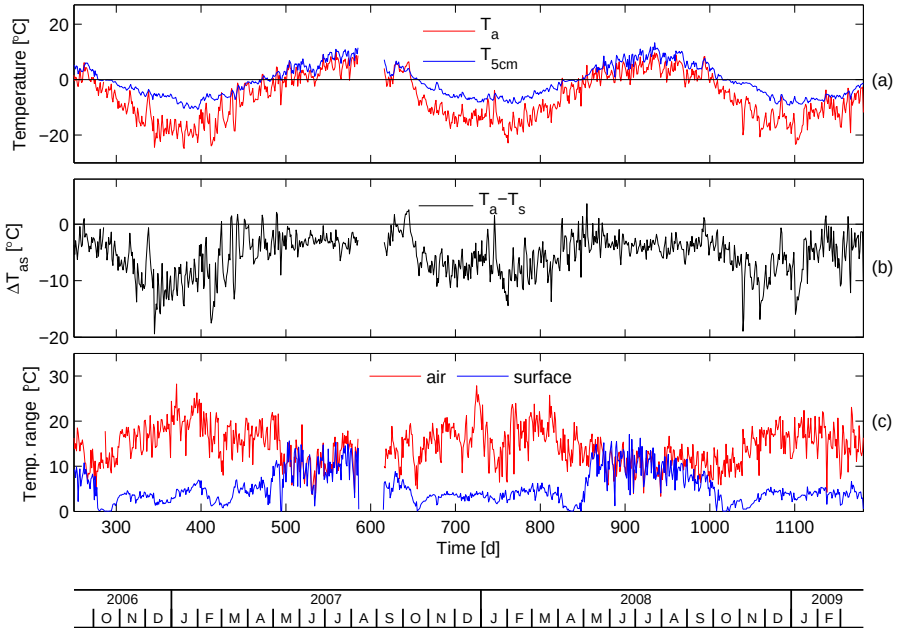

Figure 3.13. Characteristics of the air temperature T_a (2.0 m above the ground surface) and the ground surface temperature T_s (0.05 m below the surface) at Qumahe. (a) the measured air temperature and the ground surface temperature; (b) the differences between air temperature and ground surface temperature; (c) the diurnal range of air temperature and ground surface temperature.

At Qumahe, the ground surface is always wet in summer and covered with dense vegetation. With the warm weather, the evapotranspiration is expected to be very strong in summer. Besides, the interaction between air and ground surface was strengthened by the wind, which made air temperature and ground surface temperature close to each other. During the winter period, the evapotranspiration would be much weaker, because there is little available water at the frozen surface. The interaction between air and ground surface is mainly driven by radiation and convection during the winter period. Due to the surface phase change, the dynamic range of surface temperature is much smaller than that of air temperature.

3.3.2 Seasonal hydraulic and thermal dynamics of the active layer

Figure 3.14 presents the hydraulic and thermal dynamics in the profile during the measured period from September 8, 2006 to March 28, 2009. The active layer at this site is much thinner than at Chumaer. The measured depth of the soil temperature profile is down to 1.57 m. Unfortunately, there are several drifted sensors (0.2 m, 0.4 m, 0.9 m, 1.1 m, 1.25 m and 1.3 m) which were dropped. The sensors at depths 0.55 m, 0.7 m, 1.2 m, 1.45 m and 1.57 m were evaluated with corresponding given offsets. The volumetric soil water contents were measured with TDR and CS616. They were installed in two columns, and some of them measured at the

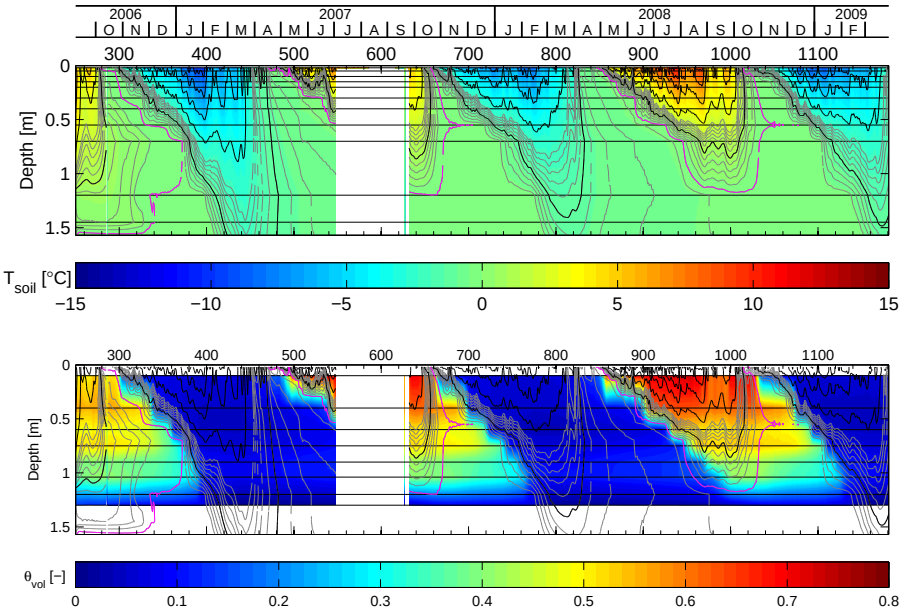

Figure 3.14. Temporal evolution of soil temperature and volumetric soil water content at Qumahe. (a) contour lines of soil temperature are drawn with increments of 2℃ (solid line) and 0.2℃ (dashed line), respectively, 0℃ magenta lines) and around 0℃ (gray lines). (b) all contour lines repeated from (a) to facilitate cross-referencing. Blank areas indicate missing data, and horizontal black lines indicate the positions of the probes.

same depth. In the following analysis, the soil water contents from TDR are used. Three typical thermal regimes can be identified in the active layer. Their characteristics are described in the following.

`(1) Spring-summer thawing regime (SST)`

In Figure 3.14, there are two complete periods of SST (SST1: day number 466-656, SST2: day number 830- around 1000). During the summer thawing period, the influence of drastic change of weather conditions was not so significant as that at Chumaer. Due to the insulating effects of the dense vegetation and high surface water content, the daily fluctuation of soil temperature was much smaller than that at Chumaer during this period. The thermal regime of the active layer is characterized by a continuously downward moving thawing front and weak reactions to the weather changes. The water infiltration was not evident in the nearly saturated soil, and the surface runoff would be expected as the major hydrological processes when there were strong rainfalls. Because of the evident sloping topography of surface the lateral flow should be the main water movement within the active layer. However, the decrease of soil water content in August and September in 2008 indicates the water loss may have resulted from the strong evaporation at the surface. Therefore, the surface runoff and lateral flow within the active layer played significant roles in the hydraulic and thermal dynamics during this period.

`(2) Autumn freezing regime (AF)`

Due to the high water content in the active layer, the zero-curtain effects are more evident than that at Chumaer. As shown in Figure 3.14, there are three AF periods, which are (AF1: day number: 280-390, AF2: day number: 660-770, AF3: day number: 1010-1120). During these periods, the disturbances from the surface were attenuated by the isothermal plateau. Particularly during AF3, the snow cover lasted for 45 days, which insulated the interaction between atmosphere and the ground surface. Therefore, the isothermal plateau lasted longer than during the other AF periods. Along with decreasing air temperature, the freezing front

moved from the surface downward and from the permafrost table upward [*Outcalt et al.*, 1990]. The latent heat was mainly released by non-conductive processes. At the frozen surface, the evaporation was limited by the low water availability. However, the large differences between air temperatures and surface temperatures might facilitate the heat convection at the surface.

(3) Winter cooling regime (WC)

Due to the long duration of AF period, the WC periods are much shorter than that at Chumaer. As shown in Figure 3.14, the durations of three periods are WC1: day number 390-470, WC2: day number 770-840, and WC3: day number 1120- –. During WC1, there were two continuous short periods of snow cover during day number 410-425 and 425-435 in Figure 3.11a. They drastically equalized the ground thermal regime. Compared with Chumaer, the soil temperatures dropped faster during the WC periods. For instance, in winter the isotherm -2℃ moved downward 0.5 m from the beginning of WC3, while it just moved a few centimeters at Chumaer at the corresponding period. This might have resulted from the higher thermal diffusivity at Qumahe. The major mechanism of heat transfer was heat conduction. Because of the large thermal diffusivity the the thermal regime responded quickly to the surface weather fluctuations.

3.4 Zuimatan

At Zuimatan, the data were recorded from September, 2006 to March, 2009. The station has been damaged several times and the solar panel and battery were often stolen. Therefore, there were several blocks of missing data (January 20, 2007 - April 7, 2007; July 17, 2007 - August 5, 2007; December 23, 2007 - March 30, 2008; June 6, 2008 - June 28, 2008; September 14, 2008 - November 7, 2008). At last, it stopped working in 2010. Some thermistors drifted with unexplained excursions in the field. Only the first kind of drift occurred in the profile, sensors at depth 0.2 m, 0.4 m, 2.22 m, 2.52 m and 2.62 m were dropped because the phase equilibrium temperature was not stable in these measurements. The left 11 thermistors worked well.

3.4.1 Interaction between atmosphere and ground surface

Meteorological conditions The characteristics of the daily mean, minimum and maximum values of air temperature at Zuimatan are shown in Figure 3.15. From day number 246 to 1182, the minimum and maximum values of daily mean air temperature were -23.9℃ and 12.4℃, respectively; the minimum and maximum measured temporal values were -31.1℃ and 18.7℃, respectively. Due to several missing data, this statistics can just give a reference. Besides, the seasonal variations of the diurnal range of air temperature are also similar to these at Chumaer. They were larger in winter than in summer. Due to the missing data, there is no complete yearly dataset to calculate the mean annual air temperature. According to the collected data, the mean annual air temperature was similar to the one at Chumaer.

The net radiation measurements are shown in Figure 3.16. The maximum net radiation was 849 W m^{-2} and the maximum daily mean net radiation was 201 W m^{-2}. Due to the missing data, it is difficult to get the mean annual net radiation at this site.

Rainfall and snow thickness were measured at Zuimatan. As shown in Figure 3.17b, the rainfall was also mainly concentrated in summer. No exact value of the sum annual rainfall can be estimated because of missing data. According to the existing data and other studies [*Xie et al.*, 2003; *Ding et al.*, 2003], the rainfall was smaller than that at Chumaer during the same time. The bias of the measured snow thickness was about 6 cm during most of the time. This should be systematic measurement error caused by the loosened soil at the beginning. Its mean

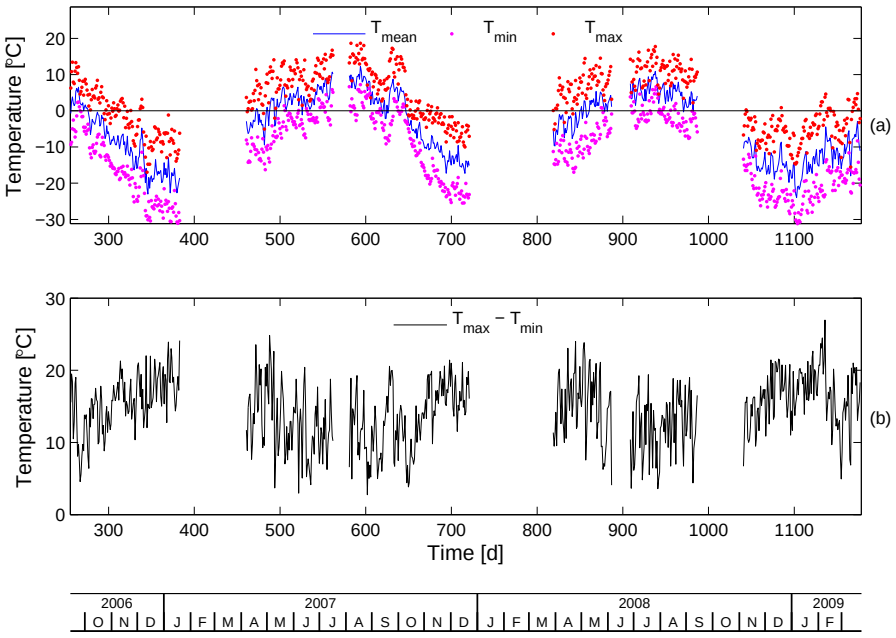

Figure 3.15. Air temperature at Zuimatan from day number 256 to 1177. (a) daily mean, maximum and minimum air temperature ($T_{mean}, T_{min}, T_{max}$). The blanks correspond to missing data. (b) diurnal range of air temperature

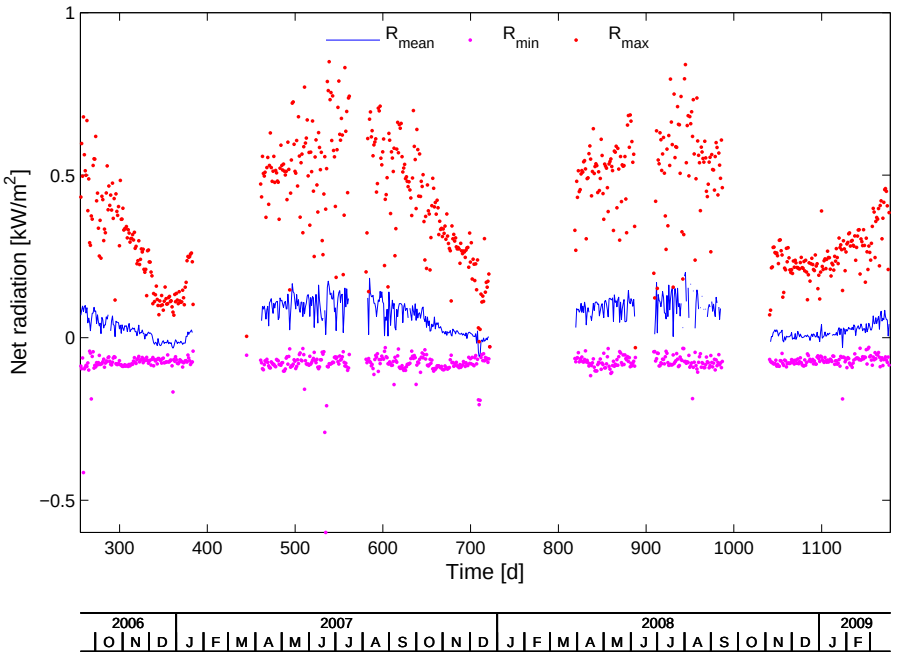

Figure 3.16. Characteristics of net radiation at Zuimatan from day number 256 to 1177. $R_{mean}, R_{min}, R_{max}$: daily mean, minimum and maximum net radiation, respectively. The blanks correspond to missing data.

dynamic range was around 3 cm when there was no snow. This may be caused by the shaking of the tower. In Figure 3.17a, notable snow covers can be found in the winter of 2008, and in

the spring of 2009. During these periods, snow cover also occurred at Chumaer, but there it was higher than at Zuimatan.

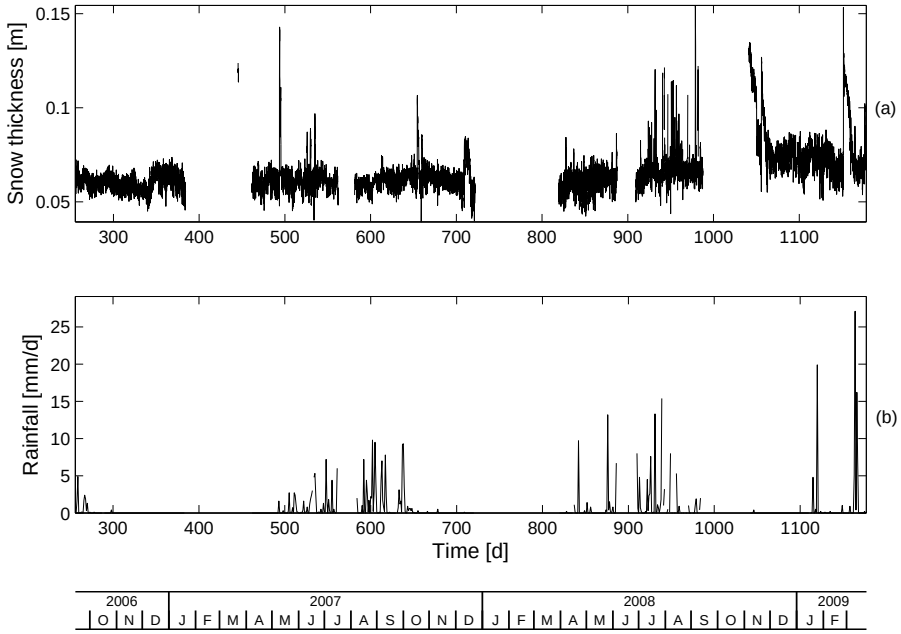

Figure 3.17. Measured precipitation at Zuimatan from day number 246 to 1182. (a) snow thickness, blanks correspond to missing data; (b) rainfall.

The wind characteristics are presented in Figure 3.18. The mean wind speed was 3.5 m s^{-1}, and the maximum wind speed reached 18.1 m s^{-1}. Usually the strongest wind occurred in spring from the middle of January to end of February. The daily fluctuation of the wind speed is shown in Figure 3.18b. Generally, the daily strong wind occurred from middle night to the morning in UTC time. In Figure 3.18c, it shows that the main wind directions are east and southeast. It was similar to the prevailing winds in the middle latitudes of northern hemisphere. Therefore, the wind might be controlled by regional factors at this site.

Characteristics of the interaction between ground surface and atmosphere The characteristics of the interaction between ground surface and atmosphere are presented in Figure 3.19. There are 5 data gaps (day numbers: 385-460, 563-580, 722-818, 888-908, 988-1040) in both measurements. They were caused by the failure of the battery. In Figure 3.19b, the difference between air and near surface temperatures were larger in winter than in summer. In winter, it increased clearly when there were snowfalls observed in November of 2008. Besides, the air temperature was larger than the near surface temperature occasionally. These events might be caused by the drastic weather changes and the response of ground temperature lagged behind. As shown in Figure 3.19c, the diurnal range of the ground surface temperature and the air temperature also shows the similar seasonal characteristic as shown in Figure 3.5c.

Due to the dry and cold weather at Zuimatan, as well as sparse vegetation on the ground surface, the evaporation was not strong. As roughly estimated by *König* [2008], the actual evaporation was 48.1 mm in October 2006. Due to the small water availability at the frozen surface in winter, evaporation should even be smaller. The interaction between air temperature and ground surface has similar effects as at Chumaer.

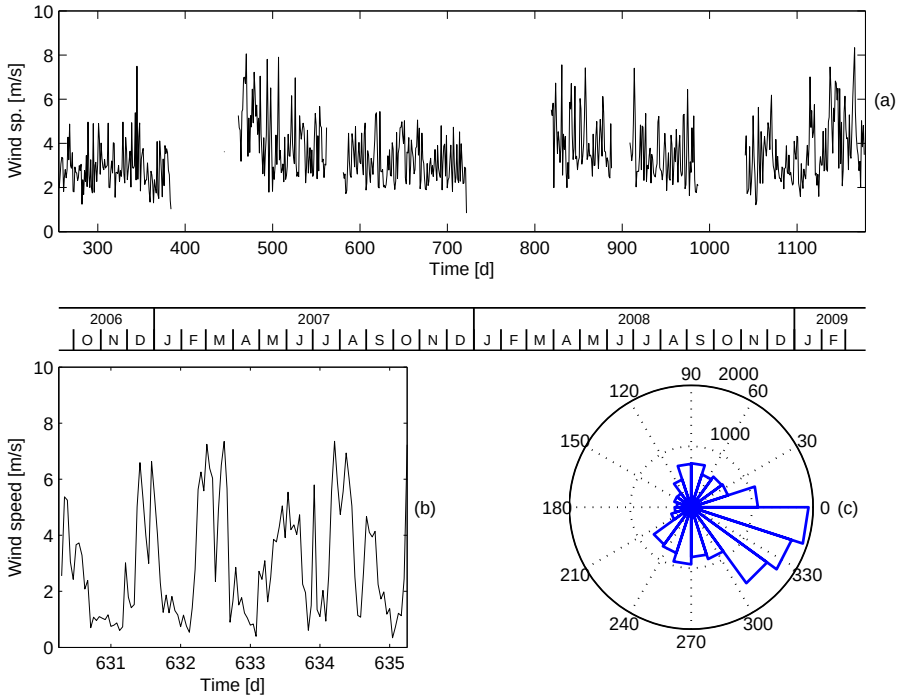

Figure 3.18. Wind characteristics at Zuimatan. (a) daily mean wind speed from day number 256 to 1177; (b) daily wind speed from day number 620 to 630; (c) statistics of wind direction.

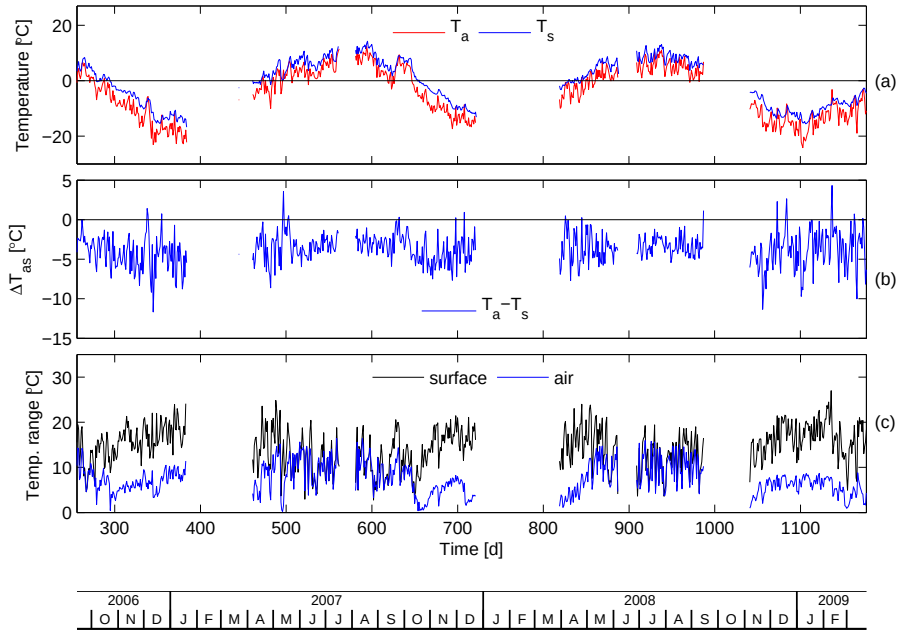

Figure 3.19. Characteristics of the air temperature T_a (2.0 m above the ground surface) and the ground surface temperature T_s (0.05 m below the surface) at Zuimatan. (a) the measured air temperature and the ground surface temperature; (b) the differences between air temperature and ground surface temperature; (c) the diurnal range of air temperature and ground surface temperature.

3.4.2 Seasonal thermal dynamics of the active layer

The thermal dynamics in the profile are shown in Figure 3.20. The data were recorded from 13 September 2006 to 24 March 2009. The strong deviation of measured soil water content

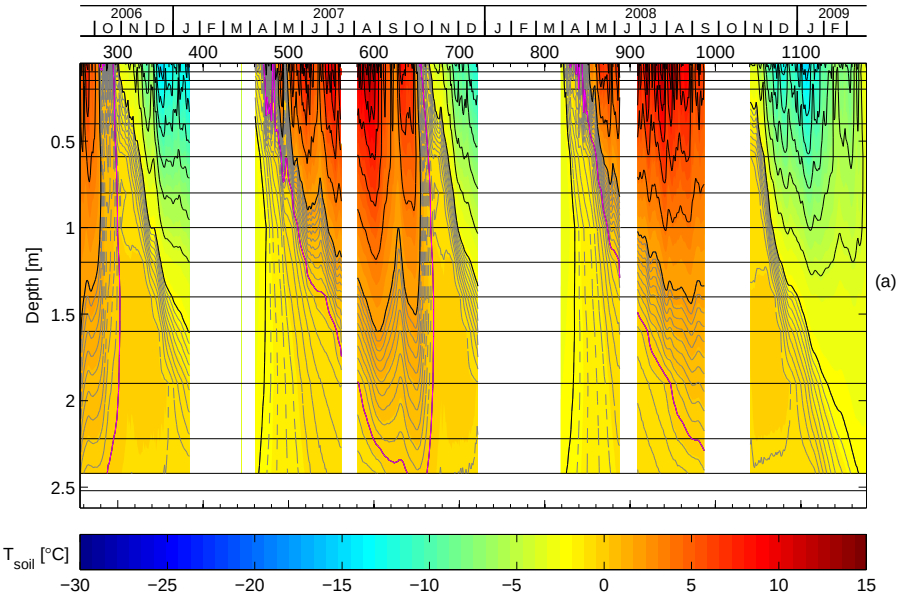

Figure 3.20. Temporal evolution of soil temperature at Zuimatan. Contour lines of soil temperature are drawn with increments of 2℃ (solid line) and 0.2℃ (dashed line), respectively, 0℃ magenta lines) and around 0℃ (gray lines). Blank areas indicate missing data, and horizontal black lines indicate the positions of the probes.

with CS616 in the upper layer demonstrates the influence of the high conductivity on the measurements. These values are not expected to be reasonable because the soil water content in thawed soil is higher than the soil porosity. Therefore, the soil water content measurements are not shown here. From the observations during the instrumentation, little groundwater at the bottom was found above the permafrost table. The influence of precipitation in summer can only cause small changes of soil water content in the upper layer. Three typical thermal regimes can be identified in the active layers. Their characteristics are described in the following.

`(1) Spring-summer thawing regime (SST)`

In Figure 3.20, there are two periods of SST (SST1: day number 466-656, SST2: day number 830- around 1000). During the summer thawing period, weather conditions had significant influences on the thermal regime. For example, as shown in Figure 3.15a, there were two clear drops of air temperature around day numbers 537 and 624 during SST1, which shows a clear cooling effect of the active layer. During these events, there were no significant changes of the rainfall and the net radiation. Therefore, the cold air temperature and the evaporation should be the main reason for cooling the active layer in such a short time. Compared with Chumaer, the soil temperature of the active layer in summer was smaller at Zuimatan. For instance, the isotherm 2℃ reached a depth of 1.6 m at day number 605 at Zuimatan, while it reached 1.9 m in profile 2 at Chumaer. With the similar weather conditions, the heat transfer in the profile 2 was stronger at Chumaer than that at Zuimatan in summer. The disturbances of air temperature drops occurred at this site in the summer of 2007, and the responses of thermal regime were similar to Chumaer.

`(2) Autumn freezing regime (AF)`

Figure 3.20 shows that the durations of AF were around 60 days, which can only be approximately estimated in AF3 (day number: 1040-1100). Because the length of the AF duration mainly depends on the soil water condition in the active layer. There was almost no zero-curtain effect in this dry active layer. During these periods, the main disturbances were air temperature,

for instance around day numbers 343 and 1085. There was one snowfall at the beginning of AF3, but its effects were not evident.

After quickly freezing of the dry active layer, it kept frozen at the near surface during this period. Accordingly, the evaporation was weakened by little unfrozen water at the surface. During this period, the daily fluctuation of soil temperature at the surface could penetrate much deeper than that at Chumaer.

(3) Winter cooling regime (WC)

During the records from day number 256 to 1177, there are three periods of WC shown in Figure 3.20. Due to missing data, only WC3 is identifiable (WC3: day number 1100-1177). During WC3, the snow cover had existed from day number 1150 to 1163, which obviously disturbed the ground thermal regime. However, the net radiation and air temperature did not vary significantly. It showed that the insulating effect of the snow cover was the major reason for quickly warming the active layer. Compared with Chumaer, the soil temperature of the active layer was lower in winter. For instance, in winter the isotherm -2℃ reached below the deepest sensor (2.42 m) at day number 1160 at Zuimatan, while it just reached 1.65 m in profile 2 at Chumaer. This may be attributed to the low water content in the active layer.

3.5 Tianshuihai

At Tianshuihai, the data were recorded from September, 2007 to December, 2009. All the sensors worked well in the field. Data from December 14, 2007 to March 23 2008 were lost by a malfunction of the memory card. The characteristics of the weather and the hydraulic and thermal dynamics are introduced in the following.

3.5.1 Interaction between atmosphere and ground surface

Meteorological conditions The measured air temperatures are shown in Figure 3.21 at Tianshuihai. The characteristics of the daily mean, minimum and maximum values of air temperature are different from the other sites on the northeastern QTP. The diurnal range of the air temperature is much larger at this site. From day number 252 to 1092, the minimum and maximum values of daily mean air temperature were -28.7℃ and 8.8℃, respectively; the minimum and maximum measured temporal values were -40.1℃ and 20.6℃, respectively. The seasonal variations of the diurnal range of the air temperature are not so obvious as at other sites. It was slightly larger in winter than that in summer. For a nearly complete year (from 2:00 December 28, 2008 to 2:00 December 28, 2009), the mean annual air temperature was -8.0℃ in 2009.

The net radiation measurements are shown in Figure 3.22. The net radiation changed smoothly, and there were no obvious disturbances by snow or something else. The maximum net radiation is 835 W m^{-2} and the maximum daily mean net radiation is 166 W m^{-2}. For an almost complete year (from 2:00 December 28, 2008 to 2:00 December 28, 2009), the mean daily net radiation in 2009 was 63 W m^{-2}.

At Tianshuihai, only the precipitation of rainfall was measured. As shown in Figure 3.23, the rainfall also concentrated in the summer of 2008, but the rainfall in the spring of 2009 was abnormally strong and very few in the summer. The problematic of strong rainfall measurement is similar to that at Qumahe, which was caused by the shaking of the tower. The abnormal large values always occurred when the wind speed was over 12 m s^{-1}. Due to limitation of the wind probe, there were missing data when the wind speed was out of the measurement range.

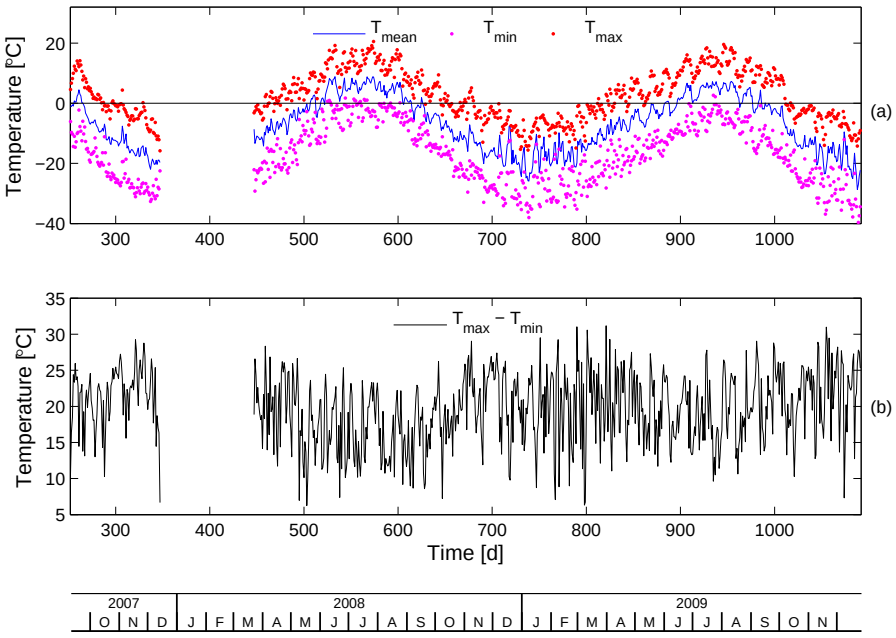

Figure 3.21. Air temperature at Tianshuihai from day number 252 to 1092. (a) daily mean, maximum and minimum air temperature ($T_{mean}, T_{min}, T_{max}$). The blanks correspond to missing data. (b) diurnal range of air temperature

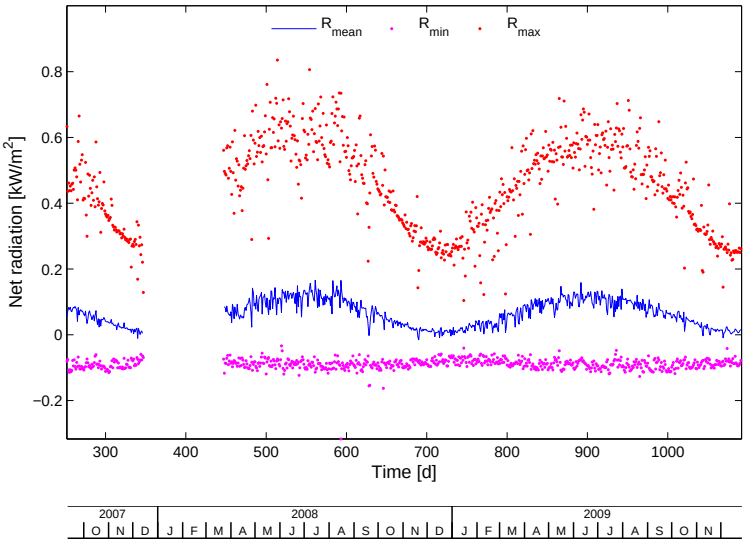

Figure 3.22. Characteristics of net radiation at Tianshuihai from day number 252 to 1092. $R_{mean}, R_{min}, R_{max}$: daily mean, minimum and maximum net radiation, respectively. The blanks correspond to missing data.

The high rainfall just occurred during these periods. Therefore, these measurements that over 12 m s^{-1} and during the day numbers 450-480, 660-860 and 1050-1092 were not considered in weather analyses.

The wind characteristics are presented in Figure 3.24. In Figure 3.24a, there was a seasonal fluctuation of the daily mean wind speed. The mean wind speed was 3.7 m s^{-1}, and the maximum wind speed reached 20.6 m s^{-1}. Usually the strongest wind occurred in spring from

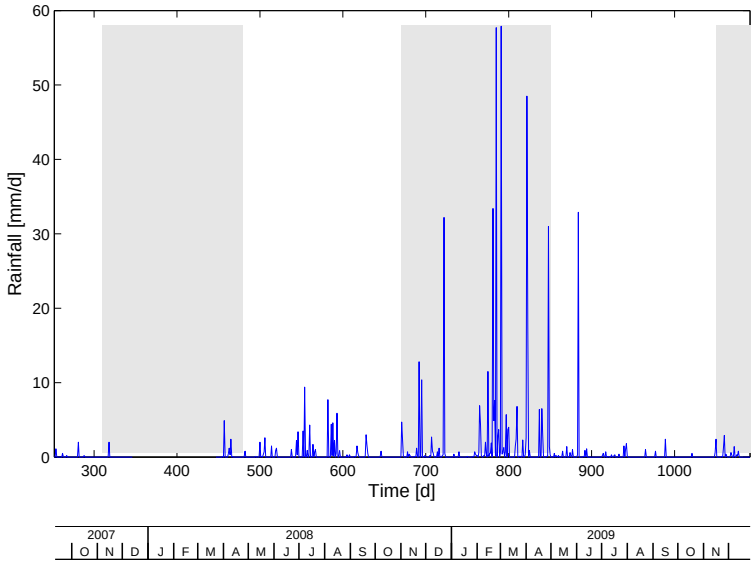

Figure 3.23. Measured precipitation at Tianshuihai from day number 252 to 1092. Gray bars mean unreasonable measurements removed in later calculation.

the middle of January to end of February. The daily fluctuation of wind speed is shown in Figure 3.24b. Generally, the daily strong wind occurred from middle night to the morning in UTC time. Figure 3.24c shows that the main wind directions were southwest in this flat area. The wind direction might be controlled by regional factors.

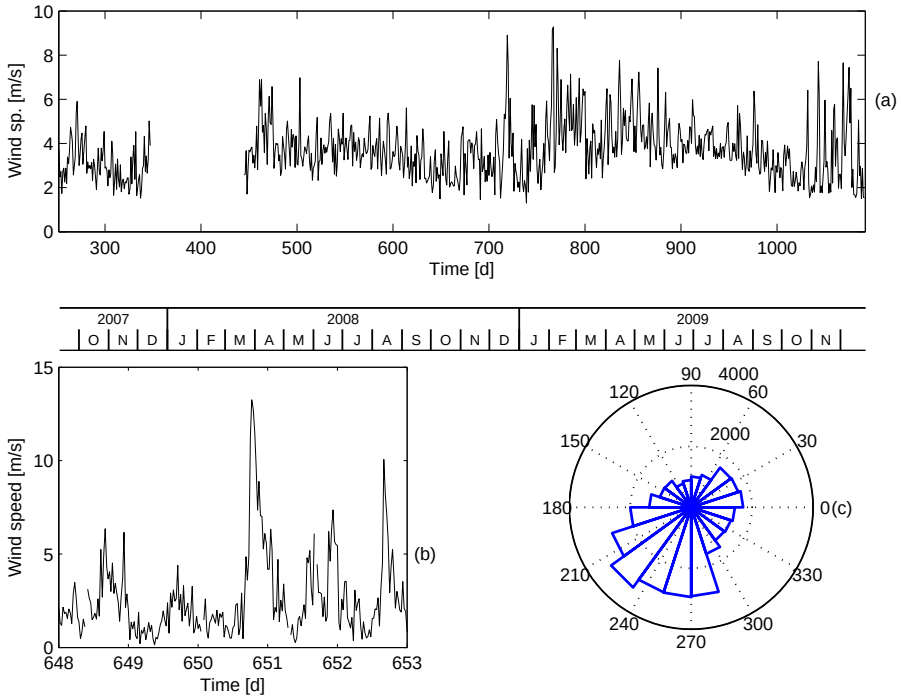

Figure 3.24. Wind characteristics at Tianshuihai. (a) daily mean wind speed from day number 252 to 1092; (b) daily wind speed from day number 648 to 653; (c) statistics of wind direction.

Characteristics of the interaction between ground surface and atmosphere The characteristics of the interaction between ground surface and atmosphere are presented in Figure 3.25. Air temperatures were measured at two depths (0.05 m and 2.0 m). The measured air temperatures are close each other at these two different heights. It indicates the strong heat exchange in the near surface above the ground. Figure 3.25b shows that the differences between air temperature and near-surface soil temperature are smaller in winter than that in summer. The air temperature was even occasionally higher than the near surface temperature in winter. As shown in Figure 3.25c, the diurnal range of the air temperature was smaller than that of the ground surface temperature during the winter periods. All these characteristics show that the interaction between air and ground surface is stronger in winter than in summer at Tianshuihai. These are completely different from the previous sites. It might be caused by the strong convection of wind at the surface.

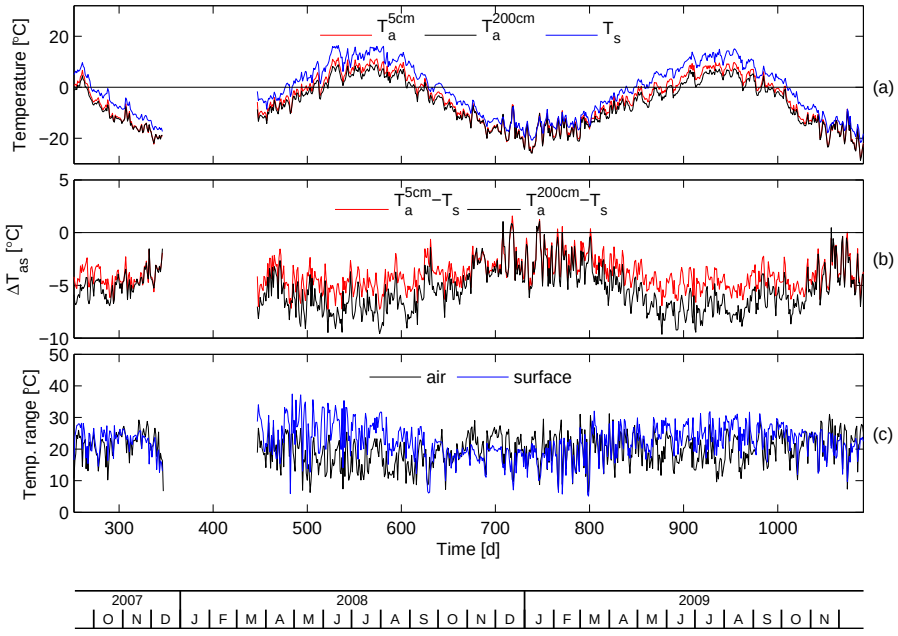

Figure 3.25. Characteristics of the air temperature and the near surface soil temperature at Tianshuihai. (a) measured air temperature (0.05 m and 2.0 m above the ground surface) and the ground surface temperature (0.04 m below the surface); (b) the differences between air temperature and ground surface temperature; (c) the diurnal range of air temperature and ground surface temperature.

Due to the extremely dry and cold weather at Tianshuihai, the evaporation should be very small. The interaction between air and ground surface should be mainly driven by radiation and heat convection. The smaller temperature difference between the air and subsurface soil, and the stronger wind in winter than in summer indicate the strong heat exchange by heat convection at the surface. In addition, seasonal variations of the differences between the diurnal range of air temperature and near surface soil temperature also indicate that wind may play a significant role in the interaction between atmosphere and subsurface at Tianshuihai.

3.5.2 Seasonal hydraulic and thermal dynamics of the active layer

The hydraulic and thermal dynamics in profile 1 and profile 2 are shown in Figure 3.26 and 3.27, respectively. TDR sensors were used here to monitor soil water dynamics. They were

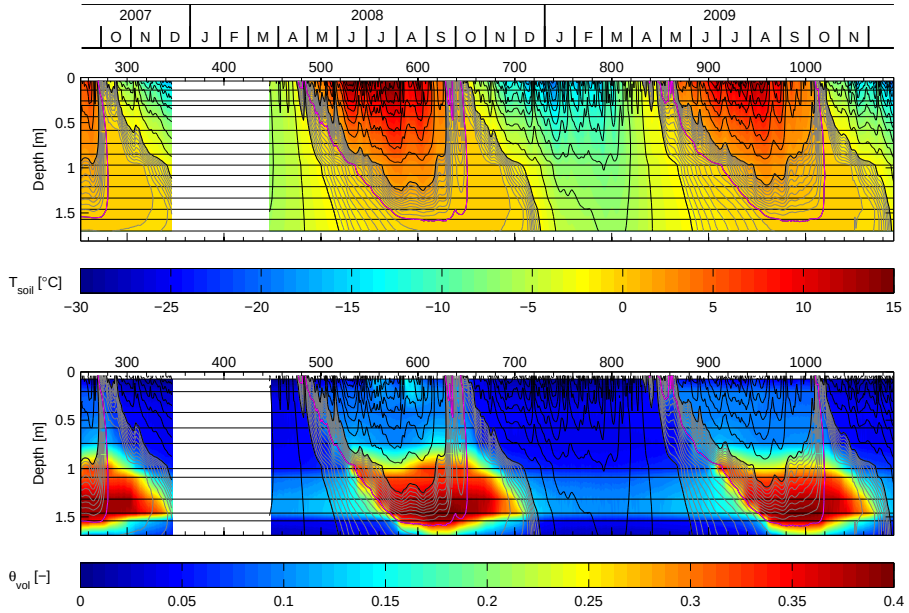

Figure 3.26. Temporal evolution of soil temperature and volumetric soil water content in profile 1 at Tianshuihai. (a) contour lines of soil temperature are drawn with increments of 2℃ (solid line) and 0.2℃ (dashed line), respectively, 0℃ magenta lines) and around 0℃ (gray lines). (b) all contour lines repeated from (a) to facilitate cross-referencing. Blank areas indicate missing data, and horizontal black lines indicate the positions of the probes.

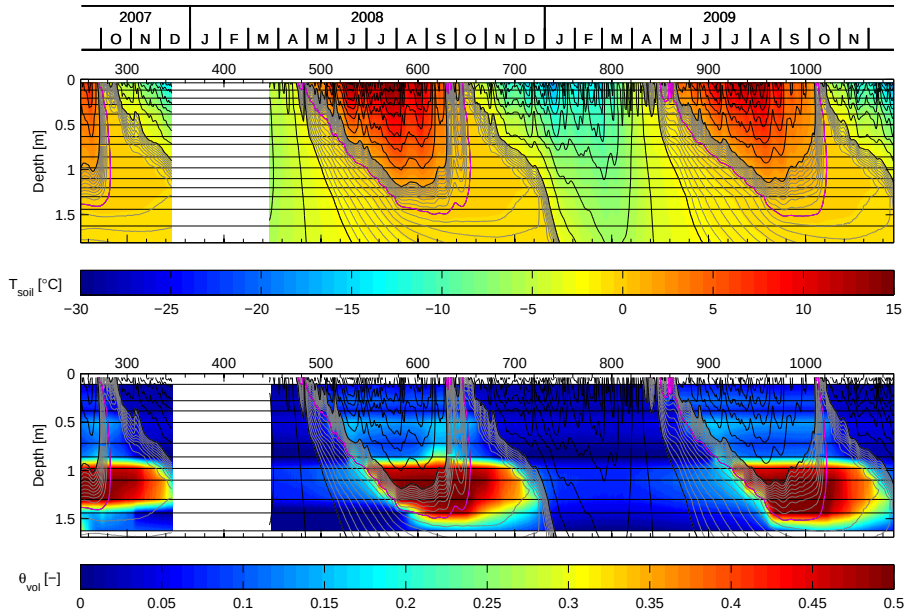

Figure 3.27. Temporal evolution of soil temperature and volumetric soil water content in profile 2 at Tianshuihai. (a) contour lines of soil temperature are drawn with increments of 2℃ (solid line) and 0.2℃ (dashed line), respectively, 0℃ magenta lines) and around 0℃ (gray lines). (b) all contour lines repeated from (a) to facilitate cross-referencing. Blank areas indicate missing data, and horizontal black lines indicate the positions of the probes.

installed deeply in the frozen ground below the permafrost table. As shown in Figure 3.26b and Figure 3.27b, there was a sharp transition in soil water content distribution. Due to the

small precipitation and strong potential evaporation, the sand and gravel in the subsurface can be dried easily. The loam layer at the bottom was close to the permafrost table, and the thawing water sinked to the impermeable permafrost table. Because it is far from the surface, the influence of evaporation is very weak. The similar thermal regimes can be identified in both profiles, so only characteristics in profile 1 were described in the following.

(1) Spring-summer thawing regime (SST)

In Figure 3.26, there were two periods of SST (SST1: day number 485-630, SSST2: day number 850-1010). During the summer thawing periods, weather conditions had significant influences on the thermal regime. For example, as shown in Figure 3.21a, the fluctuations of air temperature disturbed the thermal regime of the active layer clearly. During these events, there were no large changes in rainfall and net radiation. Therefore, the cold air temperature and the convection should be the main reasons for cooling the active layer in such a short time. Because of the strong wind and low water content at the surface, the heat convection at the surface might be the major heat transfer process.

(2) Autumn freezing regime (AF)

As shown in Figure 3.26, the durations of AF were around 80 days (AF1: day number 270-350, AF2: day number 630-720, AF3: day number 1010-1085). Because the length of the AF duration mainly depended on the amount of soil water in the active layer. There was almost no zero-curtain effect in the upper part of the active layer. Due to the low temperature below the permafrost table, the freezing front moved quickly downward, as well as from bottom up.

(3) Winter cooling regime (WC)

Due to the fast freezing during the AF periods, the duration of the WC period was much longer than at the previous sites. In Figure 3.26, during the records from day number 252 to 1092, there were two periods of WC. Due to missing data, only WC2 is complete (WC2: day number 720-840). Phase change is negligible, and heat conduction is the dominant process in the active layer. The thermal diffusivity at the high ice-content part increased immediately. During this period, the responses of the thermal regime to the weather fluctuation were much faster than that during the AF period. Thus, it led to a quick drop of the soil temperature at the bottom.

3.6 Comparison of the observational data at the study sites

3.6.1 Meteorological characteristics

With state-of-the-art soil-weather monitoring stations measurements of basic micro-meteorology (air temperature, net radiation, relative humidity, wind direction and wind speed, precipitation of rain and snow), and near surface soil temperature and moisture measurements were measured from 2006 through 2009 on a transect from northeast (Zuimatan, Qumahe, and Chumaer) to west (Tianshuihai) on the QTP. Due to non-complete measured data at Zuimatan, the estimated mean air temperature was -4.0℃ in 2008, and the measured values at Qumahe, Chumaer and Tianshuihai were -4.8℃ (2008), -4.9℃ (2008), and -8.0℃ (2009), respectively.

As a plateau continental climate region, the weather on the QTP is characterized as dry and cold. The study of *Ma et al.* [2006] shows that the ground surface of the northern plateau is a strong heat source, and precipitation is mainly controlled by the summer monsoon, which strongly influences the evaporation. Our observations at the four sites also demonstrate that the rainfall mainly concentrated in summer, and thin and short duration of snow cover in other seasons occurred. The measured mean annual rainfall in summer was around 300 mm at Zuimatan, Qumahe and Chumaer, while it was just about 50 mm at Tianshuihai. Since the potential evaporation is much larger than the actual evaporation on the QTP, the surface water

availability mainly depends on the precipitation, which strongly influences the soil-atmosphere interaction at the ground surface. On the northeastern QTP, the soil-atmosphere interaction is strongly influenced by the precipitation. Evaporation and heat convection both play significant roles in the surface heat exchange. On the western QTP, the soil-atmosphere interaction is mainly influenced by wind other than precipitation at Tianshuihai.

3.6.2 Variability of the relation between air and surface temperatures

As presented before, the air temperature is measured at 2 m above the ground surface at the study sites. The monthly mean air temperatures in a complete year of 2008 are used here to compare the differences at all study sites in Figure 3.28a. In general, the seasonal variations of air temperatures at Chumaer, Qumahe and Zuimatan on the northeastern QTP are similar, while the data from Tianshuihai site on the western QTP is much different. During the summer period from June to August, March and November, their differences are smaller than the other seasons. Although the mean annual air temperature at Tianshuihai is much lower than the other sites, the air temperature in summer season is usually higher. The main differences of monthly mean air temperature concentrate in the warming and cooling periods.

Because of the different surface characteristics at the study sites, the measured depths of surface temperature are different. For bare surface, the depth of temperature sensor is usually inserted at a depth of around 5 cm. The measured depths at Chumaer and Zuimatan are both 5 cm, and 4 cm at Tianshuihai. At Qumahe, the measured depth of surface temperature is chosen 2 cm for the wet surface with dense vegetation. The seasonal variations of monthly mean ground surface temperature at the study sites are shown in Figure 3.28b. The surface temperature at Tianshuihai is about 5℃ higher than the other sites in summer from June to August. While in the other seasons, it is always lower than the other sites. Due to too much missing data, there are no clear seasonal characteristics at Zuimatan. The differences of ground surface temperature at Chumaer and Qumahe varied with season. From January to March, it decreased from 3.76 to 0.11℃, then the difference turned negative until the middle of August. Later, the ground surface temperature at Chumaer dropped down quickly, and the absolute difference between the surface temperatures at Chumaer and Qumahe kept increasing until the end of the year.

In Figure 3.28c, it shows the variations of the monthly mean air and ground surface temperature differences at the study sites. For the same reason of missing data, there is no enough data to analyze seasonal variations of ΔT_{as}^{Z} at Zuimatan. The Chumaer and Qumahe sites present a similar seasonal varying trend. The absolute values of ΔT_{as}^{C} and ΔT_{as}^{Q} are larger in summer than in winter, and stay nearly stable from April to September. The largest difference occurred in November. Except the missing data in January and February at Tianshuihai, the ΔT_{as}^{T} shows the inverse characteristics to the other sites. The absolute value of ΔT_{as}^{T} approximately decreased from March to December. The smallest value occurred in winter other than in summer.

To investigate the relationship between air temperature and ground surface temperature at the study sites, their mean values are statistically analyzed as shown in Figure 3.29. The scatters lay in a straight strip at Chumaer, Zuimatan and Tianshuihai. At these sites, the ground surface is dry and covered with sparse vegetation or even bare soils. There are some slight differences at these sites. At Chumaer, the slope of the scatters during the freezing season changes slightly. At Zuimatan, there is no clear change of the slope, but the scatters disperse in freezing season. This may be caused by the drastic change of climatic factors such as snow and wind. At Tianshuihai, the slope of the scatters has a clear change when the daily mean air temperature is below a temperature around -17℃. These extreme cold temperatures occurred when there were strong winds. Therefore, the decreased slope may be caused by the convection.

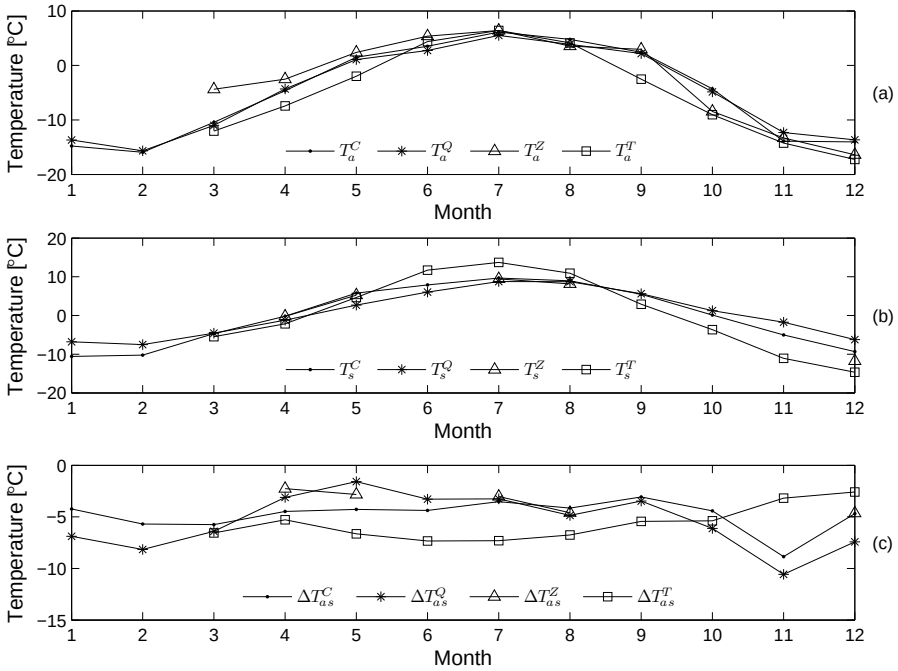

Figure 3.28. Seasonal characteristics of the air temperature and the ground surface temperature in 2008 at the study sites (C: Chumaer, Q: Qumahe, Z: Zuimatan, T: Tianshuihai). (a) monthly mean air temperature ($T_a^C, T_a^Q, T_a^Z, T_a^T$); (b) monthly mean ground surface temperature ($T_s^C, T_s^Q, T_s^Z, T_s^T$); (c) differences between monthly mean air temperature and monthly mean ground surface temperature ($\Delta T_{as}^C, \Delta T_{as}^Q, \Delta T_{as}^Z, \Delta T_{as}^T$).

For the wet surface, the slope of scatters at Qumahe turns down after the surface temperature below 0℃ in Figure 3.29. It means the variability of surface temperature decreased when the surface was frozen. The phase change would be expected as the main reason. Due to the daily surface temperature is through 0℃, a large amount of heat energy is consumed by phase change. Therefore, the surface temperature has a smaller variability during the freezing season.

3.6.3 Hydraulic-thermal patterns of the active layers

Zuimatan is located at the border of the continuous permafrost region, where permafrost degradation is very serious on the QTP. Qumahe is within the island permafrost area, the permafrost distribution is strongly dependent on local factors such as altitude, slope, orientation, soil water content and vegetation. Chumaer is within the continuous permafrost region, the permafrost is relatively stable. Tianshuihai is in a high mountainous permafrost area, the ground temperature is much lower than at the other three sites. From nearby borehole measurements and previous studies [*Zhang et al.*, 2004; *Wu and Zhang*, 2008; *Su et al.*, 1998], the estimated permafrost thicknesses are less than 50 m at Zuimatan, Qumahe and Chumaer sites, and it is over 60 m at Tianshuihai.

In the warm permafrost regions, the active layer thicknesses are around 2.65, 1.2 and 2.3 m at Zuimatan, Qumahe and Chumaer, respectively. Although they have similar weather conditions, the active layer thickness varies drastically. This is mainly attributed to the differences of local factors like vegetation and soil water content. For instance at Qumahe, the well vegetated surface and wet active layer apparently attenuate the energy flux from the surface. In the cold permafrost region, the active layer at Tianshuihai is around 1.5 m thick.

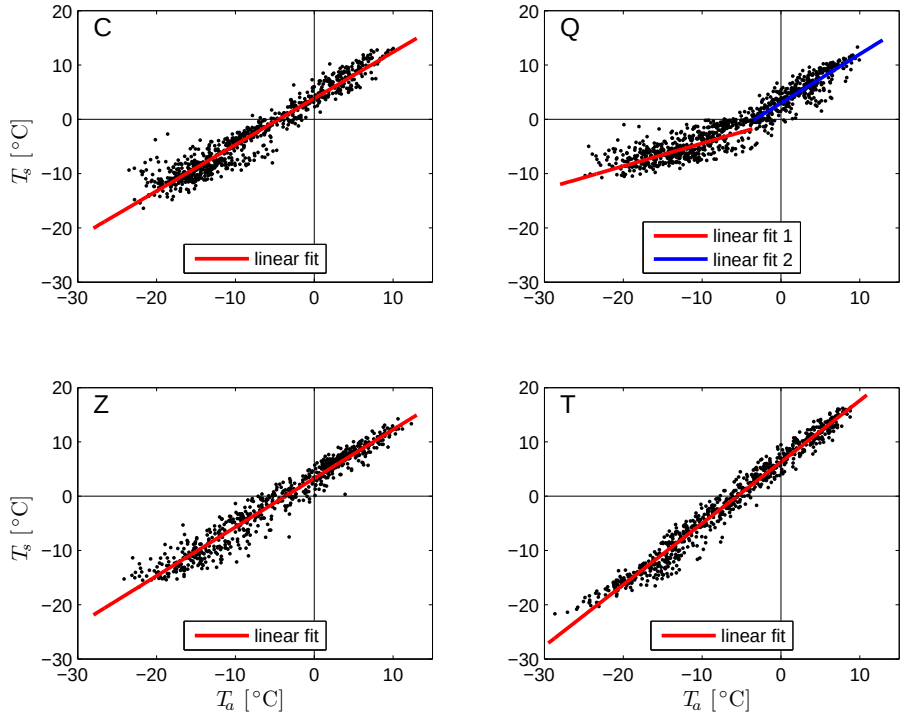

Figure 3.29. The relation between the daily mean air temperature T_a and the daily mean ground surface T_s at the study sites (C: Chumaer, Q: Qumahe, Z: Zuimatan, T: Tianshuihai).

Through analyzing the hydraulic and thermal dynamics in the active layers, their hydraulic and thermal patterns are compared. The characteristics of the three periods (SST, AF and WC) are summarized in the following. During the SST period, the thermal regime is maintained by the continuous increase heat energy from the surface, and most of the heat is used to melt the frozen soil at the thawing front. The main heat transfer processes are heat conduction at thawed and frozen parts and phase change at the thawing front. Rain water infiltration in the unsaturated active layer can influence the thermal regime. Besides, the surface runoff and groundwater flow may influence the thermal regime. The thawing front moved downward quickly in the upper layer and gradually slowed down with depth, particularly when reaching the wet layer at the bottom. The situations were similar at Zuimatan, Chumaer and Tianshuihai. Whereas, the thawing front at Qumahe was different from the other sites. It moved downward with a nearly constant speed.

During the AF period, the thermal regime was usually characterized as zero-curtain effect in autumn. It is mainly maintained by non-conductive processes. Heat transfer within the isothermal active layer was dominated by non-thermal gradients. Particularly in unsaturated active layers, vapor flux may play a significant role in removing heat energy from the freezing front. Zero-curtain effect is evidently observed at Qumahe. While in the unsaturated active layers at Zuimatan, Chumaer and Tianshuihai, the zero curtain mainly occurs at the bottom, and the durations were much shorter than that at Qumahe.

During the WC period, the thermal regime is dominated by heat conduction, and the phase change is negligible. The duration of this period and the thermal diffusivity directly impact the evolution of the underlying permafrost. At the four study sites, the durations were 77 (WC3), 70 (WC2), 60 (WC2) and 120 days (WC2) at Zuimatan, Qumahe, Chumaer and Tianshuihai, respectively. The quick drop of soil temperature near the permafrost table occurred at Qumahe

and Tianshuihai, while at Zuimatan and Chumaer sites the drop of soil temperature slowed down during this period. With a large thermal diffusivity and a long duration of WC period, it can effectively remove the thermal energy from the underlying permafrost during this period. At Qumahe, the heat transfer in the active layer should be sped up by the multiplied thermal diffusivity of the saturated soil, although the duration was the shortest one among the study sites. While at Chumaer and Zuimatan, due to the short duration and dry soil near the surface, the cooling effects on the underlying permafrost are not evident.

Facing the climate warming on the QTP, the responses of the permafrost may be different at the study sites. Since the mechanisms are different, their sensitivities to the weather change differ from each other. For instance, the dominant factors are the vegetated ground surface and wet active layer at Qumahe. The influences of the warming climate can be effectively attenuated. The permafrost may still be stable. While for the dry active layers at Chumaer, Zuimatan and Tianshuihai, the increasing air temperature can strongly reduce the duration of WC. The permafrost may continue warming in the foreseeable future at these sites. According to the classification by *Shur and Jorgenson* [2007], permafrost degradation at Zuimatan, Chumaer and Tianshuihai is climate-driven mode, whereas at Qumahe the climate warming is strongly attenuated by local factors like vegetation and soil water content. To further understand their roles in the hydraulic and thermal regimes, quantitative analysis will be given in the following chapters.

3.7 Summary

Through analyzing the observed major meteorological conditions and the hydraulic-thermal dynamics of various active layers, we can get a view of basic characteristics of the weather-permafrost interaction at Chumaer, Qumahe, Zuimatan and Tianshuihai. Air temperature is mainly influenced by the elevation at the study sites. The similar weather at Chumaer, Qumahe and Zuimatan in the northeastern QTP is characterized as dry and warm, influenced by the summer monsoon, while it is extremely dry and cold at Tianshuihai in the western QTP. The reactions of site-specific permafrost to the weather may be attributed to local factors such as topography and surface characters. Physical processes involving the surface heat exchange will be further characterized in the following chapter.

The hydraulic and thermal dynamics in various active layers also differ from site to site. In the warm permafrost region, the hydraulic and thermal pattern is characterized for a short cooling period at Chumaer, Qumahe and Zuimatan. In the cold permafrost region, it is characterized for a long cooling period at Tianshuihai. In addition to the different climate and surface characters, heat transfer in the active layer is important for understanding the permafrost at the study sites. All these factors lead to the variational active layer thickness at the study sites. The heat transfer mechanisms within the active layer will characterized in chapter 6.

4
Characterization of thermal regimes of the active layers at the study sites

4.1 Introduction

Climate warming is widely expected over the coming century, which would have significant influences on the global terrestrial system. Permafrost as one of six cryospheric indicators of global climate change, has been monitored in most cryosphere regions [*Brown et al.*, 2000]. The climate-permafrost relation is a key scientific question to understand the interaction between the atmosphere and permafrost. The active layer is the near-surface layer above permafrost, which experiences seasonal freezing and thawing. It is a zone of annual freezing and thawing between the atmosphere and permafrost. Several important sets of dynamic processes, such as biological, pedologic, geomorphic, biogeochemical, and hydrologic influence the interaction between the atmosphere and permafrost. Climate change and other changing environmental factors are thought to be the main reasons for permafrost degradation. In turn, the shrinking of permafrost might also strengthen the climate warming because of some consequences like drying ground surface and methane emission [*Anisimov and Reneva*, 2006; *Anisimov*, 2007].

The responses of permafrost to climate change are different in different regions. For instance, in the Arctic, permafrost degradation has led to dramatic distortions of terrain and changes of vegetation and hydrology [*Anisimov and Reneva*, 2006]. While in mountainous permafrost regions on the QTP, the responses of permafrost to climate change are permafrost warming, quick thickening of active layers [e.g. *Wu and Zhang*, 2008; *Wu and Zhang*, 2010], lowering lake water levels and degrading ecosystem [*Cheng and Wu*, 2007]. However, the mechanisms of the hydraulic and thermal dynamics in various active layers are still not completely understood [*Wu and Zhang*, 2008]. Along with climate warming, the changing factors related with soil moisture like precipitation, drying surface and deepening water table would strongly influence the thermal regime of the active layer. Therefore understanding of the hydraulic and thermal dynamics of various active layers would facilitate us to understand the permafrost degradation and subsequent environmental problems.

Between atmosphere and permafrost, the mechanism of heat transfer at the interface of ground surface and atmosphere is completely different from that within the active layer. Between surface and atmosphere, the complex heat transfer processes mainly include radiative, convective and conductive heat transmission, which are difficult to quantify at the interface of ground surface and atmosphere. The ground heat transfer within the active layer is widely accepted to be dominated by heat conduction, with non-conductive processes only relevant under certain conditions like water infiltration and phase change. In this chapter, the mechanisms governing the thermal regime are characterized with the energy balance at the study sites. Firstly, the interaction between the atmosphere and the ground surface was partly characterized by the relation between the air temperature and the ground surface temperature. Secondly, the ground heat transfer was characterized with two different methods. Thirdly, the thermal regime was characterized with the energy balance. The objectives of this chapter are: (1) to identify the

characteristics of the thermal regime of different active layers and their controlling factors; (2) to understand the physical mechanisms behind the hydraulic and thermal dynamics in the active layers.

4.2 Characterization of the ground heat flux

4.2.1 Introduction

At the ground surface, heat exchange between the atmosphere and ground determines the ground heat flux. The thermal regime at the surface generates the effective boundary condition for the underlying thermal regime in the active layer [*Kane et al.*, 2001]. The active layer with varying thermal properties acts as a resistor that regulates the net heat fluxes into the underlying permafrost. The rate of net heat fluxes transferred into the ground determines the thermal regime and the thaw depth of the active layer [*Hinkel*, 1997].

The heat transfer at the surface and in the subsurface is mainly controlled by the soil thermal properties and heat transfer mechanisms. There are a variety of methods to measure or calculate the ground heat flux in the soil profile. *Liebethal et al.* [2005] pointed out that in recent years many studies mainly put effort to correct the net radiation and turbulent heat fluxes for the imbalance of the energy budget, while the determination of the ground heat flux is simplified. In most studies of the ground surface energy balance in permafrost regions, the ground heat flux is usually determined by heat flux plate [e.g. *Ishikawa et al.*, 2006] or the gradient method [e.g. *Tanaka et al.*, 2001; *Yao et al.*, 2008]. In the above mentioned methods, the estimation of the effective thermal conductivity is strongly dependent on the soil properties and heat transfer mechanisms in the soil. As we know the soil temperature is mainly driven by the daily and seasonal temperature fluctuations from the surface and the geothermal heat flux upward from the interior of the Earth. The varying temperature causes soil water changes in the amount, phase in the soil. These changes of soil composition lead to variations in the soil thermal properties [*Farouki*, 1981].

In soils, heat conduction is normally assumed to be the dominating mechanism. Non-conductive heat transfer plays a significant role in certain situations in active layers [*Kane et al.*, 2001]. Due to the strong daily fluctuation of soil temperature and varying weather, it is difficult to model the complex heat transfer processes such as vertical convection, soil water infiltration and phase change near the surface. In active layers, variations of heat transfer processes may further complicate the thermal analysis. Groundwater movement, snowmelt and rainfall infiltration can have some impacts on the thermal regime of the active layer [e.g. *Hinkel and Outcalt*, 1994; *Kane et al.*, 2001; *Hinkel et al.*, 2001]. As presented by *Ishikawa et al.* [2006], evaporation and condensation exerts a clear influence on the non-conductive heat transfer dynamics in the dry active layer. Although all possible mechanisms were proposed in various analysis, quantitative validation of them is difficult. A successful example for a quantitative analysis of thermal dynamics in the active layer was shown by *Roth and Boike* [2001]. Based on the negligible water movement and approximately constant thermal properties, the approximation of pure conduction was validated successfully by projections of measured near-surface temperatures in that study. However, for normal active layers with strong vertical and temporal variability of thermal properties and heat transfer processes, the determination of ground heat flux is even more challenging on the QTP.

The large uncertainty in the determination of soil thermal properties strongly influences the accuracy of permafrost modeling [*Waelbroeck*, 1993]. Particularly at the near surface the complex heat transfer mechanisms complicate the sets of the upper boundary condition. In this

section, we use two different approaches to characterize the ground heat flux in active layers at the study sites. The objectives of this section are (1) to compare the accuracy of the ground heat flux estimation with two different approaches; (2) to characterize the heat transfer processes in the active layer with variational thermal properties at the near surface.

4.2.2 Material and methods

To study the surface energy balance in permafrost region, the ground heat flux is one important component besides the dominating net radiation and turbulent heat fluxes. There are various approaches to obtain the ground surface heat flux. One widely used approach is to measure the ground heat flux by using the output of a heat flux plate. There are several studies on the accuracy of the heat flux plate [e.g. *Massman*, 1992; *Sauer et al.*, 2003; *Weber et al.*, 2007]. Most plate estimates were still significantly lower than the actual ground surface heat flux, because it suffers from improper installation and shortcoming of different thermal conductivities of the plate and the actual soil [*van Loon et al.*, 1998]. Another one is the gradient method, which determines the soil heat flux from the vertical soil temperature gradient and thermal conductivity. Though comparing the above mentioned two approaches, the gradient method is recommended by *Liebethal et al.* [2005], because it is based on more reliable and negligible destructive measurements. They point out that the reference depth is the most important factor influencing the quality of the results. The optimum of the gradient approach is to determine heat flux by calculating from storage changes of the ground with a deep measured profile (the soil heat flux equals zero at the bottom). In the following, the gradient approach with different reference depths is introduced, and the effective thermal conductivity is estimated from time series of measurements of soil temperature and soil water content.

Ground heat flux in the active layer For frozen soil, it is usually assumed that the heat transfer is dominated by heat conduction. But for unfrozen soil, particularly in unsaturated soil the role of non-conductive heat transfer rises due to the movement of air, water vapor and water [*Kane et al.*, 2001]. In permafrost terrain, the non-conductive heat transfer in the active layer accounts for a notable amount of heat transfer during thawing. Due to the the relatively large amount of latent heat required for the phase change in the active layer, the largest component of the ground thermal energy is used to thaw the ground ice, typically comprising approximately 65-85% of the total soil heat flux [*Shirazi et al.*, 2009].

In the active layer, the energy are stored as sensible heat and latent heat. The stored energy in the active layer from the surface to the reference depth (z_r) is defined as a areal density E with respect to the reference state where the soil contains only soil matrix and its temperature is zero. It includes two kinds of energy, which are the sensible energy E_s and latent energy E_l

$$E(t) = E_s(t) + E_l(t). \tag{4.1}$$

On the left side of Equation 4.1, the first term is the summation of the sensible heat of all phases, and the second term is the latent heat of the ice. The sensible energy E_s is given as

$$E_s(t) = \sum_{\alpha \in \{s,w,i\}} c_\alpha \rho_\alpha \int_0^{z_r} \theta_\alpha(z,t) T(z,t) dz, \tag{4.2}$$

and the latent heat E_l is given as

$$E_l(t) = -L_{sf} \rho_i \int_0^{z_r} \theta_i(z,t) dz \tag{4.3}$$

where s, w, i are the three phases soil matrix, unfrozen water and ice, c_α is specific heat of the materials, L_{sf} is the latent heat of phase change from solid to fluid, θ_i is ice content.

The one-dimensional energy conservation of a volume from the surface to a certain depth in the active layer is given as [*Woo and Xia*, 1996]

$$\partial_t E_l + \partial_t E_s = j_h|_{surface} - j_h|_{bottom} \tag{4.4}$$

where E_l is the heat used for thawing the ground ice, E_s is the heat used for warming the active layer, $j_h|_{surface}$ is the heat flux from the ground surface, and $j_h|_{bottom}$ is the heat flux conducted out of the volume at the bottom. The heat flux for warming the ground is given as j_h^s, and the heat flux used for thawing the ice in the soil is given as j_h^l. Hence, j_h^s and j_h^l are calculated from the change of thermal energy of the soil. Their corresponding expressions are

$$j_h^s = \frac{\partial E_s(t)}{\partial t} \tag{4.5}$$

and

$$j_h^l = \frac{\partial E_l(t)}{\partial t}. \tag{4.6}$$

The downward heat flux at the bottom of the reference depth is

$$j_h|_{bottom} = -K_{eff} \frac{\partial T}{\partial z}|_{bottom}. \tag{4.7}$$

where K_{eff} and $\partial T/\partial t$ are the effective thermal conductivity and soil temperature gradient at the reference depth.

Choosing the reference depth is important for the gradient approach this method [*Liebethal et al.*, 2005]. Particularly for the active layer with variational thermal properties, it is very important to choose an optimal approach. In this study, Equation 4.4 is used to characterize the ground heat flux at two reference depths. For the shallow reference depth, the weights of each component in the Equation 4.4 are different from these in the approach with the deep reference depth. The changes of stored energy above the reference depth is relatively small, and a large amount of energy is transferred into the soil below. The ground heat flux j_{h1}^z in the approach with the shallow reference depth (ShalRef) is given as

$$j_{h1}^z = \frac{\partial E_s(t)}{\partial t} + \frac{\partial E_l(t)}{\partial t} - K_{eff} \frac{\partial T}{\partial z}|_{bottom}. \tag{4.8}$$

But choosing the deepest reference depth is usually the safest way to calculate the ground heat flux in permafrost regions. The ground heat flux j_{h2}^z in the approach with the deep reference depth (DeepRef) is calculated with the same expression on the right side of Equation 4.8. But usually the last term is thought to be negligible, and it can be simplified as

$$j_{h2}^z = \frac{\partial E_s(t)}{\partial t} + \frac{\partial E_l(t)}{\partial t}. \tag{4.9}$$

Estimation of the thermal conductivity Thermal properties regulate the heat transfer in the active layer, which are influenced by various factors such as soil composition, layer structure, water and associated movements. Estimating soil thermal properties is very important for modeling of the hydraulic and thermal dynamics in permafrost terrain. Due to disturbances of soil samples in laboratory studies, field investigations are crucial for estimating the thermal diffusivity. Concerning large diurnal variation of near surface temperature at the study sites,

the ratio of the amplitude method is recommended by [*Hinkel*, 1997] to estimate the apparent thermal diffusivity (ATD) above the damping depth. It has been used to estimated the thermal diffusivity of active layer in several studies [e.g. *Hinkel*, 1997; *Pringle et al.*, 2003; *Ikard et al.*, 2009]. In this method, the ratio of the periodic temperature amplitude measured at two depths is used, and the temperature pattern is assumed as an elementary sinusoidal function. The basic theory of this method is generally given as follows.

For the amplitude method, the hourly change of temperature in diurnal cycle can only be identified within damping depth. The ATD can be estimated with high temporal resolution. There are three major assumptions in this model. Firstly, it assumes a sinusoidal temperature variation at the soil surface. Secondly, the soil temperature is constant at infinite depth and equals the average soil temperature. Thirdly, the thermal diffusivity is constant throughout the estimated depth and the period. For 1-D pure heat conduction in the soil with certain boundary conditions, heat transport can be modeled by

$$\left.\begin{aligned} \frac{\partial T}{\partial t} &= D\frac{\partial^2 T}{\partial z^2} \\ T(0,t) &= T_0 + A_0\sin(\omega t) \\ T(z,t)|_{z\to\infty} &= T_0 \end{aligned}\right\} \tag{4.10}$$

where, T is the soil temperature and T_0 is the average soil temperature; z is the depth, D is the thermal diffusivity of the soil, ω is the frequency of the periodic temperature, and A_0 is the amplitude of the temperature at the surface. For this simple model, the analytical solution for the temporal soil temperature $T(z,t)$ and the amplitude at a certain depth $A(z)$ can be calculated from

$$T(z,t) = T_0 + A_0\exp(-z\sqrt{\frac{\omega}{2D}})\sin(\omega t - z\sqrt{\frac{\omega}{2D}}). \tag{4.11}$$

From 4.11, the thermal diffusivity calculated from the relationship between amplitude and depth can be estimated by field soil temperature measurements. Since the non-conductive heat transfer mechanisms such as water transport and phase change occur in the soil profile, the estimated thermal diffusivity is defined as apparent thermal diffusivity (ATD). It can be approximated as the above model, and substituted with an approximate finite difference solution. The ATD is calculated from the ratio of the periodic temperature amplitude at two depths z_i and z_{i+1} [*van Wijk and de Vries*, 1963], using

$$D = \frac{\pi}{P}[\frac{z_{i+1}-z_i}{\ln(A_i/A_{i+1})}]^2 \tag{4.12}$$

where, P is the period of the temperature ($P = 86400\ s$), A_i, A_{i+1} are the measured amplitudes at depths z_i, z_{i+1}, respectively. There are two approaches for calculating the amplitude. One approach is to search for the daily extremes of the temperature measurements, and then use these extremes to approximate the daily temperature amplitude. Another approach using all the temperature measurements is proposed by *Hinkel* [1997]. The hourly temperature changes are summed, and the daily temperature amplitude is calculated as the average temperature change multifold by one fourth period (6 hours). Since all the temperature measurements are used in this approach, it is more reliable than the method which only uses daily extremes. Using time series data of measured hourly temperature at nodes, the estimated values of thermal diffusivity D can be estimated by equation 4.12. The D is in units of $\mathrm{m^2 s^{-1}}$.

From the relation between thermal diffusivity, thermal conductivity and soil heat capacity, the effective thermal conductivity K_{eff} can be given as

$$K_{eff} = D \sum \theta_\alpha \rho_\alpha c_\alpha \tag{4.13}$$

where, θ_α, ρ_α, c_α are volume fraction, mass density and specific heat capacity, respectively, of phase α including soil matrix, water and ice. The parameters employed in the calculation at all sites are shown in Table 4.1.

Table 4.1. Soil properties of soil constituents at 20℃ [*Farouki*, 1981; *Weast*, 1985].

components	specific heat capacity	density
	kJ kg^{-1} K^{-1}	$\times 10^3$ kg m^{-3}
water	4.22	1.0
ice	2.11	0.917
soil minerals	0.733	2.65

4.2.3 Applications and discussions

In this section, the temporal variations of ATD estimated from the application of the amplitude method by using time series of soil temperature measurements are presented, and the ground heat fluxes are estimated by the gradient method with two different reference depths at three study sites. Their performances are shown in detail as follows.

Characteristics of the near-surface thermal diffusivity The temperature variations are dominated by a daily cycle near the surface. Hourly temperature and soil water content measurements were recorded at Chumaer and Qumahe, but at Tianshuihai the temperature and soil water content measurements were measured with intervals of 30 minutes and 3 hours, respectively. The accuracy of the measured soil temperature is better than ±0.02℃. In the estimation, the hourly temperature change is calculated as a mean value of all the measurements in one day (48 measurements at Tianshuihai and 24 measurements at other three sites). The mean amplitude in one day is used in equation 4.11 to estimate the ATD. The assumption of sinusoidal function of the surface temperature worked well when the weather is not disturbed by clouds and other abrupt changes.

Limited by the precision of the soil temperature measurements, this method is just used to estimate the ATD of the near surface soil (above the damping depth). The damping depth is mainly dependent on the diurnal dynamic range of surface temperature and the soil thermal properties. Active layers, located in high-altitude-low-latitude regions, are usually influenced by a large diurnal dynamic range of air temperature and the dry climate on the QTP. The daily damping depth reaches several decimeters. These conditions are favorable for the amplitude method to estimate the near-surface thermal diffusivity. Since the gradient method for calculating ground heat flux is sensitive to the reference depth, impacts of the misplacement of sensors can be reduced when the reference depth increases [*Liebethal et al.*, 2005]. The soil temperature fluctuation can not be approximated as sinusoidal function when there non-conductive processes occur, for instance, infiltration of rainfall or snow melting. In addition, during the periods of phase change, the ratio of amplitude method will fail because of the assumption of pure heat conduction in Equation 4.10. Fortunately, these periods are usually very short for dry active layers. In our calculation, all these invalid values are dropped and replaced with linearly interpolated values from adjacent values.

Chumaer is located in the warm permafrost region. From previous analysis, we know that the mean annual air temperature is about -4.94 ℃, and the mean thickness of the active layers is larger than 2 m. Since the potential evapotranspiration is larger than the actual evapotranspiration in summer, there is only a little recharge of ground water by precipitation. During the winter, the soil temperature is mainly controlled by the components of the surface energy balance. Thin occasional snow cover has very weak influence on the surface energy balance. But the strong wind facilitates the sensible heat flux. Due to the variations in soil water content in the active layer, its thermal regime is strongly influenced by the variational soil thermal properties.

Figure 4.1 shows ATDs in the near-surface estimated from the amplitude method at Chumaer. In the profiles P1 and P2, five temperature probes are installed within 30 cm, and their positions are 0.05 m, 0.1 m, 0.15 m, 0.20 m and 0.30 m below ground surface. Unfortunately, the probes at 0.20 m and 0.30 m in the profile P1, and 0.05 m in the profile P2 failed in the field. Hence, in P1 the ATDs can only be calculated with soil temperature measurements of two thermal probes at depths 0.05 m and 0.15 m; the ATDs from surface to the depth 0.30 m are calculated with two probes at depths 0.10 m and 0.30 m in P2. Since the calculation of ATD is sensitive to the errors in the distance between two probes, we should keep in mind that the quality of the estimated values in P2 is much better than that in P1.

As shown in Figure 4.1, there are three major characteristics. Firstly, the curves in frozen periods are smoother than those in thawed periods except snow cover periods. This is because of the stronger variations in soil water content and non-conductive processes in summer. The estimation of thermal diffusivity is significantly influenced by the insulation of the snow cover during the period of the day number: 1038-1067. But the effects of snow cover are influenced by its thickness. For instance, the influences of the thin snow cover are negligible during the period 345-385. Secondly, the inter-annual variations of the seasonal differences of ATD are generally more evident in P1 than in P2. In P1, ATD in frozen periods changes dramatically from 2006 to 2007, it is even smaller than that in thawed periods. But in P2, ATDs in frozen and thawed periods are close each other, and it is slightly higher in frozen periods. This may be attributed to the surface differences. In P1, the ground surface is nearly bare, and its water content can vary differently according to the weather. While in P2, the ground surface is covered with dense roots of short grass, which can keep the soil water content relatively stable during the frozen and thawed periods. Thirdly, phase change apparently takes effects during the transition period between the frozen and thawed periods. But at the near surface this period is usually very short, particularly for dry active layers.

Although Qumahe is also located in the warm permafrost region, the characteristics of the active layer are totally different from those at Chumaer. The mean air temperature is nearly the same as at Chumaer, but its active layer is very shallow. This is mainly attributed to the dense vegetation and almost saturated soil in the active layer. Since much water in the active layer supports evapotranspiration during the summer period, a large amount of input energy by solar radiation is taken away by evapotranspiration. Besides, the large heat capacity of the saturated soil further hinders the surface energy to be transferred into lower layers. While in winter, once the active layer is completely frozen, the high ice-content of the soil has a much higher thermal diffusivity, which rapidly releases the energy from the ground below permafrost table. These basic heat transfer mechanisms are typical in most saturated active layers.

The ATDs resolved from the amplitude method at Qumahe, are shown in Figure 4.2. Since the thermal diffusivity of the wet soil is much smaller than the dry soil, the damping depth is just around 20 cm at this site. We calculate the ATD from the surface to a depth 0.15 m with two probes at depths of 5 cm and 15 cm. The seasonal variations of ATD show that the difference

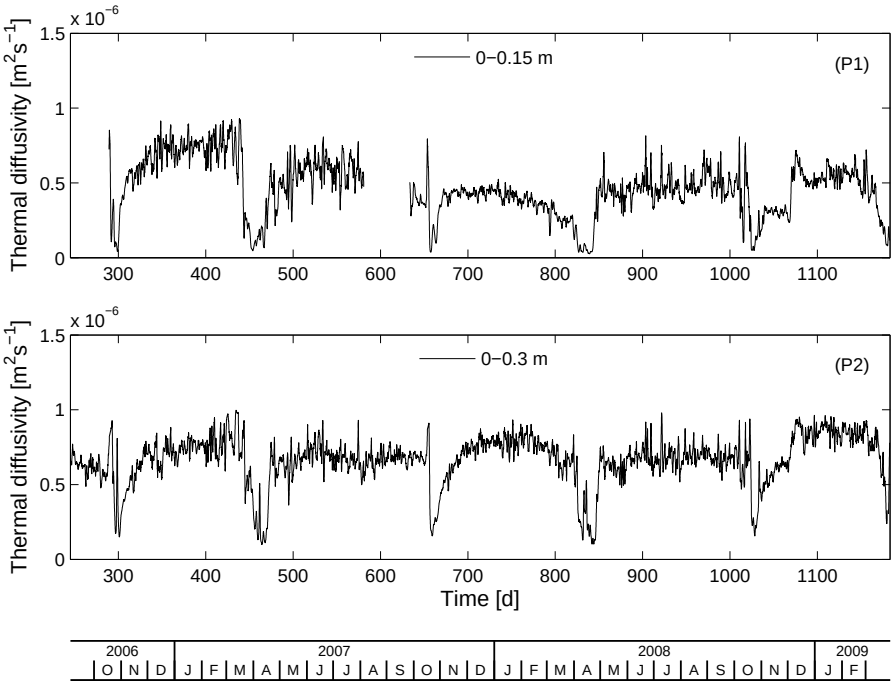

Figure 4.1. Temporal variations of apparent thermal diffusivity at the near-surface reference depth at Chumaer. The values are estimated from soil temperature measurements around the reference depth with the ratio of amplitude method (P1: 0.05 m and 0.15 m; P2: 0.10 m and 0.30 m). The blanks are missing data.

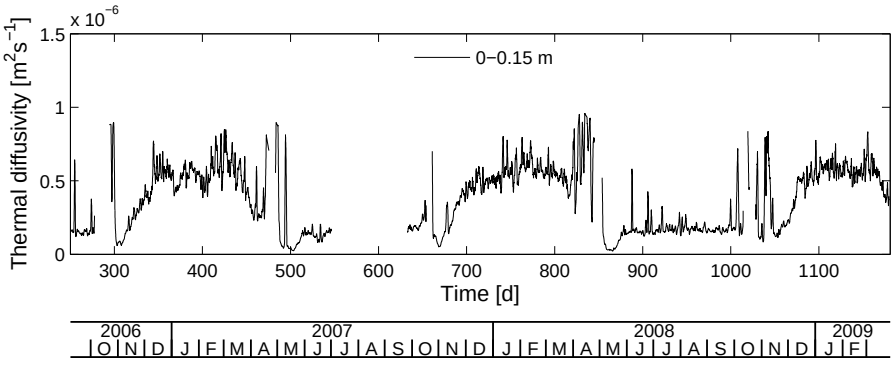

Figure 4.2. Temporal variations of apparent thermal diffusivity at the near-surface reference depth at Qumahe. The values are estimated from soil temperature measurements around the reference depth (0.05 m and 0.15 m) with the ratio of amplitude method. The blanks are missing data.

in winter-to-summer diffusivity is very high, which is commonly found in permafrost regions. In contrast to Chumaer, the fluctuations in ATD in the frozen period are much stronger than in the thawed period. It indicates that the effects of the unfrozen water in frozen periods plays an important role in the ground heat transfer. In addition, the snow cover effectively insulated heat flux downward from surface, which made the soil temperature higher, accordingly ATD reduced significantly.

Tianshuihai site is located in the cold permafrost region on western Tibetan plateau. From previous analysis we know that, the mean annual air temperature is about -6.10℃, and the active layer is around 1.5 m. Due to the dry climate, the soil temperature is mainly driven by

solar radiation. In this dry region, the influences of precipitation and evapotranspiration to the thermal regime of active layer are negligible. During the winter, the soil temperature is much lower that the other sites. Within the active layer, the soil thermal properties play an important role in the energy exchange between atmosphere and ground.

Figure 4.3 shows the temporal variations of ATDs resolved from the ratio of amplitude method at Tianshuihai. The ATDs for the layer from surface to the depth 0.31 m and 0.21 m are calculated with probes at depths 0.04 m and 0.31 m in P1, and 0.04 m and 0.21 in P2, respectively. There are large errors in the temperature measurements during the freezing periods. But the reason is still unclear. These errors should be caused by the large variations of ATD during these periods, for instance the period of day number: 750-830. Different from the other sites, the mean ATD in frozen periods is relatively smaller than that in the thawed periods.

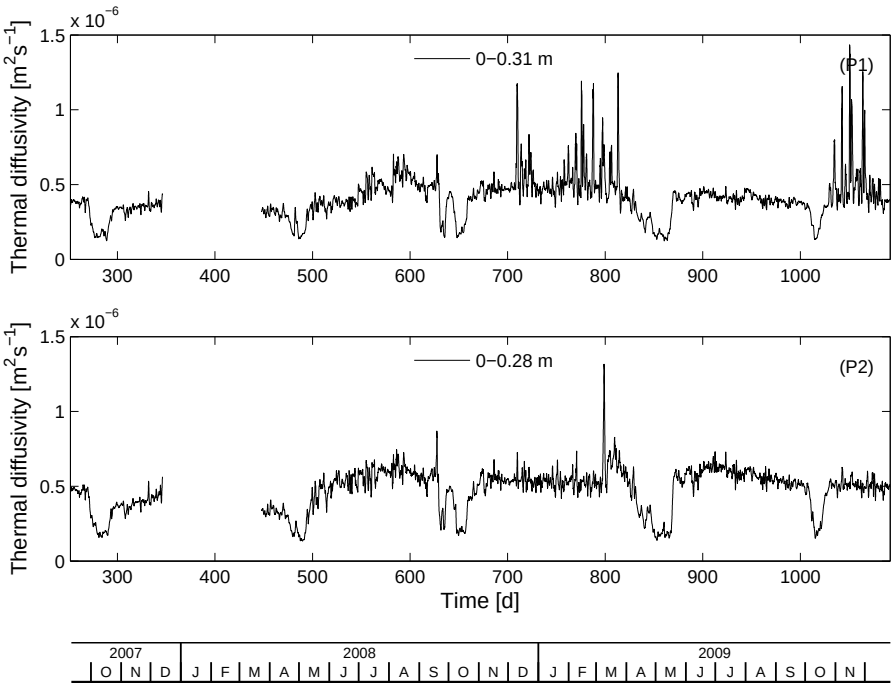

Figure 4.3. Temporal variations of apparent thermal diffusivity at the near-surface reference depth at Tianshuihai. The values are estimated from soil temperature measurements around the reference depth with the ratio of amplitude method (P1: 0.04 m and 0.31 m; P2: 0.04 m and 0.21 m). The blanks are missing data.

Table 4.2. Seasonal variations of the near-surface ATD at the study sites. D_t and D_f are estimated in the summer and winter periods, respectively.

site	profile	depth m	$\bar{D}_t \pm \sigma$ $\times 10^{-7}$	$\bar{D}_f \pm \sigma$ [m^2 s^{-1}]	$\bar{D}_f / \bar{D}_t$ [-]
C	P1	0-0.15	4.5 ± 1.7	4.6 ± 2.0	1.02
	P2	0-0.30	6.3 ± 1.4	6.7 ± 1.9	1.06
Q		0-0.15	1.8 ± 1.1	4.6 ± 1.9	2.56
T	P1	0-0.31	3.9 ± 1.1	4.2 ± 1.6	1.08
	P2	0-0.28	5.0 ± 1.4	4.5 ± 1.3	0.90

From comparison of the near-surface ATDs at this three sites, we can find that there are two major features. Firstly, the ratio of winter-to-summer diffusivity is much higher at Qumahe than the other sites. As shown in Table 4.2, $\bar{D}_f/\bar{D}_t$ at Qumahe is two times more than that at Chumaer and Tianshuihai. The seasonal variations of ATD at Chumaer and Tianshuihai with dry near surface indicate that they do not behave as common permafrost soils, whose variational thermal conductivity can lead to a certain offset between the mean annual surface temperature and the mean annual soil temperature at permafrost table. While the near surface with high water content presents a significant increase of ATD from summer to winter. Secondly, temporal variation of ATD in winter is stronger at Chumaer and Qumahe than that at Tianshuihai. As shown in Table 4.2, the standard deviation of D_f at Chumaer and Qumahe in warm permafrost region are relatively larger than that at Tianshuihai in cold permafrost region. This is because of the stronger effects of temperature dependence of ATD in winter in warm permafrost region.

Characteristics of ground heat flux at the study sites The DeepRef approach is the safest way to determine ground heat flux [*Liebethal et al.*, 2005]. The total ground heat energy above the reference depth is interpolated from all point measurements. Since the measured profile is down to permafrost table, the heat flux j_b is usually assumed negligible at the bottom of the measured profile [*Boike et al.*, 1998; *Ishikawa et al.*, 2006]. However, the exact depth is not clear in the field, which is usually determined by the rule of thumb. But its potential impacts are discussed with the values estimated with the ShalRef approach. Another reason is the difficulty of obtaining the accurate thermal conductivity, because of the significant phase at the bottom of active layer. In our calculation, it is also dropped. Since the majority of the energy from the surface ground heat flux is used for fusion of ice in the active layer, the DeepRef approach is very sensitive to the accuracy of soil water content measurements and its interpolation from point measurements. Particularly around the thawing or freezing front in saturated soils, the linear interpolation can lead to large deviations. In the ShalRef approach, the effective thermal conductivity is obtained from the ATD. The studies show that the results differ considerably from the amplitude, phase, numerical approaches [*Horton et al.*, 1983; *Hinkel*, 1997]. Therefore, the error range of the estimated effective thermal diffusivity should be kept in mind.

Due to lots of missing data and long measured periods, here we just choose a complete year-round data set from each site to take a closer look (Chumaer and Qumahe: 2008; Tianshuihai: 2009). Combining the two approaches of DeepRef and ShalRef, we characterize the ground heat flux at each site and comment on the performance of these two approaches. The values of the ground heat flux at all study sites are calculated with Equations 4.8 and 4.9.

Figure 4.4 shows the differences of ground heat flux estimated from the ShalRef and DeepRef approaches and its distribution in two profiles at Chumaer in 2008. Comparing the results from two approaches, we find that except P1, the ShalRef approach works reasonably in P2. Due to the failure of the probes at deeper depth at the near surface, the shallow measurements would lead to serious deviation in thermal conductivity. Because of the deviation of the linear interpolation around the thawing and freezing front, it causes the large peaks in the ground heat flux calculated from the DeepRef approach during the thawing and freezing periods. However, this effect is not significant in the ShalRef approach, because the front moves much faster in the dry soils at the near surface than that at the bottom with higher water content. One noteworthy point is the large difference between the two approaches during the period from late January to the end of March. It is mainly attributed to the improper assumption for the negligible downward heat flux at the bottom of the profile. At Chumaer, the deepest probe was installed above the permafrost table in both profiles. During this period there should be significant phase change below this depth, and a large amount of heat energy has been transferred though the

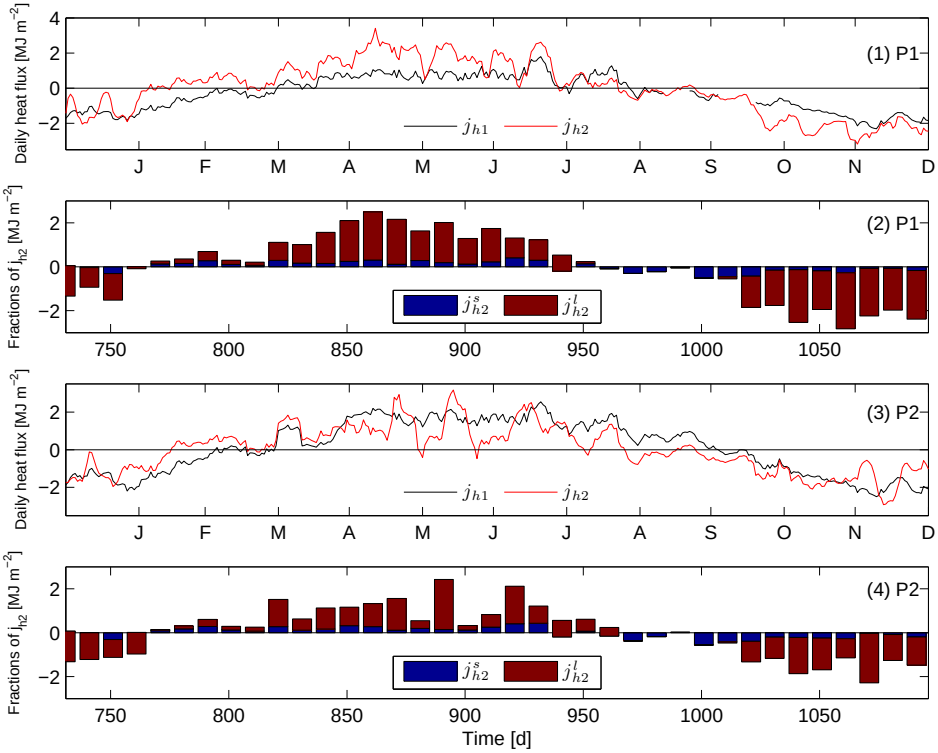

Figure 4.4. Characteristics of the estimated ground heat flux from two approaches: ShalRef approach (j_{h1}) and DeepRef approach (j_{h2}) at Chumaer in 2008. (1) and (3): comparison on the ShalRef approach (j_{h1}) and the DeepRef approach (j_{h2}) in P1 and P2, respectively; (2) and (4): fractions of the estimated ground heat flux j_{h2} in P1 and P2, respectively. j^s_{h2}: sensible heat, j^l_{h2}: latent heat.

bottom. Therefore, to avoid this large deviation, it is very important to install the probes down to the permafrost without significant phase change for the DeepRef approach.

Fractions of the ground heat flux estimated from the DeepRef approach are shown in Figure 4.4 (2) and (4). The deployed components of sensible heat and latent heat are shown as means of 10 days. The results demonstrate that the energy from the surface during the thawing and freezing periods is mainly transferred to latent heat. During the thawing period (day number: 820-999), the mean fractions j^s_{h2} and j^l_{h2} of ground heat flux are 27.9%, 72.1% in P1, and 32.9%, 67.1% in P2, respectively. During the freezing period (day number: 731-819 and 1000-1096), the mean fractions j^s_{h2} and j^l_{h2} of ground heat flux are 26.9%, 73.1% in P1, and 28.3%, 71.7% in P2, respectively. In a long term, the net ground heat flux reflects the thermal change of permafrost. Due to the bad estimation of ground heat flux in P1 with the ShalRef approach, we have to drop the j_{h1}. But the other net ground heat fluxes estimated from both approaches in P1 and P2 are all positive in Table 4.3, which indicates the evident warming trend of the permafrost at this site. The differences between two approaches mainly originate from the underestimation of the ground heat flux by non-conductive processes and an improper assumption of negligible heat flux below the reference depth in the BottRef approach.

Figure 4.5 shows the differences of ground heat flux estimated from the ShalRef and DeepRef approaches and its distribution at Qumahe in 2008. Comparing the results from the two approaches, we find that they are consistent with each other during most of the thawing period (the differences in June and July are caused by artificial interpolation of the DeepRef approach), but the major differences concentrates during the frozen period. The values from the ShalRef

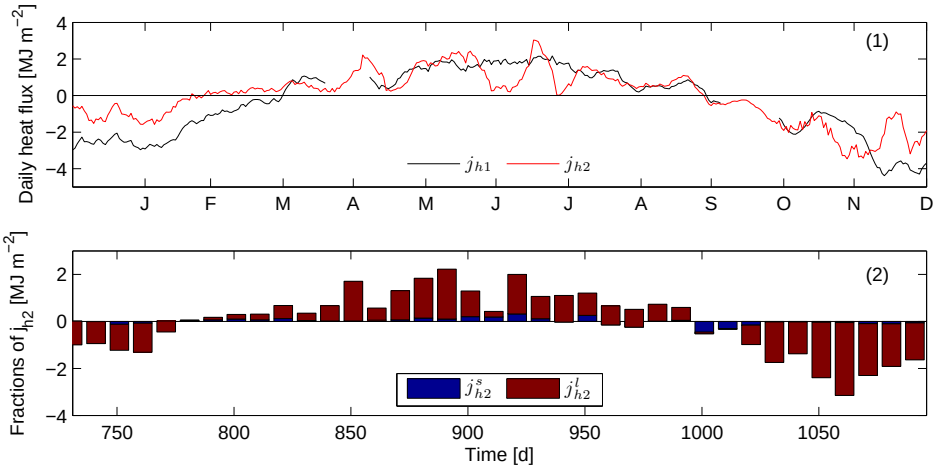

Figure 4.5. Characteristics of the estimated ground heat flux from two approaches: ShalRef approach (j_{h1}) and DeepRef approach (j_{h2}) at Qumahe in 2008. (1) comparison on the ShalRef approach (j_{h1}) and the DeepRef approach (j_{h2}); (2) fractions of the estimated ground heat flux j_{h2}. The deployed components are shown as means of 10 days. j^s_{h2}: sensible heat, j^l_{h2}: latent heat.

approach are evidently larger than these from the DeepRef approach. One possible reason is the ignored downward heat flow at the bottom. Because the active layer was totally frozen during this period, the soil with high ice content has a large thermal conductivity. The large peaks in the ground heat flux calculated from the DeepRef approach are also caused by the deviation of the linear interpolation around the thawing and freezing front during the thawing and freezing periods. Due to high soil water content, the jump of heat flux calculated from changes of the interpolated total energy is much larger than that at Chumaer. Therefore, to use the DeepRef approach in profiles like Qumahe, dense measurements in depth and deeper installation are required to get rid of above problems.

The distributions of the ground heat flux are shown in Figure 4.5 (2). The deployed components j^s_{h2} and j^l_{h2} are also shown as means of 10 days. The results demonstrate that the the energy transferred from the surface during the thawing and freezing periods are predominantly used by latent heat. During the thawing period (day number: 822-999), the mean fractions j^s_{h2} and j^l_{h2} of ground heat flux are 7.0%, and 93%, respectively. During the freezing period (day number: 731-821 and 1000-1096), the mean fractions j^s_{h2} and j^l_{h2} of the ground heat flux are 6.4%, 95.6%, respectively. From previous analysis we know that there was a thick snow cover during the winter in 2008, which lasted about two months. Due to the insulation of snow cover, the water in the active layer can not evaporate as usual. Hence, more water was stored as ice than in the last winter, which cause more energy used for fusion during the freezing period than that during the thawing period in 2008. The net ground heat fluxes estimated from the above two approaches in 2008 are shown in Table 4.3. The negative net j_{h1} and j_{h2} indicate the cooling trend of permafrost in 2008. But the large differences may be caused by both approaches. On the one hand, the ground heat flux may be overestimated in the ShalRef approach, because of phase change of unfrozen water during the freezing period in the ShalRef approach. On the other hand, the ground heat flux should be underestimated, because of the ignored ground heat flux at the bottom.

Figure 4.6 shows the differences of ground heat flux estimated from the ShalRef and DeepRef approaches and its distribution in two profiles at Tianshuihai in 2009. Comparing the results from the two approaches, we find that the ShalRef approach behaves reasonably in both profiles.

Since the water content in P1 is much smaller than in P2, the deviation of the linear interpolation around the thawing and freezing front in P1 is much weaker than that in P2. This is reason why there is a large peak in the ground heat flux calculated from the DeepRef approach in April in P2. The same effects occurred that there are evident differences between two approaches during the period from late January to the end of March. It is mainly attributed to the improper assumption for the negligible downward heat flux at the bottom of the profile. Because the active layer was totally frozen during this period, the soils with high ice content has a large thermal conductivity. Therefore, we should keep in mind the impact of j_b in the DeepRef approach.

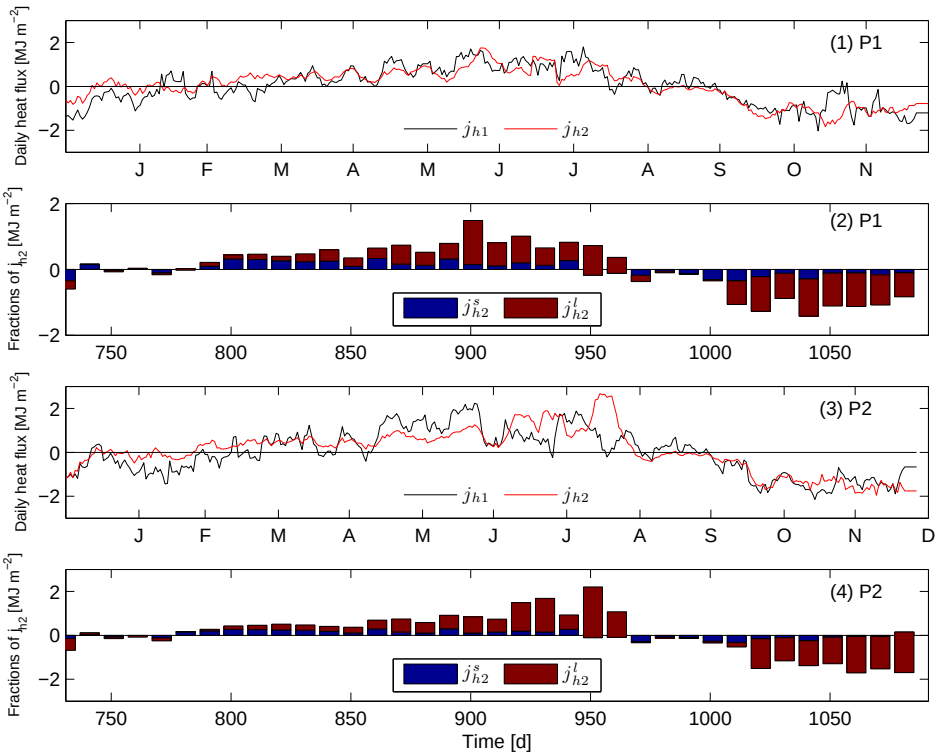

Figure 4.6. Characteristics of the estimated ground heat flux from two approaches: ShalRef approach (j_{h1}) and DeepRef approach (j_{h2}) at Tianshuihai in 2009. The deployed components are shown as means of 10 days. (1) and (3): comparison on the ShalRef approach (j_{h1}) and the DeepRef approach (j_{h2}) in P1 and P2, respectively; (2) and (4): fractions of the estimated ground heat flux j_{h2} in P1 and P2, respectively. j^s_{h2}: sensible heat, j^l_{h2}: latent heat.

The distributions of the ground heat flux are shown in Figure 4.6 (2) and (4). The deployed components of j^s_{h2}, j^l_{h2} are shown as means of 10 days. The results demonstrate that the energy transferred from the surface during the thawing and freezing periods are mainly consumed by latent heat. During the thawing period (day number: 785-1005), the mean fractions j^s_{h2} and j^l_{h2} of ground heat flux are 38.2%, 61.8% in P1, and 41.5%, 58.5% in P2, respectively. During the freezing period (day number: 731-784 and 1006-1091), the mean fractions j^s_{h2} and j^l_{h2} of ground heat flux are 38.0%, 62.0% in P1, and 39.2%, 60.8% in P2, respectively. At this site, the net ground heat fluxes estimated from the above two approaches in 2009 are shown in Table 4.3. The positive net j_{h1} and j_{h2} indicate the warming trend of permafrost in 2009 in P1, while in P2 the small negative net j_{h1} and large positive j_{h2} also show a warming trend. But the differences

may be mainly caused by the underestimated ground heat flux because of the ignored ground heat flux at the bottom.

Table 4.3. Net ground heat flux estimated with the ShalRef (j_{h1}) and DeepRef (j_{h2}) approaches at the study sites.

site	profile	net j_{h1}	net j_{h2}
		MJ m^{-2} d^{-1}	
Chumaer	P1	-94.41	0.44
	P2	41.09	2.91
Qumahe		-119.57	-9.91
Tianshuihai	P1	5.31	12.44
	P2	-4.02	22.11

Discussions For different applying conditions, the above two approaches have their respective merits and drawbacks. For the ShalRef approach, it is relatively easy to measure with simple instrumentation. In practical application, it just needs two temperature probes around the reference depth and one or more probes to measure soil water content above the reference depth. As presented by *Deming et al.* [1992], during summer the lateral water movement within the active layer would take away heat energy, which is not negligible. Besides, *Ishikawa et al.* [2006] find that the evaporated vapor produced in the upper warmer layers and condensed in the lower colder layers. This approach avoids to concern the complicated heat transfer processes below the the reference depth such as lateral ground water flow and evaporation-condensation within the active layer. To a certain extent it includes the effects of the non-conductive processes such as convection, phase change of unfrozen water, because the effective thermal conductivity is estimated from soil temperature measurements at the near surface of the dry active layer. However, this approach is strongly dependent on the accuracy of thermal conductivity estimation and the distance between the two probes. *Liebethal et al.* [2005] pointed out that the gradient approach is most sensitive to the sensor placement and soil inhomogeneity, and this sensitivity decreases as the reference depth increases. He recommends a reference depth of about 0.20 m, and for soils with a low conductivity the sufficient depth is 0.10 m. From the results from Chumaer, the shallow reference depth in P1 caused considerable deviations compared with the values from the DeepRef approach. For the DeepRef approach, it is relatively stable with intensive instrumentation, particularly when the reference depth is deep at the depth where the soil heat flux is close to zero. Its accuracy mainly depends on the measurements of soil temperature and soil water content. However, there are some drawbacks in this approach. Firstly, it is hard to measure the vapor flux from soil water content measurements. Because vaporization and vapor transport can take a large amount of energy, but the change of water amount is difficult to be measured directly. Secondly, it is difficult to obtain accurate stored energy in the active layer with ground water from point measurements by interpolation, because it is problematic to estimate soil water around the interface of ground water table by linear interpolation. Thirdly, the heat flux is strongly deviated by the interpolation of the unfrozen water content around the interface of phase change in the saturated layer. For instance at Qumahe, there are large peaks during thawing period in Figure 4.5(1).

Results of estimated ground heat flux show that the different effects of above the two approaches at the study sites. Firstly, the assumption of negligible heat flux at the bottom of active layer leads to different effects at the study sites. At Chumaer in P2 (P1 dropped for the improper reference depth), it causes large deviations during the periods of from late January

to middle of March, and from August to the beginning of October. This is mainly caused by the non-negligible heat flux at the bottom, because there was still a strong phase change during these periods below the deepest sensor. The deepest sensor is below the permafrost table at the other two sites, and the phase change below this depth can be negligible. However, due to the long period of the complete frozen active layer and high effective thermal conductivity, the heat flux is not negligible during this period. As shown in Figure 4.51, the values from DeepRef approach is evidently underestimated. At Tianshuihai, this difference is much smaller. This is because of the relative smaller thermal conductivity of dry active layer than that of saturated active layer. Secondly, it is difficult to estimate thermal diffusivity during zero-curtain period at Qumahe.

In general, the results show that the ShalRef approach works better than the DeepRef approach at the study sites besides the P1 at Chumaer. It is possible to improve the DeepRef approach with high density and deeper depth. However, this approach needs more effort and cost. Therefore, we recommend the estimation of ground heat flux from the ShalRef approach in later energy balance.

From Figures 4.4, 4.5 and 4.6, we find that most of ground heat flux is used for melting in the wet active layer. The water content distribution in the active layer has a strong impact on the ground heat flux. For the active layer with dry near surface, the difference of the near-surface thermal conductivity between winter and summer is so small that it causes a decreasing temperature offset between the surface and the permafrost table along with global warming. For instance at Chumaer, the smaller thermal conductivity in winter leads to a longer duration of freezing the active layer than that at Qumahe, although they have similar climates and total water contents in the active layer. This long phase change period hinders the release of ground heat from the underlying permafrost, which is adverse to the permafrost stability.

4.3 Characterization of the thermal regime of the active layers

4.3.1 Introduction

In permafrost regions, the active layer plays a significant role in the interaction between climate and permafrost. With different surface characteristics, and soil moisture and soil properties, the active layer thickness and permafrost distribution have a strong variability [e.g. *Stocker et al.*, 2002; *Zhang et al.*, 2005; *Anisimov and Reneva*, 2006]. Besides, the responses of permafrost to climate changes are strengthen or attenuated by the heat and mass exchange in different active layers. Studies [e.g. *Chen et al.*, 2003; *Wu and Zhang*, 2010] on the QTP show that the thickening active layer is different in continuous and discontinuous permafrost regions. *Zhang et al.* [2003a] pointed out that the dominant feature of the land-surface hydrology on the eastern QTP is the freeze-thaw cycle, which affects the water cycle components during the summer monsoon season. The permafrost degradation caused by climate warming is evident on the QTP [*Chen et al.*, 2003]. However, the relation between hydrological processes and the deepening active layer, and their mechanisms in the active layer remains poorly understood.

At the interface between the ground surface and the atmosphere, complex heat transfer processes occur in this buffer layer. They involve radiative fluxes, turbulence, conduction and evaportranspiration. Due to complex physical processes at the ground surface, the surface energy balance is usually used to characterize the interaction between the atmosphere and permafrost. The surface energy balance is usually defined with respect to a negligibly thin layer. It can be written as

$$NR + H + LE + G = 0 \tag{4.14}$$

where, NR: net radiation, H: sensible heat flux, LE: latent heat flux, G: ground heat flux. The net radiation can also be given as $NR = S\downarrow(1-\alpha) + L\downarrow - L\uparrow$, where $S\downarrow$: global radiation, α: albedo, $L\downarrow, L\uparrow$: incoming and outgoing longwave radiation.

In the surface energy balance, sensible heat flux H is mainly controlled by the temperature difference between ground surface and air. The magnitude of H is dependent on the surface turbulence, which governs the heat exchange between the surface and air. Latent heat flux LE is mainly dependent on the availability of the surface water. The major processes such as vaporization and fusion play a significant role in the energy balance between the atmosphere and permafrost. The ground heat flux G is mainly controlled by the temperature gradient and thermal diffusivity in the subsurface soil. Generally the thermal diffusivity of frozen soil is larger than that of the thawed soil. For most soils, ground heat flux is 5-9% of net radiation, while it reaches 16-18% when permafrost is present [*Karunaratne*, 2003]. Besides, in summer, the thermal gradient in the active layer increase, because the thawing front at the bottom remains around 0℃.

There are several local factors influencing on the interaction between ground surface and atmosphere. For instance, vegetation can reduce the solar radiation reaching the ground surface. Besides, the interception of precipitation and transpiration by vegetation canopy also influences the ground thermal regime through the water balance [*Smith and Riseborough*, 1996]. Snow is another important factor influencing the ground thermal regime. It can restrict the loss of thermal energy from the ground because of its low thermal conductivity. At the same time, due to the high albedo of snow, it also reduces the incoming heat energy from the atmosphere. As a result, the characteristics of snow cover is the largest single factor accounting for spatial variations in surface temperature [*Smith and Riseborough*, 1996]. In addition, besides the influence of ground surface temperature, the inter-annual variability of the snowpack is one important factor to the variability of ground temperature [*Smith and Riseborough*, 1996]. Particularly for mountain permafrost, the local factors such as altitude, slope, aspect, and snow cover dominate the permafrost distribution. Including air temperature and solar radiation, these factors determine the surface energy balance. Through monitoring these factors, the relation between climate and permafrost distribution can be explored [*Stocker et al.*, 2002].

As described in last chapter, the characteristics of the hydraulic and thermal pattern are different at the study sites. The thermal regime is governed by the interaction between the atmosphere and the active layer. Facilitated by the state-of-the-art instrumentation, the hydraulic and thermal dynamics are quantitatively characterized by the water and energy balance models. In this chapter, we characterized the hydraulic and thermal dynamics at the study sites of Chumaer, Qumahe and Tianshuihai. The objectives are (1) to quantitatively understand the characteristics of the hydraulic and thermal dynamics of various active layers, (2) to identify the major controlling factors to the thermal regime at the study sites.

4.3.2 Methods

As summarized by *Boike et al.* [1998], the basic heat energy exchange in the active layer is mainly driven by a high positive net radiation during spring and summer, and from fall the heat flux is outward for the falling air temperature. The energy and water balances govern the hydraulic and thermal dynamics in the active layer. The energy balance model has been used to investigate the seasonal variation of the heat exchange between the atmosphere and the permafrost in several permafrost areas [e.g. *Outcalt et al.*, 1990; *Boike et al.*, 1998; *Tanaka et al.*, 2003; *Ishikawa et al.*, 2006]. The method used in the study of *Boike et al.* [1998] captured the major heat transfer processes excluding the surface sensible heat flux during the summer at

that particular area. However, the sensible heat flux is nonnegligible on the QTP. Therefore, in our study that method is adapted to characterize the hydraulic and thermal dynamics at the study sites.

In this method, the studied volume for the energy balance is from the surface to the excavated bottom. All the fluxes are assumed to be perpendicular to the surface, and driving forces at the surface are net radiation flux j_{nr}, sensible heat flux j_h, vapor flux j_v and ground heat flux j_g. In addition, several processes like lateral water fluxes such as groundwater movement and surface runoff, and heat flux through the bottom are ignored in the models. In the soil, only three components of soil matrix s, ice i and unfrozen water w are considered, and the amounts of water vapor and air are ignored here. Besides, instantaneous transfer processes in the unfrozen layer are assumed. The sensible heat flux, energy and water balance models were calculated with following approaches.

Sensible heat flux estimation The sensible heat flux j_h is mainly controlled by turbulent heat transfer between ground surface and atmosphere. The eddy correlation method is widely used to estimate sensible heat flux by directly measuring the turbulence. Due to limitations of the strict requirements of instrumentation and high cost of this method, several indirect methods such as the Bowen ratio method, the gradient method, the bulk transfer method have been developed to estimate sensible heat flux. Since the main goal of our instrumentation was not to study heat transfer above the ground surface, it is difficult to estimate the sensible heat flux with existing measurements using above mentioned methods. However, concerning the strong influences of the sensible heat flux to the thermal regime of the active layers on the QTP, only a few methods just using existing measurements can be applied here. Although they may not as accurate as above mentioned methods, they still can give us some useful references for understanding the thermal regime of the active layer.

Two applicable methods are introduced to roughly estimate the sensible heat flux at the study sites. The first method just using single-level measurements of air temperature is proposed by *Wang and Bras* [1998]. This method is based on the modelling of the turbulent transfer in the lower atmosphere over a homogeneous land surface. The heat flux is derived from the model of a one-dimensional diffusion equation. *Wang and Bras* [1998] demonstrated that the sensible heat flux is expressed as a weighted average of the time history of air temperature

$$\begin{aligned} j_h(z,t) \equiv & -\rho_a C_a \, K_h \frac{\partial T}{\partial z} \\ = & \rho_a C_a \sqrt{\frac{K_h}{\pi}} \int_0^t \frac{dT(z,s)}{\sqrt{t-s}}, \end{aligned} \tag{4.15}$$

where ρ_a is the air density, C_a is the heat capacity of the air at constant pressure. K_h is the heat transfer coefficient of the turbulent flow. In application, the sensible heat flux is approximated with a varying eddy diffusivity.

The great advantage of this method is that the sensible heat flux estimation is less sensitive to the sampling error of air temperature and the eddy diffusivity parameterization than the traditional temperature gradient method [*Wang and Bras*, 1998]. The eddy diffusivity parameterization can be estimated with the Monin-Obukhov similarity theory [*Stull*, 1988] or other empirical equations [*Stull*, 1994]. However, limited by our measurements, the common methods of the eddy diffusivity parameterization are unavailable. Empirical constant values K_h were tested, but they failed because of the large seasonal variations of the eddy diffusivity on the QTP [*Li et al.*, 2000].

Another simpler empirical method was proposed by *Jacobs et al.* [1996], in which the Nusselt numbers were used to calculate the sensible heat flux for the ground surface with sparse canopies.

That study shows that the results agreed well with the sensible heat flux measured by the eddy-correlation technique. The empirical formula is

$$j_h = \frac{Nu\ K_a \Delta T}{l}, \tag{4.16}$$

where, K_a is the thermal conductivity of still air ($K_a = 0.0257$ W m^{-1} K^{-1}), ΔT is the temperature difference between air and ground surface, and l is the characteristic length of the turbulence flow. According to Kolmogorov's theory of turbulence describing turbulent fields with very high Reynolds numbers, the characteristic length l is generally from the scale of millimeters to tens of meters [*Kolmogorov*, 1980; *Bonner et al.*, 2010]. The observations [e.g. *Yang et al.*, 2004*b*; *Peng et al.*, 2005; *Song et al.*, 2006] of the structure and the evolution of the atmospheric boundary layer over the QTP show that the atmospheric boundary layer is strongly associated with the convective activities, and the near-surface turbulent layer is around 15 m. Therefore, l is set as 15 m in our calculations.

According to the criteria [*Monteith and Unsworth*, 1990], three types of convection (Free convection, Forced convection and Mixed convection) in natural conditions can be identified by the critical Rayleigh Numbers $16Re^2$ and $0.1Re^2$. Re is the surface Reynolds number defined as [*Jacobs et al.*, 1994]

$$Re = \frac{l\ u}{\nu}, \tag{4.17}$$

where, l is the horizontal characteristic length scale of the area, u is the horizontal wind speed, ν is the kinematic viscosity. In Equation 4.16, the convection coefficient h_c is a function of the Nusselt Number (Nu), in which the Rayleigh number Ra is defined as

$$Ra = \frac{l^3 g \beta \Delta T}{\nu^2} Pr, \tag{4.18}$$

where, g is gravity, β is the air expansion coefficient, ΔT is the temperature difference between the ground surface and a reference height above ground surface, and Pr is the Prandtl number. In our calculation, the ground surface temperature was measured at a few centimeters below the ground surface. Because of the strong insulation of snow cover it will be invalid when the snow cover occurs.

For a flat and horizontal surface, the Nusselt number of three types of convective heat transfer is given as

$$Nu = \begin{cases} 0.14Ra^{1/3} & (\text{free convention} : Ra > 16Re^2) \\ 0.032Re^{0.8} & (\text{forced convection} : Ra < 0.1Re^2) \\ 0.14Ra^{1/3} + 0.032Re^{0.8} & (\text{mixed convection} : 16Re^2 > Ra > 0.1Re^2). \end{cases} \tag{4.19}$$

At the study sites, the air temperature is measured at 2 m above the ground surface, and the wind speed is measured about 40 cm above the air temperature sensor. At Tianshuihai and Chumaer, the ground surfaces are covered with bare soil and sparse canopy, respectively, and the dipping surface at Qumahe is covered with dense canopy. The parameters ρ and C_p are approximately calculated as a function of specific altitude above sea level and mean annual air temperature [*Ashrae*, 1997] at each site.

Energy balance model The model to quantify the energy balance at the surface of active layers can be formulated with four major components as

$$j_{nr} - j_{vl} - j_h - j_g = 0 \tag{4.20}$$

where, j_{nr}: heat flux of net radiation, j_{vl}: latent heat flux, j_h: surface sensible heat flux, j_g: ground heat flux. j_{nr} is measured directly in the field. j_{vl} is given as

$$j_{vl} = L_{fv}\rho_w j_v. \tag{4.21}$$

where, L_{fv} is latent heat of water from fluid to vapor, and j_v is the vapor flux. j_h is calculated with the Equation 4.16. j_g is estimated with the Equation 4.8, which is based on the measured energy density (E^g) with respect to liquid water at 0℃ (detailed calculation can be found in last section).

In general, the energy balance from time t_0 to t_1 can be written as

$$E^g(t_1) - E^g(t_0) - \int_{t_0}^{t_1} j_{nr}(t)dt - L_{fv}\rho_w \int_{t_0}^{t_1} j_v(t)dt - \int_{t_0}^{t_1} j_h(t)dt = 0. \tag{4.22}$$

Water balance model In the active layer, water mainly exists as fluid and solid phases. Hence, the water balance is defined as the total water content including fluid water and solid water. The areal density of water content Θ_d in the active layer is defined as

$$\Theta_{d(t)} = \sum_{\alpha\in\{w,i\}} \int_0^d \theta_\alpha(z,t)dz. \tag{4.23}$$

The volumetric expansion of water phase change was neglected in the calculation of ice content from the measurements. Therefore, the volumetric ice content was converted to volumetric water content with an equivalent mass of ice. The study of *Wu and Qian* [2003] shows that snow cover usually occurs during winter season on the QTP, and less-snow in the northern and central QTP. Because of the short duration of snow cover and the cold weather, the snow disappearance is mainly attributed to sublimation. The negligible change of water content at the near surface during the snow cover existence indirectly indicates that the infiltration by snow melt is negligible at the study sites. Therefore, the input by snow melt in the water balance model was neglected in the calculation.

The water balance from time t_0 to t_1 in the active layer can be set as

$$\Theta_d(t_1) - \Theta_d(t_0) - \int_{t_0}^{t_1} j_r(t)dt - \int_{t_0}^{t_1} j_v(t)dt = 0. \tag{4.24}$$

Combining with above energy and water balance models, the energy residual from the estimates j_v^E (vapor flux estimated from the energy balance model) and j_v^W (vapor flux estimated from the water balance model)can be given as

$$\begin{aligned} R^E(t_1,t_0) &= \frac{L_{fv}\rho_w}{t_1-t_0}\int_{t_0}^{t_1}[j_v^E(t) - j_v^W(t)]dt \\ &= \frac{1}{t_1-t_0}[E^g(t_1) - E^g(t_0) - \int_{t_0}^{t_1} j_{nr}(t)dt - \int_{t_0}^{t_1} H(0,t)dt] \\ &- \frac{L_{fv}\rho_w}{t_1-t_0}[\Theta_d(t_1) - \Theta_d(t_0) - \int_{t_0}^{t_1} j_r(t)dt], \end{aligned} \tag{4.25}$$

and the residual formed in the water balance can be written as

$$R^W(t_1,t_0) = \frac{R^E(t_1,t_0)}{L_{fv}\rho_w}. \tag{4.26}$$

The integrals were calculated approximately from measured data using the trapezoidal rule. The corresponding material properties used in this study are shown in Table 4.1.

The values of j_v^E and j_v^W are generally negative, which means energy taken out of the surface by vapor flux. In theory, these two values should be equal. However, they are not equal in reality, because of the influences of the accuracy of measurements and their assumptions.

4.3.3 Results and discussions

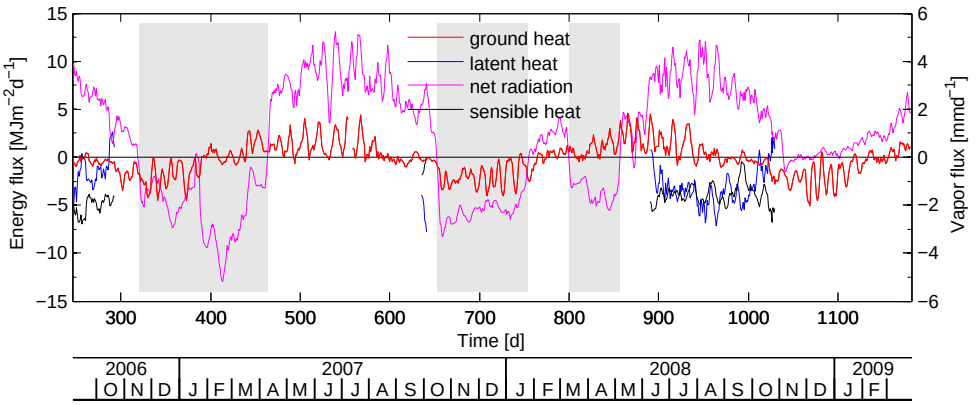

Figure 4.7. Seasonal variations of each components in energy balance model at Chumaer, which are shown as means of 5 days. Note that the gray bars represent deviated data from net radiation.

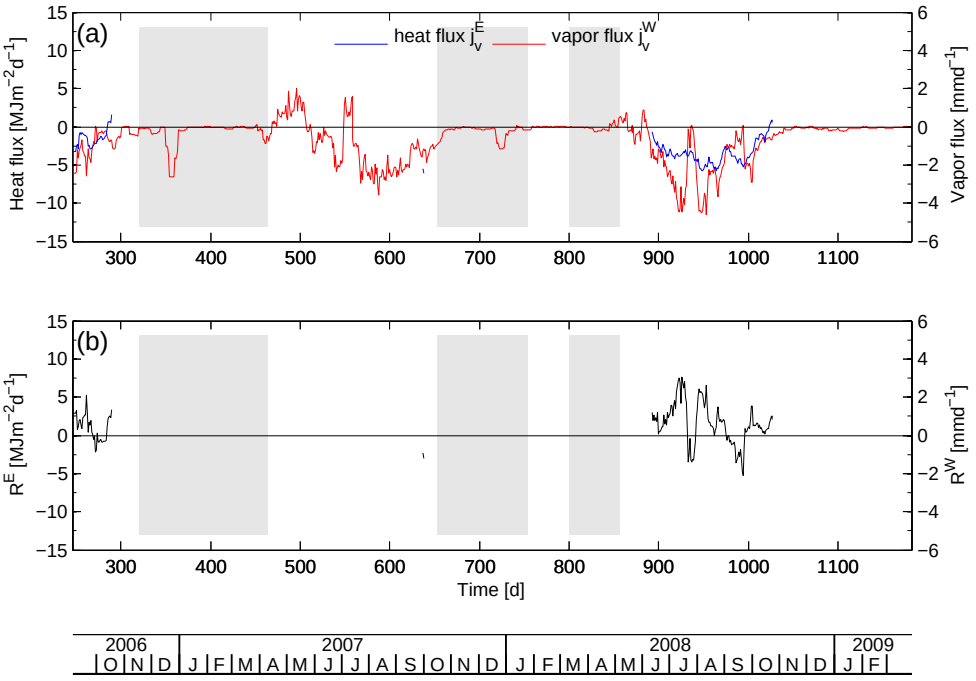

Figure 4.8. The vapor fluxes estimated with the energy and water balance models (a), and the residuals in amount of energy and water R^E, R^W (b) at Chumaer.

The thermal regime at Chumaer Due to the failure of the top sensor in P2, it is difficult to estimate sensible heat flux accurately. Therefore, the characteristics of each components in P1

are presented in Figure 4.7. Due to the deviated net radiation measurements in the gray areas, the estimated vapor flux was seriously distorted during these periods. The ground heat flux was estimated with Equation 4.9, and the peaks and troughs are caused by the interpolation of measured quantities around the thawing or freezing front. Since the ground surface temperature was measured in the soils, there were large deviations in the estimation of the sensible heat flux when snow cover occurred. Therefore, only the sensible heat fluxes estimated during SST periods are presented.

In Figure 4.8a, the vapor fluxes (j_v^E, j_v^W) were estimated from the Equations 4.22 and 4.24, respectively. Generally, $|j_v^E| < |j_v^W|$ in July and August. The residuals R^E and R^W are shown in Figure 4.8b. As a plain sandy surface at Chumaer, the surface runoff should be negligible with the measured precipitation. The large differences in July and August may be attributed to the deviation of the areal density of water content in the shallow layer. Because there were strong infiltrations in the unsaturated soil above groundwater table during this period as shown in Figure 3.6, and the linear interpolation of soil water content may cause significant errors at sharp infiltrating fronts.

In general, the input energy from net radiation were mainly released by sensible heat flux and vapor flux at the surface during SST periods, and they were comparable at this site. The vapor flux is assumed to be negligible at the frozen surface when there are no snow covers. Thus the sensible heat flux is approximately equal to the sum of the output ground heat flux and the net radiation.

The thermal regime at Qumahe The characteristics of the thermal regimes at Qumahe were different from that at Chumaer, although they had similar weather conditions. During SST period, the thermal regime was characterized as continuously downward moving thawing front and weak response to weather change. In the nearly saturated active layer, there was no evident water infiltration. But surface runoff would be expected as the major hydrological processes when there were snow melt or strong rainfalls. Besides, the lateral flow within the active layer may be non-negligible because of the dipping topography of the surface.

In Figure 4.9, net radiation and ground heat flux are presented in whole period, but for the same reason as at Chumaer the surface sensible heat flux and vapor flux are just presented during the SST periods. The ground heat flux was estimated with the Equation 4.8. In Figure 4.10a, the vapor fluxes (j_v^E, j_v^W) were estimated from the Equations 4.22 and 4.24, respectively. Generally, $|j_v^E|$ is much larger than $|j_v^W|$ at the beginning of SST period, but at the end of June $|j_v^E|$ is approximately equal to $|j_v^W|$. The differences between j_v^E and j_v^W may be attributed to the surface runoff by snow melt, which couldn't measured by the instrumentation. During the day numbers 938-942, the large positive peak of residual in Figure 4.10b indicates a large amount of the strong rainfall was lost by surface runoff.

During the periods SST1 and SST2 (days: 466-656 and 830-1000, respectively), most of the input energy from net radiation was released to atmosphere by evapotranspiration and heat convection at the ground surface. The left heat of net radiation was transferred into the subsurface to thaw the frozen soil. Besides, at the beginning of SST periods due to the slope runoff of surface melting water a large amount of net radiation was taken off by the evapotranspiration. While during the middle of SST periods, there was no large change in evapotranspiration, but the slope runoff occurred when there were heavy rainfalls. At the end of SST periods, the surface became dry, and the evapotranspiration also became weaker than before.

The thermal regime at Tianshuihai The characteristics of the thermal regimes at Tianshuihai were different from previous two sites. During SST period, the thawing front moved from surface

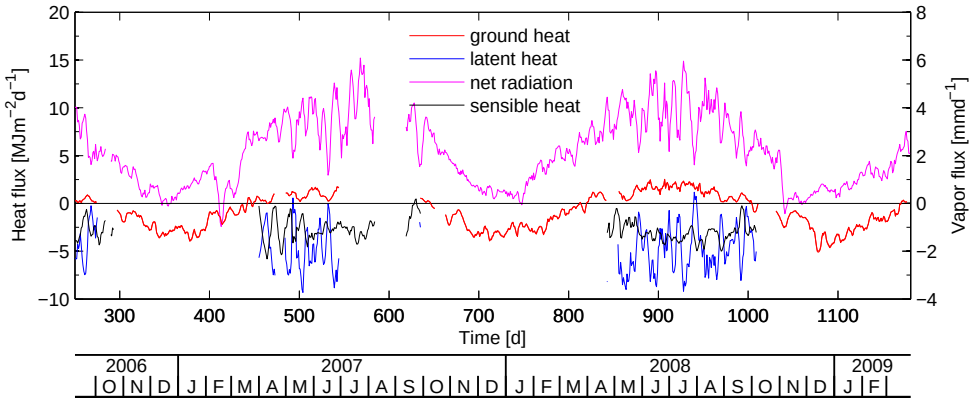

Figure 4.9. Seasonal variations of each components in energy balance model at Qumahe, which are shown as means of 5 days.

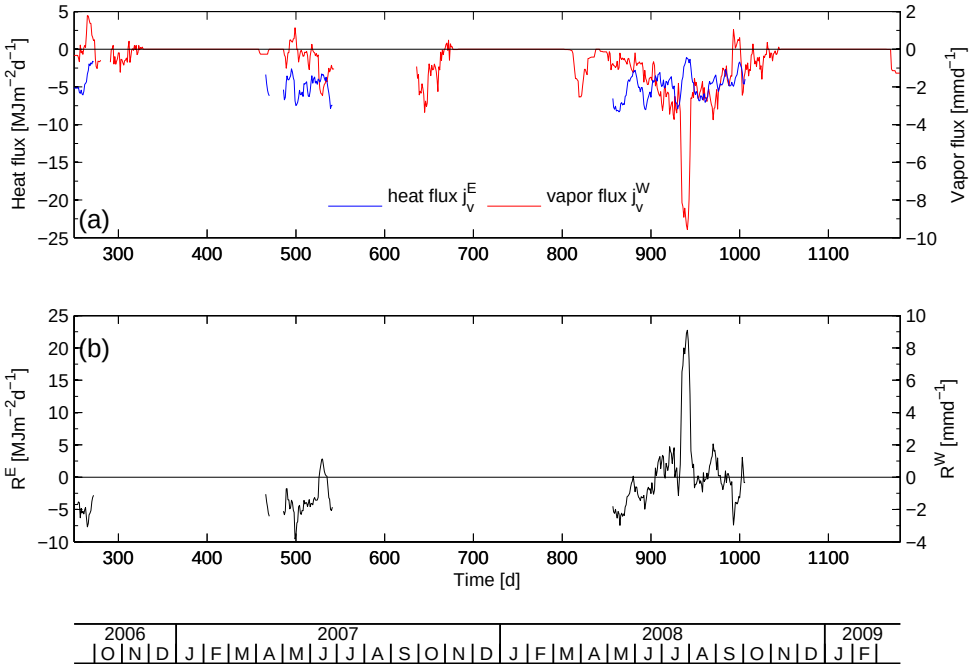

Figure 4.10. The vapor fluxes estimated with the energy and water balance models (a), and the residuals in amount of energy and water R^E, R^W (b) at Qumahe.

to bottom, and it moved faster in the upper part than at the lower part. However, there were almost no clear input water from surface to ground water. During the AF period, the freezing front went down rapidly and smoothly at the initial stage to the high water content zone. Then there was an obvious zero-curtain effect. Below the ground water table, the freezing front slowed down for strong phase change. This period existed 80, 90 and 75 days in 2007, 2008 and 2009, respectively. It was much smaller than the corresponding periods at Chumaer and Qumahe. During the WC period, the major process was heat conduction in the completely frozen profile, and the thermal regime was mainly controlled by the weather.

Since there were not evident snow covers, the sensible heat flux can be estimated for a whole year. In Figure 4.11, it shows the seasonal variations of each component of the energy balance model in P1. The ground heat flux was estimated with the Equation 4.9, and the troughs of

ground heat flux are artifacts by the interpolation of measured soil water content around the thawing or freezing front. In Figure 4.12a, the vapor fluxes (j_v^E, j_v^W) were estimated from the Equations 4.22 and 4.24, respectively. Generally, $|j_v^E| \approx |j_v^W|$. The seasonal characteristics of residuals R^E and R^W are presented in Figure 4.12b. During the period SST1 and SST2 (days: 485-630 and 850-1010), the sensible heat flux accounted for more than 90% of net radiation. The rainfalls during these periods were almost completely evaporated. The large residuals might be resulted from the low resolution of soil water content measurements in the dry active layer, because the soil water change calculated by the linear interpolation may cause significant deviations in the vapor flux. At the same time, the rain gauge would be hard to measure little rainfalls. Therefore, the estimated vapor flux from the energy balance model is more accurate than that from the water balance model.

During the periods AF1, AF2 and AF3 (day number: 270-350, 630-720 and 1010-1185, respectively), large amounts of energy were released from the refreezing soils. The released latent heat was removed by several processes. The colder surface would promote moisture transfer upward, which could take away considerable energy rapidly. During this period, the increasing negative ground flux indicated a faster release of energy from the active layer with a deepening freezing front. Besides, heat energy in the ground was mainly released to atmosphere by surface sensible heat flux, while the vapor flux was negligible. Notice that there occurred decreases of soil water at the beginning of these periods. This may be resulted from the water loss during refreezing. The temperature gradient was much smaller than that during the SST periods, and the role of non-conductive heat transfer during AF periods was more significant. The increasing ground flux may be mainly transported by non-conductive processes such as vapor transport and sublimation. However, the decreasing vapor flux at ground surface indicated that with a deepening freezing front the released latent heat might be transferred to the upper layer by vapor transport and condense at near surface. Therefore, the water loss was decreasing along with the deepening freezing front.

During the periods WC1 (incomplete) and WC2 (days: 720-840), the energy from the frozen soil was further released by heat conduction, but the ground flux was decreasing to zero and turned to positive at the end. Due to no available soil moisture for evaporation, the estimated positive vapor flux from the energy and water balance models should be both close zero.

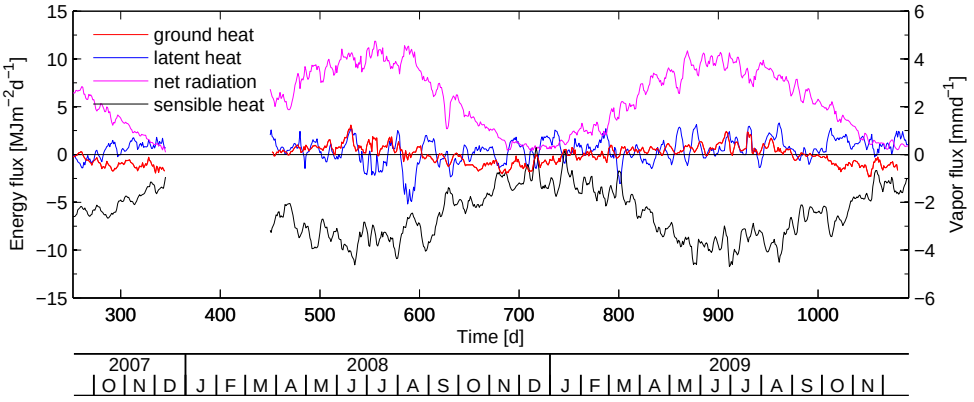

Figure 4.11. Seasonal variations of each components in energy balance model at Tianshuihai, which are shown as means of 5 days.

In general, the input energy from net radiation were mainly released by sensible heat flux at the surface during SST periods. The vapor flux is negligible for the whole year round.

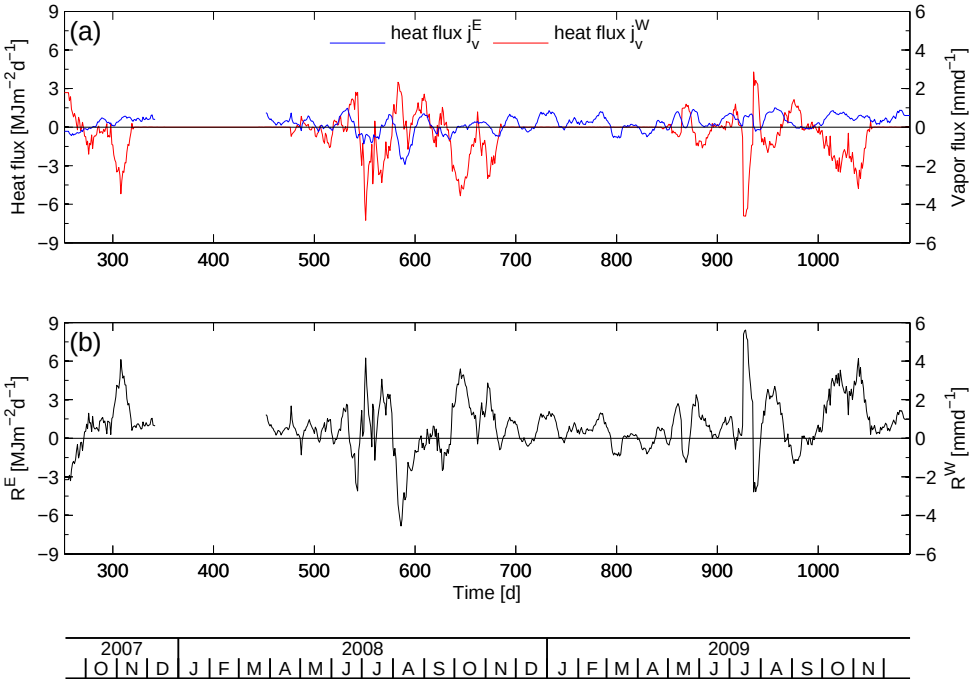

Figure 4.12. The vapor fluxes estimated with the energy and water balance models (a), and the residuals in amount of energy and water R^E, R^W (b) at Tianshuihai.

During AF and WC periods, the sensible heat flux is approximately equal to the sum of the output ground heat flux and the net radiation. The fluctuation of the sensible heat flux at Tianshuihai may be controlled by the local microclimate. Since the topography is characterized for a lake surrounding by high mountains covered with glaciers, the interaction between ground and atmosphere is strongly coupled by local daily wind. The heat exchange by surface convection should be related to the local wind circulation.

Discussion To accurately estimate vapor flux in the energy and water balance models, direct measurements of other components are very important. However, as discussed before, the direct measurements of the sensible heat flux is not so easy in situ. In the energy balance model, the sensible heat flux is usually estimated with the indirect methods. Although the method proposed by *Wang and Bras* [1998] is less sensitive to the error of the eddy diffusivity parameterization than classic approach, the large seasonal variation of the eddy diffusivity limits its application with simplified parameterizations like using empirical constant values. Therefore, the simple method using Nusselt numbers was used in the calculation. There are two major uncertainties in this method. Since there was no true ground surface temperature, the soil temperature at the depth of a few centimeters below the surface was used as ground surface temperature. This may cause a systematic error in the sensible heat flux if there is a significant difference between the true ground surface temperature and the soil temperature below. Another error may come from the characteristic length. In the calculations, it was given as a constant value at all study sites. Because the characteristic length is related to the boundary layer thickness, which is highly variable on the QTP [*Song et al.*, 2006]. However, this is still one of the challenge of the climatology and meteorology study.

Compared with some studies of the surface energy balance on the QTP, the results of the sensible heat flux estimated by the simple method are acceptable at the study sites. Several studies [e.g. *Tanaka et al.*, 2001; *Ma and Ma*, 2006; *Yao et al.*, 2008] on the northeastern

QTP calculate the surface energy balance using directly measured turbulence data and the flux-gradient methods for the estimation of the sensible heat flux. The results in Tanggula region show that the sensible heat flux in spring is higher than those in other seasons [*Yao et al.*, 2008]. The estimated sensible heat flux without snow cover at Chumaer and Qumahe in this region also show the similar seasonal characteristics. On the western QTP, similar measurements were acquired at Gaze and Shiquanhe, and the sensible heat flux was estimated with profile-flux approach [*Li et al.*, 2003]. The results show that the maximum sensible heat fluxes occurred during May to July, and the minimum values occurred in winter. The results of sensible heat flux at Tianshuihai, which is also in the western QTP, demonstrate the similar characteristics.

Applications at the study sites show that the methods used in the analysis can generally quantify the components in the energy and water balance models. The basic characteristics of hydraulic and thermal dynamics have been captured at the study sites. However, limited by the measurements and methods, the evident uncertainties of each component in the energy balance model and the water balance model are still controversial.

The results of GEWEX (Global Energy and Water cycle Experiment) Asian Monsoon Experiment on the Tibetan Plateau and CEOP (Coordinated Enhanced Observing Period) Asia-Australia Monsoon Project (CAMP) on the Tibetan Plateau (CAMP/Tibet) show that the evaporation on the ground surface is dependent on the precipitation which is mainly controlled by the summer monsoon [*Ma et al.*, 2006]. Our results at the study sites on the northeastern QTP are consistent with this conclusion. But the result at Tianshuihai on the western QTP shows monsoon does not play a significant role in the ground surface-atmosphere interaction. In addition, local factors such as the hydrological cycle and topography at Qumahe can also influence the evaporation besides precipitation.

4.4 Summary

To characterize the thermal regimes of the active layers at the study sites, we use the modified energy model and water balance model [*Boike et al.*, 1998] in this study. In the energy balance model, the directly measured component is net radiation, and the ground heat flux, sensible heat flux and latent heat flux were estimated with indirect methods.

Given the existing measurements, the ground heat flux was calculated with the gradient method at two different reference depths. The ShalRef approach just needs two probes for temperature measurements around the shallow reference depth and one or more probes for soil water content measurements above the reference depth. The DeepRef approach is a stable way to calculate the ground heat flux with intensive instrumentation. The reference depth is usually set at the bottom of the active layer, and the ground heat flux downward to the permafrost below is assumed to be negligible.

The results from our study sites show that the ShalRef approach generally works better than the DeepRef approach. Because of the instrumentation problem, the assumption of negligible ground heat flux at the bottom of the active layer in the DeepRef approach is problematic for the long duration of complete frozen active layer such as Qumahe and Tianshuihai. The deepest sensor should be installed ever deeper. In addition, another problem is the interpolation of soil water contents, which make large artificial peaks in the ground heat flux. The ShalRef approach works well with a proper reference depth. One advantage of this method is that it includes partly of the non-conductive effects at the shallow reference depth and without considering the complicate non-conductive processes below this depth. But one problem is the estimate of thermal conductivity during the zero-curtain period, for instance at Qumahe.

Therefore, we should give consideration to the instrumentation for measuring ground heat flux and corresponding method in practical application.

Due to the limited meteorological measurements, the sensible heat flux was estimated with an empirical method using Nusselt numbers. The latent heat flux was estimated with the energy balance model and the water balance model. From the applications at the study sites we found that given current accuracies of the methods for each components, the energy balance model can generally capture the major processes in the calculated periods.

With the above method, the thermal regime of the three different active layers were investigated. In the warm permafrost regions, the thick active layer at Chumaer was filled with large amount of groundwater at the lower part of the profile. While the active layer is characterized as wet and thin at Qumahe. Tianshuihai site is located in the cold permafrost region, the active layer is very dry. Due to the limitations of the methods, the thermal regimes were only characterized during the summers at Chumaer and Qumahe, but the year-round features of the thermal regime were captured at Tianshuihai for the excellent applying condition. Their characteristics are summarized as follows.

At Chumaer, the thermal regime of the active layer during the SST period is mainly controlled by the net radiation, sensible heat flux and vapor flux at the surface. The net ground heat flux in a freeze-thaw cycle of 2008 is positive, which is apparently at a strong degrading condition during the measured period. The fraction of latent heat in the active layer was around 70%. The sensible heat flux and vapor flux at the surface are comparable, but the latent heat flux is mainly dependent on the precipitation. During the AF and WC periods, sensible flux and occasional snowfalls control the thermal regime.

At Qumahe, the thermal regime of the active layer during the SST period is similar to that at Chumaer. But the net ground heat flux in a freeze-thaw cycle of 2008 is negative and the vapor flux is stronger than that at Chumaer. Due to the wet active layer and surface runoff, evaporation plays a significant role in preventing warming the active layer. Due to the high water content in the saturated active layer at Qumahe, the latent heat dominates the ground heat, which is over 90%. During the AF and WC periods, the factors controlling the thermal regime are almost the same as at Chumaer.

At Tianshuihai, the thermal regime of the active layer is completely different from the above two sites. The net ground heat flux in a freeze-thaw cycle of 2008 is negative, and the fraction of latent heat in the active layer was only 60%. The surface sensible heat flux is much stronger than those at other sites during the SST period. Due to the dry ground with little precipitation, actual evaporation is negligible at this site. But during the AF and WC periods, the sensible heat flux is reduced and comparable with the other sites. The strong sensible heat flux during the SST period may be related to the local microclimate.

In general, the mechanisms of the thermal regime at Chumaer and Qumahe are controlled by regional factors like the monsoon. While, the mechanisms of the thermal regime at Tianshuihai is controlled by local factors like wind. Since the mechanisms are different these different permafrost sites, their sensitivity to the climate warming can not be the same. Therefore, to predict permafrost degradation accurately, we must consider the different physical processes in the permafrost modelling.

5
Monitoring field-scale soil water dynamics with multi-channel GPR

5.1 Introduction

Water is a fundamental constituent of life on the Earth. It is indispensable for human and other organisms. Like energy, water has become the most critical resource in the world. Water management and associated researches are more and more important. Particularly, the quantity of water in soils is one of the key factors for monitoring the hydrological cycle. Based on the relations between the physical properties and water content in a porous material, many new techniques have been used to measure soil water content in soils.

Soil water is a key variable for understanding the hydrological processes in the vadose zone. Along with the advance of technology in the last century, the accuracy of the measurement of the electrical properties of materials is much better than before. It facilitates the accurate measurement of the dielectric permittivity of a porous material related to water content. For the close relationship between the measured bulk permittivity and the volumetric water content, a variety of electromagnetic methods like TDR, Ground-penetrating radar (GPR) and remote sensing have been used to measure soil water content. At the point-scale, soil water dynamics can be monitored accurately by time domain reflectometry (TDR) with high temporal resolution [*Laurent et al.*, 2005]. But its limitations are invasive and governed with high cost for large scale applications. Due to the non-invasiveness and large scale applicability of GPR, it is widely used to measure soil water content at the field scale. The GPR ground wave method has been used to measure the spatial variability of soil water content in several studies [e.g. *Huisman et al.*, 2001; *Grote et al.*, 2003; *Galagedara et al.*, 2003; *Huisman et al.*, 2003*b*]. However, the measured depth of the ground wave method is unknown so far. Although the bore-hole GPR is also often used to monitor soil water dynamics, its spatial resolution is impacted by the bore-hole separation distance [*Huisman et al.*, 2003*a*]. With the same lateral resolution as the GPR ground wave method but greater depths, the GPR reflection method is a promising method to monitor near-surface soil water dynamics over large areas. Recent case studies have shown that this method has the potential to measure soil water content at the field scale [e.g. *Garambois et al.*, 2002; *Gerhards et al.*, 2008; *Bradford*, 2008]. Besides, it also has been attempted to monitor temporal soil water content variations with known reflector depths in the field [e.g. *Lunt et al.*, 2005; *Wollschläger and Roth*, 2005]. However, because of depending on the reflector depth from boreholes or soil profiles, these methods are difficult to meet practical requirements for field-scale applications.

The spatial heterogeneity of the soil water content usually results from variations in soil texture, land use, and surface cover. With GPR ground wave measurements, *Huisman et al.* [2003*b*] found that the variation of soil water content was larger than 6% at a short distance and the development of spatial water content variation in time can also be accurately monitored with GPR. With GPR reflection method, *Loeffler and Bano* [2004] reported a measured soil water content range from 6% to 44.9% derived with the CRIM model in a sand box. Besides, combing

boreholes and the GPR reflection method *Lunt et al.* [2005] found the soil water content varied in a large range from the dry season to the wet season. But the applicability of GPR to monitor soil water dynamics at the field scale has not been reported so far.

As a new method, multi-channel GPR can continuously and simultaneously measure reflector depth and mean soil water content [*Gerhards et al.*, 2008]. It supports a possibility to get field-scale data with high quality for hydrological modeling or remote sensing studies, but its applicability needs further tests. In the study by *Gerhards et al.* [2008], the calculation of absolute travel times has some uncertainties because of interferences from near-field effects, ground wave and instruments. This problem was reduced by air wave adaption. The main uncertainty of the soil water content in the study by *Gerhards et al.* [2008] stems from the air wave adaption.

In this chapter, the applicability of multi-channel GPR to monitor field-scale soil water dynamics was assessed at a test site with sandy layered soils. The objectives were: (1) to investigate the accuracy of the multi-channel GPR; (2) to test the feasibility of the multi-channel GPR method to monitor field-scale soil water dynamics.

5.2 Theoretical background of multi-channel GPR

5.2.1 Principles of electromagnetic wave propagation

The material properties control the behavior of electromagnetic energy in a porous media. These are dielectric permittivity ε, electrical conductivity σ and magnetic permeability μ. When an alternating electric field is applied to a material, polarization processes undergo and influence the electric field energy. The energy stored during the polarization processes determines the real dielectric permittivity at that frequency. In addition, a small amount of energy is lost due to molecular relaxation. The electrical conductivity determines the imaginary components of the dielectric permittivity at that frequency. The dielectric permittivity with real and imaginary parts is used to measure the ability of a material to store electrical charge. For convenience, the dielectric permittivity is written as

$$\varepsilon_r = \frac{\varepsilon}{\varepsilon_0} \tag{5.1}$$

where, the relative permittivity ε_r is given as the ratio of the permittivity of the material to the free space permittivity ε_0. The complex relative permittivity ε_r^* representing energy storage and energy loss is given by [*Robinson et al.*, 2003]

$$\varepsilon_r^* = \varepsilon_r^{'} - j(\varepsilon_r^{''} + \frac{\sigma}{2\pi f \varepsilon_0}) \tag{5.2}$$

The real part of the relative dielectric permittivity $\varepsilon_r^{'}$ is associated with energy storage for the polarization processes, and the imaginary parts are associated with energy losses for the molecular relaxation $\varepsilon_r^{''}$ and electrical conductivity σ, in which f is the frequency of the electromagnetic field.

The velocity of an electromagnetic wave in the medium depends on the material electromagnetic properties. Its mathematical form is given by [*Huisman et al.*, 2003a]

$$v = \frac{c_0}{\sqrt{\varepsilon_r^{'}\mu_r \frac{1 + \sqrt{1 + (\varepsilon_r^{''} + \frac{\sigma}{2\pi f \varepsilon_0})^2}}{2}}} \tag{5.3}$$

where, c_0 is the free space electromagnetic wave velocity (3×10^8 ms^{-1}), μ_r is the relative magnetic permeability of the medium.

The above review of electromagnetic wave propagation shows that the frequency of the applied electric field impacts the velocity. Since the frequency of the applied electric field changes the dissipated energy and stored energy through the charge movements, the frequency used in the electromagnetic methods for measuring soil water content has to be considered. At low frequencies, the responses of the electric field result in maximum energy storage and minimum energy loss [*Neal*, 2004]. At high frequencies, the responses of the electric field result in charge storage proportional to the distance moved and a proportionally small energy loss through dissipation [*Neal*, 2004]. At intermediate frequencies, the responses of the electric field result in maximum energy loss and an averaged energy storage between the values at low and high frequency limits [*Neal*, 2004]. In addition, the energy loss by conduction is also dependent on frequency. There is a transition frequency for typical earth materials [*Neal*, 2004]. Below the low-frequency limit, energy losses are larger than the energy stored by polarization processes. Above this limit, the energy losses due to conduction are approximately independent of frequency. But for high-frequency propagation, it limited by scattering losses. Most GPR measurements work within a frequency range of 10 MHz to 1 GHz, and the influence of relaxation of permittivity in this range is very small [*Huisman et al.*, 2003a]. Therefore, for low-loss and nonmagnetic materials, Equation 5.3 can be simplified to:

$$v = \frac{c_0}{\sqrt{\varepsilon_r'}} \tag{5.4}$$

5.2.2 Relationship between soil water content and permittivity

We envisage soil as a three-component system, consisting of the soil matrix, a gaseous phase and the liquid water phase. The relative dielectric permittivity of air is 1, and those for common minerals in soils are smaller than 10 [e.g. *Davis and Annan*, 1989; *Robinson et al.*, 2003]. While the real part of the permittivity of water is about 80. This large contrast in permittivity is the base of the electromagnetic methods for measuring soil water content.

The effective dielectric permittivity of a soil mainly depends on the components, particularly soil water content plays an crucial role. Variations in soil water content can dominate changes in the effective dielectric permittivity of the soils. A widely used relationship between effective permittivity and volumetric water content was proposed by *Topp et al.* [1980]. It was determined empirically from a variety of soils. Another theoretical approach was based on the relationship between the volume fractions and the relative dielectric permittivity of the soil constituents [*Dobson et al.*, 1985; *Roth et al.*, 1990]. In this model, the relationship between ϵ_c and the volumetric soil water content θ [-] is estimated based on the Complex Refractive Index Method (CRIM). For a three-phase medium, the following equation is usually used to quantify the relation among ϵ_c, volumetric water content θ, porosity ϕ, and the relative dielectric permittivities ϵ_w [-], ϵ_a [-], ϵ_s [-] of water, air and soil matrix,

$$\sqrt{\epsilon_c} = \theta\sqrt{\epsilon_w} + [1-\phi]\sqrt{\epsilon_s} + [\phi-\theta]\sqrt{\epsilon_a}. \tag{5.5}$$

It is important to notice that the above proposed relationships between soil water content and permittivity are obtained from point measurements. It is reasonable to neglect the influences of the soil structure within the measured scale. However, GPR is usually used at the field scale, and the scale effects of the permittivity-water content relationships should be considered. The study by *Chan and Knight* [1999] with laboratory measurements show that the layered structure caused

significant errors in the soil water content estimation. According to the modelling of field-scale relationships between soil water content and permittivity in heterogeneous system, *Moysey and Knight* [2004] pointed out that the importance of scale effects are strongly dependent on the heterogeneity of soil water content in the soils. In the multi-channel GPR evaluation, the CRIM model was used to evaluate the soil water content presuming the soil to be a homogeneous medium and neglecting structural effects on soil water content.

5.2.3 The multi-channel GPR method

GPR is a widely used geophysical method for exploring subsurface information with extremely high resolution. The basic GPR usually includes a transmitter, which can radiate short pulses of high-frequency electromagnetic waves, and a receiver, which records the signal from the transmitter. More detailed information about the instrument can be found in the studies [e.g. *Gerhards*, 2008; *Slob et al.*, 2010]. For the GPR reflection method, its principles involved are similar to seismic reflection. But the reflections appear at boundaries with contrasts in dielectric permittivities instead of acoustic impedances. When the electromagnetic wave encounters a significant discontinuity with respect to the material electrical properties (ε_r, μ_r or σ), some energy is reflected, and its amount depends on the contrasts of the properties.

For the surface-based GPR, the electromagnetic waves along different propagation paths include air wave, ground wave, reflected wave and refracted wave. All of these waves have been investigated to measure soil water content. Soil water content estimation using reflected waves is used here. Based on the traditional common midpoint (CMP) method, *Gerhards et al.* [2008] proposed a multi-channel GPR technique to simultaneously measure soil water content and reflector geometry. It uses a series of GPR antennas with different antenna separations to acquire the information of the ground. This study is based on their work and the aim is to further explore the possible applications of multichannel GPR.

5.3 Optimization of multi-channel GPR to measure spatial variation of soil permittivity

5.3.1 The algorithm of multi-channel GPR evaluation

In this chapter, evaluation of relative dielectric permittivity and reflector depth was done by applying the multi-channel evaluation procedure of [*Gerhards et al.*, 2008] except the air wave adaption. In this method, the basic travel time model is given as

$$t(x,a) = \frac{\sqrt{\epsilon_c}}{c_0} \cos\alpha \sqrt{4d^2 + a^2}\,, \tag{5.6}$$

where ϵ_c [-] is the relative dielectric permittivity of the soil, c_0 is the speed of light in vacuum (0.3 m ns^{-1}), α is the angle of the incline of the reflector, and d [m] represents the reflector depth beneath the measured position x. The parameters (ϵ_c, d, α) at every position are determined with all the travel times from multi-channel radargrams. It is solved as a minimization problem using N measured points and K antenna separations, and the cost function is given as

$$C(\epsilon_c, d, \alpha) = \sum_{(n,k)}^{(N,K)} \left(t_{refl}(x_n, a_k) - t_{model}(x_n, a_k)\right)^2 . \tag{5.7}$$

where $C(\epsilon_c, d, \alpha)$ is the missfit between the model and data, t_{refl} [ns] and t_{model} [ns] are the measured and modeled reflected wave travel times for N measurements around x_0 obtained from K antenna separations, x_n (n = 1, ..., N) are measurement points around x_0, and a_k (k = 1, ..., K) are the antenna separations. For the minimization of equation 5.7, the Gauss-Newton method is used here.

5.3.2 Monte Carlo uncertainty analysis of multi-channel GPR method

From the above algorithm of the multi-channel GPR evaluation, we see that there are $N \times K$ input quantities with different uncertainties and three output quantities. Besides, the parameter estimation of the cost function will yield certain errors. To investigate the accuracy of this method, it is very important to understand its uncertainty propagation. For this kind of non-linear problem Monte Carlo simulation is a straight forward method to calculate total uncertainty in the output variables [*Fishman*, 1996].

Means and variances of the input variables are required for the Monte Carlo simulation. There are two kinds of variables, one is the travel time, whose error mainly comes from time resolution of sampling, preprocessing, and reflection picking; the other one is antenna separation, whose error mainly comes from measuring due to ground surface roughness, and lateral resolution of measurement distance. Although there is some correlation between the errors from antenna separation and travel time, the error of the antenna separation measurement is usually very small. Therefore, they are set as independent variables which are normally distributed. The procedure of Monte Carlo uncertainty analysis is shown in Figure 5.1. From this analysis, the values of output quantities like reflector depth, soil permittivity and the angle of the incline and their errors, and also the covariance between variables can be calculated.

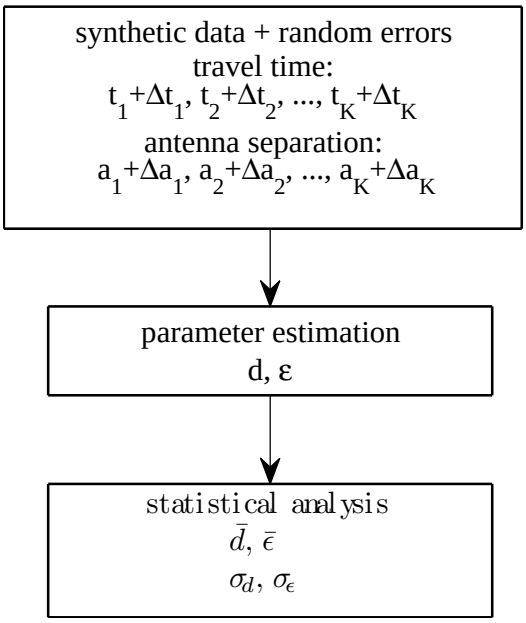

Figure 5.1. Flow chart for assessing the accuracy of the multi-channel GPR method with Monte Carlo simulations.

Here the instruments include three shielded antennas with a central frequency of 200 MHz (TR 200 K2) and a DAD K2-MCH control unit, manufactured by IDS (Ingegneria dei Sistemi S.p.A., Italy), composed as a multi-channel GPR system. A schematic diagram of the multi-channel

GPR used in our measurements is shown in Figure 5.2. All antennas are arranged in tandem with a rope. The following accuracy analysis and field measurements are all based on this GPR system. In the measurements, the air WARR data were used to calibrate the time-zero, which prevents the interference with the ground wave. Therefore, due to the relatively accurate time-zero calibration, the air wave adaption was not used in the evaluation. The zero-times of the six channels outside the antenna boxes can be determined, while two channels within the antenna boxes 2 and 3 (Figure 5.2), remain fixed in the box. The absolute travel times of these two channels can be calculated by directly picking the air wave in the air WARR measurements.

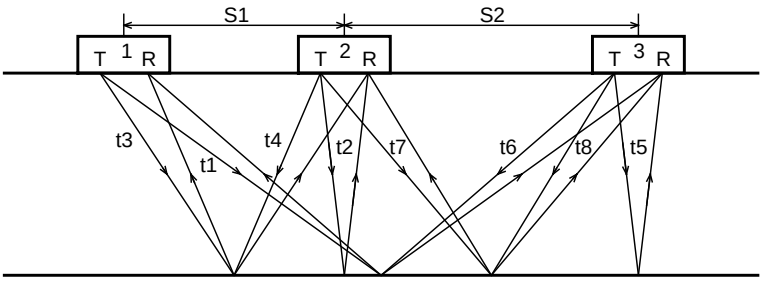

Figure 5.2. The setup of the multi-channel GPR system and the travel times of its eight travel paths.

5.3.3 Accuracy assessment of multi-channel GPR: synthetic example

There are several factors controlling the accuracy of multi-channel GPR method. GPR itself such as frequency, time resolution of sampling and lateral resolution has certain precision, these factors can affect the accuracy of measurements. Besides, errors from time-zero calibration and data processing such as picking and parameter estimation can also affect the final results of the multi-channel GPR method. In the following studies, all above measurement errors are assumed to be reduced as small as possible, and these errors in travel time are simplified as one value. The aim is to optimize the multi-channel GPR measurements through analyzing the error propagation in the multi-channel GPR evaluation.

In order to find the optimal setup for the antenna separations for various permittivity–reflector depth combinations we conducted Monte Carlo simulations [*Fishman*, 1996] to estimate the total uncertainty of the output parameters. The procedure of the Monte Carlo analysis is shown in Figure 5.1. The travel times of the reflected waves for each antenna separation of the 8-channel GPR array were calculated using a ray approach. To address the study problems, we assume a flat lying reflector with a depth of 2 m, which limits the issue of the angle of incline α. According to the typical range of dielectric permittivities of sand given by *Daniels* [2004] (measured at 100 MHz), the range of soil dielectric permittivities was set from 3.5 to 35.5, and the range of space S2 was set from 0.4 m to 4 m while space S1 was adapted for each realization to keep the ratio S1 : S2 = 3 : 5. In accordance to the field measurements discussed below, the temporal resolution of the calculated travel times was set to 0.156 ns.

In the Monte Carlo simulations we assumed normal distributed errors in travel times and antenna separations. The polar method from *Marsaglia and Bray* [1964] is applied to generate normal variates. Due to the non-determined time-zero from the GPR instrument, we apply air WARR measurements to determine the zero-offset. However, its accuracy is still hard to validate, which is beyond the scope of this study. The random error in travel time was set as mean 0 ns and standard deviations 0.5-1.0 ns. The antenna separation error for each channel was set as mean 0 m and standard deviation 0.03 m.

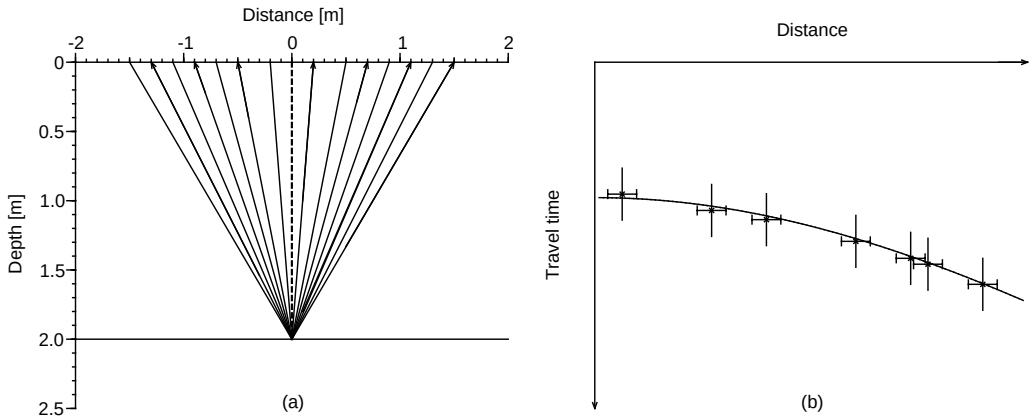

Figure 5.3. The reflector model for Monte Carlo simulations, (a) CMP paths from the eight channels of multi-channel GPR, (b) hyperbola fit in multi-channel GPR evaluation.

In practical application of the multi-channel GPR, the user is often beset by two situations in accuracy. One is how to choose antenna separation, and another one is how does the chosen antenna separation influence the accuracy at different conditions such as changing soil water contents. Therefore, given a reasonable travel-time error level (standard deviation 0.5 ns), we take the 2-m reflector model and simulate the influences of antenna separation and soil dielectric permittivity to the accuracy of multi-channel GPR evaluation at these two different measure conditions in the Monte Carlo simulations. For each simulated condition, the mean values of the estimated reflector depth d', soil dielectric permittivity ϵ_r' and their standard deviations $\sigma_{d'}$ and $\sigma_{\epsilon_r'}$ in the 20,000 trials are calculated respectively. For the first case, we simulate the conditions with a constant soil dielectric permittivity $\epsilon_r = 12.5$ and a varying antenna setup (represented by the maximum antenna separation a_{max}). As shown in Figure 5.4 (1) and (2), $d' - d$, $\sigma_{d'}$, $\epsilon_r' - \epsilon_r$ and $\sigma_{\epsilon_r'}$ are all reducing significantly by increasing the antenna separation at the beginning and nearly constant at the end. But there is a peak in $\epsilon_r' - \epsilon_r$ within the simulated range. For the second case, we use a constant antenna separation setup $a_{max} = 3.39$ m and a varying soil dielectric permittivity. In Figure 5.4 (3) and (4), $d' - d$ and $\sigma_{d'}$ also decrease but much smaller than the first case. $\epsilon_r' - \epsilon_r$ and $\sigma_{\epsilon_r'}$ change differently with varying soil dielectric permittivity. The error in ϵ_r' increases with soil dielectric permittivity, while the error in d' decreases. The same trend is in the variations of the standard deviations.

From the above two simulated cases, we can find that characteristics of the error propagation in the multi-channel GPR algorithm. Under the condition of operational errors and current GPR instrument, it is very important to improve the accuracy of the multi-channel GPR method by choosing proper setup according the measure conditions. For a general use, here we explored the accuracy of all the simulated conditions within the same range of the soil dielectric permittivity and the space S2 as the above two cases. To avoid to the effect of the reflector scale, the ratio of antenna separation to depth was used here. In addition, due to the unknown uncertainty in travel time, it was set as mean 0 ns and two different standard deviations 0.5 ns and 1.0 ns.

As shown in Figure 5.4, the standard deviations of the estimated reflector depth and soil dielectric permittivity are much larger than their respective absolute errors. Hence, only $\sigma_{d'}$ and $\sigma_{\epsilon_r'}$ are presented in Figure 5.5. These contour plots show the influences of the multi-channel GPR antenna separation and the measure conditions. In Figure 5.5, the standard deviation of the estimated reflector depth $\sigma_{d'}$ decreases significantly with increasing a_{max}/d, and ϵ_r, no matter how large the given random error in travel time is. But the absolute error of

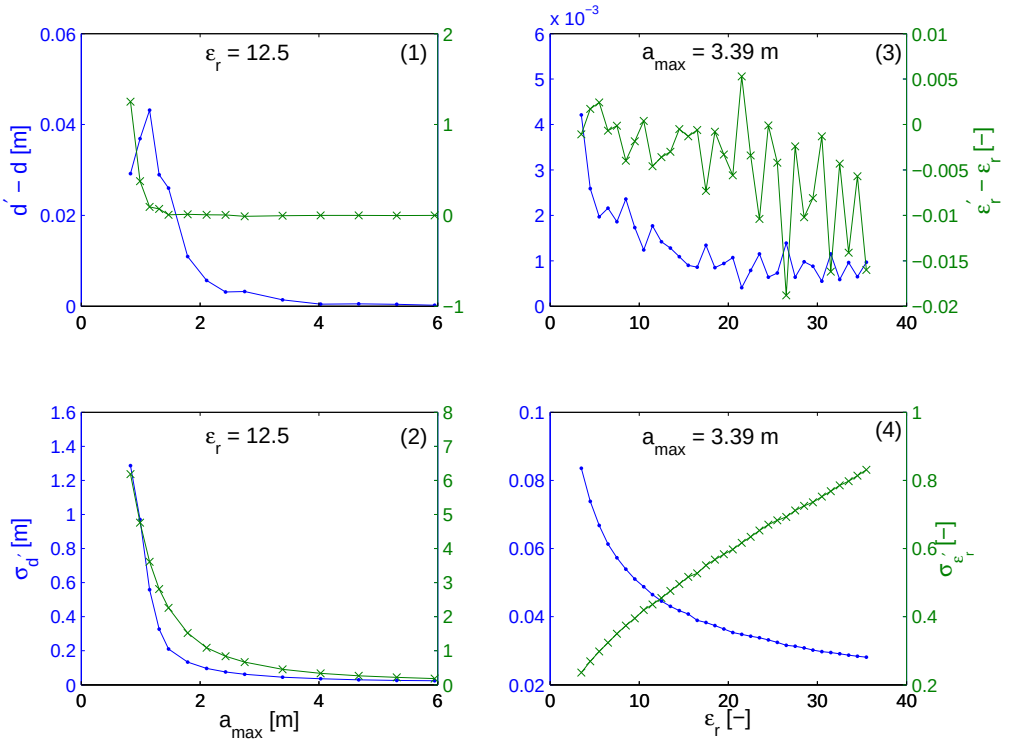

Figure 5.4. The influences of antenna separation and soil dielectric permittivity to the accuracy of multi-channel GPR evaluation at two different measure conditions in Monte Carlo simulations. (1) and (2): a constant soil dielectric permittivity but changing the antenna separation. (3) and (4): a constant antenna separation setup but changing the soil dielectric permittivity. d, d' and $\sigma_{d'}$: the real reflector depth, the estimated reflector depth and the standard deviation, respectively. ϵ_r, ϵ'_r and $\sigma_{\epsilon'_r}$: the real soil dielectric permittivity, the estimated soil dielectric permittivity and the standard deviation, respectively.

the estimated soil dielectric permittivity ϵ'_r increases with the ϵ_r, this is because of the different sensitivity of d' and ϵ_r in the error propagation. As shown in Equation 5.6, the order of the soil dielectric permittivity is a square of the reflector depth. Therefore, the accuracy of the multi-channel GPR is more sensitive to the a_{max}/d than the ϵ'_r. When the error of the soil dielectric permittivity was converted into a relative error, we found that the relative error of the estimated soil dielectric permittivity decreases with the a_{max}/d and ϵ_r. It indicates that with the same antenna separation the absolute error in the ϵ'_r for the wet soil is larger than that for the dry soil, although the relative error is smaller for the wet soil. In practical application, to keep comparable accuracy when measuring different soils, we should change the antenna separation to reduce the influence of the varying soil dielectric permittivity on the accuracy.

The effective soil dielectric permittivity mainly depends on the components, particularly soil moisture plays an crucial role. Variation of soil moisture can dominate changes in the effective dielectric permittivity of soil. In the multi-channel GPR method, the measured soil dielectric permittivity is thought as a mean value of the whole volume of soil between antenna separations. Therefore, the longer the antenna separation is, the larger the measured volume of soil. To reflect the lateral heterogeneity of soil dielectric permittivity, the antenna separation should be as small as possible. However, from above analysis we know the accuracy of multi-channel GPR method is strongly dependent on the antenna separation. Long antenna separations can improve the accuracy, but it is also limited by the attenuation of electromagnetic wave and decrease of signal intensity due to geometrical spreading in soils. Therefore, choosing an optimal

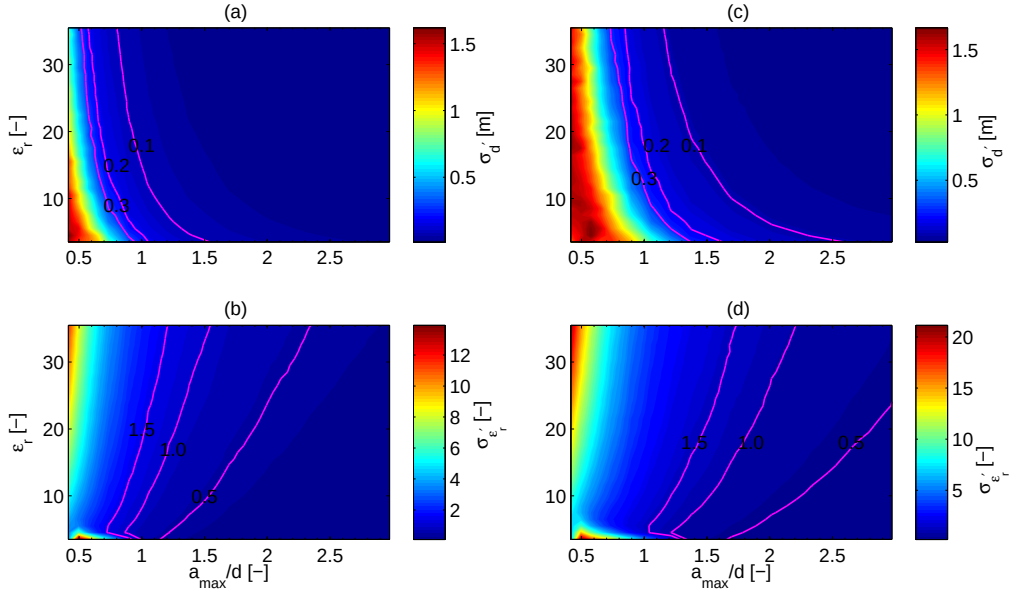

Figure 5.5. The influence of permittivity ϵ'_r and the ratio of the maximum antenna separation to depth a_{max}/d on the accuracy of the multi-channel GPR with two given error levels for travel time in Monte Carlo simulations. a and b are the changes of the standard deviation of the estimated reflector depth $\sigma_{d'}$ and $\sigma_{\epsilon'_r}$ with a standard deviation 0.5 ns in travel time error, respectively; c and d are the changes of the standard deviation of the estimated reflector depth $\sigma_{d'}$ and $\sigma_{\epsilon'_r}$ with a standard deviation 1.0 ns in travel time error, respectively.

antenna separation is very important for multi-channel GPR to measure the spatial and temporal variations of field-scale soil dielectric permittivity.

5.4 Application to field data

5.4.1 Materials and methods

According to the previous analysis, it is necessary to optimize the multi-channel GPR measurement setup. To verify the accuracy analysis and test its feasibility to measure the spatial variation of soil water content, time series of measurements were tested at a site, which is located close to Oftersheim near Heidelberg (49°21´N, 8°37´E), Germany. Sediments at this site are deposited by the flowing water of the Rhine. Ancient dunes which formed during glacial times [*Löscher and Haag*, 1989], can be found in this region. At one borehole, the top layer is brown loamy silt to a depth of 0.25 m. From a depth of 0.25-0.86 m the sediment is a medium sand. From 0.86 to 1.79 m is a coarse sand, which includes gravels (1 cm maximum diameter) close the upper interface. Below this till 2 m is medium sand. During the measurement period, the soil surface was covered with grass.

The surveys took place from July to November, 2008, and were conducted about once a week and twelve times of similar measurements in total. The GPR data were collected by using a time window of 80 ns, 512 samples per scan and 12 stacks per trace, and the trace interval is 0.05 m. All the data were dewowed to remove low frequency signal saturation. In the multi-channel GPR evaluation, the travel times from available channels are analyzed like a small CMP measurement which allows a simultaneous mapping of reflector depth and average water content [*Gerhards et al.*, 2008; *Wollschläger et al.*, 2010].

Radargrams from one measurement in the profile are shown in Figure 5.6. Two distinct reflections indicated by red and blue picks displayed in Figure 5.6 were used to estimate the depths and soil permittivities of two layers. Other small structures were ignored here because of a lack of continuity and visibility in different radargrams. These two reflections were well identifiable at different permittivities, mainly determined by different soil water contents throughout the complete time series. Different antenna separations were applied in these measurements to map the two reflectors. For the first layer, S1 = 1.0 m and S2 = 1.5 m; for the second layer, S1 = 1.2 m and S2 = 2.0 m.

The accuracy of the relative dielectric permittivity can be estimated directly from the multi-channel GPR evaluation. But from the conversion of the relative dielectric permittivity to soil water content it includes several uncertain factors, which depend on the applied model. For instance, the parameters porosity and temperature-dependent dielectric permittivity of water can influence the accuracy of the CRIM model. To get a comprehensive estimation of accuracy of the multi-channel GPR, these factors should be considered in future. However, due to our main objective of assessing the algorithm of multi-channel GPR method, the conversion of relative dielectric permittivity to soil water content is directly used without considering these factors.

To estimate soil water content from permittivity, Equation 5.5 was employed with following parameters: for the sand, $\epsilon_s = 5.0$ [*Davis and Annan*, 1989]; $\epsilon_a = 1$; and $\phi = 0.37$; and $\epsilon_w = 84.0$, corresponding to a temperature of 10 ℃ [*Kaatze*, 1989]. Since from the multichannel GPR evaluation we just calculate the mean volumetric water content of the layer from surface to the reflector depth, the value of the layer between two reflectors $\theta_{int,2}$ can be determined by

$$\theta_{int,2} = \frac{\theta_2 d_2 - \theta_1 d_1}{d_2 - d_1}, \tag{5.8}$$

where, d_1 and θ_1 are the depth from surface to the the first layer bottom, and corresponding mean volumetric water content, respectively, and d_2, θ_2 are the values for the layer from surface to the second layer bottom.

5.4.2 Results

Parameters of reflector depth, permittivity, and the angle of the incline are estimated simultaneously in multi-channel GPR evaluation. Among these parameters, the reflector depth and the angle of the incline are constant in various soil water content conditions, which is convenient to analyze the precision of this method. But measuring the angle of the incline of layer interfaces is impractical. In contrast, the permittivity is a transient variable, which is mainly dependent on the soil water content at the measured time. There is no reliable independent measurement available to directly measure the soil permittivity of a large sample (e.g. 3 m × 2 m) at a given antenna separation. Therefore, only reflector depth is chosen to validate the accuracy of the multi-channel GPR method here.

To check the accuracy of the multi-channel GPR method, a time series of measurements from the same profile was conducted at different soil water content conditions. Since the accuracy of these experiments mainly depends on the antenna separation and soil water content conditions, antenna separations were adjusted to make the errors of depth and soil permittivity smaller than 0.1 m and 0.5, respectively.

Accuracy analysis Figure 5.7a shows the mean and standard deviation of the estimated depths of the upper and lower reflector as calculated for the different dates of the measured time series. The standard deviation of d along the profile is within the range 0.06±0.05 m for the

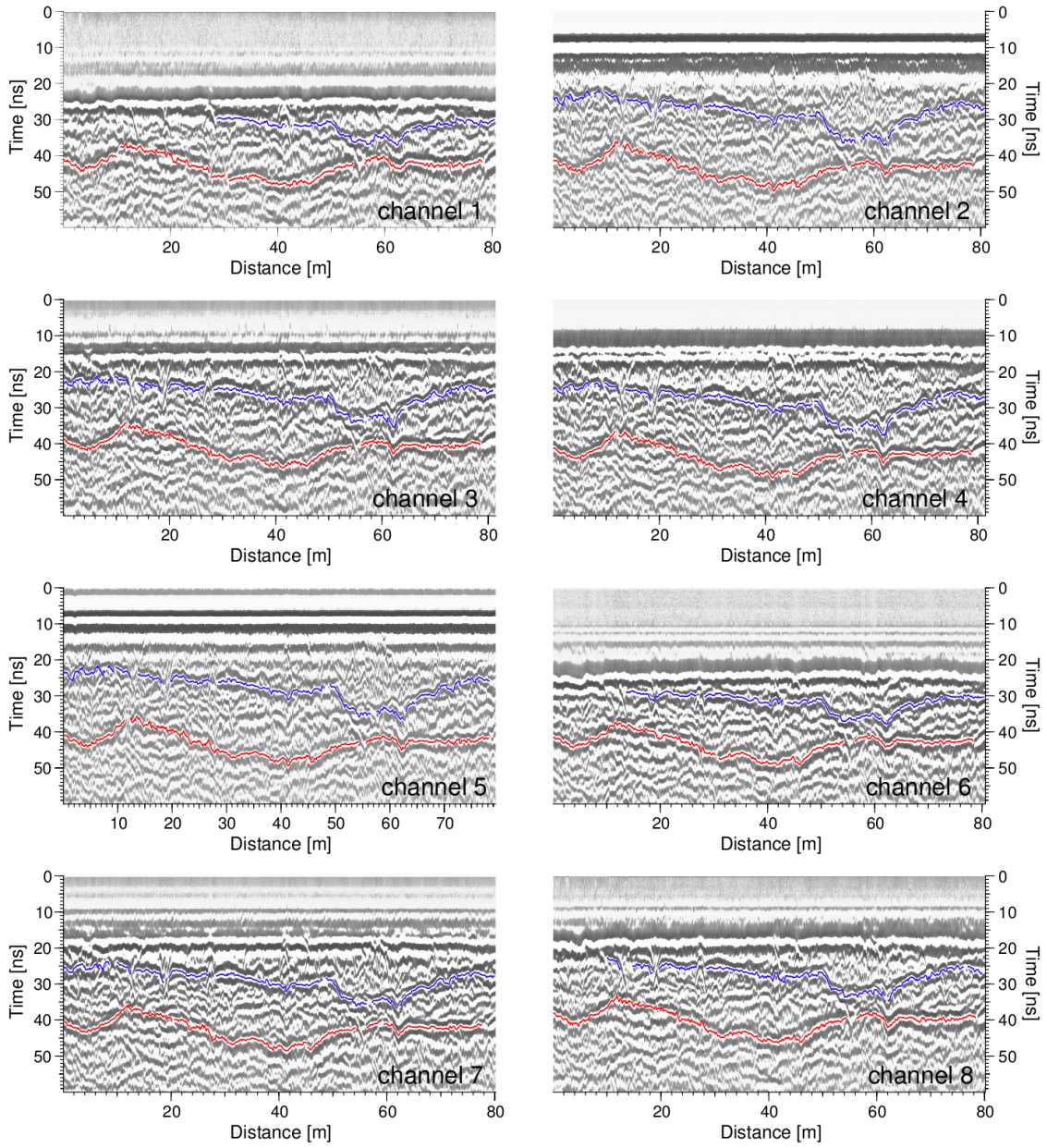

Figure 5.6. Measured radargrams from eight channels for different antenna separations (a1 = 2.69 m, a2 = a5 = 0.19 m, a3 = 1.19 m, a4 = 0.81 m, a6 = 2.31 m, a7 = 2.19 m, a8 = 1.81 m). Blue line and red line are the investigated reflections.

upper reflector and 0.07±0.02 m for the lower reflector which we presume to be acceptable for large-scale measurements of this kind. Generally, this standard deviation is consistent with our accuracy assessment obtained from the Monte Carlo simulations (Sect. 5.3.3) which is 0.06 m for an antenna separation to depth ratio of 1.70 at an average dielectric permittivity of 7 (upper reflector) and 0.07 m for an antenna separation to depth ratio of 1.55 at an average dielectric permittivity of 7.5 (lower reflector) in Figure 5.5a. One noteworthy feature is the larger standard deviation in the depth of the upper reflector in the section between 55 m and 65 m compared to the other parts of the survey line. One possible reason for this may be the smaller ratio of antenna separation to reflector depth in this depression compared to the other sections of

the profile. In addition, in this part of the measurement line the boundaries of both layers are rather close to each other so that we were not able to properly pick the lower reflector in this section of the profile. It is likely that the wavelets from both reflections overlap which may have altered the wavelet of the upper reflector as well. Consequently, the estimated depths may not be reliable along this part of the profile.

As discussed in Sect. 5.3.3, the observed variations in estimated reflector depths may result from uncertainties in travel time estimates, antenna separations and the accuracy of the evaluation algorithm itself. The time series measurements introduce one further uncertainty as they require measurements being located along exactly the same profile. Small lateral shifts of the survey line may consequently lead to slight variations in the estimated reflector depths. We assessed this uncertainty by conducting a cross-covariance analysis for the calculated depths of both reflectors in order to estimate the similarity of the measured structures with respect to the structure of the first measurement date. Figure 5.7b shows the normalized cross-covariances for the depths of both reflections. The estimated distance shifts are less than 0.1 m. Hence, we consider the influence of lateral shifts of the survey line on the estimated reflector depth be small for this survey.

For ground-truth validation of the estimated reflector depths, two boreholes with a maximum depth of 2 m were drilled on the profile line at positions 3 m (b1) and 70 m (b2) (Figure 5.7a). Due to instrument limitations, it was not possible to drill any deeper. Evident transitions at 0.86 m in borehole b1 can be identified. The estimated average reflector depths from the multi-channel GPR surveys at these locations resulted in depths of 0.87 ± 0.05 m, and 1.14 ± 0.02 m. This agrees sufficiently well with the borehole observations.

Measured field-scale soil water dynamics at the test site To account for the accuracy of the multi-channel GPR method and the dynamic range of the field-scale soil water content, the capability of multi-channel GPR method should be noticed. Combining the accuracy analysis of the Monte Carlo simulation and the validation of the reflector depth in our measurements, it can be deduced that the average error of soil permittivity in multi-channel GPR measurements at this test site should be less than 0.5. This error was directly transfered to soil water content without considering the original errors in Equation 5.5. In the following, the measured spatial variation of soil water content at two different conditions based on this accuracy are discussed.

At the test site, the responses of the soil water dynamics to atmospheric forcing were different in depth. The soil water content of the shallow layer was highly influenced by the conditions at the ground surface such as daily fluctuations in evaporation and precipitation. Daily precipitation and lag time of measurements after the rain are the key factors to the amounts of measured soil water content in the sandy area. Two typical measurements at different water content conditions are presented in Figure 5.8. The measurement was conducted after a long drought in Figure 5.8a. The soil water distribution was approximately in equilibrium. The lateral distribution of mean soil water content of the first layer is nearly uniform, while at the most central part of the second layer it was larger than that of the corresponding upper part, and at both ends of the profile it was a little smaller than that of the corresponding upper parts. In Figure 5.8b, the measurement was conducted after a strong precipitation. The variations of soil water content of both layers are obviously different. For example, the mean water contents in the first layer at sections 2-20 m and 69-80.5 m increased by about 3%, while the change in the most central part of the first layer is small. This is mainly because with the same amount of precipitation at the surface, the thicker the layer, the smaller the increase of average soil water content is. Besides, the increase of soil water content in the second layer was much smaller than that of the first layer. Its variation mainly related to the amount of infiltration from the upper layer and the thickness of the second layer. By the way, we should keep in mind that estimated

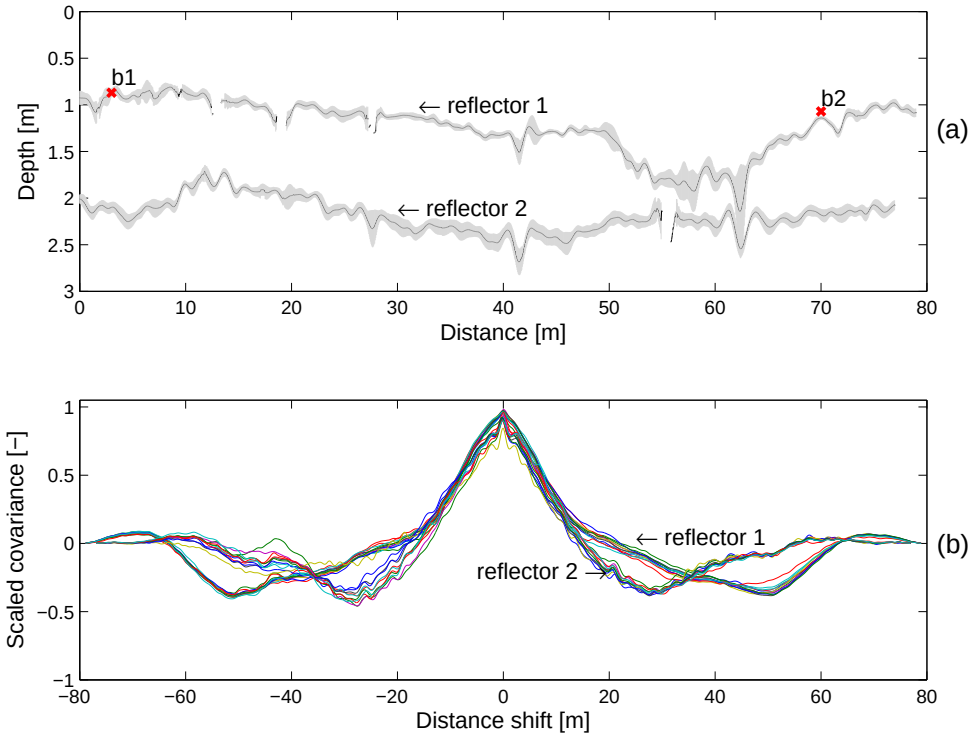

Figure 5.7. The characteristics of the measured reflector depth from a time series of measurements. (a) the mean depth (blue line) and its standard deviation (gray band) from twelve measurements of the upper and lower reflectors in the profile, and boreholes b1 and b2; (b) the normalized cross-covariances of the measured reflector depth from the first measurement and the later measurements. Note that various colors represent the different measure dates.

reflector depth and soil water content in the section from 53 m to 62 m for the first layer are affected by the interference of the lower reflector as well as low accuracy of GPR setup due to the small ratio of antenna separation to the reflector depth.

In general, the mean volumetric water content of both layers is obviously higher than before. In lateral distribution, the mean volumetric water contents at both ends are a slightly higher than those in the corresponding lower parts. While in the most central part of the first layer it is lower than that of corresponding lower part, particularly at the part from 10 m to 25 m it is very low and increases very little.

5.5 Discussion and conclusions

Assuming reasonable errors from current GPR instruments and signal processing, the accuracy of the multi-channel GPR method was explored by Monte Carlo simulation according various measure conditions. We found that the accuracy of the multi-channel GPR method is strongly related to the maximal antenna separation (the minimal one is constant in our case) and soil dielectric permittivity except the uncertainties in the measurements and signal processing. On the one hand increasing the maximal antenna separation can effectively to reduce the error propagation in multi-channel GPR evaluation; on the other hand, the maximum possible antenna separation is limited due to decreasing signal quality and lateral resolution with increasing antenna separation. Optimization of multi-channel GPR setup is essential to the accuracy of

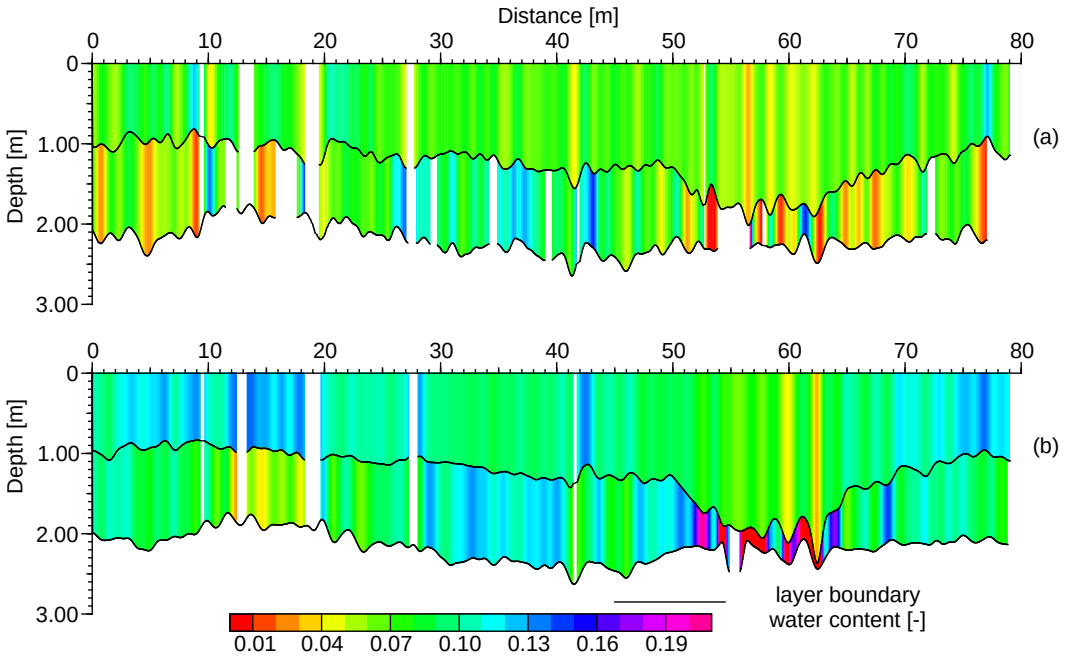

Figure 5.8. The characteristics of soil water content distribution in the profile (a: dry; b: wet). Open areas correspond to nonpickable reflections. Notice that in vertical direction the water content for each layer is just a mean value of that layer measured at one position.

measurements when measuring different reflector depths or varying soil water contents. Due to the evident influences of the assumed uncertainty in travel time, reducing the unknown uncertainty from time-zero calibration would further improve the accuracy of multi-channel GPR method.

Through a time series of measurements in the field, the accuracy of multi-channel GPR was verified with drilling data, and was found consistent with Monte Carlo simulations. Besides, the spatial variation of soil water content of the ground with two reflectors was measured with multi-channel GPR at the test site. The results showed that with a proper setup it is possible to monitor the spatial soil water dynamics in the field.

On account of the accuracy of the multi-channel GPR method and dynamic range of field-scale soil water content, we should choose a suitable setup for different reflector depths and soil water content conditions. For example, the soil water dynamic range is very small in dry regions, and it will be hard to detect the small changes with the multi-channel GPR method. Besides, for deep reflectors, the effects of temporal precipitation may not be detected, because the variations of average water content in the thick layers would be small even when there is a temporally strong rainfall. In practical applications, multi-channel GPR should be accurate enough to identify the soil water dynamics and its lateral sampling also should be as small as possible.

6
Thermal characterization of active layers at the study sites

6.1 Introduction

Permafrost has been identified as one of six cryosheric indicators of global climate change within the international framework of the World Meteorological Organization (WMO) Global Climate Observing System [*Brown et al.*, 2000]. Hence, the climate-permafrost relation is a key scientific question, which includes the effects of the driving force of changing climate, impacts on permafrost hydrology, the influences of greenhouse gases emission like methane, carbon dioxide, and the impacts of local environmental factors on permafrost degradation. Besides, since global warming exerts more and more evident influences on permafrost in cryospheric regions, the environmental consequences of permafrost degradation are one hot topic in permafrost research.

Permafrost modeling is an effective approach to help us to understand the evolution of permafrost with climate change. *Riseborough et al.* [2008] summarized advances in permafrost modeling since the 2003 permafrost conference in Zürich, Switzerland. There are mainly three types of process-based permafrost models, which can be classified by temporal, thermal and spatial criteria. The first type is the transient model (e.g. numerical models). It defines the temporal progression of a ground temperature profile by solving the energy balance at the surface and the heat conduction equation in the subsurface [e.g. *Goodrich*, 1982; *Zhang et al.*, 2003*b*; *Marchenko et al.*, 2008]. The second type is the equilibrium model. It defines the existence of permafrost [e.g. *Carlson*, 1952; *Nelson and Outcalt*, 1987], active layer thickness [e.g. *Kudryavtsev et al.*, 1974; *Lunardini*, 1981; *Romanovsky and Osterkamp*, 1997], permafrost temperature [e.g. *Kudryavtsev et al.*, 1974; *Smith and Riseborough*, 1996], relying on empirical or statistical relations between atmosphere and ground. These two kinds of models both have been implemented in spatial models to simulate and predict the permafrost distribution at various scales [e.g. *Anisimov and Nelson*, 1996; *Anisimov et al.*, 1997; *Zhang et al.*, 2005; *Zhang et al.*, 2006*b*]. However, spatial and temporal variations of the thermal properties of soils in the active layer have significant influences in all models described above.

Riseborough et al. [2008] present a review of recent advances in permafrost modeling. In this work, the authors analyze spatial permafrost models in both Arctic and high mountain environments and its future challenges, and point out that one important direction is parameterizing the effects of sub-grid scale variability in surface processes and properties on small-scale spatial models. Soil thermal conductivity is difficult to estimate in the field, since in addition to volumetric water content it also depends on mineral composition (particularly quartz content), porosity, temperature, depth [*Farouki*, 1981] and ground surface characteristics [*Ikard et al.*, 2009]. In permafrost parameterization literature, commonly used formulations for predicting soil thermal conductivity are semi-empirical methods, which are presented in the comprehensive review of *Farouki* [1986]. In the field, since soil properties can vary from point to point, these semi-empirical or empirical methods can just give a mean value from measured points, and it

requires laboursome work to yield a representative value. Meanwhile, in large scale modeling, these models are quite sensitive to the variations of soil thermal conductivity [*Waelbroeck*, 1993]. Especially for the simplified empirical models, they strongly depend on the thermal properties [*Riseborough et al.*, 2008].

As we know the thermal properties are controlled by several important factors such as soil water content, non-conductive processes, temperature dependence. Therefore, it is necessary to assess the influences of these factors, and find an effective way to improve the parameterization for permafrost modeling. At the field scale, GPR is a promising tool to measure active layer thickness and soil water content in permafrost research [e.g. *Kneisel et al.*, 2008; *Brosten et al.*, 2009; *Wollschläger et al.*, 2010; *Westermann et al.*, 2010]. Multi-channel GPR method has a potential to supply two important parameters: soil water content and thaw depth for permafrost modeling. In this chapter, firstly we characterize the heat transfer in the active layers at the study sites by using the transfer function method. Secondly, a new method of upscaling thermal conductivity is proposed and discussed.

6.2 Characterization of heat transfer in various active layers

Soil heat transfer includes conductive process and intra-porous convective process [*de Silans et al.*, 1996]. Usually, heat conduction process is the dominant one, and the intra-porous convective process is negligible. Therefore, the soil thermal regime is often characterized by heat conduction with temperature boundary conditions, and soil thermal diffusivity is considered as an apparent value. It is controlled by several factors. In unfrozen soils, the thermal conductivity varies with water content. For a dry soil, water is held by adhesive forces at the surface of the soil particles. The water films work as a bridge to effectively improve the heat transfer between grains. But the effect of increasing soil water content depends on the soil texture [*Farouki*, 1981]. For instance, the thermal diffusivity of sand increases rapidly with soil water content, and slows down and even decreases when the soil water content is over a certain range. In frozen soils, ice plays an important role in thermal diffusivity, which is about eight times that of water. Therefore, thermal diffusivity in the active layer can vary differently during freeze-thaw cycles.

The apparent soil thermal diffusivity (D_h^{app}) can be determined by several methods. One kind is to estimate the thermal conductivity with theoretical or semi-empirical models [e.g. *de Vries*, 1963; *Johansen*, 1975]. They need the volume fraction of soil constituents, and are just used for uniform soils. For natural soils, it will be hard to meet these requirements. Another kind of method is to estimate field soil thermal diffusivity from temperature time series analysis. Most of them are deduced from analytical solutions of one-dimensional heat conduction equation with the constant thermal diffusivity in a semi-infinite domain [*Horton et al.*, 1983]. A variety of methods have been used to estimate the thermal diffusivity from in-situ temperature measurements based on the assumption of pure conductive transport and constant thermal diffusivity in permafrost areas. They include simple Fourier methods [e.g. *Carson*, 1963; *Adams et al.*, 1976], the perturbed Fourier method [e.g. *Horton et al.*, 1983; *Hurley and Wiltshire*, 1993], and the graphical finite difference method [e.g. *Zhang and Osterkamp*, 1995; *Hinkel*, 1997]. Each of them has individual hypotheses. Since the hypotheses of various methods are not always fulfilled at different conditions, their accuracy are noteworthy. The transfer function method has been applied in a permafrost area by *Roth and Boike* [2001]. Further improvements of this method are discussed in the thesis of *Ludin* [2010]. Concerning the abrupt changes in air temperature on on the QTP, the transfer function method with an improvement for the initial

condition was applied at three different conditions. Its applicability of characterizing the heat transfer in various active layers were discussed.

6.2.1 Method

For a one-dimensional case, the heat transfer in a homogeneous soil can be expressed through the heat diffusion equation

$$\frac{\partial[CT]}{\partial t} - \frac{\partial^2[KT]}{\partial z^2} = 0 \ , \tag{6.1}$$

where soil properties such as heat capacity and thermal conductivity C, K are assumed to be independent of time t and space z. Therefore, they are replaced with the thermal diffusivity $D = K/C$. For a half-space $[0, \infty)$ spatial domain, the heat thermal dynamics can be described with the following model

$$\left.\begin{aligned} \frac{\partial T}{\partial t} &= D\frac{\partial^2 T}{\partial z^2} \\ T(0,t) &= T_0(t) \\ T(z,t_0) &= 0 \end{aligned}\right\} \tag{6.2}$$

where, the initial condition is set to zero, the upper boundary condition is given by the soil surface temperature T_0, and the lower boundary condition is free. The analytical solution can be obtained with the help of transfer functions. It is expressed [*Jury and Roth*, 1990] as the convolution integral

$$T_{proj}(t,z) = T(z,t_0) + \int_{t_0}^{t} T_0(\tau) p_t(t-\tau, z) d_\tau, \tag{6.3}$$

with the transfer function

$$p_t(t,z) = \frac{z}{2\sqrt{\pi D t^3}} \exp(-\frac{z^2}{4Dt}). \tag{6.4}$$

In the calculation, the initial temperature $T(z,t_0)$ is set as a reference point with measured temperature at depth z and time t_0. In the projection, there are two approaches to include this initial thermal condition. One is spin-up of the system, needed for equilibrating the system because of the perturbation of soil temperature at the beginning. The calculations by *Ludin* [2010] show, the spin-up time is needed at least four times of the time of the decay of the maximum of the travel time. Another approach is to solve the differential equation based on an initial energy distribution. In our calculation, a combination of both approaches was used. Details of this method can be found in the thesis of *Ludin* [2010].

From equation 6.4, the soil temperature at any depth can be calculated from the surface soil temperature. But the soil thermal diffusivity is unknown and difficult to measure. It is estimated from a time series of measured data and projected data. The objective function is set as

$$min_{D,T_{ref}} \| (T_{proj}(z,t) - T_{meas}(z,t))|_{z=z_p} \|_2^2. \tag{6.5}$$

In our calculation, the above objective function is optimized with the Levenberg-Marquardt algorithm. The thermal diffusivity D and reference temperature T_{ref} can be estimated. In theory, the reference temperature corresponds to the first measured soil temperature $T_{meas}(z_p, t_0)$ at depth z_p. However, in our calculation the reference temperature is assumed to be close to $T_{meas}(z_p, t_0)$. In addition, for ideal conditions, the surface temperature should be measured at the depth $z = 0$. However, this is difficult to get from field measurements. Hence, in our applications, the temperature measured with the top sensor at a depth of a few centimeters is taken to correspond to the surface temperature.

6.2.2 Results

From previous chapters, we already know the hydraulic and thermal characteristics at Chumaer, Tianshuihai and Qumahe. Due to the differences of the interaction between atmosphere and permafrost at these sites, the heat transfer near the surface differs from each other. In addition, soil heterogeneity and variational soil water content in the active layers can further strengthen these differences. In the following, heat transfer in the active layers were characterized by the transfer function method.

Since the major discrepancy of thermal diffusivity originates from the state of water in the soil, the D_h^{app} of the active layer at thawed and frozen conditions were estimated separately. As a matter of comparison, the apparent thermal diffusivity D_t, D_f in summer and winter periods were estimated with the same number of measurements. Because of the assumptions of pure heat conduction and infinite domain for the lower boundary, the transfer function method will be invalid when it is applied close to the thawing front during summer. To project to greater depths, the period was chosen during the late summer. The winter period was chosen during the later winter when the active layer was completely frozen. Because of the strong variability of heat transfer and thermal properties near the surface, the parameter estimation approach does not work properly. The quality of parameter estimation in the objective function of equation 6.5 is assessed by the residuals r_t, r_f during summer and winter, respectively.

Chumaer At Chumaer, permafrost is characterized by a thick active layer and large amount of groundwater. The air temperature varied from -36.5℃ and 21.4℃, and its mean annual value was about -5.0℃. During summer, the soil temperature was influenced by surface processes such as solar radiation, and monsoon rainfalls. During winter, the soil temperature was mainly driven by surface heat convection, and sporadic snowfalls disturbed the surface energy balance. Two periods were chosen to represent the heat transfer in summer and in winter, which can basically meet the requirements of the heat transfer function method. The applied periods in winter and summer were chosen from day number 745 to 807 and from day number 940 to 1002 for profile 1, respectively. While for profile 2 they are from day number 745 to 807 and from day number 932.5 to 995 in winter and summer, respectively. Since the uppermost soil temperature sensor at depth 0.05 m was broken in profile 2, the upper temperature boundary conditions for profile 1 and 2 were defined as the measured soil temperatures at the depth of 0.05 m and 0.1 m, respectively. The D_h^{app} at each depth was estimated with Equation 6.5, which represents the mean value for the domain from surface to the projected depth. The estimated D_h^{app} of two profiles in winter and in summer are shown in Table 6.1.

Due to the strong diurnal fluctuation of the surface energy flux on the QTP, the daily damping depth of dry active layers can reach several decimeters. The inverse parameter estimation in Equation 6.5 does not work properly within the damping depth when the D_h^{app} is not constant. Because in the algorithm the D_h^{app} will be changed significantly to fit the daily amplitude and long-term mean value of soil temperature. This near-surface effect seriously influence the accuracy of the D_h^{app} when there is a significant change in the D_h^{app}. Since the near-surface soil temperature fluctuated close to the phase change temperature during summer and winter at Chumaer, the estimated D_h^{app} within the damping depth (approximately 0.5 m at this site) were strongly influenced.

There are three noticeable features of the estimated D_h^{app} at Chumaer. Firstly, the near-surface effect in profile 1 is more significant than that in profile 2. For instance, the D_h^{app} at the depth of 0.15 m is much larger than adjacent values in profile 1. Secondly, the D_h^{app} below the daily damping depth varied with depth. Although the near-surface effect still influences the D_h^{app} estimation, this influence was attenuated with depth. The quality of the parameter estimation

Table 6.1. Seasonal variations of D_h^{app} of the active layer in two profiles at Chumaer. D_t and D_f are estimated in the summer and winter periods, respectively.

P1					P2				
depth [m]	D_h^{app} $\times 10^{-7}$ [m^2 s^{-1}]		residual [℃]		depth [m]	D_h^{app} $\times 10^{-7}$ [m^2 s^{-1}]		residual [℃]	
	D_t	D_f	r_t	r_f		D_t	D_f	r_t	r_f
0.1	3.3	2.4	0.77	0.48	0.15	2.7	2.4	1.41	1.08
0.15	14.5	4.7	0.29	0.29	0.2	8.8	8.1	0.20	0.27
0.5	4.8	4.7	0.23	0.16	0.3	7.2	7.9	0.16	0.14
0.9	5.5	5.4	0.17	0.14	0.5	6.1	7.3	0.17	0.14
1.1	5.6	5.6	0.16	0.13	0.7	5.8	6.3	0.13	0.16
1.3	5.7	5.9	0.15	0.13	0.9	5.9	5.4	0.09	0.16
1.5	3.2	3.9	0.10	0.09	1.1	6.2	4.9	0.08	0.15
1.9	4.0	5.1	0.08	0.08	1.3	6.3	5.4	0.08	0.14
2.0	4.8	6.8	0.08	0.07	1.5	6.4	5.5	0.09	0.13
					1.7	6.0	5.7	0.09	0.12

of the D_h^{app} increases with depth as expected. As shown in Table 6.1, the D_h^{app} in profile 1 increases from the depth 0.5 m to the maximal value at the depth 1.3 m, and then rapidly decreases. Oppositely, in profile 2 the D_h^{app} decreases from the depth 0.5 m to its minimal value in the middle, and then increases slowly. Apparently, the D_h^{app} were not homogeneous in both active layers. Thirdly, the ratio of the winter-to-summer diffusivity varied differently in the two profiles. In profile 1, r_t and r_f are comparable at the same depth, while r_t is clearly smaller than r_f at the lower depths in profile 2. In general, there is no significant change of the D_h^{app} from winter to summer in both profiles. The residuals r_t and r_f demonstrate that the influences factors changed differently in season. The change of the D_h^{app} was influenced by several factors such as soil heterogeneity, temperature and other non-conductive processes. The reasons for D_h^{app} changes with depth and season will be discussed further in the later discussion.

With the above estimated D_h^{app} the differences between measured temperature and projected temperature at each depth can be calculated. Because of the clear seasonal change of the residual in the D_h^{app} estimation in profile 2, the patterns of temperature differences ($T_{meas} - T_{proj}$) in depth and time are shown in Figures 6.1 and 6.2. In Figure 6.1, the pattern is related to the surface temperature fluctuations. As we know the D_h^{app} of the frozen soil is dependent on the temperature, and particularly when the temperature is close to the phase change temperature. Due to the different sensitivity of D_h^{app} to the temperatures during the period from day number 760 to 790 and other periods, the D_f is underestimated at lower temperature ($T_{meas} - T_{proj} > 0$) and overestimated at the temperature close to the phase change temperature ($T_{meas} - T_{proj} < 0$). In Figure 6.2, the pattern is mainly caused by the occurrence of the daily freeze-thaw process and precipitation. However, their influences are relative smaller compared to the temperature dependence of the D_h^{app} in winter.

From these comparisons, two important clues can be found. One is the relation between the pattern of temperature differences and the surface air and soil temperature fluctuations. It indicates that the temporal variation of heat transfer mechanism in the active layer is mainly induced by the non-conductive processes. Another one is the change of the pattern of temperature differences in depth and time. The fluctuations of the temperature differences mainly originated from the upper layer and attenuated in depth, which means that the temporal variations of D_h^{app} are mainly located at the upper layer.

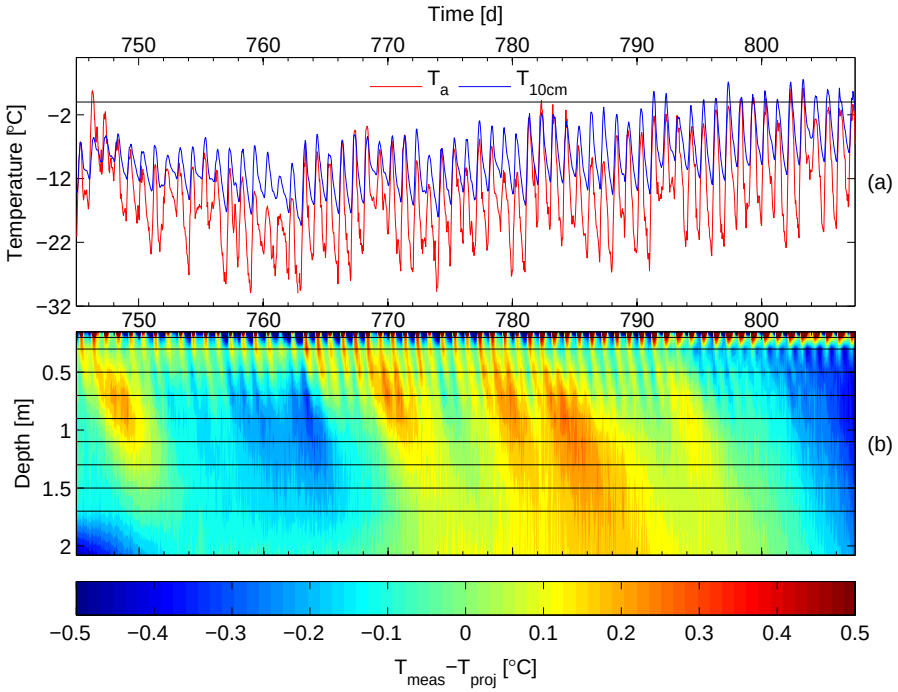

Figure 6.1. The pattern of the air and near-surface soil temperature and the projection during the winter period at Chumaer. (a) fluctuations of air temperature and near-surface temperature; (b) the differences between measured temperatures and projected temperatures. The black lines are the projected depths.

Tianshuihai At Tianshuihai, the mean annual air temperature is much colder than that at Chumaer. The air temperature varied from -40.1 and 20.6℃, and its mean annual value was about -8.0℃. Due to little precipitation in this area, the ground surface is extremely dry during the whole year. Therefore, soil temperature was influenced by solar radiation and surface sensible heat flux. Two periods were chosen to represent the heat transfer in summer and in winter, which can basically meet the requirements of the heat transfer function method. In Table 6.2, the D_h^{app} were estimated with the same method as at Chumaer. The upper temperature boundary conditions for both profiles were defined as the measured soil temperatures at the depth of 0.04 m. The applied periods in summer and in winter are from day number 575 to 617 and from day number 783 to 825, respectively.

The features of the estimated D_h^{app} at Tianshuihai are similar to those at Chumaer. As shown in Table 6.2, the D_h^{app} varied in a small range with depth. The deviation in estimated D_h^{app} near the surface is much stronger than that at lower depth. Comparing the D_h^{app} in summer and in winter, we can find that below the daily damping depth, D_t and D_f are comparable at the same depth, but the residuals r_t and r_f are different in both profiles. r_t is clearly larger than r_f. In general, there is no significant change of D_h^{app} from winter to summer in both profiles. The residuals r_t and r_f demonstrate that the influences factors changed differently in season.

With the above estimated D_h^{app} the differences between measured temperature and projected temperature at each depth can be calculated. Because of the similar results in the D_h^{app} estimation in both profiles, the patterns of temperature differences $T_{meas} - T_{proj}$ in profile 1 were presented in Figures 6.3 and 6.4. The scattered large differences in Figure 6.3 were caused by the disturbed temperature measurements due to technical malfunction. One significant feature at Tianshuihai is that the projection is much better in winter than in summer. While it is reverse

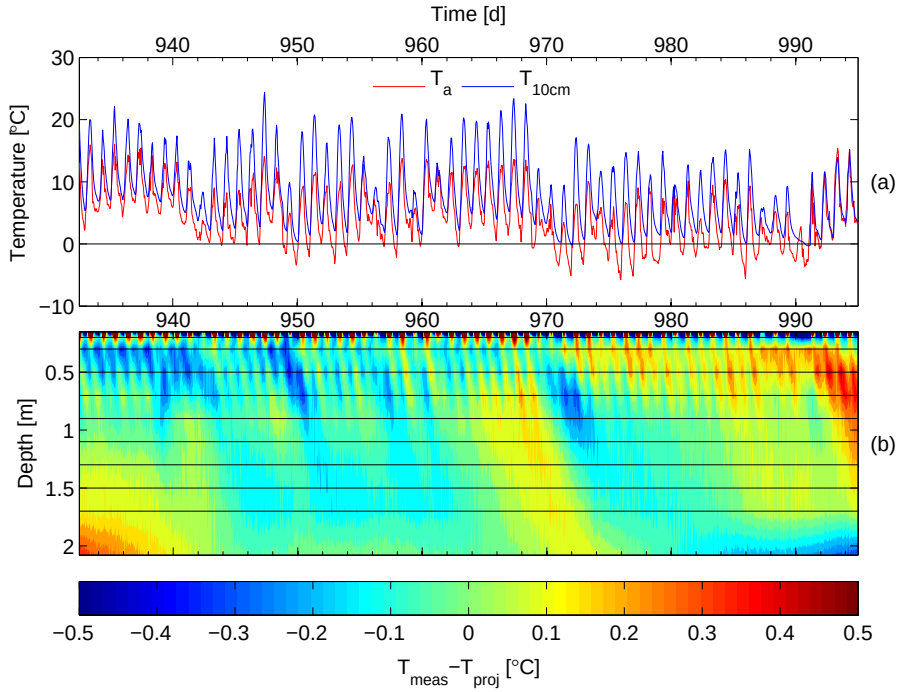

Figure 6.2. The pattern of the air and near-surface soil temperature and the projection during the summer period at Chumaer. (a) fluctuations of air temperature and near-surface temperature; (b) the differences between measured temperatures and projected temperatures. The black lines are the projected depths.

Table 6.2. Seasonal variations of D_h^{app} of the active layer in two profiles at Tianshuihai. D_t and D_f are estimated in the summer and winter periods, respectively.

P1					P2				
depth [m]	D_h^{app} $\times 10^{-7}$ [m^2 s^{-1}]		residual [°C]		depth [m]	D_h^{app} $\times 10^{-7}$ [m^2 s^{-1}]		residual [°C]	
	D_t	D_f	r_t	r_f		D_t	D_f	r_t	r_f
0.14	2.8	2.8	0.48	0.48	0.12	6.3	3.6	0.28	0.46
0.26	4.6	5.2	0.31	0.27	0.21	6.2	5.6	0.25	0.29
0.31	4.4	4.9	0.31	0.28	0.28	6.1	6.5	0.25	0.22
0.44	4.1	4.2	0.29	0.25	0.39	4.6	4.6	0.25	0.19
0.59	4.0	4.0	0.27	0.19	0.51	4.6	5.1	0.22	0.14
0.73	4.1	4.0	0.27	0.16	0.64	4.7	5.8	0.20	0.12
0.85	4.2	4.2	0.27	0.14	0.72	4.0	4.5	0.19	0.11
0.97	3.4	3.4	0.25	0.09	0.86	4.0	4.5	0.18	0.08
1.09	3.9	4.0	0.25	0.08	0.98	3.8	4.7	0.17	0.07
1.21	4.0	4.3	0.23	0.07	1.1	3.4	5.0	0.14	0.06
1.34	4.0	4.8	0.22	0.06	1.2	3.1	5.2	0.11	0.05
1.46	3.7	5.1	0.20	0.06	1.3	2.7	5.2	0.10	0.04
1.57	4.1	5.5	0.26	0.05	1.44	3.3	5.9	0.19	0.04
1.7	4.8	6.2	0.27	0.05	1.63		6.3		0.03
					1.81		6.3		0.03

at Chumaer. It means the temporal change of D_h^{app} during the winter at Tianshuihai was much weaker than that during the summer. As shown in Figure 6.3, the large differences might be caused by the drastic change from extreme low temperature to high temperature, which may lead certain variation in D_f. While in Figure 6.4, the evident patterns might be caused by the occurrence of daily freeze-thaw process near the surface, which significantly changes the D_t. Comparing the pattern of the temperature differences $T_{meas} - T_{proj}$ and the surface air and soil temperature fluctuations, we can find that the temporal variation of the heat transfer mechanism in the active layer is induced by the surface drastic change of temperature. The fluctuations of the temperature differences mainly originated from the upper layer because of the temporal variations of D_h^{app}.

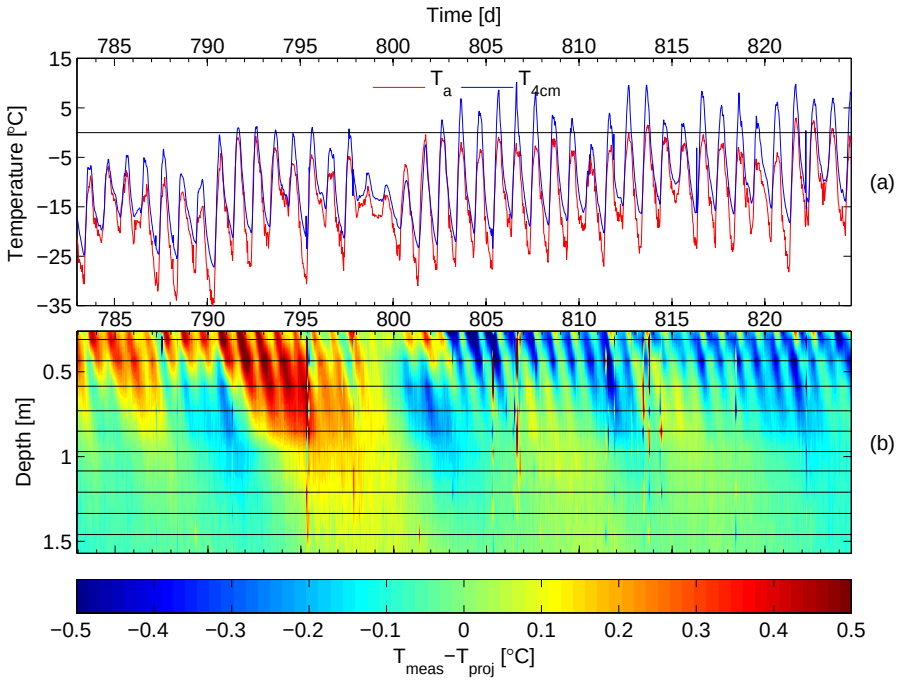

Figure 6.3. The pattern of the air and near-surface soil temperature and the projection during the winter period at Tianshuihai. (a) fluctuations of air temperature and near-surface temperature; (b) the differences between measured temperatures and projected temperatures. The black lines are the projected depths.

Qumahe At Qumahe, the air temperatures are similar to that at Chumaer. The air temperature varied from -35.6 and 10.0℃, and its mean annual value was about -5.0℃. Since the active layer is wet and covered with dense vegetation, the active layer is thin and warm. Two periods were chosen to represent the heat transfer in summer and in winter. In Table 6.3, the D_h^{app} were estimated with the same method as at Chumaer. The upper temperature boundary condition was defined as the measured soil temperatures at the depth of 0.02 m. The applied periods in winter and in summer are from day number 750 to 812, and from day number 950 to 1012, respectively.

The features of the estimated D_h^{app} at Qumahe are different from the above two sites. The near-surface effect was much stronger in summer than in winter. Due to high water content in the active layer, the daily damping depth is extremely shallow. As shown in Table 6.3, the D_h^{app} below the damping depth decreases with depth. Comparing the D_h^{app} in summer and in winter, we can find that D_t is always smaller than D_f at the same depth, and the residuals r_t is larger

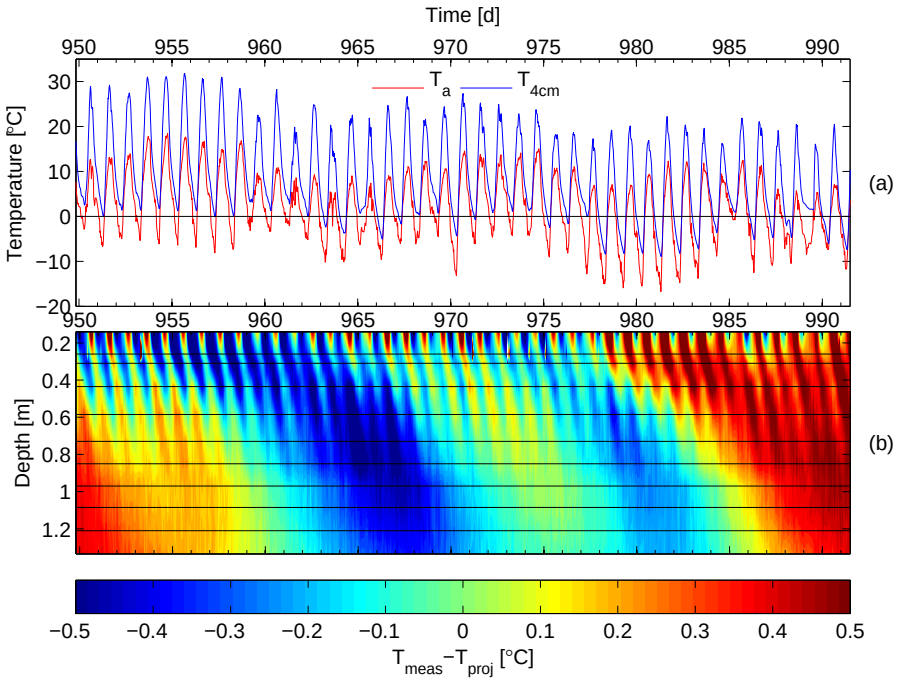

Figure 6.4. The pattern of the air and near-surface soil temperature and the projection during the summer period at Tianshuihai. (a) fluctuations of air temperature and near-surface temperature; (b) the differences between measured temperatures and projected temperatures. The black lines are the projected depths.

than r_f. In general, there is a significant change of D_h^{app} from winter to summer in the active layer.

Table 6.3. Seasonal variations of the D_h^{app} of the active layer in two profiles at Qumahe. D_t and D_f are estimated in the summer and winter periods, respectively.

depth	D_h^{app} $\times 10^{-7}$ [m^2 s^{-1}]		residual [°C]	
[m]	D_t	D_f	r_t	r_f
0.1	3.3	6.8	0.31	0.29
0.15	1.0	3.6	0.26	0.20
0.3	1.0	2.5	0.33	0.21
0.55	0.6	1.4	0.30	0.16
0.70	0.5	1.1	0.18	0.20
1.20		0.9		0.16
1.45		0.7		0.14
1.57		0.6		0.12

With the above estimated D_h^{app} the differences between measured temperature and projected temperature at each depth are shown in Figures 6.5 and 6.6. One evident feature at Qumahe is that the projection is much better in winter than in summer. As shown in Figure 6.5, the soil temperature at the depth of 2 cm is nearly constant during the whole period, while the relation between the pattern of temperature differences ($T_{meas} - T_{proj}$) is not clear. The large temperature differences at the lower part originates from temperature dependence of the D_h^{app}

when the soil temperature is close to the phase change temperature. In Figure 6.6, the pattern of $T_{meas} - T_{proj}$ shows a closer relation with the near-surface temperature in summer than in winter. This is because of the daily freeze-thaw process. Due to the high water content near the surface, the phase change needs a large amount of energy, which retards the soil freezing. This process occurs commonly at this site during summer. But when it is absent like during periods 960-970 and 990-1002 shown in Figure 6.6, the heat transfer is dominated by heat conduction. Compared to the mean D_h^{app} for the whole period, the D_h^{app} is underestimated during the periods without significant daily freeze-thaw process ($T_{meas} - T_{proj} > 0$), and overestimated during the other periods ($T_{meas} - T_{proj} < 0$). In general, the heat transfer mechanism in the active layer is sensitive to the temperature during winter, while it is mainly influenced by the near-surface daily freeze-thaw process.

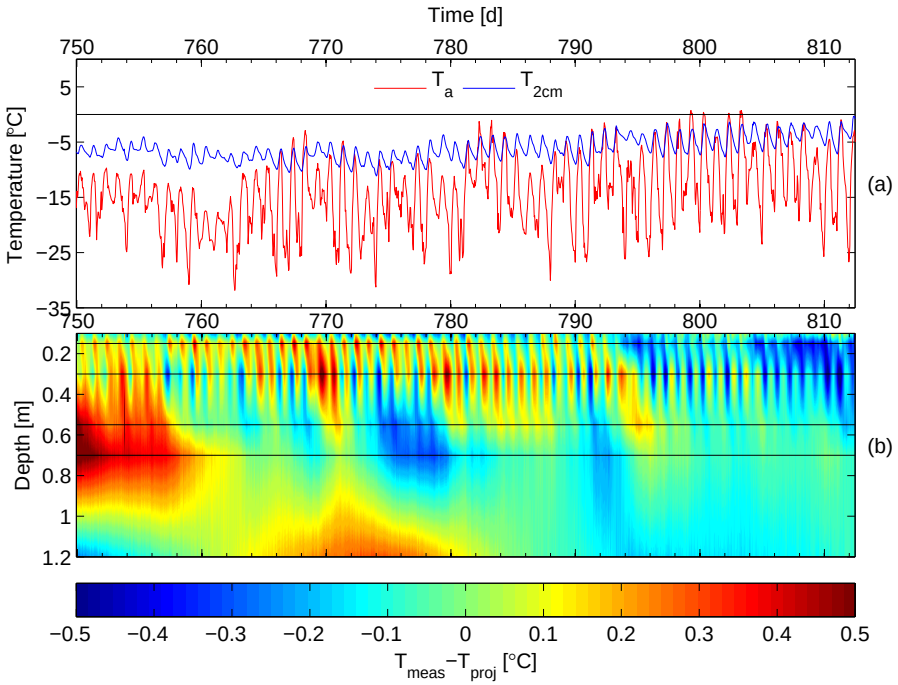

Figure 6.5. The pattern of the air and near-surface soil temperature and the projection during the winter period at Qumahe. (a) fluctuations of air temperature and near-surface temperature; (b) the differences between measured temperatures and projected temperatures. The black lines are the projected depths.

6.2.3 Discussion

Influences of various factors on D_h^{app} estimation In the transfer function method, the assumption of a constant thermal diffusivity and homogeneous soil influences the projection. For natural soils, these assumptions can not be perfectly fulfilled. Therefore, influences of non-conductive processes can be identified by analyzing the temperature projection. The variation in D_h^{app} can be caused by a variety of factors. They mainly include temporal and spatial variations in soil constituents (water or ice content), and heat transfer processes.

In temporal, the D_h^{app} shows a high variability near the surface at the study sites. In permafrost regions, the near-surface D_h^{app} is usually influenced by phase transitions during summer, which can be caused by precipitation and evaporation [*Kane et al.*, 2001]. During

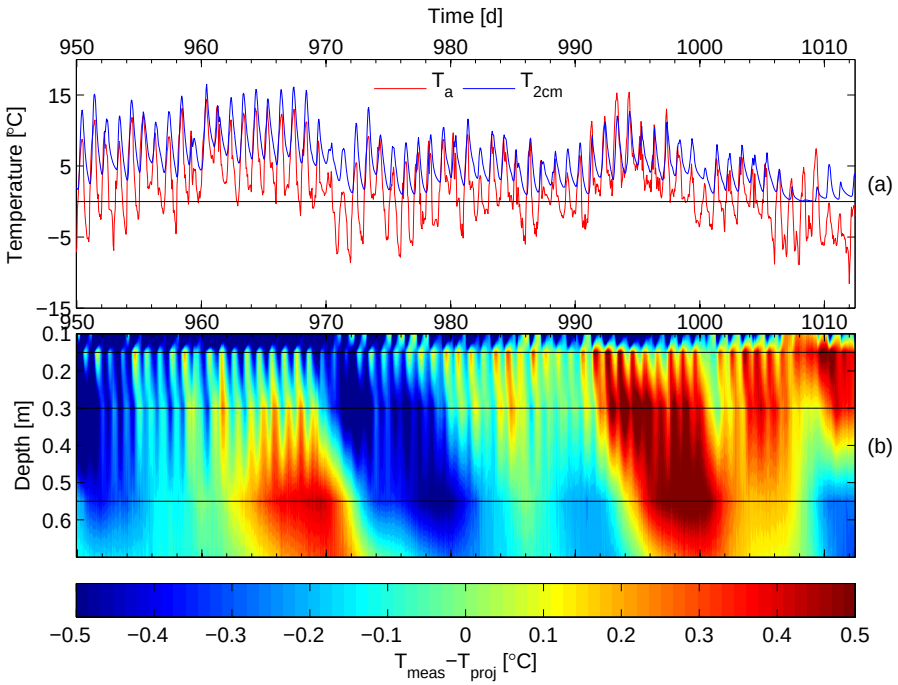

Figure 6.6. The pattern of the air and near-surface soil temperature and the projection during the summer period at Qumahe. (a) fluctuations of air temperature and near-surface temperature; (b) the differences between measured temperatures and projected temperatures. The black lines are the projected depths.

winter, the D_h^{app} is more stable than during summer, because less meteorological disturbances influence the heat transfer in the frozen soil. From the above analysis of the air temperature and near-surface soil temperature we can find that daily freeze-thaw process occurs commonly near the surface during winter and summer at the study sites due to the large dynamic range of air temperature. However, the influence of the daily freeze-thaw process on the surface soil-weather interaction mainly depends on the soil water content. For instance, the soil at the depth of 4 cm experienced from completely frozen to thawed in 24 hours no matter in summer or in winter at Tianshuihai. While at Qumahe the soil at the depth of 2 cm could not be completely frozen or thawed in one day, although the air temperature experienced the positive to negative or the other way round. As mentioned before, the estimated D_h^{app} within the daily damping depth can deviate seriously from the transfer function method, when soil thermal properties change significantly for non-conductive heat transfer processes such as daily freeze-thaw, infiltration.

Since we use a constant D_h^{app} for the whole estimated period in the project, the long term change of soil temperature in winter in warm permafrost region can undermine the assumption of constant D_h^{app}. To include the phase change in the heat conduction model, the latent heat is usually included in terms of an apparent heat capacity (C_a)

$$C_a(T) = C_s(T) + \rho_w L_w (\frac{\partial \theta_w}{\partial T}), \tag{6.6}$$

where, C_s is the volumetric heat capacity of frozen soil, ρ_w and L_w are the mass density of water and the latent heat of ice fusion, respectively. The derivative of the water content with respect to temperature $\frac{\partial \theta_w}{\partial T}$ can be identified from the freezing characteristic curve. As shown in Figure 6.7, the value of $\frac{\partial \theta_w}{\partial T}$ can be negligible for the cold soil, while it is sensitive to the temperature variation when the soil temperature is close to 0℃. Besides, the water content also plays a

significant role. The freezing characteristics at the study sites show that the near-surface D_h^{app} are sensitive to soil temperature change in winter at Chumaer and Qumahe, but the influence of the phase change is negligible at Tianshuihai because of the extremely dry soil near the surface.

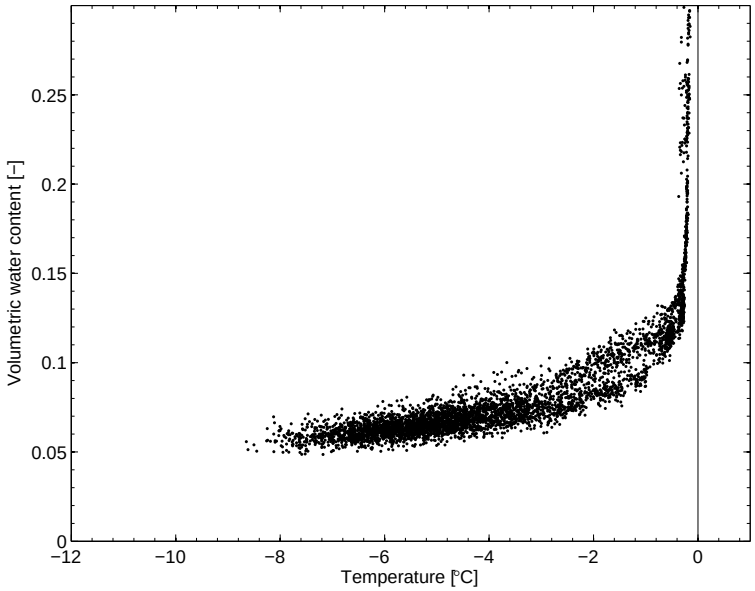

Figure 6.7. Near-surface soil freezing characteristic (depth: 10 cm) at Qumahe.

From comparison of the near-surface projection at Chumaer, Tianshuihai and Qumahe, we can find that the pattern of temperature differences $T_{meas} - T_{proj}$ is mainly related to the near-surface non-conductive processes of daily freeze-thaw and high variability of D_h^{app} around the phase change temperature. The transfer function method could not be directly used to characterize non-conductive heat transfer processes, which can only be deduced from other observations. Although the diurnal dynamic range of surface heat flux is large on the QTP, the damping depth of ground temperature varies significantly for different soil water contents. It is about 0.5 m at Chumaer and Tianshuihai, while at Qumahe it reduces to about 0.3 m. From the estimated D_h^{app} at the study sites, we can find that it shows a high variability within the damping depth. It may be caused by various non-conductive processes. The similar phenomenon has been found in the study of the soil thermal properties along a soil moisture gradient in the McMurdo Dry Valleys, Antarctica, by *Ikard et al.* [2009]. Therefore, the temporal variation of non-conductive processes and the temperature dependence of soil thermal properties near the surface on the QTP can not be ignored in the heat transfer analysis, particularly for the analytical method like the transfer function method.

In spatial, the influence of the soil heterogeneity on D_h^{app} estimation is mainly complicated by the active layers with ground water and near-zero soil temperature. The ground water concentrates at the lower part, for instance, at Tianshuihai. The thermal properties are different from the above layer. Besides, in the warm permafrost region the wet active layer is characterized for near-zero soil temperature at the lower part in winter, which makes the soil properties different from the upper part. According to the measured freezing characteristic, phase change plays an important role in this temperature range. As a typical case at Qumahe shown in Table 6.3, the estimated D_h^{app} in winter decreases from surface to bottom, although the active layer is nearly homogeneous. Because of the assumption of homogeneous medium for the heat transfer

function method, the soil heterogeneity can influence the D_h^{app} estimation. As discussed in the study of *König* [2008], the Levenberg-Marquardt algorithm used in the parameter estimation can make the D_h^{app} underestimated at the edge of the layer interface in the layered medium. However, concerning homogeneity, the heat transfer function method can be applied to the layered soil if the whole medium for projection is so large that the soil heterogeneity is negligible at the applied scale. For natural soil, this is often the case in the field.

Variability of thermal diffusivity in various active layers The variations of the D_h^{app} in depth and season are usually attributed to the soil heterogeneity and soil temperature. The studies in permafrost areas [e.g. *Hinkel*, 1997; *Pringle et al.*, 2003; *Ikard et al.*, 2009] show that the D_h^{app} varies with depth and time, and it is usually larger in winter than in summer. But the estimated D_h^{app} at the study sites on the QTP show different characteristics. Due to the influence of the non-conductive processes near the surface the deviation of the estimated D_h^{app} within the daily damping depth can vary in one or more orders. Because of the significant daily freeze-thaw process it is difficult for the parameter estimation algorithm. But when we project from upper boundary to deeper depth, the influence of the daily fluctuation of soil temperature on the algorithm is very weak. Aside from the non-conductive processes near the surface, which influence the D_h^{app} estimation from the transfer function method, other factors like soil heterogeneity and ground water can not ignored. To check the soil heterogeneity, the mean volumetric water contents were calculated for each period.

The variability of the estimated D_h^{app} in two profiles at Chumaer is shown in Figure 6.8. The exceptional value occurs at 0.15 m depth in summer period in Figure 6.8(3). It may be originated from the crack. Since the surface clods with dense root (about 0.15 m in depth) can not join together as before, which can lead to cracks during the freeze-thaw cycle. Therefore, non-conductive processes like daily evaporation and condensation, water infiltration can speed up ground heat transfer within this depth during summer. Below the near surface, variations of D_h^{app} in depth are mainly attributed to two reasons at Chumaer. Firstly, soil heterogeneity in the active layer leads to the variations of the D_h^{app} with depth. Because of the smooth change of the soil water content around the groundwater table (about 1.3 m), there is only a slight change in soil temperature gradient distribution and D_h^{app} in profile 1 (P1). The noticeable decrease of D_h^{app} at depth 1.5 m in winter should be caused by the interface of contrasting soil properties. According to the soil texture analysis presented in the thesis of *König* [2008], the large contrast of the coarse fragment content around 1.5 m might be the major reason for the significant decrease of the D_h^{app} with depth, while in profile 2 (P2), there is only one significant change in the D_h^{app} around the groundwater table. Secondly, near-zero soil temperature below the groundwater table shown in Figure 6.8(2) and (5), makes the estimated D_h^{app} smaller than in the upper layer, although the ice content is much higher in the deeper layer.

The variations of the D_h^{app} throughout the seasons are mainly related to the influence of phase change in winter. In Figure 6.8(3) and (6), the estimated D_h^{app} in P1 are close to each other at the same depth, while the D_h^{app} is even smaller in winter than that in summer below the depth 0.9 m in P2. The difference may be caused by soil water content differences, which can significantly influence the amount of latent heat by phase change.

Variations of the estimated D_h^{app} with depth at Tianshuihai are similar to those at Chumaer. As shown in Figure 6.9, the sandy soil in the active layer P1 is nearly homogeneous, but the drastic change of D_h^{app} at the depth 0.97 m is caused by the jump of soil water content at the groundwater table. Below this depth, the increase in D_h^{app} was caused by the high ice content in the lower layer. In P2, there are two evident changes of D_h^{app} at the depths of 0.635 m and 0.72 m. From field observation of the soil texture and measured soil water content distribution, we can deduce that the upper one is related to the soil texture change, while the lower one should

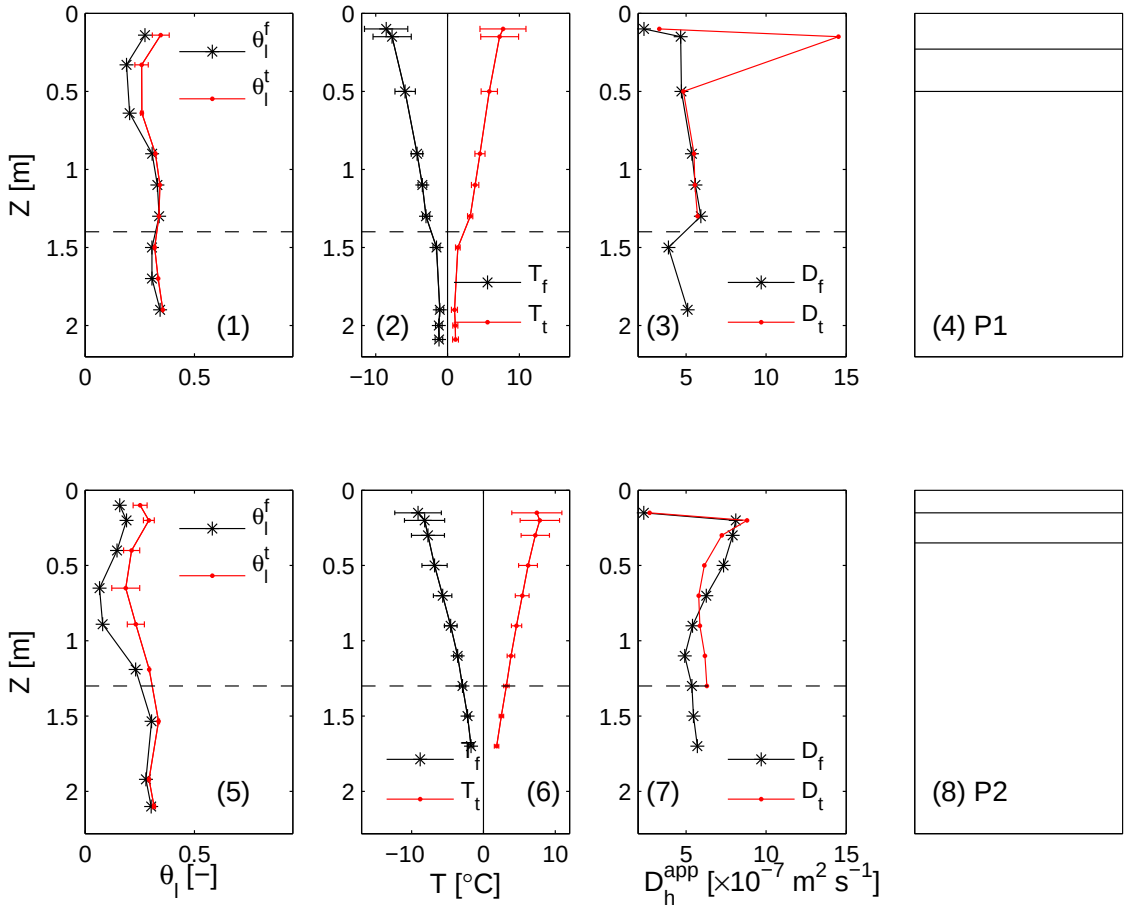

Figure 6.8. Variability of the estimated apparent thermal diffusivity and related factors in depth and in season in two profiles (P1 and P2) at Chumaer. (1) and (5): θ_l^f and θ_l^t are the measured mean water content in winter and summer, respectively. (2) and (6): T_f and T_t are the measured mean soil temperature in winter and summer, respectively. (3) and (7) D_f and D_t are the estimated apparent thermal diffusivity (D_h^{app}) in winter and summer, respectively. (4) and (8) the sketch of the active layer structure. Detailed descriptions of the soil texture can be found in pp.12-13. Note: the D_h^{app} at each depth represents the value for the domain from surface to the depth, and θ_l^f is the measured liquid water content just before freezing. They are the same in Figure 6.9 and 6.10

be related to the soil water content change. Because of the low soil temperature (< -5℃) in winter at Tianshuihai, the influence of the phase change is negligible. However, the D_h^{app} do not increase significantly because of the extreme dry soil in the upper layer.

As shown in Figure 6.10, the estimated D_h^{app} in winter and in summer both gradually decrease with depth. Since the soil temperature in the active layer at Qumahe is close to 0℃, it makes the D_h^{app} sensitive to the soil temperature variation in depth. According to Equation 6.6, the closer to 0℃ the soil temperature is, the smaller the D_h^{app}. While during summer, the slight decrease of D_h^{app} may be related to the soil water content distribution. Because of the high water content the D_h^{app} in winter are much larger than in summer.

Challenges for permafrost modeling From the above analysis, we can find that heat transfer in various active layers varies differently on the QTP. For the warm permafrost at Chumaer and Qumahe, the heat transfer near the surface is significantly influenced by the daily freeze-thaw process. Besides heat transfer in the frozen soil with near-zero soil temperature is still evidently

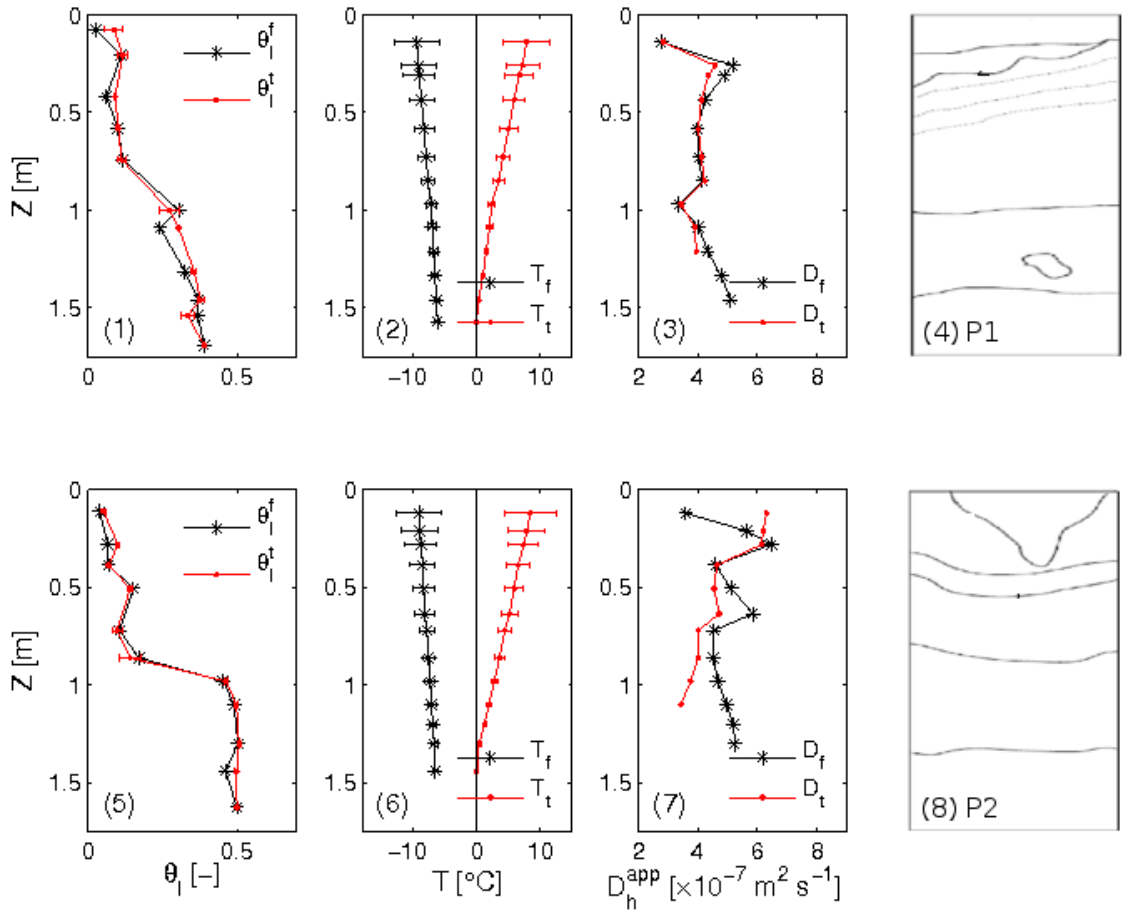

Figure 6.9. Variability of the estimated apparent thermal diffusivity and related factors in depth and in season in two profiles (P1 and P2) at Tianshuihai. (1) and (5): θ_l^f and θ_l^t are the measured mean water content in winter and summer, respectively. (2) and (6): T_f and T_t are the measured mean soil temperature in winter and summer, respectively. (3) and (7) D_f and D_t are the estimated apparent thermal diffusivity (D_h^{app}) in winter and summer, respectively. (4) and (8) the sketch of the active layer structure. Detailed descriptions of the soil texture can be found in pp.18-19.

influenced by the phase change. For the cold permafrost at Tianshuihai, the heat transfer near the surface is still influenced by the daily freeze-thaw processes, but the temperature dependence of the D_h^{app} is much weaker in winter in the lower part than the other sites. The near-surface dry soil in the active layer leads to no significant change between winter and summer. In addition, the soil heterogeneity further complicates the estimation of the D_h^{app} with the transfer function method at Chumaer and Tianshuihai.

In permafrost modeling, the model is still suffering from incomplete representation of physical processes. Particularly like the cases at the above study sites, weather-induced temporal processes like infiltration, evaporation, sublimation and wind convection near the surface may be not easy to reproduce by numerical modeling. But their influences are evident in the above characterization. Therefore, these processes should be considered properly in future permafrost modeling. In addition, the inaccurate parameterizations of soil thermal properties, such as thermal diffusivity for variational water phase and temperature dependence, also influence the accuracy of permafrost modeling. For mapping permafrost distribution, several simple models such as the Stefan model and TTOP model are used in several studies [e.g. *Nelson and Outcalt*,

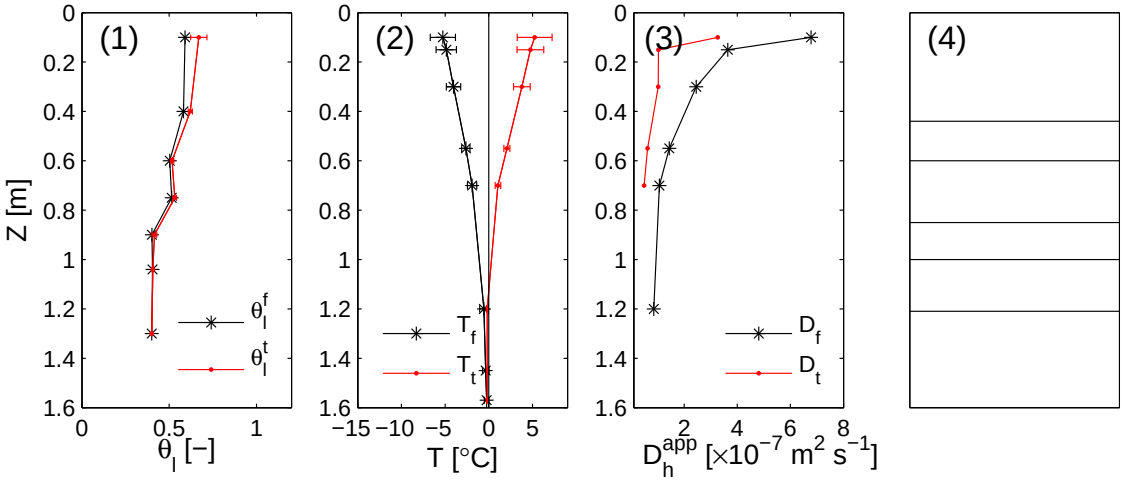

Figure 6.10. Variability of the estimated apparent thermal diffusivity and related factors in depth and in season at Qumahe. (1) θ_l^f and θ_l^t are the measured mean water content in winter and summer, respectively. (2) T_f and T_t are the measured mean soil temperature in winter and summer, respectively. (3) D_f and D_t are the estimated apparent thermal diffusivity (D_h^{app}) in winter and summer, respectively. (4) the sketch of the active layer structure. Detailed descriptions of the soil texture can be found in pp.14.

1987; *Zhang et al.*, 2005; *Etzelmuller et al.*, 2007; *Juliussen and Humlum*, 2007]. However, due to the effects of non-conductive processes and the variation in properties of various active layers, the empirical parameterizations for thermal conductivity can give a probable range, but the spatial variability of thermal properties, seasonal variation of active layer soil water content should be explored further [*Riseborough*, 2004]. Better representative parameterizations are still demanding at present. Concerning the above challenges, a new method is introduced in the following.

6.3 Field-scale parameterization of soil thermal conductivity with multi-channel GPR

From above analyses we know that the parameterization of soil thermal diffusivity using pure heat conductive model would have problems in the warm permafrost regions on the QTP due to the non-negligible influence of non-conductive processes. In addition, spatial variability of soil thermal properties also complex soil thermal conductivity parameterization. Based on the great advantages of the multi-channel GPR shown in the last chapter, it would be a promising tool to bridge the scale gap between point measurements and regional measurements for soil thermal conductivity parameterization. In this section, a field-scale parametrization of soil thermal conductivity with multi-channel GPR is proposed and discussed.

6.3.1 Method

The Stefan model A variety of equilibrium climate-permafrost models have been proposed to characterize thawing and freezing in the active layer using the surface freezing index (I_{fs}) and thawing index (I_{ts}). These indices are seasonally integrated temperatures. In practical calculations, it is the sum of the daily mean temperatures for the duration of the season. In climate-permafrost models, the freezing and thawing indices are usually used to define the

air and ground surface relation. Because of the complex energy exchange between surface and atmosphere, the ground temperature is difficult to measure. Therefore, in practical applications, the surface temperatures used to calculate these indices are often measured at a few centimeters below the surface [*Riseborough*, 2004].

One of the simplest models for estimating the active layer thickness is the Stefan equation

$$X = \sqrt{\frac{2kI}{L}} \tag{6.7}$$

where, X is the depth of freezing and thawing, k is the thermal conductivity, I is the surface freezing or thawing index, L is the volumetric latent heat of fusion ($L = L_w \times \theta$, with L_w: water latent heat for fusion).

In the Stefan model, it is assumed that the heat energy from the surface is transferred to the freezing or thawing front for fusion, and the diffusive effects are small relative to the rate of phase change at the front [*Lunardini*, 1981]. To identify applicability of the Stefan model, the Stefan number Ste is suggested as

$$Ste = \frac{C|T_s - T_f|}{L} \tag{6.8}$$

where C is the volumetric heat capacity, T_s, T_f are the surface temperature and soil melting temperature, respectively. Aside from requiring a small Stefan number, the initial temperature of the soil should be close to the fusion temperature (normally 0℃).

In practical application, soil properties can be approximately measured or estimated empirically from points. The Stefan model just needs the summer air or ground surface temperature measurements for estimation of the maximal thaw depth. Due to its simplicity, it is widely used for spatial active-layer characterization [e.g. *Nelson and Outcalt*, 1987; *Zhang et al.*, 2005]. However, the soil thermal conductivity is difficult to represent the spatial variability and non-conductive processes.

The TTOP model As a simplified model, *Lunardini* [1978] suggests an empirical relationship between ground surface temperature and air temperature to characterize the surface energy balance. N-factors account for the complex processes within the atmosphere-soil system. They are influenced by vegetation and snow cover. The surface temperature can be estimated from the air temperature by the N-factor method. Because of the simplicity and easy acquirability of air temperature, the N-factor is an effective way to support the upper boundary for modeling the ground thermal regime. It is widely used to model the spatial permafrost distribution [e.g. *Henry and Smith*, 2001; *Etzelmuller et al.*, 2007; *Juliussen and Humlum*, 2007; *Juliussen and Humlum*, 2008].

The N-factor is defined as

$$\begin{aligned} N_t &= \frac{\int_0^t (T_t - T_s)dt}{\int_0^t (T_t - T_a)dt} \\ N_f &= \frac{\int_0^t (T_f - T_s)dt}{\int_0^t (T_f - T_a)dt} \end{aligned} \tag{6.9}$$

where, N_t, N_f are the thawing N-factor and the freezing N-factor, T_s, T_a are the ground surface and air temperature, respectively, T_f (T_t) is the freezing (thawing) temperature of 0℃, and t is the time duration of thawing or freezing seasons. The numerators of the fraction of N_t, N_f correspond to the seasonal thawing and freezing indices of the ground surface, and the denominators correspond to the seasonal thawing and freezing indices of air.

In practice, the integration of temperature over time is usually summarized as degree-days, and the n-factor is calculated as the ratio of ground surface temperature degree-days (DDT_s) to air temperature degree-days (DDT_a) for the thawing or freezing season

$$\begin{aligned} n_t &= \frac{DDT_s}{DDT_a} \\ n_f &= \frac{DDF_s}{DDF_a}. \end{aligned} \tag{6.10}$$

The mean annual air and ground surface temperatures (MAAT, MAST) are calculated as

$$\begin{aligned} MAAT &= (DDT_a - DDF_a)/P \\ MAST &= (n_t DDT_s - n_f DDF_s)/P, \end{aligned} \tag{6.11}$$

where P is the period (365 days).

The calculation of n-factors requires daily measurements of air temperature and surface temperature. The air temperature is typically measured at a certain height above the ground surface. While the surface temperature is the ideal definition of temperature at the interface between atmosphere and ground surface. In practice, its measured position ranges from a few centimeters to tens of centimeters in several permafrost studies [*Karunaratne*, 2003].

To calculate the thawing and freezing days, it is necessary to define the beginning and end of the thawing and freezing seasons. Concerning the variability of the freezing point during the spring and fall, and the inconsistence of the beginning and end of the thawing and freezing seasons for air and ground surface, usually the surface temperature is chosen to define the thawing and freezing seasons because of the lower variability of surface temperature [*Karunaratne*, 2003].

Since n-factors summarize the surface energy balance, it can be used to investigate the thermal regime of the permafrost. Combining the n-factors, air degree-days and thermal conductivities for the thawing and freezing seasons, *Jorgenson and Kreig* [1988] first use n-factors to predict permafrost distribution within a small watershed [*Karunaratne*, 2003]. Incorporating the thawing n-factor into the Stefan model, it increased the accuracy of the estimation of the active layer thickness [*Klene et al.*, 2001]. Besides, *Smith and Riseborough* [1996] used n-factors in a model to predict the temperature at the top of permafrost (TOPP) with air temperature and subsurface thermal conditions. From a sensitivity analysis of the model, *Smith and Riseborough* [1996] pointed out that the relative influence of various controlling factors would make the air, surface and permafrost temperature change different under any set of conditions.

Below the surface, heat transfer is usually dominated by heat conduction. However, under certain circumstances non-conductive processes may become important within the active layer [e.g. *Farouki*, 1981; *Outcalt et al.*, 1990; *Hinkel and Outcalt*, 1994]. Due to the variability of thermal properties in the active layer, this leads to a thermal offset effect. This thermal offset is defined as the difference between the mean annual surface temperature (MAST) and mean annual soil temperature at the top of permafrost (T_{top}). It is determined by several factors such as the conductivity ratio of the thawed soil and the frozen soil, soil moisture at the surface, and snow cover. The thermal regime in the active layer is strongly influenced by this thermal offset. T_{top} can be estimated by the TTOP model using n-factors [*Smith and Riseborough*, 1996] as follows:

$$T_{top} = \frac{K_t DDT_s - K_f DDF_s}{K_f P}, \tag{6.12}$$

where, K_t, K_f are the thermal conductivities of the thawed ground and the frozen ground, respectively, which can be defined as the thermal conductivity ratio $r_k = K_t/K_f$, DDT_s, DDF_s are thawing and freezing indices (note: here the unit is ℃·day, whereas in I the unit is ℃·s), and P is period (365 days).

Inverse parameterization from point to field scale Based on the above two described models, the thermal conductivities of thawed ground and frozen ground can be estimated, if we know the maximum thaw depth, the total water content in the active layer and soil temperature at the surface and bottom of the active layer. From point measurements, for instance soil-weather monitoring sites, meteorological data, soil temperature and soil water content can be obtained with state-of-the-art instrumentation. Here we present an alternative method to estimate the thermal conductivity, although there are several methods for estimates of the effective thermal diffusivity using time series of measured soil temperatures [e.g. *Carson*, 1963; *Adams et al.*, 1976; *Horton et al.*, 1983; *Hurley and Wiltshire*, 1993; *Zhang and Osterkamp*, 1995; *Hinkel*, 1997; *Pringle et al.*, 2003].

In this method, it is assumed that the requirements of the Stefan model and TTOP model are satisfied. Based on these two models, the thermal conductivity can be estimated as follows. From equation 6.7, the apparent thermal conductivity of the thawed soil k_t can be estimated as

$$k_t = \frac{L_w \theta X^2}{2 I_{ts}}, \tag{6.13}$$

where L_w is the latent heat of fusion for water, and θ is the mean volumetric soil water content. From equations 6.12 and 6.13, the apparent thermal conductivity of the frozen soil K_f can be estimated as

$$K_f = \frac{k_t DDT_s}{T_{top} P + DDF_s}. \tag{6.14}$$

Since multi-channel GPR can be used to quickly measure the active layer thickness and its soil water content at the field scale [*Gerhards et al.*, 2008], it is a promising tool for field-scale parameterization of thermal conductivity. As presented in the last chapter, the accuracy of reflector depth and soil water content can reach around ±10 cm and ±3%. In addition, multi-channel GPR also has been used to measure spatial variations and water content of active layers in permafrost regions [e.g. *Gerhards et al.*, 2008; *Wollschläger et al.*, 2010], and the results are exciting at the study sites. Hence, in principle, using multi-channel GPR, lateral variations in thermal conductivity should be obtainable without disturbing the active layer.

6.3.2 Inverse parameterizations at the study sites

For all these considered profiles, the thermal diffusivity at each depth of the studied profiles are shown in Tables 6.1, 6.2,6.3. The heat capacity for each depth is the arithmetic mean of the heat capacities during the each period of the thawed or frozen thermal diffusivity estimate. The volumetric heat capacity of the soil above the considered depth is determined by the geometric mean of all heat capacity values calculated at each measured depth. The values shown in Table 6.5 are the arithmetic mean of different depths above the permafrost table and their standard deviations.

Due to the lower variability of the surface temperature compared to the air temperature, the n-factor seasons are defined from the surface temperature. The freezing season starts from the day when the daily mean ground surface temperature is positive and keeps negative in the following half month, and ends when the daily mean ground surface temperature is negative and keeps positive in the following half month. While in the thawing season it is just the inverse case.

The changes in surface temperature often lag behind the changes in air temperature, because of the higher heat capacity of soil compared to air. To stay consistent with the definition of surface thawing and freezing seasons, the beginning and end of air thawing and freezing seasons are defined to be the same in the n-factors calculation.

At Chumaer, Qumahe and Zuimatan, two freezing n-factors were calculated from 2006 to 2008 during the freezing seasons, and two thawing n-factors were calculated from 2007 to 2008 during the thawing seasons. Due to data missing problems, the n-factors were calculated with a preprocessing of linear interpolation. For a short-time data gap, linear interpolation is an effective approach, but for the large periods, the accuracy will be reduced by the linear interpolation.

At Chumaer, there is a large data gap from day number 472 to 586 in air temperature measurements shown in Figure 3.1, and it crosses from the first freezing season to the subsequent thawing season. The deviation of the first freezing index is negligible for the short gap during this calculated period. But the deviation of the first thawing index is much stronger, because the data gap almost accounts for half of the subsequent thawing season. In the ground surface temperature measurements, there is also a data gap from day number 582 to 632, which almost accounts for one third of the first thawing season. Unfortunately, this data gap occurred during a period with strong fluctuations, and the linear interpolation has a strong deviation. At Qumahe, one clear data gap occurred from day number 586 to 615 in the first thawing period in the air and ground surface temperature measurements. This data gap just locates in the warmest period in the summer, the deviation of air and ground surface thawing index is serious with linear interpolation. At Zuimatan, there are three large data gaps at day number 385-460, 722-818 and 988-1040 in the air and ground surface temperature measurements. The linear interpolation might cause certain deviations, which made the first and second freezing indices smaller. At Tianshuihai, there is a large data gap from day number 347 to 446 in the air and ground surface temperature measurements. Because the data gap crossed the peak, then the linear interpolation makes the first freezing index smaller than true value. After linear interpolation, the thawing and freezing n-factors were derived using equation 6.9. All the thawing and freezing n-factors are presented in Table 6.4.

Because of several missing data in the first freeze-thaw cycle, they caused obvious deviations in Table 6.4. For instance, there are large missing data gaps in air temperature measurements during the thawing season at Chumaer and Qumahe, while it is much better at Zuimatan. Thus, during 2006-2007 the air thawing index at Zuimatan is 180 and 224℃·*day* larger than at Chumaer and Qumahe, respectively. To get a general impression of the differences of soil-atmosphere interactions at all study sites, the second freeze-thaw cycle (2007-2008) was chosen. First of all, all data were measured at the same time. Besides, there are fewer missing data during this period. Although there is a large data gap in this period at Tianshuihai, the complete data in the period 2008-2009 can give a reference for comparison. The largest freezing and thawing index of air and ground surface are both at Tianshuihai. But the thawing n-factor is not the largest one. For missing data during freezing period, the freezing n-factor at Tianshuihai is the largest one but deviated somehow, and it is up to 0.78 during the period 2008-2009. Considering the missing data at Zuimatan, the freezing and thawing characteristics of air temperature are quite similar and the MAAT during the period 2007-2008 are -4.9℃, -4.9℃ and -3.7℃ at Chumaer, Qumahe and Zuimatan, respectively. At Qumahe, the freezing and thawing indices are much smaller than at the other sites, and the freezing and thawing n-factors are also smaller. Apparently, the processes at the surface at Qumahe are totally different from the other sites. It may be attributed to the surface soil moisture and vegetation. The heat transfer mechanisms at the surface should be similar at Chumaer and Zuimatan. Although the surface characteristics

Table 6.4. Seasonal thawing and freezing indices of air and ground surface (DDT_a, DDF_a, DDT_s, DDF_s in [℃·*day*]), n-factors (thawing and freezing factors: n_t, n_f [-]) and estimated mean annual air and ground surface temperature (MAAT, MAST in [℃]) at the study sites during three freeze-thaw cycles.

		Chumaer	Qumahe	Zuimatan	Tianshuihai
2006-2007	DDF_s	1326	802	1411	-
	DDT_s	1324	635	1306	-
	DDF_a	2276	2381	2249	-
	DDT_a	575	531	755	-
	n_t	2.30	1.20	1.73	-
	n_f	0.58	0.34	0.63	-
	MAAT	-4.7	-5.1	-4.1	-
	MAST	6.2	1.3	3.8	-
2007-2008	DDF_s	1296	791	1189	1722
	DDT_s	1197	853	1087	1369
	DDF_a	2267	2217	1907	2508
	DDT_a	491	447	570	639
	n_t	2.44	1.91	1.91	2.14
	n_f	0.57	0.36	0.62	0.69
	MAAT	-4.9	-4.9	-3.7	-5.1
	MAST	5.5	2.1	3.1	4.8
2008-2009	DDF_s	-	-	-	2110
	DDT_s	-	-	-	1225
	DDF_a	-	-	-	2694
	DDT_a	-	-	-	469
	n_t	-	-	-	2.61
	n_f	-	-	-	0.78
	MAAT	-	-	-	-6.1
	MAST	-	-	-	3.2

are similar at Chumaer, Zuimatan and Tianshuihai, the strong temperature fluctuations of the air at the ground surface indicate that the climatic factors play a more important role at Tianshuihai.

Surface thawing and freezing indices (DDT_s, DDF_s) calculated in yearly periods, are shown in Table 6.4 for all study sites. Due to missing data at Chumaer, Qumahe and Tianshuihai, we just choose one complete freeze-thaw cycle of measured data for each site: from 2007 to 2008 at Chumaer and Qumahe, and from 2008 to 2009 at Tianshuihai. The total water content is calculated from point measurements by linear interpolation. The thaw depth is identified by the contour line 0℃ from the interpolation of soil temperature measurements. Due to the high density of measured layers, its error should be within half the distance of two interpolated sensors (about 10 cm). In the calculation, the deepest sensor is thought located at the maximum thaw depth at Chumaer. However, the deepest temperature sensors are still above the permafrost table. Therefore, the maximum thaw depths of both profiles are underestimated at Chumaer.

In Table 6.5, the apparent thermal conductivity in summer and in winter are estimated by the inverse method and the transfer function. Here we should keep in mind that the apparent thermal conductivity from the inverse method represents a mean value from surface to the maximum thawed depth in summer or in winter, and it includes non-conductive processes. While due to

Table 6.5. Estimated thermal conductivity of thawed soil and frozen soil by the inverse method (A) and the transfer function method (B) at Chumaer (C), Qumahe (Q) and Tianshuihai (T).

site		d	θ	T_{top}^m	K_t	K_f	K_t	K_f
		[m]	[−]	℃	W m^{-1} K^{-1}			
					A		B	
C	P1	2.09	0.29	-0.14	2.02	1.95	2.35 ± 0.49	1.72 ± 0.23
	P2	2.28	0.22	-0.21	1.84	1.81	2.54 ± 0.18	1.67 ± 0.18
T	P1	1.60	0.23	-2.26	0.91	0.87	1.16 ± 0.09	1.29 ± 0.31
	P2	1.53	0.28	-2.26	1.03	0.99	1.13 ± 0.05	1.40 ± 0.26
Q		1.15	0.65	-0.41	1.47	1.93	0.38 ± 0.03	0.41 ± 0.05

the limit of the transfer function method, it cannot be applied to the thawing or freezing front. Therefore, as a reference for the inverse method, the mean values of the estimations at the projected depths close to the front were calculated in summer and in winter. From comparison of the results from the two methods, we can find that the absolute values of thermal conductivity at Chumaer and Tianshuihai are approximately consistent, while at Qumahe, apparent thermal conductivities calculated from the different methods differ significantly. The main reason is that the non-conductive processes account for a significant weight at Qumahe, but the apparent thermal conductivity from the transfer function method cannot include these effects.

6.3.3 Discussion

Interpreting the differences between the presented two methods From the above comparison of the thermal conductivity estimated with the two methods in Table 6.5, we can find that the values are approximately consistent with each other at Chumaer and Tianshuihai, while there is a large difference at Qumahe. This discrepancy is mainly attributed to two reasons. One is the applicability of the respective methods, the other one is the variability of thermal diffusivity at the different sites.

For the applicability of both methods, their assumptions have to be considered. In the Stefan model, the first assumption is to ignore sensible heat, which includes the initial temperature of the frozen soil (close phase-change temperature), and all heat flow is used for fusion at the thawing or freezing front. *Romanovsky and Osterkamp* [1997] pointed out that the assumption of this initial temperature can cause significant errors in applying the Stefan model to cold permafrost. On the QTP, most of the permafrost is warm. Hence, this assumption might be reasonable. However, at the study sites, the ground temperature at Tianshuihai is about 3℃ lower than at the other two sites. Therefore, the deviations of the thermal conductivity at Tianshuihai may be slightly larger than the other sites. In the n-factor model, equilibrium (quasi-steady state) is assumed. With a changing climate, the inter-annual variation or long term trend in the upper boundary conditions can result in transient departures from equilibrium [*Riseborough*, 2007]. But generally, these assumptions in the inverse method are appropriate at all study sites.

The parameter estimation is sensitive to the assumption in the transfer function method. Since it assumes pure heat conduction in the soil profile, its application is restricted strongly. For cold permafrost, this assumption works properly [*Roth and Boike*, 2001], but for warm permafrost, the unfrozen water exerts significant influences on the thermal properties. Thus, we have to consider these non-conductive processes and their variations in this method. As discussed before, the non-conductive processes such as infiltration of rainfall in summer, vapor flux in unsaturated soils and unfrozen water effects in frozen soils, impact the estimation of the

D_h^{app}. The worst case for applying the transfer function method is at Qumahe. Due to the high water content in the warm permafrost, the impacts of the unfrozen water can not be neglected. The effect of unfrozen water on the effective frozen thermal conductivity has been discussed by *Riseborough* [2002]. He pointed out that failure to take the effect of unfrozen water into account will produce significant errors, the largest error occurring around 0℃. Since the total water content is much larger than that of the other sites, the changing amount of unfrozen water at Qumahe is much more significant. Besides, due to the dipping slope of the active layer, lateral water flow in summer can also impair the assumption of pure heat conduction in the profile at Qumahe. Therefore, the estimated thermal conductivity values from the transfer function method at Qumahe are seriously impacted by non-conductive processes.

Aside from the influence of the applicability of the methods, the spatial and temporal variability of the thermal conductivity should be taken into account, implementing the mean values of thawed or frozen thermal conductivity during summer or winter.

Temporally, the apparent thermal conductivity of active layer depends on state of system, which varies during the season. Since the thermal conductivity of ice is more than three times the thermal conductivity of water, the thermal conductivity of the saturated frozen soil is usually larger than that of the thawed soil. According to the empirical estimation of thermal properties from *Johansen* [1975], the ratio of the thawed thermal conductivity k_t to the frozen thermal conductivity K_f is a function of volumetric water content [*Riseborough*, 2004]. In unsaturated soils, the thawed thermal conductivity can be larger than the frozen thermal conductivity, when the soil water content reduces to a certain range. Besides, due to drainage and evaporation, there can be large differences of total water content in winter and in summer. As shown in Figures 6.8, 6.10 and 6.9, there is significant water loss from summer to winter at these study sites. Hence, this kind of water content difference can change the ratio of the thawed thermal conductivity to the frozen thermal conductivity. In addition, non-conductive heat transfer processes occur at a certain time, causing the effective thermal diffusivity to change with time [e.g. *Kane et al.*, 2001; *Riseborough*, 2004].

Spatially, the thermal conductivity of the active layer relates to the changes of the soil constituents. In a vertical profile, the soil density and saturation typically increases with depth in seasonally frozen ground, while in permafrost regions, the soil dry bulk density decreases with depth due to ground ice accumulation [*Riseborough*, 2004]. Therefore, the ratio of the thawed thermal conductivity to the frozen thermal conductivity in permafrost or unsaturated seasonally frozen ground will increase with depth. Besides, the thermal conductivity strongly varies with stratification in depth [*Pringle et al.*, 2003]. In the lateral direction, the constituents of the active layer can vary significantly, and accordingly the thermal conductivity has a large variability. As presented by *Ikard et al.* [2009], studying the active layers across a soil moisture gradient in Antarctica shows that the apparent thermal diffusivity increases with increasing soil water content across the landscape.

In brief, due to evident influence of non-conductive processes in warm permafrost regions on the QTP the transfer function method, as well as other Fourier-methods and other conduction approaches is strongly limited by its prerequisite in thermal conductivity parameterization for climate-permafrost modeling. Whereas, the inverse method includes the influences of variational complex processes in space and time, which enlarges the representations of physical processes in active layers.

Application of multi-channel GPR for field-scale parameterization As presented above, the applied inverse method supports an alternative way of estimating seasonal soil thermal conductivity at point monitoring sites. Since it includes variations of soil constituents in depth and effects of non-conductive heat transfer processes, its results should be closer to the true

effective thermal conductivity than the empirical methods using pure heat conductive process. But this method needs more validation in future work. For a field-scale parameterization, multi-channel GPR constitutes an opportunity to quickly measure active layer depth and its soil water content. Therefore, this tool may further help us to do field-scale parameterizations of thermal conductivity as shown in Figure 6.11.

The hypothesis for this approach is that the upper boundary condition of energy flux is the same in the measured field, namely there is no significant difference in net radiation. In the application of multi-channel GPR, the thawed thermal conductivity can be easily estimated from meteorological data and the GPR measurements when the active layer reaches its maximum thaw depth. But for a frozen thermal conductivity estimation, we need another parameter of the mean annual temperature at the top of the permafrost T_{top}. Since T_{top} of different active layer can vary differently at the field scale, it may impair the accuracy of thermal conductivity estimation of frozen soils when we use a constant value from the weather station measurements.

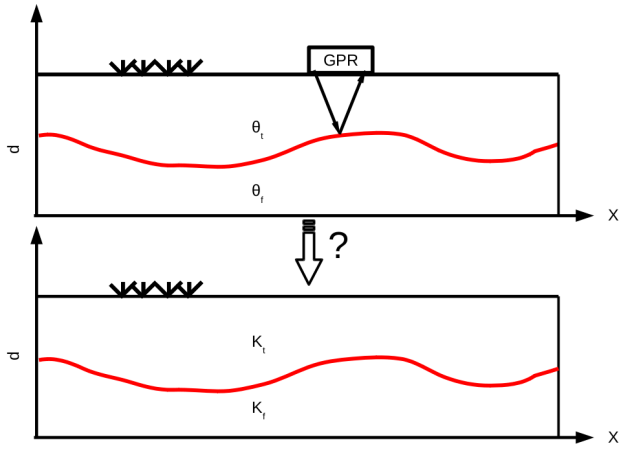

Figure 6.11. The sketch of applying multi-channel GPR to measure field-scale thermal conductivity distribution.

6.4 Conclusions

Through characterizing the heat transfer in three different active layers with the transfer function method, results demonstrate that the application of this method is influenced by three important factors. Firstly, given the large daily dynamic range of air temperature, the heat transfer near the surface is disturbed by the non-conductive process of daily freeze-thaw. Secondly, for the warm permafrost the high variability of D_h^{app} with a near-zero soil temperature strongly influence the the application of the transfer function method, for instance at Qumahe. Thirdly, aside from the non-conductive processes near the surface, other factors like soil heterogeneity and ground water can also complicate this method. The variation of apparent thermal diffusivity in time and depth can not be ignored in thermal parameterizations for permafrost modeling in the warm permafrost region.

Variations of the mean estimated D_h^{app} with season at Tianshuihai are similar to those at Chumaer. The mean estimated D_h^{app} varies in a small range. The active layers with dry surface

at Chumaer and Tianshuihai have almost lost the property of making evident temperature offset between ground surface and permafrost table by varying thermal property. This may be one important reason for the sensitive response of dry permafrost to climate change on the QTP.

Based on empirical climate-permafrost models, an inverse method for thermal conductivity parameterization is developed. Assuming equilibrium of the permafrost soil, the Stefan model and the n-factor model are used to estimate the effective thermal conductivity at the monitoring sites. Opposed to the empirical thermal conductivity parameterization, the inverse method enlarges the parameterization which can include the influences of variational complex processes in space and time. The transfer function method would be impaired by the temporal variations of non-conductive processes and its assumption of dominant heat conduction. The comparison of both methods shows that the estimated values of the thermal conductivity are consistent at Chumaer and Tianshuihai, although the value estimated from the inverse method is smaller than that from the geometric mean based on the transfer function method; at Qumahe, there is a large discrepancy between the two methods, which is attributed to their different representation of heat transfer processes. The transfer function method would fail when the non-conductive processes play a significant role like at Qumahe.

In view of the capability of multi-channel GPR for measuring reflector depths and soil water content in chapter 5, the inverse parameterization is suggested to be extended to field-scale parameterization with multi-channel GPR. In future work, further field measurements and validation are needed to corroborate.

7
Summary and conclusions

To investigate the characteristics of permafrost degradation on the QTP, four study sites (Chumaer, Qumahe, Zuimatan and Tianshuihai) with different permafrost states were selected. The hydraulic and thermal dynamics of the active layers were explored in this thesis. The principal objectives of this thesis were: 1) to understand the physical mechanisms governing the permafrost-atmosphere interaction through characterizing the hydraulic and thermal dynamics of the active layers at the study sites; 2) to explore the feasibility of the multi-channel GPR to quantify the field-scale thermal properties of various active layers on the QTP.

Concerning characteristics of permafrost and performances of the instruments in the field, the measured data have to be cleaned. Two points were proposed to improve the data evaluation in chapter 2. Based on the characteristics of the heat transfer around the thawing or freezing front, a semi-interpolation was proposed to calculate the soil temperature at the position of soil water content sensors. It effectively improved the accuracy of the temperature interpolation. Since the measure conditions at the study sites were out of the applying range of the empirical formula supplied by Campbell Scientific, Inc. for CS616 evaluation, a new method for evaluating the soil water content was proposed. The comparison of TDR and CS616 at Qumahe showed that this method can effectively extend the application of CS616 to our measure conditions.

Hydraulic and thermal dynamics of various active layers To study the hydraulic and thermal dynamics of various active layers at the four study sites, two steps were taken into account. Firstly, the characteristics of the permafrost were analyzed based on the observations from the soil-weather monitoring stations in chapter 3. Secondly, physical mechanisms between permafrost and atmosphere were further investigated by the quantitative analyses in chapter 4. Through analyzing the observed major meteorological conditions and the hydraulic-thermal dynamics, we can get a view of the characteristics of the weather-permafrost interaction at these permafrost sites. A modified energy balance model was applied to characterize the thermal regimes at Chumaer, Qumahe and Tianshuihai. From the applications we found that given current accuracies of the methods for each components, the energy balance model can generally capture the major processes in the calculated periods. The characteristics and physical processes of hydraulic and thermal dynamics in the active layers at the study sites are summarized as follows.

The heat exchange through the soil-atmosphere interaction at the study sites are dominated by different local factors. In the warm permafrost regions, the thick active layer at Chumaer was filled with a large amount of groundwater at the lower part of the active layer. While the active layer is nearly saturated and thin at Qumahe. Chumaer, Qumahe and Zuimatan sites are located in the warm permafrost region on the northeastern QTP. The surface heat exchange was strongly influenced by the summer monsoon at these sites. The seasonally variational surface heat exchange is more significant at Qumahe than the other sites because of the dense vegetation and wet surface. The Tianshuihai site is located in the cold permafrost region on the western

QTP. The active layer is extremely dry near the surface. Therefore, the influence of precipitation was negligible.

The hydraulic and thermal pattern depends on a number of factors. Soil water content in the active layers influenced the duration of the thermal period by changing the heat flux and thermal properties in the freeze-thaw cycles. At Chumaer, the thermal regime of the active layer during the SST period is mainly controlled by the net radiation, sensible heat flux and latent heat flux at the surface. The latter two components at the surface are comparable, but the latent heat flux is mainly dependent on the precipitation. During the SST period, the thermal regime of the active layer at Qumahe is similar to that at Chumaer. But evaporation plays a significant role in preventing warming the active layer due to the wet active layer and surface runoff. Besides, the latent heat dominates the ground heat, which is over 90% in the saturated active layer at Qumahe. At Tianshuihai, the thermal regime of the active layer is completely different from the above two sites. The surface sensible heat flux is much larger than those at other sites during the SST period. Due to the dry ground surface with little precipitation, actual evaporation is negligible at this site. But during the AF and WC periods, the sensible heat flux is reduced and comparable with the other sites. The strong sensible heat flux during the SST period may be related to the local microclimate. In general, the mechanisms of the thermal regime at Chumaer and Qumahe are controlled by regional factors like the monsoon. While, the mechanisms of the thermal regime at Tianshuihai is controlled by local factors like local mountainous atmosphere circulation.

Heat transfer in the active layers at the study sites were characterized by the transfer function method in chapter 6. Following conclusions can be drawn: (1) temporal non-conductive processes like daily freeze-thaw cycle, infiltration, evaporation and convection significantly influence the heat transfer near the surface in various degree at the study sites; (2) for warm permafrost, non-conductive heat transfer processes still play a significant role in ground heat transfer during the winter at Chumaer and Qumahe. For the cold permafrost, there is non-significant change in ground heat transfer between winter and summer at Tianshuihai due to the dry near-surface soil; (3) variability of the estimated thermal diffusivity at various active layers are influenced by soil heterogeneity and non-conductive processes. These characteristics of the heat transfer mechanisms and soil heterogeneity at the study sites apparently challenge the suitability of the commonly used soil thermal conductivity parameterizations for permafrost modeling at diverse scales on the QTP.

Quantification of field-scale soil properties with multi-channel GPR The analyses in chapter 5 show that the multi-channel GPR is applicable to monitor field-scale soil water dynamics. The accuracy analysis shows that the accuracy of multi-channel GPR is strongly related to the antenna separation. Optimization of multi-channel GPR setup for different reflector depths or soil water content is essential to the accuracy of the results. Results from a time series of field measurements indicate that – at the investigated site – given the current measurement uncertainties, the depth of the dominant reflectors can be identified with an accuracy of about 0.1 m, and the uncertainty in variational soil dielectric permittivity is about 0.5. The field application demonstrates that multi-channel GPR is promising to monitor the spatial and temporal soil water dynamics in the field.

The thermal conductivity was estimated with the transfer function method by using time series of soil temperature and soil water content measurements in chapter 6. But it was impaired by the temporal variations of non-conductive processes, for instance at Qumahe. Based on empirical climate-permafrost models, an inverse parameterization for thermal conductivity is developed. Assuming a thermal equilibrium in the permafrost, the Stefan model and the n-factor model were used to estimate the effective thermal conductivity at the study sites. Opposed to the empirical

thermal conductivity parameterization, the inverse method also includes non-conductive heat transfer effects. The comparison of both methods shows that the estimated values of the thermal conductivity are approximately consistent at Chumaer and Tianshuihai, although the value estimated from the inverse method is smaller than the geometric mean value estimated with the transfer function method. Values estimated from the inverse method at Qumahe are reasonable, whereas the transfer function method failed because of the significant influence of the non-conductive processes.

Results from the inverse parameterization at the stations provided the basis for field-scale parameterization of soil thermal conductivity with multi-channel GPR. In view of the capability of the multi-channel GPR to accurately measure reflector depths and soil water content in chapter 5, it indicates the possibility of quantifying the field-scale thermal property in active layers. Use of multi-channel GPR in the field-scale parameterization has not been validated yet. Future analyses will help to verify if this approach is feasible.

Bibliography

Adams, W. M., G. Watts and G. Mason, 1976: Estimation of thermal diffusivity from field observations of temperature as a function of time and depth., *American Mineralogist*, **61**, 560–569.

Anisimov, O. A., 2007: Potential feedback of thawing permafrost to the global climate system through methane emission, *Environmental Research Letters*, **2**, (4), doi:10.1088/1748–9326/2/4/045016.

Anisimov, O. and F. Nelson, 1996: Permafrost distribution in the Northern Hemisphere under scenarios of climatic change, *Global and Planetary Change*, **14**, (1-2), 59–72.

Anisimov, O. and S. Reneva, 2006: Permafrost and changing climate: the Russian perspective, *Ambio*, **35**, (4), 169–175.

Anisimov, O., N. Shiklomanov and F. Nelson, 1997: Effects of global warming on permafrost and active-layer thickness: results from transient general circulation models, *Global and Planetary Change*, **15**, 61–77.

Ashrae, 1997: *ASHRAE Handbook-Fundamentals*, Atlanta: American Society of Heating, Refrigerating and Air-Conditioning Engineers, Inc.

Bai, H., Z. Ma and W. Dong, 2005: Relationship between Qinghai-Xizang Plateau region monsoon features and abnormal climate in China, *Journal of applied meteorological science*, **16**, (4), 484–491.

Barnett, T. P., J. C. Adam and D. P. Lettenmaier, 2005: Potential impacts of a warming climate on water availability in snow-dominated regions, *Nature*, **438**, 303–309.

Boike, J., K. Roth and P. P. Overduin, 1998: Thermal and hydrologic dynamics of the active layer at a continuous permafrost site (Taymyr Peninsula, Siberia), *Water Resources Research*, **34**, (3), 355–363.

Bonner, C. S., M. C. B. Ashley, X. Cui, L. Feng, X. Gong and et al. et al., 2010: Thickness of the Atmospheric Boundary Layer Above Dome A, Antarctica, during 2009, *Publications of the Astronomical Society of the Pacific*, **122**, (895), 1122–1131.

Bradford, J. H., 2008: Measuring water content heterogeneity using multifold GPR with reflection tomography, *Vadose Zone Journal*, **7**, 184–193.

Brosten, T. R., J. H. Bradford, J. P. McNamara, M. N. Gooseff, J. P. Zarnetske, W. B. Bowden and M. E. Johnston, 2009: Estimating 3D variation in active-layer thickness beneath arctic streams using Ground-penetrating radar, *Journal of Hydrology*, **373**, 479–486.

Brown, J., K. M. Hinkel and F. E. Nelson, 2000: The circumpolar active layer monitoring (CALM) program: research design and initial results, *Polar Geography*, **24**, (3), 165–253.

Carlson, H., 1952: Calculation of depth of thaw in frozen ground. Frost action in soils Highway Research Board, Special Report Number 2, 192–223.

Carson, J. E., 1963: Analysis of soil and air temperatures by Fourier techniques, *Journal of Geophysical Research*, **68**, (8), 2217–2232.

Chan, C. Y. and R. J. Knight, 1999: Determining water content and saturation from dielectric measurements in layered materials, *Water Resources Research*, **35**, (1), 85–93.

Chen, W., Y. Zhang, J. Cihlar, S. L. Smith and D. W. Riseborough, 2003: Changes in soil temperature and active layer thickness during the twentieth century in a region in western Canada, *Journal of Geophysical Research*, **108**, doi:10.1029/2002JD003355.

Cheng, G. and D. Francesco, 1992: Distribution of mountain permafrost and climate, *Permafrost and Periglacial Processes*, **3**, 83–91.

Cheng, G. and T. Wu, 2007: Responses of permafrost to climate change and their environmental significance, Qinghai-Tibet Plateau, *Journal of Geophysical Research*, **112**, doi:10.1029/2006JF000631.

Cheng, G. and L. Zhao, 2000: The problems associated with permafrost in the development of the Qinghai-Xizang Plateau (in Chinese), *Quaternary Sciences*, **20**, (6), 521–531.

Daniels, D., 2004: *Ground Penetrating Radar*, Knoval (Institution of Engineering and Technology).

Davis, J. L. and A. P. Annan, 1989: Ground-penetrating radar for high resolution mapping of soil and rock stratigraphy, *Geophysical Prospecting*, **37**, 531–551.

Deming, D., J. Sass, A. Lachenbruch and R. D. Rito, 1992: Heat flow and subsurface temperature as evidence for basin-scale ground-water, *GSA Bulletin*, **104**, (5), 528–542.

de Silans, A. M. B. P., B. A. Monteny and J. P. Lhomme, 1996: Apparent soil thermal diffusivity, a case study: HAPEX-Sahel experiment, *Agricultural and Forest Meteorology*, **81**, 201–216.

de Vries, D., 1963: *Physics of Plant Environments*, chapter Thermal properties of soils, 210–235, North-Holland.

Ding, Y., J. Yang, S. Liu, R. Chen, G. Wang, Y. Shen, J. Wang, C. Xie and S. Zhang, 2003: Eco-environment range in the source regions of the Yangtze and Yellow rivers, *Journal of Geographical Sciences*, **13**, 172–180.

Dobson, M., F. Ulaby, M. Hallikainen and M. El-Rayes, 1985: Microwave dielectric behavior of wet soil-part II: dielectric mixing models, *Geoscience and Remote Sensing, IEEE Transactions on*, **GE-23**, (1), 35–46.

Esch, D. C., M.ASCE and T. E. Osterkamp, 1990: Cold regions engineering: climatic warming concerns for Alaska, *Journal of Cold Regions Engineering*, **4**, (1), 6–14.

Etzelmuller, B., H. Farbrot, A. Guomundsson, O. H. O.E., Tveito and H. Bjornsson, 2007: The regional distribution of mountain permafrost in Iceland, *Permafrost and Periglacial Processes*, **18**, 185–199.

Farouki, O. T., 1981: Thermal properties of soils, Bericht, U.S. Army cold regions research and engineering laboratory.

Farouki, O., 1986: Thermal properties of soils, *Series on Rock and Soil Mechanic*, **11**, 136.

Fishman, G. S., 1996: *Monte Carlo: concepts, algorithms, and applications*, Springer Verlag.

Galagedara, L. W., G. W. Parkin and J. D. Redman, 2003: An analysis of the Ground-penetrating radar direct ground wave method for soil water content measurement, *Hydrological Processes*, **17**, 3615–3628.

Garambois, S., P. Sénéchal and H. Perroud, 2002: On the use of combined geophysical methods to assess water content and water conductivity of near-surface formations, *Journal of Hydrology*, **259**, 32–48.

Gerhards, H., 2008: *Ground penetrating radar as a quantitative tool with applications in soil hydrology*, Dissertation, Heidelberg University.

Gerhards, H., U. Wollschläger, Q. Yu, P. Schiwek, X. Pan and K. Roth, 2008: Continuous and simultaneous measurement of reflector depth and average soil-water content with multichannel ground-penetrating radar, *Geophysics*, **71**, doi:10.1190/1.2943669.

Goodrich, L., 1982: The influence of snow cover on the ground thermal regime, *Canadian Geotechnical Journal*, **19**, 421–432.

Grote, K., S. Hubbard and Y. Rubin, 2003: Field-scale estimation of volumetric water content using ground-penetrating radar ground wave techniques, *Water Resources Research*, **39**, (11).

Grotzinger, J., T. H. Jordan, F. Press and R. Siever, 2007: *Understanding Earth*, W.H. Freeman.

Hancock, P. and B. J. Skinner, 2000: *Permafrost and climate change*, The Oxford Companion to the Earth.

Harris, C., L. U. Arenson, H. H. Christiansen and et. al et. al, 2009: Permafrost and climate in Europe: monitoring and modelling thermal, geomorphological and geotechnical responses, *Earth-Science Reviews*, **92**, (3-4), 117–171.

He, Y., 1991: Application of electrical prospecting on permafrost along Xiangjiang-Xizang highway (in Chinese), *Journal of Glaciology and Geocryology*, **13**, (3), 255–259.

Henry, K. and M. Smith, 2001: A model-based map of ground temperatures for the permafrost regions of Canada, *Permafrost and Periglacial Processes*, **12**, (4), 389–398.

Hinkel, K. M., 1997: Estimating seasonal values of thermal diffusivity in thawed and frozen soils using temperature time series, *Cold Regions Science and Technology*, **26**, 1–15.

Hinkel, K. M. and S. I. Outcalt, 1994: Identification of heat-transfer processes during soil cooling, freezing, and thaw in central Alaska, *Permafrost Periglacial Processes*, **5**, (4), 217–235.

Hinkel, K. M., F. Paetzold, F. E. Nelson and J. G. Bockheim, 2001: Patterns of soil temperature and moisture in the active layer and upper permafrost at Barrow, Alaska: 1993-1999, *Global and Planetary Change*, **29**, 293–309.

Hoelzle, M., M. Wegmann and B. Krummenacher, 1999: Miniature temperature dataloggers for mapping and monitoring of permafrost in high mountain areas: first experience from the Swiss Alps, *Permafrost and Periglacial Processes*, **12**, 113–124.

Horton, R., P. J. Wierenga and D. R. Nielsen, 1983: Evaluation of methods for determining the apparent thermal diffusivity of soil near the surface, *Soil Science Society of America Journal*, **47**, 25–32.

Huang, Y., D. Guo and X. Zhao, 1993: The desertification in the permafrost region of Qinghai-Xizang Plateau and its influences on environment (in Chinese), *Journal of Glaciology and Geocryology*, **15**, (1), 52–57.

Huisman, J. A., C. Sperl, W. Bouten and J. M. Verstraten, 2001: Soil water content measurements at different scales: accuracy of time domain reflectometry and ground-penetrating radar, *Journal of Hydrology*, **245**, 48–58.

Huisman, J. A., J. D. Hubbard, J. D. Redman and A. P. Annan, 2003*a*: Measuring soil water content with ground penetrating radar: a review, *Vadose Zone Journal*, **2**, 476–491.

Huisman, J. A., J. J. J. C. Snepvangers, W. Bouten and G. B. M. Heuvelink, 2003*b*: Monitoring temporal development of spatial soil water content variation: comparison of ground penetrating radar and time domain reflectometry, *Vadose Zone Journal*, **2**, 519–529.

Hurley, S. and R. Wiltshire, 1993: Computing thermal diffusivity from soil temperature measurements, *Computers and Geosciences*, **19**, 475–477.

Ikard, S. J., M. N. Gooseff, J. E. Barrett and C. Takacs-Vesbach, 2009: Thermal characterisation of active layer across a soil moisture gradient in the McMurdo Dry Valleys, Antarctica, *Permafrost and Periglacial Processes*, **20**, 27–39.

Ishikawa, M., Y. Zhang, T. Kadota and T. Ohata, 2006: Hydrothermal regimes of the dry active layer, *Water Resources Research*, **42**, doi:10.1029/2005WR004200.

Jacobs, A. F. G., J. H. Boxel and R. M. M. El-Kilani, 1994: Nighttime free convection characteristics within a plant canopy, *Boundary-Layer Meteorology*, **71**, (4), 375–391.

Jacobs, A. F. G., A. Verhoef and H. A. R. DeBruin, 1996: Sensible heat flux from sparse vegetation estimated using Nusselt numbers, *Physics and Chemistry of the Earth*, **21**, 107–110.

Jiang, H. and K. Wang, 2001: Analysis of the surface temperature on the Tibetan plateau from satellite, *Adatmospheric sciences*, **18**, (6), 1215–1223.

Jin, L., N. Qin and X. Mao, 2005: Features of runoff in the upper reaches of the Tongtian river and its climatic probobility forecast in recent 45 years (in Chinese), *climatic and environmental research*, **10**, (2), 220–228.

Jin, H., L. Zhao, S. Wang and R. Jin, 2006: Thermal regimes and degradation modes of permafrost along the Qinghai-Tibet Highway (in Chinese), *Science China, Series D: Earth Sciences*, **49**, (D11), 1–14.

Jin, H. J., X. L. Chang and S. L. Wang, 2007: Evolution of permafrost on the Qinghai-Xizang (Tibet) Plateau since the end of the late Pleistocene, *Journal of Geophysical Research*, **112**, doi:10.1029/2006JF000521.

Jin, H., Q. Yu, S. Wang and L. Lu, 2008: Changes in permafrost environments along the Qinghai-Tibet engineering corridor induced by anthropogenic activities and climate warming, *Cold Regions Science and Technology*, **53**, (3), 317–333.

Johansen, O., 1975: *Thermal conductivity of soils*, Dissertation, PhD Thesis, Trondheim, Norway (CRREL draft translation 637, 1977).

Jorgenson, M. and R. Kreig, 1988: A model for mapping permafrost distribution based on landscape component maps and climatic variables, in *5th International Conference on Permafrost*.

Jorgenson, M., C. Racine, J. Walters and T. Osterkamp, 2001: Permafrost degradation and ecological changes associated with a warming climate in central Alaska, *Climatic Change*, **48**, (4), 551–579.

Juliussen, H. and O. Humlum, 2007: Towards a TTOP ground temperature model for mountainous terrain in central-eastern Norway, *Permafrost and Periglacial Processes*, **18**, 161–184.

Juliussen, H. and O. Humlum, 2008: Thermal regime of openwork block Fields on the mountains Elgahogna and Solen, central-eastern Norway, *Permafrost and Periglacial Processes*, **19**, 1–18.

Jury, W. A. and K. Roth, 1990: *Transfer functions and solute movement through soils: theory and applications*, Birkhauser Verlag.

Kaatze, U., 1989: Complex permittivity of water as a function of frequency and temperature, *Journal of Chemical and Engineering Data*, **34**, 371–374.

Kane, D. L., L. D. Hinzman and J. P. Zarling, 1991: Thermal response of the active layer to climatic warming in a permafrost environment, *Cold Regions Science and Technology*, **19**, (2), 111–122.

Kane, D. L., K. M. Hinkel, D. J. Goering, L. D. Hinzman and S. I. Outcalt, 2001: Non-conductive heat transfer associated with frozen soils, *Global and Planetary Change*, **29**, 275–292.

Karunaratne, K. C., 2003: N-factors and the relations between air and surface temperature in discontinuous permafrost near Mayo, Yukon territory, Master's thesis, Carleton University.

Klene, A. E., F. E. Nelson and N. Shiklomanov, 2001: The N-factor in natural landscapes: variability of air and soil-surface temperatures, Kuparuk River Basin, Alaska, U.S.A, *Arctic, Antarctic and Alpine Research*, **33**, (2), 140–148.

Kneisel, C., C. Hauck, R. Fortier and B. Moorman, 2008: Advances in geophysical methods for permafrost investigation, *Permafrost and Periglacial Processes*, **19**, 157–178.

Kolmogorov, A. N., 1980: *Proceedings of the Royal Society*.

König, K., November 2008: Thermal dynamics of permafrost sites on the Qinghai-Tibet Plateau, Diploma thesis, Heidelberg University, Heidelberg.

Kudryavtsev, V., L. Garagulya, K. Kondratyeva and V. Melamed, 1974: *Fundamentals of frost forecasting in geological engineering investigations*, Cold Regions Reseach and Engineering Laboratory: Hanover, NH.

Laurent, J. P., P. Ruelle, L. Delage, A. Zairi, B. B. Nouna and T. Adjmi, 2005: Monitoring soil water content profiles with a commercial TDR system: comparative field tests and laboratory calibration, *Vadose Zone Journal*, **4**, (4), 1030–1036.

Li, S., 1991: Premary study of lacustrine sedimentation and lake evolution in southern slope of western Kunlun mountains (in Chinese), *Scientia Geographica Sinica*, **11**, 336–342.

Li, X. and G. Cheng, 1999: A GIS-aided response model of high-altitude permafrost to global change (in Chinese), *Science in China Series (D: Earth Sciences)*, **42**, (1), 72–79.

Liebethal, C., B. Huwe and T. Foken, 2005: Sensitivity analysis for two ground heat flux calculation approaches, *Agricultural and Forest Meteorology*, **132**, (3-4), 253–262.

Li, J., S. Wen, Q. Zhang, F. Wang, B. Zheng and B. Li, 1979: Time and magnitude of the uplift of the Qinghai-Xizang Plateau (in Chinese), *Scientia Sinica (Series B)*, **6**, 608–616.

Li, G., T. Duan and Y. Gong, 2000: The bulk transfer coefficients and surface fluxes on the western Tibetan Plateau (in Chinese), *Chinese Science Bulletin*, **45**, (13), 1221–1226.

Li, D., G. Ji and L. Lv, 2001: The impact of the Tibetan Plateau surface heating field intensity on the Northern Hemispherical general circulations and weather and the climate of China (in Chinese), *Science in China (series D)*, **44**, 390–399.

Li, G., T. Duan and G. Wu, 2003: The intersity of surface heat source and surface heat balance on the western Qinghai-Xizang Plateau (in Chinese), *Scientia Geographica Sinica*, **23**, (1), 13–18.

Li, L., F. Li, A. Guo and X. Zhu, 2006: Study on the climate change trend and Its catastrophe over "Sanjiangyuan" region in recent 43 years (in Chinese), *Journal of natural resources*, **21**, (1), 79–85.

Li, S., H. Zhang, Y. Shi and Z. Zhu, 2008: A high resolution MIS 3 environmental change record derived from lacustrine deposit of Tianshuihai lake. Qinghai-Tibet Plateau (in Chinese), *Quaternary Sciences*, **1**, 122–131.

Liu, X. and B. Chen, 2000: Climatic warming in the Tibetan Plateau during recent decades, *Ineternational journal of climatology*, **20**, 1729–1742.

Loeffler, O. and M. Bano, 2004: Ground penetrating radar measurements in a controlled vadose zone influence of the water content, *Vadose Zone Journal*, **3**, 1082–1092.

Löscher, M. and T. Haag, 1989: Zum Alter der Dünen im nördlichen Oberrheingraben bei Heidelberg und zur Genese ihrer Bänderparabraunerden, *Eiszeitalter und Gegenwart*, **39**, 98–108.

Ludin, A. R., 2010: Permafrost temperature analysis and projection from Samoylov Island in the Lena River Delta, Siberia, Diploma thesis, Heidelberg university.

Lunardini, V., 1978: Theory of N-factors and correlation of data, in *In Proceedings of the Third International Conference on Permafrost*.

Lunardini, V., 1981: *Heat transfer in cold climates*, Van Nostrand Reinhold: New York.

Lunt, I. A., S. S. Hubbard and Y. Rubin, 2005: Soil moisture content estimation using ground-penetrating radar reflection data, *Journal of Hydrology*, **307**, 254–269.

Ma, W. and Y. Ma, 2006: The annual variations on land surface energy in the northern Tibetan Plateau (in Chinese), *Environmental Geology*, **50**, (5), 645–650.

Ma, Z., P. Du and H. Hong, 2003: *Structure and dynamics of the Earth*, Guangdong Science and Technology Press.

Ma, Y., T. Yao and J. Wang, 2006: Experimental study of energy and water cycle in Tibetan Plateau — The progress introduction on the study of GAME/Tibet and CAMP/Tibet, *Plateau Meteorology*, **25**, (2), 344–351.

Marchenko, S., V. Romanovsky and G. Tipenko, 2008, Numerical modeling of spatial permafrost dynamics in Alaska.

Marsaglia, G. and T. A. Bray, 1964: A convenient method for generating normal variables, *SIAM Review*, **6**, (3), 260–264.

Massman, W. J., 1992: Correcting errors associated with soil heat flux measurements and estimating soil thermal properties from soil temperature and heat flux plate data, *Agricultural and Forest Meteorology*, **59**, (3-4), 249–266.

Matsuoka, N. and O. Humlum, 2003: Monitoring periglacial processes: new methodology and technology, *Permafrost and Periglacial Processes*, **14**, 299–303.

Molnar, P., P. England and J. Martinod, 1993: Mantle dynamics, the uplift of the Tibetan Plateau, and the Indian monsoon, *Rev. Geophys*, **31**, 357–96.

Monteith, J. L. and M. H. Unsworth, 1990: *Principles of environmental physics*, Edward Arnold, London.

Moysey, S. and R. Knight, 2004: Modeling the field-scale relationship between dielectric constant and water content in heterogeneous systems, *Water Resources Research*, **40**, doi:10.1029/2003WR002589.

Neal, A., 2004: Ground-penetrating radar and its use in sedimentology: principles, problems and progress, *Earth-Science Reviews*, **66**, (3-4), 261–330.

Nelson, F. and S. Outcalt, 1987: A computational method for prediction and regionalization of permafrost, *Arctic and Alpine Research*, **19**, (3), 279–288.

Osterkamp, T. E., 2007: Characteristics of the recent warming of permafrost in Alaska, *Journal of Geophysical Research*, **112**, doi:10.1029/2006JF000578.

Osterkamp, T., L. Viereck, Y. Shur, M. Jorgensen, C. Racine, A. Doyle and R. Boone, 2000: Observations of thermokarst and its impact on boreal forests in Alaska, U.S.A., *Arctic, Antarctic and Alpine Research*, **32**, 303–315.

Outcalt, S. and K. Hinkel, 1989: Night-frost modulation of nearsurface soil-water ion concentration and thermal fields, *Physical Geography*, **10**, 336–348.

Outcalt, S., F. Nelson and K. Hinkel, 1990: The zero-curtain effect: heat and mass transfer across an isothermal region in freezing soil, *Water Resources Research*, **26**, (7), 1509–1516.

Pavlov, A. and S. Grechishchev, 1999: The monitoring and prediction of permafrost temperature, distribution and geocryological processes within russia under global climate changes, in *Advances in Cold-Region Thermal Engineering and Sciences*, edited by K. Hutter, Y. Wang, and H. Beer, vol. 533 of *Lecture Notes in Physics*, 503–510, Springer Berlin / Heidelberg.

Peng, X., Q. Wu and M. Tian, 2003: The effect of groundwater table lowering on ecological environment in the headwater s of the Yellow River (in Chinese), *Journal of Glaciology and Geocryology*, **25**, (6), 667–671.

Peng, Y., H. Zhang, H. Liu, L. Bian, S. Li, L. Kang, J. Chen, M. Zhou and X. Xu, 2005: Characteristics of micro-meteorology in the surface layer over Tibetan Plateau area (in Chinese), *Acta Scientiarum Naturalium Universitatis Pekinensis*, **41**, (2), 180–190.

Pidwirny, M., 2006: *Fundamentals of physical geography*.

Pringle, D. J., W. W. Dickinson, H. J. Trodahl and A. R. Pyne, 2003: Depth and seasonal variations in the thermal properties of Antarctic Dry Valley permafrost from temperature time series analysis, *Journal of Geophysical Research*, **108**, doi:10.1029/2002JB002364.

Prowse, T. D., F. J. Wrona, J. D. Reist, J. J. Gibson, J. E. Hobbie, L. M. J. Levesque and W. F. Vincent, 2006: Climate change effects on hydroecology of arctic freshwater ecosystems, *AMBIO: A Journal of the Human Environment*, **35**, (7), 347–358.

Ramage, C., 1971: *International Geophysics Series*, chapter Monsoon Meteorology, 296 pp, Academic Press, San Diego, Calif.

Raymo, M. E. and W. F. Ruddiman, 1992: Tectonic forcing of late Cenozoic climate, *Nature*, **359**, 117–122.

Riseborough, D., 2002: The mean annual temperature at the top of permafrost, the TTOP model, and the effect of unfrozen water, *Permafrost and Periglacial Processes*, **13**, (2), 137–143.

Riseborough, D., 2004: *Exploring the parameters of a simple model of the permafrost-climate relationship*, Dissertation, Carleton University.

Riseborough, D., 2007: The effect of transient conditions on an equilibrium permafrost-climate model, *Permafrost and Periglacial Processes*, **18**, 21–32.

Riseborough, D., N.Shiklomanov, B.Etzelmuller, S.Gruber and S.Marchenko, 2008: Recent advances in permafrost modeling, *Permafrost and Periglacial Processes*, **19**, (2), 137–156.

Robinson, D. A., S. B. Jones, J. M. Wraith, D. Or and S. P. Friedman, 2003: A review of advances in dielectric and electrical conductivity measurement in soils using time domain reflectometry, *Vadose Zone Journal*, **2**, (4), 444–475.

Robinson, D. A., M. G. Schaap, D. Or and S. B. Jones, 2005: On the effective measurement frequency of time domain reflectometry in dispersive and nonconductive dielectric materials, *Water Resources Research*, **41**, doi:10.1029/2004WR003816.

Romanovsky, V. E. and T. E. Osterkamp, 1995: Interannual variations of the thermal regime of the active layer and near-surface permafrost in northern Alaska, *Permafrost and Periglacial Processes*, **6**, 313–335.

Romanovsky, V. and T. Osterkamp, 1997: Thawing of the active layer on the coastal plain of the Alaskan. Arctic, *Permafrost and Periglacial Processes*, **8**, (1), 1–22.

Roth, K. and J. Boike, 2001: Quantifying the thermal dynamics of a permafrost site near Ny-. ålesund, Svalbard, *Water Resources Research*, **37**, (12), 2901–2914.

Roth, K., R. Schulin, H. Flühler and W. Attinger, 1990: Calibration of time domain reflectometry for water content measurement using a composite dielectric approach, *Water Resources Research*, **26**, 2267–2273.

Rowley, D. B. and B. S. Currie, 2006: Palaeo-altimetry of the late Eocene to Miocene Lunpola basin, central Tibet, *Nature*, **439**, 677–681.

Sauer, T. J., D. W. Meek, T. E. Ochsner, A. R. Harris and R. Horton, 2003: Errors in heat flux measurement by flux plates of constrasting design and thermal conductivity, *Vadose Zone Journal*, **2**, (4), 580–588.

Shi, Y., B. Zheng and S. Li, 1990: Last glaciation and maximum glaciation on the Qinghai-Xizang Plateau (in Chinese), *Journal of Glaciology and Geocryology*, **12**, 1–29.

Shirazi, T., D. M. Allen, W. L. Quinton and J. W. Pomeroy, 2009: Estimating soil thaw energy in sub-Alpine tundra at the hillslope scale, Wolf Creek, Yukon Territory, Canada, *Hydrology Research*, **40**, (1), 1–18.

Shur, Y. L. and M. T. Jorgenson, 2007: Patterns of permafrost formation and degradation in relation to climate and ecosystems, *Permafrost and Periglacial Processes*, **18**, 7–19.

Slob, E., M. Sato and G. Olhoeft, 2010: Surface and borehole ground-penetrating-radar developments, *Geophysics*, **75**, (5), 75A103–75A120.

Smith, M. W. and D. W. Riseborough, 1996: Permafrost monitoring and detection of climate change, *Permafrost and Periglacial Processes*, **7**, 301–309.

Smith, C., M. Clark, G. Broll, C. L. Ping, J. M. Kimble and G. Luo, 1999: Characterization of selected soils from the Lhasa region of Qinghai-Xizang Plateau, SW China, *Permafrost and Periglacial Processes*, **10**, (3), 211–222.

Song, X., H. Zhang, X. Liu, S. Fan, H. Liu, F. Hu, S. Li, M. Zhou, L. Bian and X. Xu, 2006: Determination of atmospheric boundary layer height in unstable conditions over the middle Tibetan Plateau (in Chinese), *Acta Scientiarum Naturalium Universitatis Pekinensis*, **42**, (3), 328–333.

Stocker, C. M., M. Hoelzle and W. Haeberli, 2002: Modelling alpine permafrost distribution based on energy-balance data; a first step, *Permafrost and Periglacial Processes*, **13**, 271–282.

Stull, R. B., 1988: *An introduction to boundary layer meteorology*, Kluwer Acad., Norwell, Mass.

Stull, R. B., 1994: A convective transport theory for surface fluxes, *Journal of the Atmospheric Sciences*, **51**, (1), 3–22.

Su, Z., Z. Xie and Z. Wang, 1998: *Kala Kunlun mountains – Kunlun mountains region: glacial and environment*, Sciences Press.

Tanaka, K., H. Ishikawa, T. Hayashi, I. Tamagawa and Y. Ma, 2001: Surface energy budget at Amdo on the Tibetan Plateau using GAME/Tibet IOP98 data, *Journal of Meteorological Society of Japan*, **79**, 505–517.

Tanaka, K., I. Tamagawa, H. Ishikawa, Y. Ma and Z. Hu, 2003: Surface energy budget and closure of the eastern Tibetan Plateau during the GAME-Tibet IOP 1998, *Journal of Hydrology*, **283**, (1), 169–183.

Tang, M., 1995: The interannual oscillation of the plateau monsoon and its reason (in Chinese), *Scientia Meteorologica Sinica*, **15**, (4), 64–68.

Tang, M., Z. Shen and Y. Chen, 1979: The average climatic characteristics of the plateau monsoon (in Chinese), *Acta Geographica Sinica*, **34**, (1), 33–41.

Topp, G. C., J. L. Davis and A. P. Annan, 1980: Electromagnetic determination of soil water content: measurement in coaxial transmission lines, *Water Resources Research*, **16**, 574–582.

Trenberth, K., D. Stepaniak and J. Caron, 2000: The global monsoon as seen through the divergent atmospheric circulation, *Journal of Climate*, **13**, 3969–3993.

Van der Voo, R., W. Spakman and H. Bijwaard, 1999: Tethyan subducted slabs under India, *Earth and Planetary Science Letters*, **171**, 7–20.

van Loon, W. K. P., H. M. H. Bastings and E. J. Moors, 1998: Calibration of soil heat flux sensors, *Agricultural and Forest Meteorology*, **92**, (1), 1–8.

van Wijk, W. and D. de Vries, 1963: *Periodic temperature variations in a homogeneous soil*, North Holland Publ. Co.

Waelbroeck, C., 1993: Climate-soil processes in the presence of permafrost: a systems modelling approach, *Ecological Modelling*, **3-4**, 185–225.

Wang, S., 1997: Study of permafrost degradation in the Qinghai-Xizang Plateau (in Chinese), *Advances in Earth Science*, **12**, (2), 164–167.

Wang, J. and R. L. Bras, 1998: A new method for estimation of sensible heat flux from air temperature, *Water Resources Research*, **34**, (9), 2281–2288.

Wang, G. and G. Chen, 1998: On some problems of eco-environment research in the source regions of the Yangtze and Yellow rivers (in Chinese), *Adances in Earth Sciences*, **13**, (Suppl.), 11–17.

Wang, B. and H. M. French, 1994: Climate controls and high-altitude permafrost, Qinghai-Xizang (Tibet) Plateau, China, *Permafrost and Periglacial Processes*, **5**, (2), 87–100.

Wang, S., Q. Lin and L. Zhao, 1999: Permafrost along the Qingahi-Kang Highway (National Highway No.214) (in Chinese), *Journal of glaciology and geocryology*, **22**, (2), 42–49.

Wang, S., L. Zhao and S. Li, 2002: Interaction between permafrost and desertification on the Qinghai-Tibet Plateau (in Chinese), *Journal of dersert research*, **22**, (1), 33–39.

Wang, G., H. Hu, G. Li and N. Li, 2009*a*: Impacts of changes in vegetation cover on soil water heat coupling in an alpine meadow of the Qinghai-Tibet Plateau, China, *Hydrology and Earth System Sciences*, **13**, 327–341.

Wang, G., H. Hu and T. Li, 2009*b*: The influence of freeze-thaw cycles of active soil layer on surface runoff in a permafrost watershed, *Journal of Hydrology*, **375**, (3-4), 438–449.

Weast, R. C., 1985: *Handbook of Chemistry and Physics*, CRC Press, 67th ed.

Weber, S., A. Graf and B. G. Heusinkveld, 2007: Accuracy of soil heat flux plate measurements in coarse substrates – Field measurements versus a laboratory test, *Theoretical and Applied Climatology*, **89**, 109–114.

Westermann, S., U. Wollschläger and J. Boike, 2010: Monitoring of active layer dynamics at a permafrost site on Svalbard using multi-channel ground-penetrating radar, *The Cryosphere*, **4**, 475–487.

White, D., L. Hinzman, L. Alessa, J. Cassano, M. Chambers, K. Falkner, J. Francis, W. J. G. Jr., M. Holland, R. M. Holmes, H. Huntington, D. Kane, A. Kliskey, C. Lee, J. McClelland, B. Peterson, T. S. Rupp, F. Straneo, M. Steele, R. Woodgate, D. Yang, K. Yoshikawa and T. Zhang, 2007: The arctic freshwater system: Changes and impacts, *Journal of Geophysical Research*, **112**, doi:10.1029/2006JG000353.

Wollschläger, U. and K. Roth, 2005: Estimation of temporal changes of volumetric soil water content from ground penetrating radar reflections, *Subsurface Sensing Technologies and Applications*, **6**, 207–218.

Wollschläger, U., H. Gerhards, Q. Yu and K. Roth, 2010: Multi-channel ground-penetrating radar to explore spatial variations in thaw depth and moisture content in the active layer of a permafrost site, *The Cryosphere Discuss.*, **4**, 269–283.

Woo, M. and Z. Xia, 1996: Effects of hydrology in the thermal conditions of the active layer, *Nordic Hydrologiy*, **27**, 129–142.

Wu, Q., 2007: Responses of permafrost on the Qinghai-Tibet Plateau, China, to climate change and engineering construction, *Arctic, Antarctic, and Alpine Research*, **39**, (4), 682–687.

Wu, T. and Z. Qian, 2003: The relation between the Tibetan winter snow and the Asian summer monsoon and rainfall: an observational investigation, *Journal of Climate*, **16**, 2038–2051.

Wu, H. and X. Yu, 2002: The hydrological characteristics in the source area of Yangtze river and Tongtianhe river basin (in Chinese), *Hydrology*, **22**, (1), 52–53.

Wu, Q. and T. Zhang, 2008: Recent permafrost warming on the Qinghai-Tibetan Plateau, *Journal of Geophysical Research*, **13**, doi:10.1029/2007JD009539.

Wu, Q. and T. Zhang, 2010: Changes in active layer thickness over the Qinghai-Tibetan Plateau from 1995 to 2007, *Journal of Geophysical Research*, **115**, doi:10.1029/2009JD012974.

Wu, Q., Z. Lu and Y. Liu, 2005: Permafrost monitoring and its recent changes in Qinghai-Tibet Plateau (in Chinese), *Adances in climate change research*, **1**, (1), 26–28.

Xie, C., Y. Ding, S. Liu and G. Wang, 2003: Comparison analysis of runoff change in the source regions of the Yangtze and Yellow River (in Chinese), *Journal of Glaciology and Geocryology*, **25**, (4), 414–422.

Xu, Y., Y. Ding and D. Li, 2003: Climatic change over Qinghai and Xizang in 21st century (in Chinese), *Plateau meteorology*, **22**, (5), 451–457.

Yang, Z. and M. Woo, 1990: Streamflow characteristics of the eastern Qinghai Plateau (in Chinese), *Journal of Glaciology and Geocryology*, **12**, (3), 219–226.

Yang, J., Y. Ding, R. Chen and Y. Shen, 2004*a*: Permafrost change and lts effect on eco-environment in the source regions of the Yangtze and Yellow rivers (in Chinese), *Journal of Mountain Science*, **22**, (3), 278–285.

Yang, K., T. Koike, H. Fujii, T. Tamura, X. Xu, L. Bian and M. Zhou, 2004*b*: The daytime evolution of the atmospheric boundary layer and convection over the Tibetan Plateau: observations and simulations, *Journal of the Meteorological Society of Japan*, **82**, (6), 1777–1792.

Yang, M., S. Wang, T. Yao, X. Gou, A. Lu and X. Guo, 2004*c*: Desertification and its relationship with permafrost degradation in Qinghai-Xizang (Tibet) Plateau, *Cold Regions Science and Technology*, **39**, (1), 47–53.

Yang, J., Y. Ding and R. Chen, 2007: Climatic causes of ecological and environmental variations in the source regions of the Yangtze and Yellow Rivers of China (in Chinese), *Environmental Geology*, **53**, 113–121.

Yao, J., L. Zhao, Y. Ding, L. Gu, K. Jiao, Y. Qiao and Y. Wang, 2008: The surface energy budget and evapotranspiration in the Tanggula region on the Tibetan Plateau, *Cold Regions Science and Technology*, **52**, 326–340.

Ye, D., 1981: Some characteristics of the summer circulation over the Qinghai-Xizang (Tibet) Plateau and its neighborhood, *Bulletin American Meteorological Society*, **62**, (1), 14–19.

Yin, A. and T. Harrison, 2000: Geologic evolution of the Himalayan-Tibetan orogen, *Annual Review of Earth and Planetary Sciences*, **28**, 211–280.

Zhang, Y., 1996: Division and evolution of the Hoh xil-Bayan Har sedimentary basin (in Chinese), *Qinghai Geology*, **1**, 1–17.

Zhang, T. and T. E. Osterkamp, 1995: Considerations in determining thermal diffusivity from temperature time series using finite difference methods, *Cold Regions Science and Technology*, **23**, 333–341.

Zhang, T., T. Osterkamp and K. Stamnes, 1996: Influence of the depth hoar layer of the seasonal snow cover on the ground thermal regime, *Water Resources Research*, **32**, (7), 2075–2086.

Zhang, Y., T. Ohata and T. Kadota, 2003*a*: Land-surface hydrological processes in the permafrost region of the eastern Tibetan Plateau, *Journal of Hydrology*, **283**, 41–56.

Zhang, Y., W. Chen and J. Cihlar, 2003*b*: A process-based model for quantifying the impact of climate change on permafrost thermal regimes, *Journal of Geophysical Research*, **108**, doi:10.1029/2002JD003354.

Zhang, S., Y. Wang, Y. Zhao, Y. Huang, Y. Li, W. Shi and X. Shang, 2004: Permafrost degradation and its environmental sequent in the source regions of the Yellow River (in Chinese), *Journal of Glaciology and Geocryology*, **26**, (1), 1–6.

Zhang, T., O. Frauenfeld, M. Serreze, A. Etringer, C. Oelke, J. McCreight, R. Barry, D. Gilichinsky, D. Yang, H. Ye, F. Ling and S. Chudinova, 2005: Spatial and temporal variability in active layer thickness over the Russian Arctic drainage basin, *Journal of Geophysical Research-Atmospheres*, **110**, D16101. DOI:10.1029/2004JD005642.

Zhang, W., S. Li, T. Wu and Q. Pang, 2006*a*: Changes of the differences between ground and air temperature over the Qinghai-Xizang Plateau (in Chinese), *ACTA geographica sinica*, **61**, (9), 899–910.

Zhang, Y., W. Chen and D. Riseborough, 2006*b*: Temporal and spatial changes of permafrost in Canada since the end of the Little Ice Age, *Journal of Geophysical Research*, **111**, doi: 10.1029/2006JD007284.

Zhang, T., R. G. Barry, K. Knowles, J. A. Heginbottom and J. Brown, 2008: Statistics and characteristics of permafrost and ground-ice distribution in the Northern Hemisphere, *Polar Geography*, **31**, (1), 47–68.

Zhao, L., G. Cheng and S. Li, 2000: Thawing and freezing processes of active layer in Wudaoliang region of Tibetan Plateau (in Chinese), *Chinese Science Bulletin*, **45**, (23), 2181–2186.

Zhao, L., Q. Wu, S. Marchenko and N. Sharkhuu, 2010: Thermal state of permafrost and active layer in Central Asia during the international polar year, *Permafrost and Periglacial Processes*, **21**, (2), 198–207.

Zhou, Y., 1965: *Permafrost conditions in the Fenhuo Shan Mountains, in monograph on the permafrost along the Qinghai-Tibet Highway*, 1–10, Sciences Press, Beijing.

Zhou, Y. and D. Guo, 1982: Principal characteristics of permafrost in China (in Chinese), *Journal of Glaciology and Geocryology*, **4**, 1–19.

Zhou, Y., D. Guo, G. Qiu, G. Cheng and S. Li, 2000: *Geocryology in China (in Chinese)*, Sciences Press, Beijing.

Zhou, N., N. Qin, Q. Tu and D. Li, 2005: Analyses on regional characteristics of temperature changes over Qinghai-Xizang Plateau in recent 50 years (in Chinese), *Plateau meteorology*, **24**, (3), 344–349.

Zhu, L., Z. Wu, E. Zang, B. Pan, Y. Liu and G. Tao, 1996: Difference of permafrost degeneration in the east of the Tibetan Plateau (in Chinese), *Journal of Glaciology and Geocryology*, **18**, (2), 104–110.

Zimov, S. A., E. A. G. Schuur and F. S. Chapin III, 2006: CLIMATE CHANGE: permafrost and the global carbon budget, *Science*, **312**, 1612–1613.

Part I

Appendix

A
Installation at the study sites

A.1 Temperature sensors

Table A.1. Position of soil temperature sensors installed at all the stations.

Chumaer		Qumahe	Zuimatan	Tianshuihai	
P1	P2			P1	P2
0.05	0.05	0.02	0.05	0.04	0.04
0.1	0.1	0.05	0.1	0.14	0.12
0.15	0.15	0.1	0.15	0.26	0.21
0.2	0.2	0.15	0.2	0.31	0.28
0.3	0.3	0.2	0.4	0.435	0.385
0.5	0.5	0.3	0.59	0.585	0.505
0.7	0.7	0.4	0.8	0.73	0.635
0.9	0.9	0.55	1.0	0.85	0.72
1.1	1.1	0.7	1.2	0.97	0.86
1.3	1.3	0.9	1.4	1.085	0.98
1.5	1.5	1.1	1.6	1.21	1.1
1.7	1.7	1.2	1.9	1.335	1.2
1.9	1.9	1.25	2.22	1.46	1.3
2.0	2.08	1.3	2.42	1.57	1.44
2.09	2.18	1.45	2.52	1.7	1.625
	2.28	1.57	2.62		1.81

A.2 TDR & CS616 sensors

Table A.2. Position of soil water content sensors installed at all the stations.

Chumaer		Qumahe		Zuimatan		Tianshuihai	
P1	P2					P1	P2
CS616		CS616	TDR	CS616	TDR	TDR	
0.14	0.1	0.05	0.1	0.1	0.05	0.075	0.11
0.33	0.2	0.1	0.4	0.19	0.1	0.205	0.28
0.64	0.4	0.2	0.6	0.295	0.2	0.42	0.385
0.9	0.65	0.3	0.75	0.445	0.3	0.58	0.505
1.1	0.89	0.4	0.9	0.575	0.4	0.74	0.72
1.3	1.19	0.6	1.04	0.735	0.6	1.00	0.86
1.5	1.54	0.75	1.2	0.9	0.75	1.09	0.98
1.7	1.92	0.9	1.3	1.05	0.9	1.315	1.10
1.9	2.1			1.23		1.46	1.30
2.09	2.28			1.49		1.54	1.44
						1.69	1.625

B
Topography of the study regions

B.1 Chumaer & Qumahe

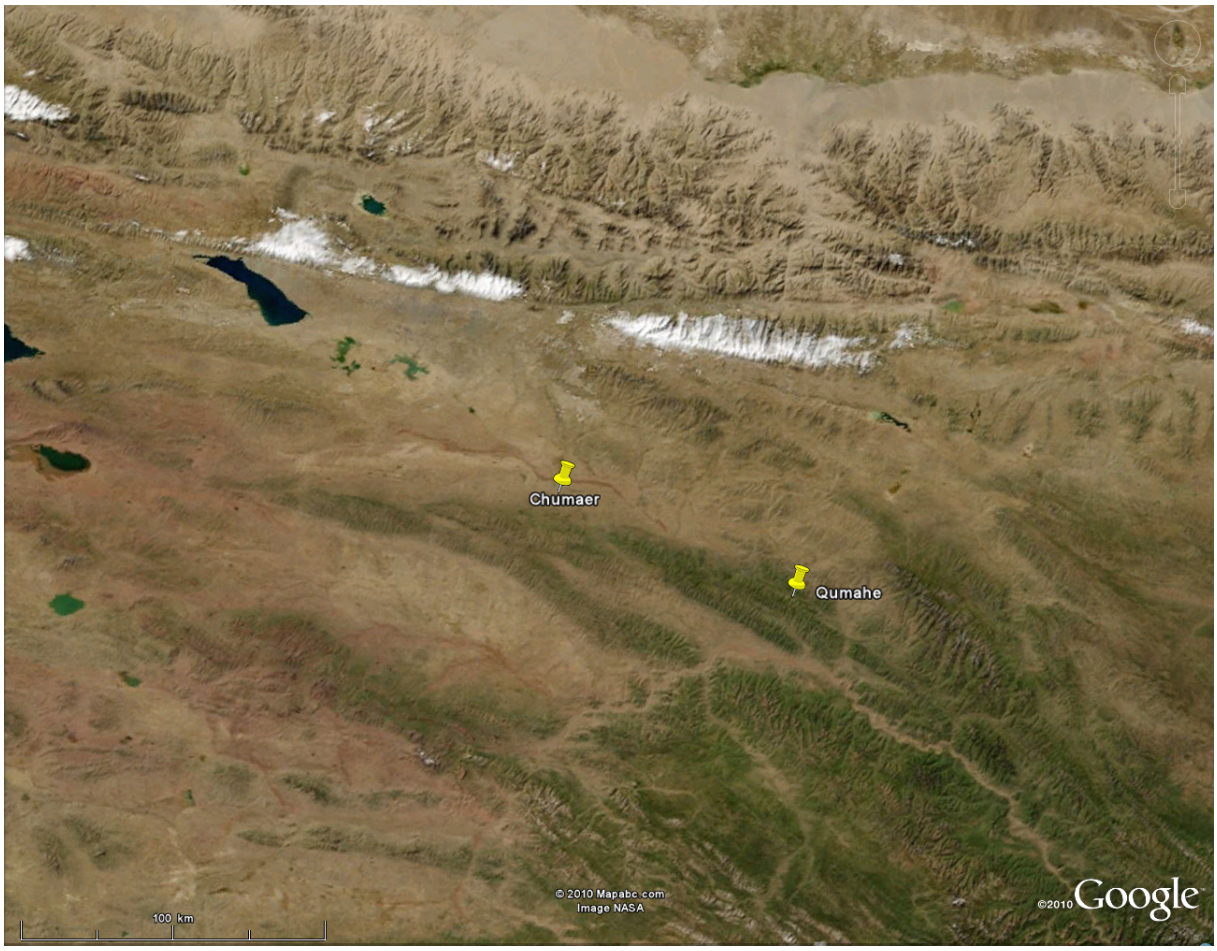

Figure B.1. Topography in the Chumaer & Qumahe region. This satellite image is from Google Earth.

B.2 Zuimatan

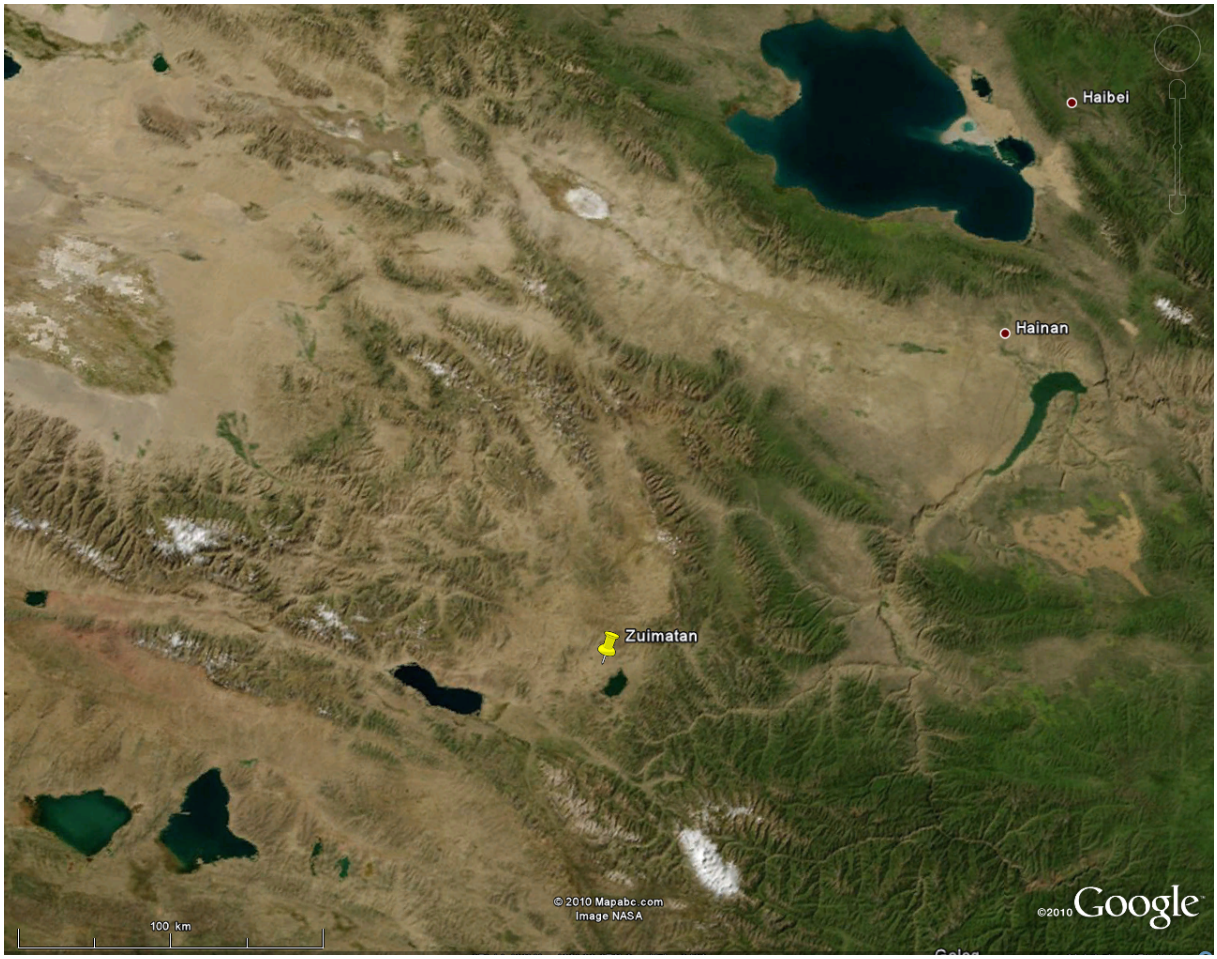

Figure B.2. Topography in the Zuimatan region. This satellite image is from Google Earth.

B.3 Tianshuihai

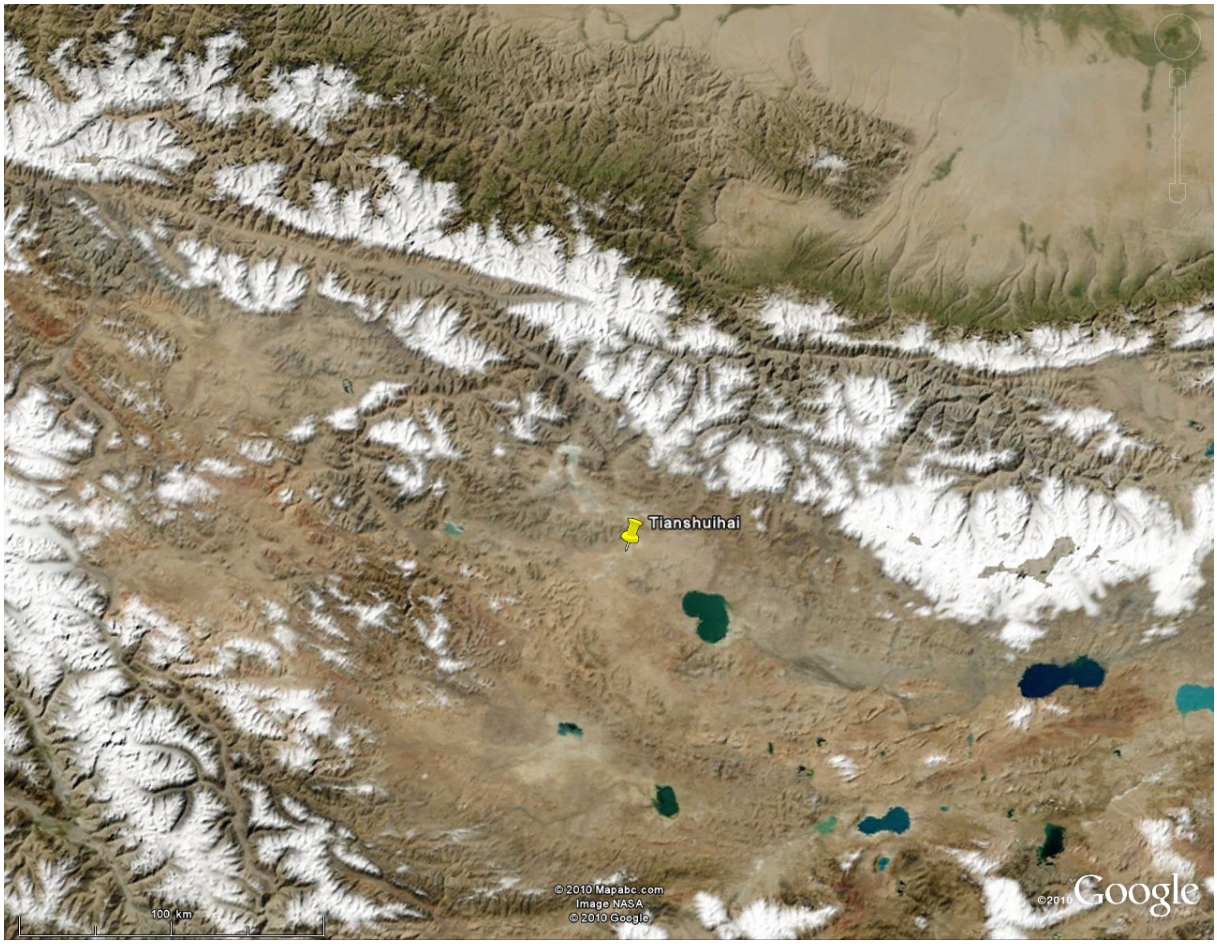

Figure B.3. Topography in the Tianshuihai region. This satellite image is from Google Earth.

Eidesstattliche Erklärung

zur Anfertigung der Dissertation

Ich erkläre hiermit an Eides Statt, dass ich die vorliegende Arbeit mit dem Titel "Hydraulic and Thermal Dynamics at Various Permafrost Sites on the Qinghai-Tibet Plateau " selbständig sowie ohne unzulässige Hilfe Dritter und ohne Benutzung anderer als der angegebenen Hilfsmittel angefertigt habe. Die aus anderen Quellen direkt oder indirekt übernommenen Daten und Konzepte sind unter Angabe der Quelle gekennzeichnet.

Heidelberg, 15.02.2011 Xicai Pan